A SELF-INFLATING VP/MMA HYDROGEL EXPANDER AS A POTENTIAL TREATMENT FOR CROHN'S DISEASE PROBLEM

SASZA CHYNTARA NABILLA

Oriel College

University of Oxford



DPhil Supervisor

Prof. Jan Tadeusz Czernuszka

A thesis submitted for the degree of

Doctor of Philosophy

Trinity Term 2022

A Self-inflating VP/MMA Hydrogel Expander as a Potential Treatment for Crohn's Disease Problem

Sasza Chyntara Nabilla, Oriel College

DPhil Thesis, Trinity Term 2022

Abstract

Crohn's disease (CD) is associated with chronic inflammation in regions throughout the gastrointestinal (GI) tract but is most likely to develop at the end of the small intestine and the first part of the colon. A single massive resection or multiple repeated resections in CD leads to short bowel syndrome (SBS). Therefore, a novel treatment to cure SBS is needed. Poly (vinyl pyrrolidone-methyl methacrylate) hydrogel is chosen as a self-inflating expander device to address the issue of inadequate functional intestinal length in SBS. The hydrogel employs mechanotransduction, wherein mechanical force elongates the intestine and activates cellular mechanisms regulating growth.

In this study, the VP/MMA hydrogel was designed by varying the composition ratio of each monomer and size. The ratios of VP to MMA were 95:5wt%, 90:10wt%, and 85:15wt%. The shape of hydrogel was cylindrical with the sizes of 12mmD & 3mmL (A), 6mmD & 3mmL (B), 6mmD & 6mmL (C), 6mmD & 9mmL (D), 3mmD & 3mmL (E). These variables influenced the pore size structure, swelling capacity, swelling force, and mechanical property. Finally, the hydrogel with a composition ratio of 85:15 wt% VP/MMA (VP85) was chosen for *ex vivo* and *in vivo* studies. The reason is due to the pressure generated during swelling (77.9 kPa) close to the required stress value to stretch the small intestine (78.9 kPa). Due to the small size of the rat intestine, the 2mmD & 2mmL hydrogel was chosen. A stretched segment of the intestine was found to lengthen 2.5-folds from the original length on days 1 and 7. Histological intestine sample after being stretched using hydrogel showed a significantly greater muscularis thickness, crypt depth and villous height.

Declaration

The research described in this thesis was carried out by the author at the Department of Materials, University of Oxford (2017-2022), under the supervision of Professor Jan T Czernuszka.

No part of this work has been previously submitted for a degree at this or any other university. This work is entirely original, and where the work of others is included it has been clearly acknowledged and references. A full list of references is included at the end of this thesis.

Below is a list of the presentation of the work resulting from this thesis (as of the date of submission):

1. S.C. Nabilla, R.J. Chung, J.T. Czernuszka, "Swelling Force of Hydrogel Tissue Expander Induces Intestinal Lengthening", 2022, 32nd Annual Conference of the European Society for Biomaterials, Bordeaux, France.

Acknowledgement

I would like to express my deepest gratitude to my supervisor, Prof. Jan Tadeusz Czernuszka, who guides and teaches me during my study at Materials, University of Oxford. Because of his excellent idea, help, support, encouragement, patience, and motivation, I can finish my study at the right time. In addition, it is fantastic and memorable when I am being a part of his team in the Biomaterials group. I learned everything from the beginning, starting with how the idea was first created, making a research plan, collecting the literature, designing the experiment, and implanting the final product for *in vivo* study. Therefore, not only has my knowledge about paperwork increased but also my experimental skill.

I would like to thank former and current members of the biomaterials group such as Sonia Iftekhar, Mu-Huan Lee, Chenguang Qu, Hazal Gezmis, Ilayda Karadag, Zhaoying Ma, Yang (Jim) Xu, Fangxin Li, and Xue Min for sharing their knowledge and giving their hands to help me during experiments, providing support from the beginning to the end of the project, and showing their encouragement during the difficult time. I would also like to thank Ujang Purnama and Cher-rin Chong at the Department of Physiology, at the University of Oxford, my research would not have been possible without their help such as collecting the GI tract samples to study the physiology of the samples. I also need to thank the University of Oxford, Oriel College, and the Department of Materials to provide academic support and funding to continue my study and travel to the conference.

I also have to thank our collaborator in Taiwan, Prof. Ren-Jei Chung, and his students (Thu Trang Nguyen, Yancheng Liu, Song (Ray) Long Chen, Shengrui (Terry)

Wu, Hyu Wen, Ruihua (Alice) Zhong, Qingyi (Rita), Minxuan (Cena) Ye, Sharon Chen, and Min Chin) at the Department of Chemical Engineering & Biotechnology, at the National Taipei University of Technology (NTUT) to allow me to conduct research in their laboratory to prepare samples, test the mechanical properties of GI tracts and observe the morphology of the tissues, *ex vivo* and *in vivo* (animal) studies. I would like to thank Mr Zack Peng from the Office of International Affairs, at the National Taipei University of Technology (NTUT) to help me to provide a Taiwan Experience Education Program (TEEP)@Asia Plus scholarship during my stay in Taiwan.

Finally, I would like to thank my parents, Zainul Arifin and Saptarijani Puspitadjati, who have always been my teacher in life and the best role models. Without their emotional and funding support, I couldn't finish my study on time. I also have a special word for my husband, Andre Aribowo, thank you for accompanying me and giving better suggestions as well as rock-steady support in the final submission. I would also like to thank my mother-in-law, Rita Indah, who always support and encourage me to finish my study. Thanks to my brother and sister (Dhio Rizaldy Divaranda, Sella Anggraini Harahap, Michael Aribowo, and Katherine Lee) who encourage me. I could not have done any of this without you.

Table of Contents

Abstract i

Declaration ii

Acknowledgement iii

Table of Contents v

List of Figures viii

List of Tables xix

Abbreviations and Acronyms xxii

1. Introduction 2

1.1 Objectives 2

1.2 Thesis Outline 4

2.1 Crohn's Disease and Management of Short Bowel Syndrome 7

2.2 Development of Intestinal Lengthening Research for SBS Patients 13

2.3 Self-inflating Hydrogel Tissue Expander 24

2.3.1 Effect of Hydrophilicity/Hydrophobicity 29

2.3.2 The Microstructure of Hydrogel 29

2.3.3 Mechanisms of Hydrogel Swelling 34

2.3.4 Kinetics of Hydrogel Swelling 35

2.3.5 Mechanical Properties of Hydrogel 39

2.4 Structure, Properties, and Function of Gastrointestinal (GI) Tracts 43

2.4.1 Esophagus 44

2.4.2 Stomach 47

2.4.3 Small intestine 51

2.4.4 Large intestine 55

2.5 Summary 58

3.1 Introduction 60

3.2 Synthesis of VP/MMA Xerogels 61
3.3 Nuclear Magnetic Resonance (NMR).....66
3.4 Fourier Transform Infra-Red (FTIR).....67
3.5 Water Contact Angle (WCA) 68
3.6 Scanning Electron Microscope (SEM) 69
3.7 Compression Testing 69
3.8 Volume Swelling and Gel Fraction Measurement.....70
3.9 Swelling Force Measurement 71
3.10 Differential Scanning Calorimetry (DSC) 71
3.11 Anisotropic Hydrogels.....72
3.12 Mechanical Testing of GI Tract Tissues.....73
3.13 SEM of GI Tract Tissues 75
3.14 *Ex vivo* Study 76
3.15 *In vivo* Study 78
3.16 Statistical Analysis.....80
3.17 Summary.....81
4.1 Introduction.....83
4.2 Characterization of Hydrogels.....84
4.2.1 Chemical Structures and Purities of the Monomers 84
4.2.2 Functional Group of VP/MMA Copolymers.....88
4.2.3 Wettability and Surface Energy.....92
4.2.4 Microarchitecture of Hydrogels 96
4.2.5 Mechanical Properties of Hydrogels 98
4.2.6 Glass Transition Temperature 107
4.3 Swelling Behaviour Study of Hydrogels 110

4.3.1 Volume Swelling and Diffusion of Hydrogels in DI Water.....110
4.3.1.1 Effect of Chemical Composition on the Swelling.....112
4.3.1.2 Effect of Hydrogel Size on the Swelling Behaviour.....125
4.3.2 Volume Swelling and Diffusion of Hydrogels in PBS.....133
4.3.2.1 Effect of Composition Ratio on Swelling.....133
4.3.2.2 Effect of Hydrogel Sizes on Swelling.....137
4.4 Swelling Force and Swelling Pressure of the Hydrogels.....141
4.5 Anisotropic Hydrogels.....152
4.5.1 Volume Swelling and Swelling Kinetic of Anisotropic Gels.....155
4.5.1.1 Effect of Chemical Composition on the Swelling of Anisotropic Gels.155
4.5.1.2 Effect of Sizes on the Swelling of Anisotropic Gels.....160
4.5.2. Swelling Force and Swelling Pressure of Anisotropic Gels.....164
4.6 Summary.....169
5.1 Introduction.....173
5.2 Mechanical Properties of GI Tract.....173
5.3 Morphology of GI Tract Tissues.....180
5.4 Intestinal Lengthening Studies.....187
5.4.1 *Ex vivo* Study.....187
5.4.2 *In vivo* Study.....191
5.5 Summary.....207
6.1 Thesis Conclusion.....210
6.2 Future Work.....212
References.....214

List of Figures

Figure 2.1 Endoscopic findings of (A) Healthy colon (B) Irregular, serpiginous ulcer and cobblestone appearance in the colon (C) Scar formation of longitudinal ulcer (mucosal healing)..... 7

Figure 2.2 Schematic representation of the intestinal architectural distortion in CD-associated strictures 8

Figure 2.3 (A&B) Immunohistochemical staining for α-smooth muscle actin within myofibroblast (MFB) of the muscularis mucosa (MM) to the submucosa (SM) interface viewed at 100x. (A) MFB localised to the MM in the normal bowel (B) The disrupted MM in stricture bowel with MFB interposed throughout the SM (C&D) Immunohistochemical staining with Masson Trichrome of the muscularis propria (MP) was viewed at 20x. (C) The well-organised fibres of the muscle layers (D) The disrupted, thickness MP in stricture intestine with a greater collagen content interposed between fibres..... 9

Figure 2.4 Staining images of unaffected and inflamed ileum and colon. (A-C-E-G) H&E staining (B-D-F-H) Trichrome staining 9

Figure 2.5 mRNA expression of Col1-A1 in unaffected and inflamed areas of the intestine..... 10

Figure 2.6 Young's modulus of normal intestine (N=5) compared with CD-unaffected (n=11) and CD-stricture (n=11)..... 12

Figure 2.7 Photograph of jejunal segments (A) Before and (B) After lengthening and H&E appearance of the (C) Normal and (D) Lengthen jejunum (magnification x 40) 16

Figure 2.8 (A) Schematic diagram of the intestinal lengthening (B) Histology of the unlengthened and lengthened bowel (x200 magnification) 17
Figure 2.9 Microscopic appearance of normal rat jejunum (A) Treated jejunal segment (B) After 1 week of saline distension (x40) 18
Figure 2.10 The prototype of (A) Dual hydraulic piston fully, extended (B) SMA actuated device, partially extended 19
Figure 2.11 Photographs of (A) Nickel-titanium spring (B) Tissue expander device in final configuration 21
Figure 2.12 Photograph of the spring device, the bowel configuration at device placement, and lengthened bowel. Px= proximal, Ds= distal, A= anastomosis 22
Figure 2.13 (A) A 2.5-3 cm segment of the small intestine was isolated (B) The catheter was inserted into the isolated segment and PEG was injected through the catheter, then the catheter was removed and the end sutured closed (c) PEG pulled abdominal fluid into the intestinal lumen (D) Final image of the stretched segment after PEG injection 23
Figure 2.14 Rectangular OSMED expander (from left to right): with silicone envelope, without silicone envelope, after complete inflation 25
Figure 2.15 Chemical structure of poly(vinylpyrrolidone) 26
Figure 2.16 Structure of PMMA made by free radical polymerization from MMA . 27
Figure 2.17 Definition of hydrogel ξ in the ideal crosslinked network 31
Figure 2.18 Effects of crosslinker/initiator modification on the number of crosslinkers per unit volume, volume swelling ratio, and mesh size 32
Figure 2.19 A model of Fickian and non-Fickian diffusion 37
Figure 2.20 Swelling curves as indicators of transport types 37

Figure 2.21 Schematics of different types of mechanical testing set-ups for testing hydrogel mechanical properties (A) Tension (B) Compression (C) Confined compression (D) Indentation (E) Shear rheometry (F) DMA three-point bending ... 42
Figure 2.22 Mechanical test types of displacement-time (x-t) or force-time (F-t) for (A) Fixed rate for varying rates (B) Static creep or relaxation at fixed force or displacement and (C) Sinusoidal loading at varying frequency 42
Figure 2.23 GI tract system consists of four major parts: esophagus, stomach, small and large intestines..... 44
Figure 2.24 (A) Schematic representation of the histological configuration of esophagus (B) Optical microscope picture of an esophagus section 45
Figure 2.25 (A) SEM images of the distribution of collagen fibres within submucosa (B) Schematic representation of fibre arrangement..... 46
Figure 2.26 Structure of human stomach and gastric wall 48
Figure 2.27 Tensile failure stress-stretch ratio curves of the stomach stripes at different orientations and locations (A) Smaller curvature (B) Greater curvature..... 50
Figure 2.28 Structure of the small intestinal wall..... 52
Figure 2.29 (A) Collagen fiber bundles with some branching and anastomosis (a,b,c) x300 (B) Collagen fiber composed of densely packed collagen fibrils (arrow) about 80 nm in diameter x9000 53
Figure 2.30 Mechanical testing of human cadaveric and surgically removed axial specimens of the small intestine at 2λ strain rate. B is the strain level at which a sharp increase of stress begins..... 55
Figure 2.31 Schematic representation of colon structural configurations (A) Different distributions of fibrous elements characterize the different tissues leading to specific

anisotropic properties (B) Muscular layer in the axial direction within taenia coli layer (C) Circumferential direction within muscularis externa layer (D) Submucosa layer (E) An overall isotropic configuration for mucosa 56
Figure 3.1 Polymerisation of VP/MMA until xerogels formed 62
Figure 3.2 (A) Hydrogels washed in DI water for 7 days (B) Re-dried hydrogel sample 63
Figure 3.3 An AIBN molecule breaking into two free radical molecules and a nitrogen molecule 64
Figure 3.4 Initiation reaction where VP molecule reacts with a free radical (produced by the initiator) to form another free radical 64
Figure 3.5 Propagation reaction where the free radical continuous to react with VP and MMA monomers to form a polymer chain. R1 represents the NVP component and R2 represents the MMA component 65
Figure 3.6 Allyl methacrylate molecules as a crosslinker 65
Figure 3.7 A 5mm NMR tube used for the NMR experiment 66
Figure 3.8 FTIR Varian Excalibur FTS 3500 instrument 68
Figure 3.9 Swelling force measurement of hydrogels 71
Figure 3.10 Schematic of the interior of DSC 72
Figure 3.11 Thermostatically-controlled hydraulic press and anisotropic gel sample 73
Figure 3.12 (A) Tissue sample (B) Tensile test in longitudinal and (C) Circumferential directions 74

Figure 3.13 (A) Design illustration of hydrogel expander device consists of an SS plate, two hydrogels, and one intestine sample in the middle (B) The hydrogel expander device at different sizes used for *ex vivo* study 77
Figure 3.14 The failed design of the hydrogel expander device used to stretch intestines (A,B) First (C,D) Second method in the condition (A,C) Before (B,D) After stretching 77
Figure 3.15 Photograph of the intestine during implantation with a hydrogel device80
Figure 4.1 NMR spectrum of VP before and after distillation 85
Figure 4.2 NMR spectrum of MMA before and after distillation 86
Figure 4.3 % Purity of VP and MMA monomers before and after distillation 87
Figure 4.4 FTIR spectra of (A) pure PMMA (B) pure PVP (C) VP85 (D) VP90 (E) VP95 91
Figure 4.5 Contact angle and interface energies..... 93
Figure 4.6 Effect of VP/MMA compositions on the water contact angle 94
Figure 4.7 SEM images of freeze-dried VP/MMA hydrogels (A-D) VP85 (B-E) VP90 (C-F) VP95 with magnifications of (A-C) 1000x (D-F) 2000x..... 97
Figure 4.8 Compressive stress-strain curve of xerogels (dry state) and hydrogels (wet state) at various VP/MMA composition 99
Figure 4.9 Stress-strain curves of VP/MMA hydrogels at various sizes..... 104
Figure 4.10 Illustration showing the samples with sizes of 6mmD and 9mmL buckled during the compression test 106
Figure 4.11 Maximum allowable stress showing line drawn from Euler's formula (black curve line) and stress data from experiments (red dot)..... 107

Figure 4.12 DSC spectrum of VP95 xerogel showing the glass transition temperature is taken to be middle of the sloped region 109
Figure 4.13 T_g values of various VP/MMA compositions obtained from G-T equation and DSC measurement..... 110
Figure 4.14 Photograph of the swelling process of the hydrogel as a function of time 111
Figure 4.15 Schematic illustration of the shape changes hydrogel sample from initial to equilibrium stage upon the free swelling condition in DI water 112
Figure 4.16 Effect of polymer composition ratio on the gel fraction 112
Figure 4.17 Volume swelling ratio of VP/MMA hydrogels at various composition ratios..... 114
Figure 4.18 Initial swelling rate of VP/MMA hydrogel at various compositions as a function of time..... 114
Figure 4.19 Equilibrium swelling ratio as a function of VP composition 115
Figure 4.20 A clathrate cage structure around the hydrophobe..... 117
Figure 4.21 Water uptake of various composition ratios of VP/MMA hydrogel as a function of time..... 118
Figure 4.22 Natural logarithm of water uptake as of function of ln t 118
Figure 4.23 The diffusion coefficients of hydrogels as a function of VP composition 121
Figure 4.24 Effective crosslinking density as a function of VP composition..... 122
Figure 4.25 Molecular weight between crosslinks as a function of VP/MMA composition ratios..... 123

Figure 4.26 Calculated correlation length (ξ) as a function of the volume fraction ($\upsilon 2, s-1/2$) of the swollen VP/MMA hydrogels 124
Figure 4.27 Volume swelling of the hydrogel at various sizes plotted as a function of time 127
Figure 4.28 Volume swelling ratio of various hydrogel sizes as a function of time 127
Figure 4.29 Initial swelling rate of VP/MMA hydrogel at various sizes..... 129
Figure 4.30 Equilibrium volume swelling ratio of VP/MMA hydrogel at various sizes 129
Figure 4.31 Water uptake of various hydrogel sizes as a function of time..... 130
Figure 4.32 Natural logarithmic water uptake at various hydrogel sizes as a function of time 131
Figure 4.33 Volume swelling ratio of VP/MMA hydrogels at various composition ratios as a function of time swelled in DI water at room temperature and PBS at 37˚C 134
Figure 4.34 Illustration of hydrogel swelling in PBS and DI water at the initial stage (t=0) and equilibrium 136
Figure 4.35 Volume swelling of VP/MMA hydrogels at various hydrogel sizes immersed in DI water at room temperature and PBS at 37˚C as a function of time 138
Figure 4.36 Volume swelling ratio of VP/MMA hydrogels at various sizes immersed in DI water at room temperature and PBS at 37˚C as a function of time 139
Figure 4.37 Swelling force of VP/MMA hydrogels at various composition ratios as a function of time..... 142
Figure 4.38 Swelling pressure of various composition VP/MMA hydrogels as a function of time..... 144

Figure 4.39 Inverse relationship between volume swelling ratio and swelling pressure of hydrogels at the various VP/MMA composition 145
Figure 4.40 Linear relationship between the swelling pressure and elastic modulus of hydrogel samples as a function of VP concentration 147
Figure 4.41 Swelling force of various sizes of VP/MMA hydrogels as a function of time 148
Figure 4.42 Swelling pressure of VP/MMA hydrogels at various sizes as a function of time 149
Figure 4.43 Illustration of the swelling pressure generation obtained from various surface areas of hydrogels 150
Figure 4.44 SEM image of freeze-dried VP/MMA swollen gels (A-C) Isotropic and (D) Anisotropic at composition ratios of (A, D) VP85 (B, E) VP90 (C, F) VP95 at a magnification of 2000x 153
Figure 4.45 Volume swelling ratio of isotropic and anisotropic VP/MMA hydrogels at various composition ratios versus time 156
Figure 4.46 Length swelling ratio of isotropic and anisotropic VP/MMA gels at various composition ratios plotted as a function of time 157
Figure 4.47 Volume swelling ratio of isotropic and anisotropic gels at various sizes as a function of time 161
Figure 4.48 Length swelling ratio of isotropic and anisotropic hydrogels at various hydrogel sizes against time 162
Figure 4.49 Swelling force of isotropic and anisotropic hydrogels of various composition ratios as a function of time 165

Figure 4.50 Swelling pressure of isotropic and anisotropic VP/MMA hydrogels of various composition ratios swelled as a function of time 166
Figure 4.51 Swelling force of isotropic and anisotropic hydrogels at various sizes plotted as a function of time 168
Figure 4.52 Swelling pressure of isotropic and anisotropic VP/MMA hydrogels at various sizes as a function of time 168
Figure 5.1 Stress-strain curve of rat longitudinal specimens of esophagus 175
Figure 5.2 Stress-strain curves of rat longitudinal and circumferential specimens of stomach 176
Figure 5.3 Stress-strain curves of rat longitudinal and circumferential specimens of the small intestine 177
Figure 5.4 Stress-strain curves of rat longitudinal and circumferential large intestine specimens 178
Figure 5.5 SEM images of GI tract tissues (A-C) Esophagus, (D-F) Stomach (G-I) Small intestine (J-L) Large intestine at a magnification of 1000x, 5000x, and 20,000x, respectively 182
Figure 5.6 Diameter of (a) Collagen fiber and (b) Fibril bundles in the tissue 182
Figure 5.7 (A) Collagen bundles and (B) Fibrils diameter of esophagus, stomach, small intestine, and large intestine 183
Figure 5.8 SEM images of small intestine after stretched with (A-C) 0% (D-F) 10% (G-I) 20% (J-L) 30% (M-O) 40% (P-R) 50% strain 185
Figure 5.9 Crimp angle (θ_1) of undulations collagen fibre at 0% strain 186
Figure 5.10 Illustration of tilted wave configuration of collagen fibres in the small intestine 186

Figure 5.11 Photograph of intestinal lengthening using hydrogel sizes of (A) 3mmD & 3mmL (B) 2mmD & 2mmL (C) 1mmD & 1mmL observed at day 0, 1, and 7, respectively 189
Figure 5.12 *Ex vivo* study showing a change of intestinal length after being stretched with three different hydrogel sizes as a function of time..... 190
Figure 5.13 Intestinal lengthening ratio after the intestine is stretched with three different hydrogel sizes as a function of time..... 190
Figure 5.14 (A) Rat condition on day 4 after the intestine was stretched with 3mmD & 3mmL hydrogel device (B) Normal rat condition 192
Figure 5.15 Photograph of isolated-control and stretched-intestines attachment to the metal plate using biomedical grade cyanoacrylate adhesive (yellow arrow) at (A, B, E, F) Day 0 and (C, D, G, H) Day 4, respectively 194
Figure 5.16 Significant change in length and diameter of an isolated-control segment and stretched-intestine at day 0 and day 4 after hydrogel devices removal 194
Figure 5.17 H&E-staining of (A-B) Isolated-control and (C-D) Stretched-intestinal segments attached to a metal plate using cyanoacrylate adhesive observed on day 4 with magnifications 17x (A, C) and (B, D) 26x 195
Figure 5.18 Photograph of an isolated-control and stretched-segment of rat intestine observed at (A, D) Day 0, (B-E) Day 1, (C, F) and Day 7 197
Figure 5.19 Measurement of (A) Intestinal length (B) Diameter (C) Weight and (D) Surface area of both isolated-control and stretched-intestine on day 0, 1, and 7 200
Figure 5.20 H&E staining of normal, isolated-control, and stretched-intestinal segments observed on (A-C) Day 1 and (D-F) Day 7 201

Figure 5.21 Summary of histological measurement showing muscular thickness, crypt depth, and villous height in normal, isolated-control, and stretched-intestine on day 1 and 7 202
Figure 5.22 Illustration of tissue stretching by using hydrogel expander device activated cell proliferation 203
Figure 5.23 Verhoef-Van Gieson staining of isolated-control and stretched-intestinal segments on (A-B) Day 1 and (C-D) Day 7, respectively, at 17x magnification 205
Figure 5.24 Thickness of collagen in the submucosa layer of the isolated-control and stretched-intestinal segments on days 1 and 7, respectively 205
Figure 5.25 Immunohistochemistry for PECAM-1 (CD31) staining in the normal intestine, isolated-control, and hydrogel-stretched intestine on (A-C) Day 1 and (D-F) Day 7, respectively, at 17x magnification 207

List of Tables

Table 2.1 Relative amount of collagen types I, III, and V in the control, inflamed, and stricture intestine 11

Table 2.2 Summary of mechanical enterogenesis methods 14

Table 2.3 Porosity of hydrogels related to the rate of swelling 33

Table 2.4 Exponent of n for various diffusion types 38

Table 2.5 Several factors affecting the mechanical properties of hydrogels 39

Table 3.1 Parameter of the tissue samples for tensile test measurement 75

Table 4.1 Vibrational frequencies observed in the FTIR spectra of 100% PVP 91

Table 4.2 Vibrational frequencies observed in the FTIR spectra of 100% PMMA .. 92

Table 4.3 Contact angle and work of adhesion of VP/MMA hydrogels at various composition ratios 95

Table 4.4 Effect of composition ratios on the pore size, area, and volume of the hydrogels 97

Table 4.5 Young's modulus of xerogels (dry condition) and hydrogels (wet condition) of different VP/MMA composition 101

Table 4.6 Elastic modulus and effective crosslinking density of various VP/MMA composition ratio 103

Table 4.7 Elastic modulus of VP85 hydrogel at various hydrogel sizes 104

Table 4.8 Samples size and slenderness ratio used in this study 106

Table 4.9 The diffusion exponent (n) and the diffusion mechanism of VP/MMA . 120

Table 4.10 The diffusion coefficient and volume fraction of VP/MMA hydrogels 122

Table 4.11 Structure characterization parameters of VP/MMA hydrogels with varied VP composition ratios..... 125

Table 4.12 Sizes of the VP/MMA hydrogel used in this study 126

Table 4.13 Effect of hydrogel sizes on the initial swelling rate and equilibrium swelling ratio 128

Table 4.14 The diffusion exponent, type of diffusion, and diffusion coefficient of VP/MMA hydrogel at various sizes..... 133

Table 4.15 Initial swelling rate and equilibrium volume swelling ratio of 6mmD, 6mmL hydrogel at various compositions swelled in DI water at room temperature and PBS at 37˚C 135

Table 4.16 Diffusion exponent and diffusion coefficient of hydrogels at various composition ratios swelled in DI water at room temperature and PBS at 37˚C 137

Table 4.17 The diffusion exponent (n) and the diffusion coefficient of VP/MMA hydrogels at various sizes immersed in DI water at room temperature and PBS at 37˚C 141

Table 4.18 Swelling force, swelling pressure, and volume swelling ratio of various VP/MMA composition 143

Table 4.19 Swelling pressure, osmotic pressure, and elastic contractile force of VP/MMA hydrogels at various VP compositions measured at 48 hours of swelling 146

Table 4.20 Effect of hydrogel sizes on the swelling force and the swelling pressure 151

Table 4.21 Effect of hydrogel sizes on the swelling pressure, osmotic pressure, and elastic contractility (at 48 hours of swelling)..... 152

Table 4.22 Length to diameter ratios of isotropic and anisotropic polymer structure at various VP/MMA compositions 154
Table 4.23 Pore size, area, and volume of isotropic and anisotropic VP/MMA hydrogels at various composition ratios 155
Table 4.24 Equilibrium volume, length, and radius swelling ratios of isotropic and anisotropic VP/MMA hydrogels at various composition ratios 158
Table 4.25 Diffusion exponent (n) and the diffusion coefficient (D) of isotropic and anisotropic hydrogels of various VP/MMA composition ratios 159
Table 4.26 Equilibrium volume, length, and radius swelling ratio of isotropic and anisotropic gels at various sizes 162
Table 4.27 Diffusion exponent, type of diffusion, and diffusion coefficient of isotropic and anisotropic gels at various sizes 164
Table 4.28 Maximum swelling force and swelling pressure at 120 hours for both isotropic and anisotropic hydrogels at various composition 167
Table 4.29 Maximum swelling force and swelling pressure of isotropic and anisotropic hydrogels at various sizes 169
Table 5.1 Stress-strain parameters of various GI tissues in longitudinal and circumferential directions 180
Table 5.2 Strain, length, and crimp angle of the fibres 187
Table 5.3 Assessment of tissue condition in both isolated-control and stretched-intestinal groups showing the length, diameter, weight, and surface area of the intestines after immediate hydrogel removal 199

Abbreviations and Acronyms

AIBN	2,2’-Azobis (2methylpropionitrile)
ATR	Attenuated total reflectance
$CaCl_2$	Calcium chloride
CaH_2	Calcium hydride
$CDCl_3$	Deuterated chloroform
CD	Crohn’s disease
Cp	Heat capacity
DI water	Deionized water
DMA	Dynamic mechanical analyzer
DSC	Differential scanning calorimetry
ECM	Extracellular matrix
EGDMA	Ethylene glycol dimethacrylate
EWC	Equilibrium water content
FAK	Focal adhesion kinase
FTIR	Fourier transform infrared
GAG	Glycosaminoglycans
GI	Gastrointestinal
G-T	Gordon-Taylor
HDMS	Hexamethyldisilazane
H&E	Hematoxylin and eosin

IF	Intestinal failure
MEHQ	Monomethyl ether hydroquinone
MFB	Myofibroblast
MM	Muscularis mucosa
MMA	Methyl methacrylate
MMP	Matrix metalloproteinase
MP	Muscularis propria
mRNA	Messenger ribonucleic acid
NaCl	Sodium chloride
$NaHSO_3$	Sodium bisulfite
NaOH	Sodium hydroxide
NMR	Nuclear magnetic resonance
NVP	N-vinyl pyrrolidone
PBS	Phosphate buffered saline
PCL	Polycaprolactone
PECAM-1	Platelet-endothelial cell adhesion molecule-1
PEG	Polyethylene glycol
PHEMA	Poly (2-hydroxyethyl methacrylate)
PMMA	Polymethyl methacrylate
PN	Parenteral nutrition
PVA	Polyvinyl alcohol
PVDF	Poly (vinylidene fluoride)

PVP	Poly (vinyl-pyrrolidone)
qNMR	Quantitative NMR
SBS	Short bowel syndrome
SBT	Small bowel transplantation
SD	Sprague-Dawley
SEM	Scanning electron microscope
SM	Submucosa
SMA	Shape memory alloy
SPH	Super porous hydrogel
SRSB	Segmental reversal of the small bowel
STEP	Serial transverse of enteroplasty
UTM	Universal testing machine
VA	Vertebral augmentation
WCA	Water contact angle

Chapter 1: Introduction

1. Introduction

1.1 Objectives

Crohn's disease (CD) defines as a chronic and long-lasting illness that primarily affects the entire gastrointestinal (GI) tract, from the mouth, esophagus, stomach, intestine, and anus. In about half of cases, it affects the small intestine, most often the lower part called the ileum. In some cases, it affects both the small and large intestines. The hallmark of CD is an excess inflammation along with the entire thickness of the GI tract wall from the mucosa layer and sometimes reaching the thin outermost serosa layer. An abnormal inflammation reaction results from an incorrect response of the immune system when attacking viruses, bacteria, or food in the gut causing inflammation that leads to bowel injury. People with CD are more susceptible to intestinal infections that might lead to complications such as stricture, perforation, fistula, and cancer. These complications often need treatment with surgery. Approximately 35% of CD patients required surgery during the year of diagnosis, 12% during the 1st year and 8% in the 2nd year, and from then on a mean annual surgery rate of 5% was found [1]. After 10 years the cumulative probability of surgical treatment was 61% and that of surgical treatment more than once was 39% [2].

Multiple resections and a progressive reduction in bowel length may eventually lead to the development of short bowel syndrome (SBS) [3]. It had been reported up to 75% of SBS cases result from single massive intestinal resection and 25% from multiple sequential resections [4]. Intestinal failure (IF) is likely to develop in SBS patients with loss of two-thirds length of the small intestine which refers to a condition that results in inadequate digestion or inability to maintain nutritional, fluid, and/or electrolyte homeostasis while consuming a normal and healthy diet [5], [6]. SBS is also

associated with significant morbidity and mortality, reduced quality of life, and high health care costs [7]. The mortality is estimated to be as high as 20-40% [8], [9].

The combination of nutritional, medical, and surgical treatments is part of SBS management. All of these treatments might carry severe side effects such as liver disease, sepsis, bowel obstruction, and potential carcinogenesis [10]–[13]. Intestinal transplantation could be considered a better therapeutic option for patients with complicated intestinal failure. Although a viable option, transplantation is costly. Major complications of transplantation include rejection, infection, graft versus host disease, chronic renal failure, and death [14]. The 5-year survival rate of transplantation is quite low at 54% [15]. A new strategy is required to further solve the problem related to inadequate length in SBS. Tissue expansion is a well-established surgical technique to cause the body to grow an additional amount of normal tissue. The idea of a self-inflating tissue expander became attractive and widely known for being painless during clinic visits [16]. The expander is made from a solid material called hydrogel based on vinyl pyrrolidone (VP) and methyl methacrylate (MMA) materials that absorb body fluid, especially water from the surrounding tissue due to an osmotic driving force.

In this study, the VP/MMA hydrogel can be used to lengthen and grow the small intestine tissue through the phenomenon called *mechanotransduction* (the translation of mechanical signals to biochemicals which affect cell function). The composition ratio and sizes of hydrogel will be varied to determine the swelling and mechanical properties of the devices. The anisotropic hydrogel will also be introduced to improve the polymer structure and swelling properties. The swelling pressure of the hydrogels should be sufficient to allow for the extension of the small intestine while not causing

necrosis or other tissue damage during extension. Hence, it is also important to know about the biomechanical properties (strength and modulus) and morphology of the GI tract tissues. Finally, the chosen hydrogel device will be prepared for *ex vivo* and *in vivo* studies and then demonstrated to extend the small intestine safely without compromising bowel function.

1.2 Thesis Outline

Chapter 2 starts with a literature review related to this study. Chronic bowel damage in CD is reviewed following the high possibility for patients to remain at risk for short bowel syndrome (SBS). Intestinal failure and management of SBS (a combination of nutritional, medical, and surgical approaches) are mentioned. There are still complication risks, therefore intestinal lengthening study for SBS patients is developed. A self-inflating hydrogel expander is introduced as a novel method to overcome limitations that come from the previous intestinal lengthening method. Hydrogels are reviewed focusing on their microstructure and chemical composition that affects the thermodynamics and kinetics of hydrogel swelling as well as mechanical properties. The structure, mechanical properties, and function of the GI tract (esophagus, stomach, small, and large intestine) are also reviewed for reference.

Chapter 3 demonstrates the method to synthesize and characterize the isotropic and anisotropic VP/MMA hydrogels. The swelling behaviour and swelling force measurement will be performed as a function of the composition ratios and sizes of the hydrogel. The morphology of GI tracts with the variation of strains will also be observed. *Ex vivo* and *in vivo* studies in Sprague Dawley (SD) rats will be conducted.

Chapter 4 explains the characterisation of the hydrogels including the chemical structure and purities of monomer, the functional group of VP/MMA, glass transition temperature (T_g), wettability, microarchitecture, and mechanical properties. Swelling behaviour study of hydrogels in different media such as water and PBS as a function of hydrogel compositions and sizes will be observed. The swelling force and swelling pressure of the hydrogels of various compositions and sizes will be examined. The isotropic hydrogel studies will be compared with the anisotropic hydrogels from the microstructure, swelling behaviour, and swelling force results.

Chapter 5 discusses the mechanical properties and morphology of GI tract tissues under unloading and loading conditions. In the *ex vivo* study, the small intestine will be stretched using a hydrogel device and will be implanted inside the SD rats *in vivo*. The changes in the intestinal length, diameter, and weight will be measured and the histology of tissues will be observed.

Finally, Chapter 6 summarises the conclusions of this study and concerns with future work.

Chapter 2: Literature Review

2.1 Crohn's Disease and Management of Short Bowel Syndrome

Crohn's disease (CD) is a chronic disease that causes inflammation and irritation in the gastrointestinal (GI) tract resulting from a complex interplay between genetic susceptibility, immunological, and microbial factors [17]. The incidence of CD in the UK is approximately 10-14 cases per 100,000 person-years and is most often diagnosed in adolescents and adults between the ages of 17 and 40 years [18], [19]. Crohn's can affect any part of the GI tract starting from the mouth to the anus, most commonly affecting the end of the small intestine (ileum) and the beginning of the colon [20]. Often occurring in patches, it causes inflammation, deep ulcers and scarring to the intestinal wall (Figure 2.1). The inflamed intestine shows thickening of all layers of the intestinal wall, but a narrowing of the intestinal lumen, making it harder for food to pass through [21]–[23]. This narrowing is called intestinal stricture (Figure 2.2) which is caused by an accumulation of extracellular matrix (ECM) and expansion of mesenchymal cells [24], [25].

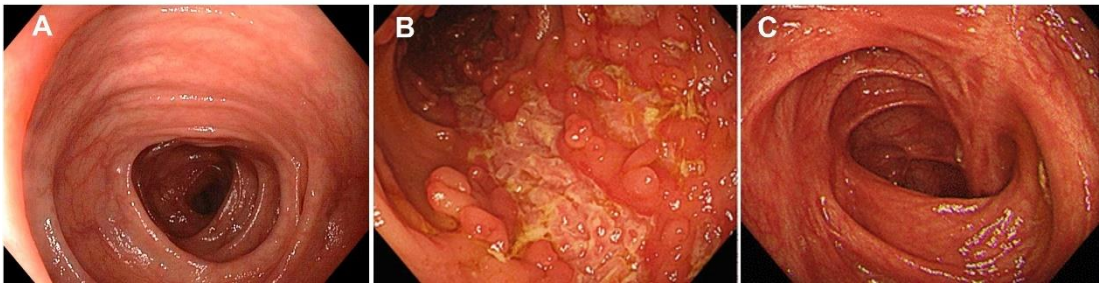


Figure 2.1 Endoscopic findings of (A) Healthy colon (B) Irregular, serpiginous ulcer and cobblestone appearance in the colon (C) Scar formation of longitudinal ulcer (mucosal healing) [26]

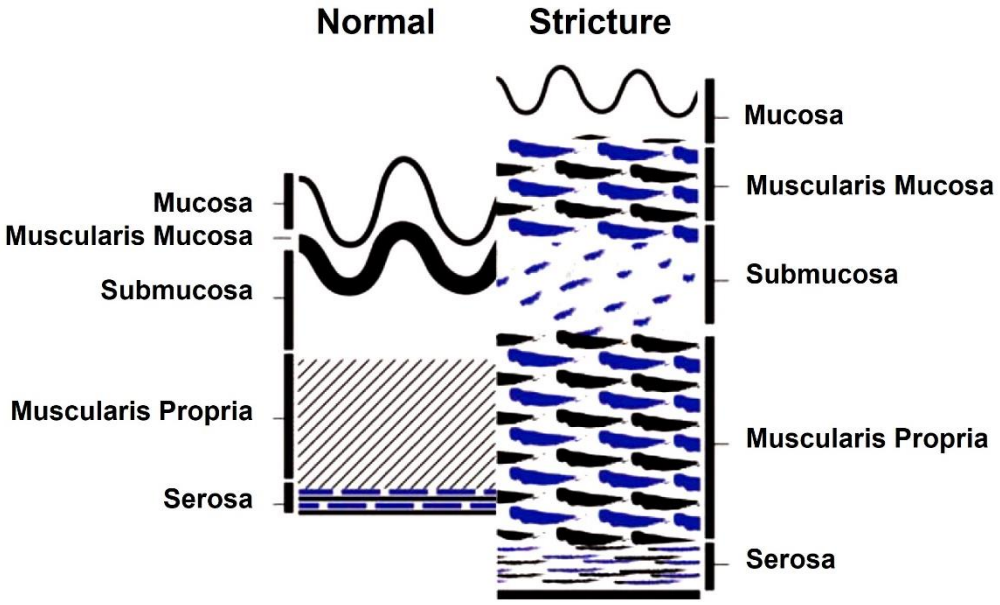


Figure 2.2 Schematic representation of the intestinal architectural distortion in CD-associated strictures [24]

Histological images of intestinal stricture demonstrated the appearance of disruption and expansion of the muscularis mucosa and smooth muscle cells in the submucosa with dense collagen deposition (Figure 2.3 A & B) [24]. Collagen septae extended through a disorganized muscularis propria (MP) to form a greatly thickened muscularis (Figure 2.3 C & D). Histologic studies of inflamed ileum and colon (Figure 2.4 C & G) showed the distorted mucosal structure, increased thickness of mucosa, increased density of infiltrating lymphocytes in the lamina propria, and disorientation of crypt compared to unaffected tissue (Figure 2.4 A & E) [27]. Trichrome staining images showed increasing blue-staining collagen in the inflamed tissue (Figure 2.4 D & H) compared to unaffected tissue (Figure 2.4 B & F).

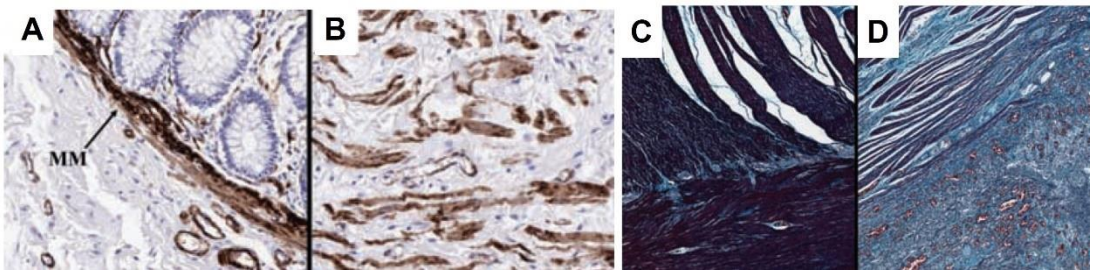


Figure 2.3 (A&B) Immunohistochemical staining for α-smooth muscle actin within myofibroblast (MFB) of the muscularis mucosa (MM) to the submucosa (SM) interface viewed at 100x. (A) MFB localised to the MM in the normal bowel (B) The disrupted MM in stricture bowel with MFB interposed throughout the SM (C&D) Immunohistochemical staining with Masson Trichrome of the muscularis propria (MP) was viewed at 20x (C) The well-organised fibres of the muscle layers (D) The disrupted, thickness MP in stricture intestine with a greater collagen content interposed between fibres [24]

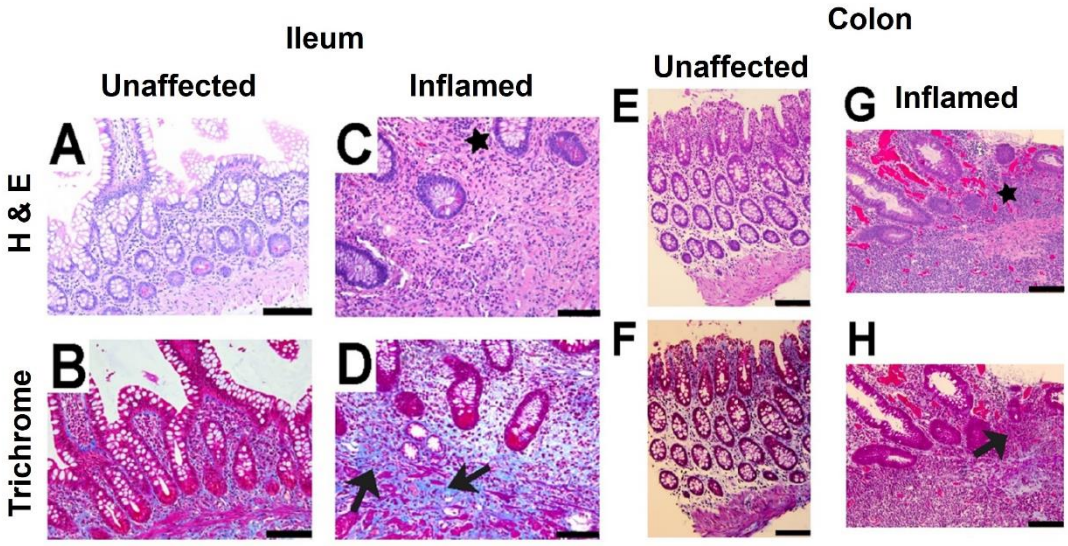


Figure 2.4 Staining images of unaffected and inflamed ileum and colon. (A-C-E-G) H&E staining (B-D-F-H) Trichrome staining. Black arrows (↑) highlight significant collagen clustering while black stars (*) illustrate disrupted mucosal layer in inflamed tissue compared to unaffected tissue segments. Scale bar 100 µm [27]

Collagen is the major abundant fibrous protein in the ECM and a number of each subtype has different functions. The collagen content of submucosa labelled by Masson's Trichrome was quantified and presented in Figure 2.5 [27]. Expression of collagen type I was upregulated in the inflamed intestine compared to the unaffected tissue. In the normal intestine, the major collagen subtypes are type I (68%), followed by types III (20%) and V (12%) [28]. In the strictured intestine, the proportion of types III and V collagen were increased by 20% and 42%, respectively over the normal intestine (Table 2.1) [28], [29]. These subtypes are characteristically found in greater amounts in healing tissue, and type III collagen has a greater propensity for contraction [30]–[32]. These collagen subtypes overexpression in the intestine of patients with CD creates an ECM suited to scar contraction and stricture formation. The role of type V collagen serves as a connector between the two smooth muscle cell layers and the interstitial collagens of the submucosal matrix [28]. The type V collagen in the strictured intestine was observed in the dense, expanded submucosa, both around vessels and diffusely in the area of smooth muscle cells of the muscularis mucosa.

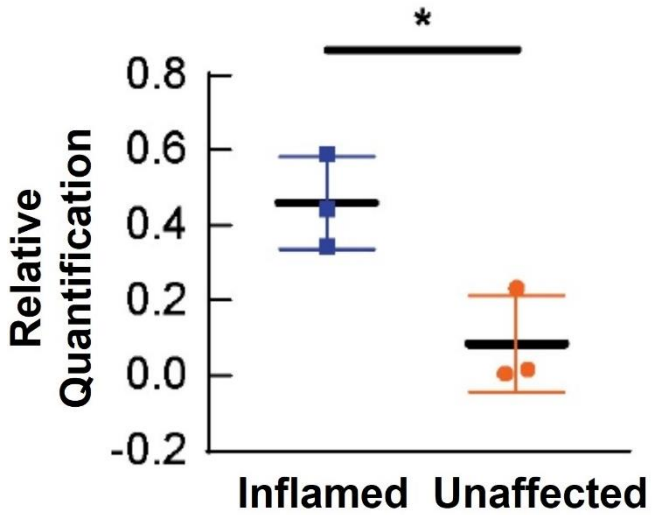


Figure 2.5 mRNA expression of Col1-A1 in unaffected and inflamed areas of the intestine. n=9 for each group, *p= 0.01 [27]

Table 2.1 Relative amount of collagen types I, III, and V in the control, inflamed, and stricture intestine [28]

Specimens	n	Collagen types (%)		
		I	III	V
Control	17	68 ± 2	20 ± 2	12 ± 1
Inflamed intestine	9	69 ± 4	18 ± 3	13 ± 2
Strictured intestine	14	58 ± 2[a]	24 ± 3	17 ± 1[a]

[a] Significantly different ($p < 0.05$) from normal ileum by Bonferroni's two-tailed t-test

Bowel stiffness is associated with wall deformability and intestinal function [33], [34]. Changes in the wall stiffness induced by diseases reflect tissue remodelling and might impair gut motility [35]–[37]. Chronic inflammation in CD is characterized by modified tissue stiffness. Several mechanical tests including ultrasound elasticity imaging, micro-elastometer or a multi-scale indenter have been used to estimate the stiffness of CD [27], [38], [39]. The studies demonstrated in inflamed human ileum (0.9 ± 0.4 kPa) was stiffer than unaffected region (0.6 ± 0.3 kPa), and inflamed human colon (1.1 ± 0.4 kPa) was also significantly stiffer than unaffected colon tissue (0.7 ± 0.5 kPa) [27]. CD stricture of human intestinal tissue was physiologically stiffer (16.7 kPa) than either normal intestine (2.9 kPa) or unaffected surgical margin (2.6 kPa), and it was nearly 6-fold less compliant (Figure 2.6) [38]. The wall stiffness increased in regions with inflamed and strictured intestines due to increasing the CollagenIA1 and MMP3 gene expressions that indicate active wound healing with concurrent fibrosis and inflammation.

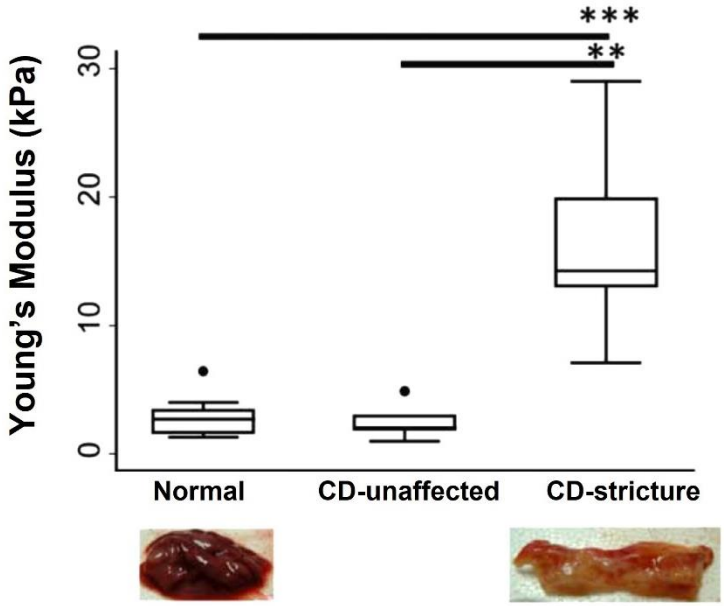


Figure 2.6 Young's modulus of normal intestine (n=5) compared with CD-unaffected (n=11) and CD-stricture (n=11) $^{**}p<0.01$, $^{***}p<0.001$ [38]

Developing an effective treatment for Crohn's disease is required a deep understanding. Despite the advances in medical therapies, surgical resection continues to play an essential role in CD treatment [40]. It was reported that the cumulative rates of intestinal resection were 44%, 61%, and 71% at 1, 5, and 7 years after diagnosis [41]. There are risks for recurrent disease and further resection. The need for resection of recurrent CD might be related to the age of diagnosis, site of initial disease, and complications [41]–[47]. The cumulative relapse rate was 33% and 44% at 5 and 10 years after the first intestinal resection. A progressive reduction in bowel length leads to the development of short bowel syndrome (SBS) [48], [49]. SBS refers to a condition in which patients exhibit malabsorption-induced diarrhea, bacterial overgrowth, dehydration, electrolyte disturbances, and malnutrition due to poor nutrient processing capability [49], [50].

Management of the SBS is developed based on the residual length and sites of the remaining intestine, the degree of intestinal adaptation, and the patient's ability to adhere to medication and dietary regimens. SBS management requires a combination of nutritional, medical, and surgical approaches such as parenteral nutrition (PN), teduglutide, segmental reversal of the small bowel (SRSB), Bianchi procedure, serial transverse enteroplasty (STEP), and small bowel transplantation (SBT). The goal is to provide adequate fluid and nutritional intake while minimizing complications and increasing the quality of life. Despite the success of SBS treatment, many complications might occur including intravenous catheter complications, liver problems, staple line leakage, interloop abscess, fistulae formation, bowel obstruction, allograft rejection, malignancy, graft failure, renal dysfunction and death [51]–[58].

2.2 Development of Intestinal Lengthening Research for SBS Patients

The intestinal lengthening procedure is feasible and efficacious in the management of SBS. The overarching goals of lengthening techniques are to achieve uniformity in the diameter of the intestine along its length and to maintain an adequate absorptive surface to allow maximal weaning from PN. Mechanical stretching appears to be a viable method for increasing the length of the intestine. This might provide a new method for the treatment of patients with SBS. There were several approaches for bowel lengthening via mechanical force (*mechanical enterogenesis*), all using the basic principle of a stretch as the mode of applying mechanical force, as summarized in Table 2.2.

Table 2.2 Summary of *mechanical enterogenesis* methods

Author	Year	Animal Model	Device	% Lengthening	Ref
Park et al.	2004	Rat	Screw	210%	[59]
Chang et al.	2006	Rat	Screw	213%	[60]
Shekherdimian et al.	2009	Rat	Screw	240%	[61]
Safford et al.	2005	Rat	Double barrel ostomy	149%	[62]
Puapong et al.	2006	Rat	Saline dilatation	32%	[63]
Spencer et al.	2006	Pig	Hydraulic piston	45%	[64]
Luntz et al.	2006	Pig	Hydraulic extender & SMA actuation	69%	[65]
Shekherdimian et al.	2010	Rat	Nitinol spring	250%	[66]
Stark et al.	2011	Rat	Nitinol spring in a gelatin capsule	230%	[67]
Huynh et al.	2017	Mice	Nitinol spring in a gelatin capsule	90%	[68]
Dubrovsky et al.	2019	Pig	Nitinol spring in a gelatin capsule	56-68%	[69] [70]

Sullins et al.	2014	Rat	PCL spring in a gelatin capsule	170-200%	[71], [72]
Scott et al.	2015	Rat	PCL spring in a gelatin capsule	170%	[73]
Scott et al.	2016	Rat	PCL spring in a gelatin capsule	221%	[74]
Okawada et al.	2011	Mice	PEG	18%	[75]
Sueyoshi et al.	2014	Mice	PEG	26%	[76]

The small intestines (jejunum) of rats were gradually stretched by using a metal screw within 3 weeks (Figure 2.7) [59], [61]. Through serial lengthening, the intestinal segments were successfully elongated to 210-240% of their original length. The mean weight of the intestinal segment was also increased compared with the normal intestine. Hypertrophy of the smooth muscle layer was observed in the lengthened groups. However, the most frequent complication encountered was the dislodgement of the screw expander device. This was related to the duration and the length of protruding screw outside the abdominal cavity. Chang et al. studied the ability of stretched bowel to maintain its length after removal of the expander by comparing two groups: (a) the lengthened rat jejunum was measured after achieving a maximal expansion of the stretching device, and (b) the expander was removed after maximal stretch, but the segment was retrieved 3 weeks later, allowing to recoil [60]. Both groups showed greater than three-fold lengthening of the jejunal segment, and there was no statically significant difference between the two groups in terms of length.

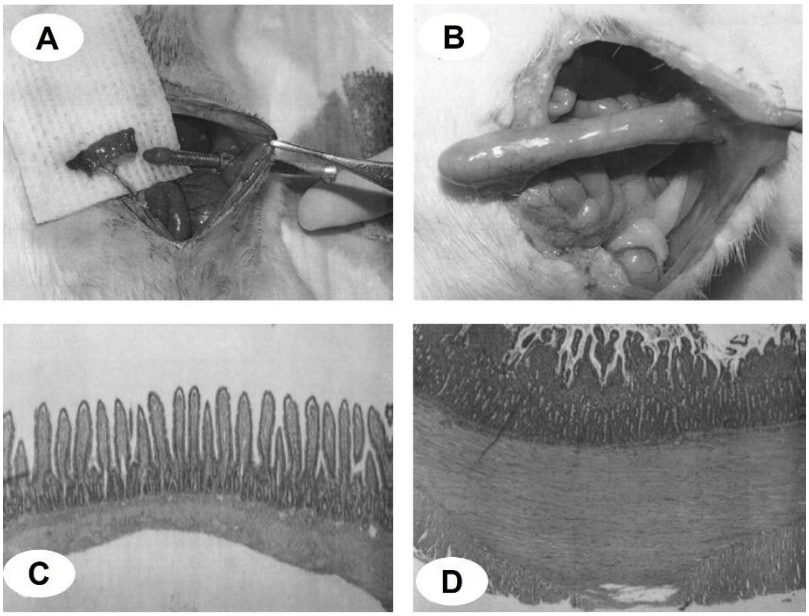


Figure 2.7 Photograph of jejunal segments (A) Before and (B) After lengthening and H&E appearance of the (C) Normal and (D) Lengthen jejunum (magnification x 40) [59]

A double-barrelled blind loop ostomy (Figure 2.8) was implanted and longitudinal tension was applied on a segment of bowel juvenile rat for 30 days [62]. The screw was placed inside the lumen and gradually advanced (1-3 mm/day) until the maximal length was achieved. On day 0, the mean length of the lengthened segment was 7.6 mm. After 30 days, the lengthened limb of the bowel with tension increased to 24.8 mm, and once the tension was removed, the final length of the bowel was 18.8 mm. There was still a significant lengthening of 149% compared to controls. However, there was a decrease in the length by 25% after the removal of the device. Limitation in this study was the bowel obstruction found on days 1-3 of the procedure, leaks development at the anastomosis where the segment of the bowel was removed, and tight strictures at the anastomosis.

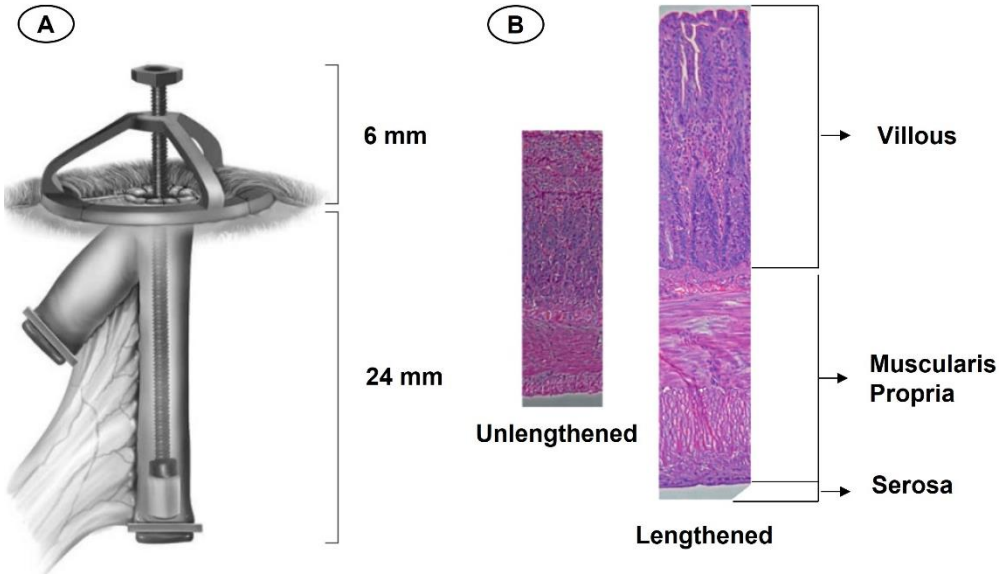


Figure 2.8 (A) Schematic diagram of the intestinal lengthening using double-barrelled blind loop ostomy (B) Histology of the unlengthened and lengthened bowel (x200 magnification) [62]

Fluid infusion could be used as an alternative method to lengthen the intestine [63]. A segment of the jejunum was surgically isolated from the remaining small intestine. The distal aspect of the segment was oversewn, and the proximal aspect was sewn to the abdominal wall with a catheter placed inside. An infusion was begun at a rate of 0.2 ml/h for 1 week. Pre-distension isolated jejunum segments of SD rat was measured at approximately 3.1 cm. After saline distension, the segment length was increased to approximately 4.1 cm. It represented a significant increase in length of 32% as compared with the starting length. The histology results showed a noticeably increased diameter in the distended segments as compared with controls. However, there did not appear to be any significant alterations in the villi and crypts of the distended intestine. The smooth muscle layers of the distended segments were markedly hypertrophied compared with controls (Figure 2.9).

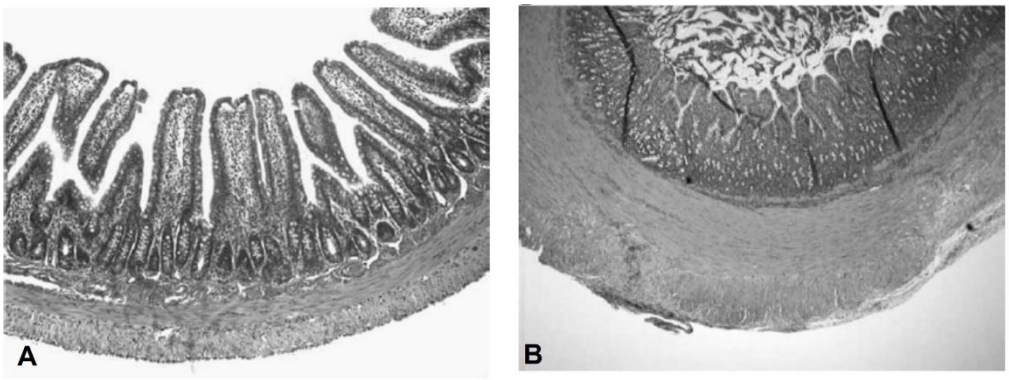


Figure 2.9 Microscopic appearance of normal rat jejunum (A) Treated jejunal segment (B) After 1 week of saline distension (x40) [63]

Mechanical forces were applied with the use of the hydraulic-lengthening device to the jejunum segments of female Yorkshire pigs [64]. The device used telescopic syringes the size of 3mL and 1mL (Figure 2.10). The piston chambers of the syringes were connected internally, then the fluid was injected into the device producing incremental elongation. Both ends of the device were coated with soft silicone bumpers to avoid bowel injury. After 7 days, the stretch segments were significantly elongated to 45% more than the control segment. However, after the removal of control devices, the intestine tended to recoil to a shorter length than its original length. In addition to macroscopic growth, the mucosal thickness was significantly greater in stretch than in control segments (772 ± 134 vs 647 ± 75 μm). Villous height (353 ± 76 vs 324 ± 76 μm) and muscularis propria (1099 ± 172 vs 1012 ± 229 μm) were not significantly different in both stretch and control segments. However, villous width was reduced in the stretch segment (143 ± 23 vs 149 ± 24). In contrast, crypt depth was increased markedly in stretch segments versus control (450 ± 95 vs 341 ± 64 μm). Epithelial proliferation in stretch segments was increased more than 2-fold greater than in the controls segment (26.3% vs 12.1%). The increase in epithelial proliferation was

consistent with the observed increase in crypt depth in stretch segments. The design limitations included the need for an external device for controlling the expansion of the piston as well as the restriction on the maximal length of expansion inherent in the design. The piston could only expand to double its original length and because it was made of a non-compliant material, it could not bend to accommodate the abdomen once the maximal width of the abdomen was achieved.

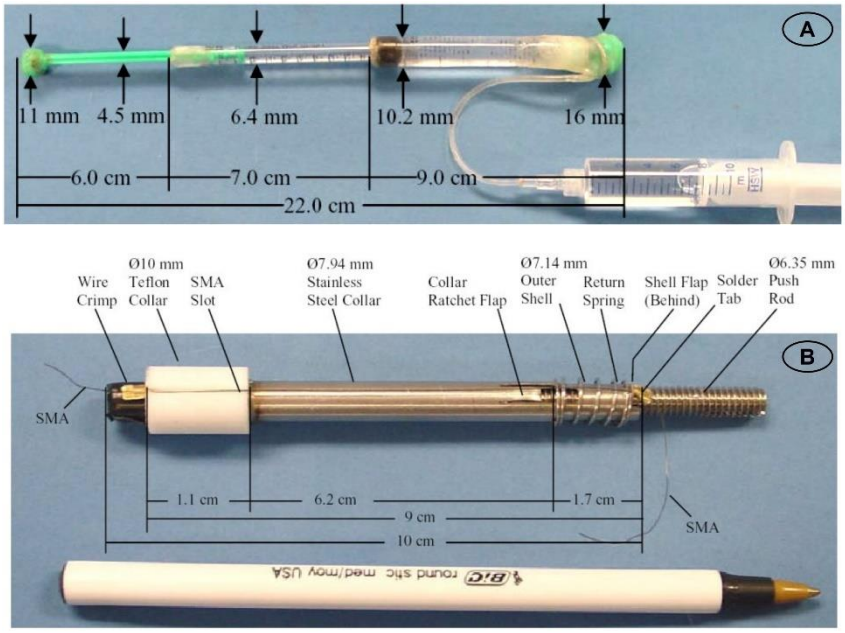


Figure 2.10 The prototype of (A) Dual hydraulic piston fully, extended (B) SMA actuated device, partially extended [65]

A dual concentric hydraulic piston and a shape memory alloy (SMA) actuated devices (Figure 2.10) were used to slowly extend the section of the bowel, allowing the bowel section to stretch approximately double its initial length [65]. The hydraulic extender was tested *in vivo* in 11 pigs (3 years old) for 7 days. After the extension procedure, the lengthened segments were significantly longer than the controls (17.6 cm vs 10.4 cm), by 69%, with a 69% increase in weight (29.4 vs 17.4 gr) and an 88%

increase in surface area (86.7 vs 46.1 cm^2). This method has the potential to become a useful clinical device, however, it had several important shortcomings for its use in human patients such as could not be fully implanted because the fluid pump and source design were too large, large variability in friction between the pistons and syringes made the applied force and motion irregular and unpredictable, no failsafe existed in the device to prevent overextension in the bowel, the extended length could not be directly controlled, and the device could not precisely maintain a position under changing load. SMA actuated device was employed to improve the hydraulic extender device. The *ex vivo* results showed that the device could elongate the bowel section, however, the bowel tension was particularly too large for this device due to the mesentery (vasculature) being attached to the bowel, and after extending by 38 mm, a 38% increase in length, the bowel slipped when actuated.

Intestinal lengthening procedures using wire spring design were continuously developed in rat and pig jejunum. Firstly, the bowel lengthening could accomplish using bare springs (d = 3.4 mm, F= 1.7 N) made of the biocompatible materials nickel-titanium (Nitinol devices, Figure 2.11) [66]. Intestinal segments were successfully lengthened from 1.3 ± 0.3 cm to 4.4 ± 0.5 cm, a 250% increase in length. Maximum spring length was achieved on postoperative day 36. The intestinal weight of lengthened segment was increased twice compared to that of the control group. Muscular layer hypertrophy and villous atrophy were observed in the intestinal architecture after lengthening. Hypertrophy appears to be a physiologic response to the applied mechanical forces. The villous atrophy is caused by the build-up of the mucous and subsequent increase in intraluminal pressure inside the isolated segments. The limitation of this device was the presence of the exposed wire ends that present a risk

to adjacent peritoneal structures. It was reported that there was morbidity associated with these wires, with only one animal having wire penetration into the liver noted at the time of specimen retrieval. Further modifications are needed to reduce the potential for injury.

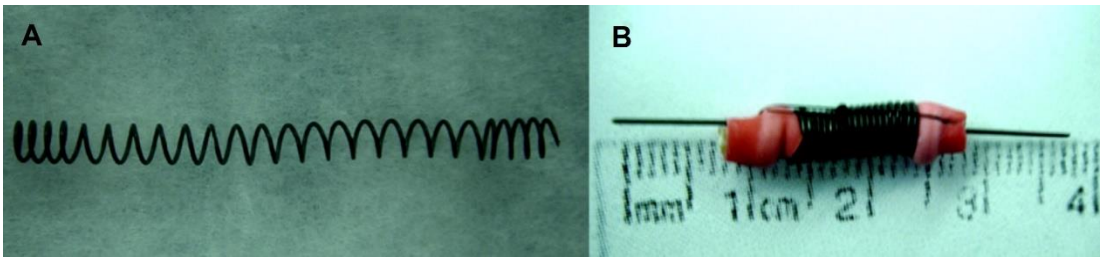


Figure 2.11 Photographs of (A) Nickel-titanium spring (B) Tissue expander device in final configuration [66]

Intestinal lengthening could be achieved by using a spring made from polycaprolactone (PCL), a biodegradables polymer used in absorbable sutures, with the spring constants of 1-5 N/m [71]–[74]. PCL springs were placed into gelatine capsules and coated with cellulose acetate phthalate for delayed expansion (Figure 2.12) [71]. The original length of the jejunum segment of SD rats was 1.0 cm. Overall, the increase in intestinal length of the lengthened and re-lengthened versus control segments were approximately 170-221% vs 40-46%. PCL spring devices had either partially degraded or were not present in the lengthened at the time of exploration. Lengthened jejunum had a greater circumference (1.5 ± 0.3 cm vs 1.0 ± 0.1 cm) and thicker muscularis propria (297 ± 58 vs 104 ± 28 μm) when compared to normal jejunum. Additionally, the re-lengthened jejunum had a greater circumference (3.4 ± 0.5 cm vs 2.1 ± 0.7 cm) and thicker muscularis propria (400 ± 51 vs 69 ± 17 μm) when compared to the normal jejunum. Crypt depth was increased from 162 ± 27 μm to 270 ± 77 μm in the lengthened jejunum. However, re-lengthened segments had an

increased crypt depth (250 ± 50 µm) almost similar to that initially lengthened segment. While the success of restoring lengthened jejunum was encouraging, its clinical impact was diminished by the loss of tissue that occurs when intestinal anastomoses were created.

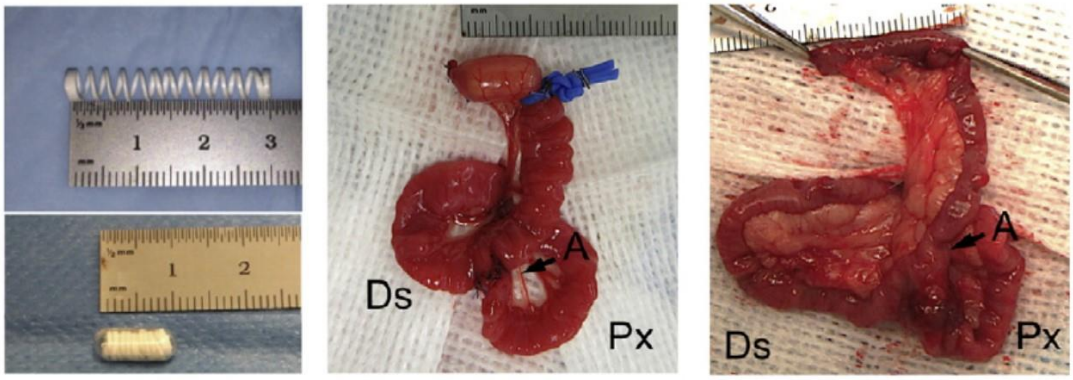


Figure 2.12 Photograph of the spring device, the bowel configuration at device placement, and lengthened bowel. Px= proximal, Ds= distal, A= anastomosis [71]

High molecular weight polyethene glycol (PEG) was used to stretch the bowel in an isolated small intestine segment, and this stretching would lead to intestinal growth [75], [76]. The catheter was inserted inside the lumen of the isolated segment and an average of 350 µl of PEG was gently instilled to fully inflate the segment (Figure 2.13). After the PEG injection, the catheter was gradually removed, and the distal side was closed. The PEG-stretched segments were significantly longer (1.4-fold increase) and had significantly increased diameters (1.3-fold increase) compared to controls. Villous height was significantly increased in the PEG-stretch group (20.3%) compared to controls. Crypt depth was also increased in the PEG-stretch group (19.2%) compared to controls.

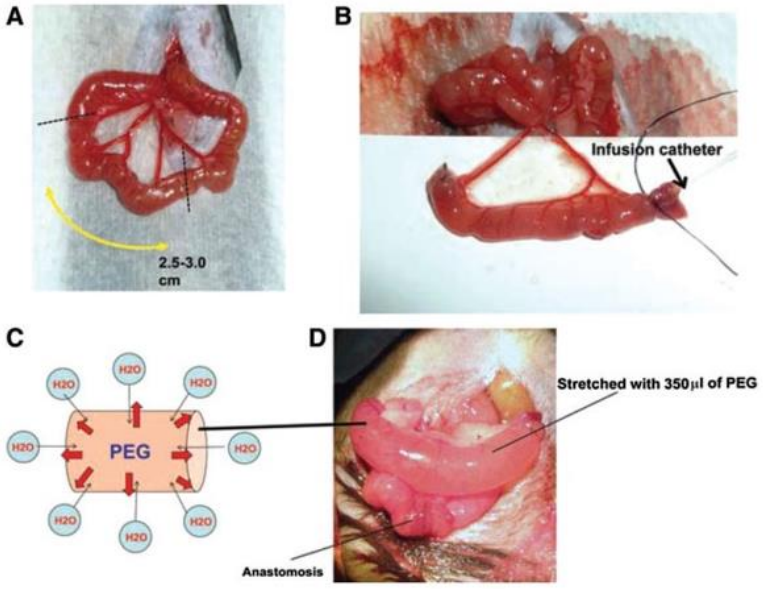


Figure 2.13 (A) A 2.5-3 cm segment of the small intestine was isolated (B) The catheter was inserted into the isolated segment and PEG was injected through the catheter, then the catheter was removed and the end sutured closed (C) PEG pulled abdominal fluid into the intestinal lumen (D) Final image of the stretched segment after PEG injection [76]

Several methods of applying mechanical force to an intestinal segment had been developed such as using a screw device, hydraulic extender and SMA actuation, repeated injections of saline solution, nickel-titanium spring wire, polycaprolactone (PCL) spring, and PEG. Most of these techniques incorporate a device that is at least partly outside the abdominal cavity, introducing risks such as dislodgment, damage to the exterior component, infection, obstruction, and increased inflammation. A biodegradable polycaprolactone spring device showed a significant improvement in the lengthening and histology results. While these modifications have increased the feasibility of the device, there are still limitations to its applicability such as buckling problems, loss of mechanical integrity of the polymer due to degradation and the loss

of tissue that occurs when intestinal anastomoses were created. Therefore, a novel method is still required to overcome these limitations.

2.3 Self-inflating Hydrogel Tissue Expander

A self-inflating tissue expander is an important device for generating extra skin or tissue for use in reconstructive surgery. It had a long history of successful use in clinical applications, dating back to 1982 developed by Austad and Rose [77], to induce an excess of tissue immediately adjacent to a defect offers exciting possibilities [78]. The tissue expander is implanted and it absorbs body fluid due to an osmotic driving force [79]. The tissue responds to pressure by expanding, recruiting adjoining tissue, and increasing its mitotic rate. Tissue gain is mainly due to stretch (approximately 70%) but also due to growth (approximately 30%).

The tissue expander has a shape made from hydrogel (Figure 2.14) [80]–[82]. Hydrogel is a three-dimensional network of hydrophilic polymer chains that can absorb large quantities of water or biological fluids. It is considered to have great potential when applied for biomedical purposes [83]–[86]. This is because they are expected to be potential alternative natural tissues, with relatively high water contents, soft and rubbery consistency, biocompatibility, and low interface tension with water or biological fluids [87]–[90]. This low interfacial tension property would reduce the tendency of the proteins in body fluid to adsorb and unfold upon adsorption. Minimal protein interaction is important for the biological acceptance of foreign materials as the denaturation of proteins by surfaces might serve as a trigger mechanism for the initiation of thrombosis or other biological rejection mechanisms.

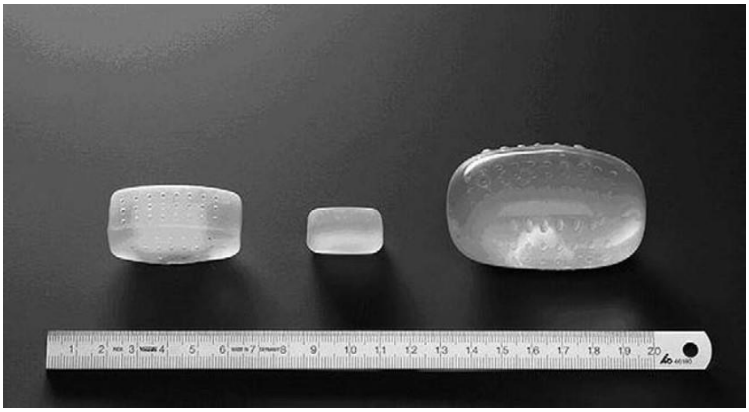


Figure 2.14 Rectangular OSMED expander (from left to right): with silicone envelope, without silicone envelope, after complete inflation [81]

Hydrogel comprises natural or synthetic polymers [91]. Natural polymers are biocompatible, biodegradable, and contain biologically recognizable moieties. However, they lack desired mechanical properties, which must be close to the mechanical properties of the application site. Also, they might trigger immune or inflammatory responses upon introduction to the human body. In contrast, a synthetic hydrogel is chosen because it can be designed to yield desired mechanical properties and other favourable properties. Poly (N-vinyl-2-pyrrolidone) (PVP) gel is a synthetic polymer consisting of linear 1-vinyl-2-pyrrolidone groups. PVP (C_6H_9NO) has a carbon chain containing an amide group in the side substituent and has a poly-*N*-vinyl amide structure (Figure 2.15). PVP has a unique combination of extraordinary physical and chemical properties such as biocompatibility, non-toxicity, chemical stability, good solubility in water and many organic solvents such as butanol, chloroform, and dichloromethane which makes it suitable as a biomaterial in numerous significant medical and non-medical applications (pharmaceutical industry and medicine) [92], [93]. Starting as a blood plasma expander for trauma victims [94], PVP has been used

extensively in biomedical applications as a common ingredient in drug manufacture (tablets, granules, pellets, hydrogels) [95]–[98]. PVP in combination with other polymers or monomers has been mentioned in various studies to produce soft contact lenses, disinfectants for contact lens solutions, and other ophthalmic solutions since it can reduce eye irritation. The hydrophilicity of PVP makes it suitable for contact lens manufacturing since wettability is an important factor that increases comfort during utilization, by moisture retention and reduction of the coefficient of friction [99], [100].

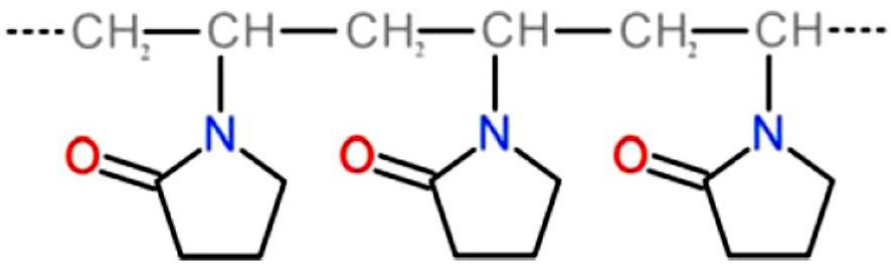


Figure 2.15 Chemical structure of poly(vinylpyrrolidone) [93]

Polymethylmethacrylate (PMMA) is a vinyl polymer, made by free radical vinyl polymerization, from the monomer methyl methacrylate (MMA) (Figure 2.16). MMA (CH_2=C[CH_3]CO_2CH_3) is one member of a huge family of methacrylate esters in which the group attached can be the alkyl or aryl group. The presence of pendant methyl (CH_3) groups hinders the crystalline packing of the polymer chains. Since they are not allowed to rotate freely around the C-C bond, the resulting structure is tough and rigid. PMMA is a strong but lightweight polymer processing with a compressive strength between 85 and 110 MPa and a tensile strength between 30 and 50 MPa [101]. The mechanical properties of PMMA can be tuned by varying the mixing ratios of monomers and initiators during polymerization. PMMA can be used in orthopedics applications, for example, it is used to fill voids left by mismatches between host bone

and implant, thus creating immediate stability. The transfer and distribution of forces from implant to bone is thereby subject to a more physiologic transition as a result of the mechanical properties of PMMA, which approximate bone. PMMA had also been used for vertebral augmentation (VA). Gilbert et al [102] first reported successful results after injecting PMMA in the management of painful hemangiomas of the vertebral body. PMMA could be used in dental applications for the fabrication of complete denture bases [103]. In addition to strength and stability in aqueous environments, PMMA possesses excellent optical properties [104]. PMMA provides an opportunity for the fabrication of ocular devices and results in the development of modern-day contact lenses. PMMA lenses are lathe cut from rods or buttons of PMMA obtained by bulk free-radical polymerization of methyl methacrylate.

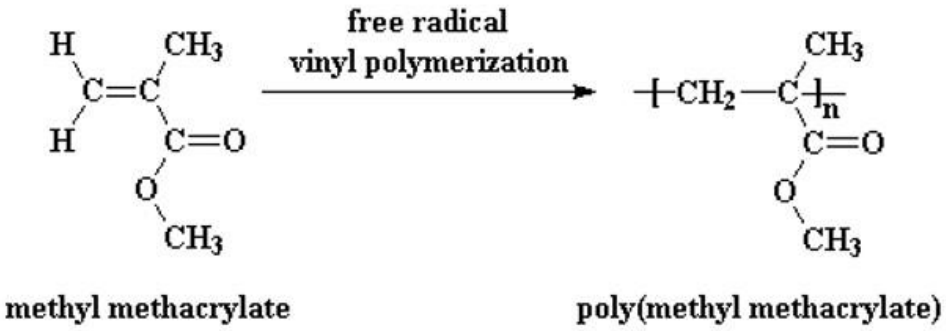


Figure 2.16 Structure of PMMA made by free radical polymerization from MMA

VP and MMA copolymerization has been used in congenital anophthalmia [105], breast reconstruction [106], and cleft palate [78] repair with limited success. The application has been limited largely because of the rapid expansion rate and the uncontrolled swelling which leads to tissue necrosis and other complications. It had been reported that the most widely used method of controlling the rapid expansion is to wrap the VP/MMA hydrogel with a semi-permeable silicone membrane [107].

However, surgeons often wish to craft the prepared expanders into suitable shapes for fitting in irregularly shaped defects. Thus, the silicone membrane could be quite an inconvenience in real plastic surgeries.

IPN hydrogel tissue expander was introduced by crosslinking functionalized poly(lactic-co-glycolic-acid) (PLGA) in the presence of a VP/MMA hydrogel base [108]. VP/MMA was prepared by thermal polymerization with allyl methacrylate (0.2wt%) as the crosslinker and azobisisobutyronitrile (AIBN) (0.2wt%) as the initiator synthesized by Polymeric Science Ltd. PLGA, as the secondary polymer network, penetrating through the VP/MMA hydrogel. The incorporation of PLGA into the hydrogel largely decreased the volume expansion ratio. However, the time needed to reach the equilibrium swelling state is still too fast. The VP/MMA base and IPN hydrogels reached the maximum swelling condition in about 1 to 3 days. Therefore, a further study focusing on the design of the hydrogel tissue expander needs to be developed such as varying the composition ratio of monomers, adjusting the concentration crosslinker and initiator, varying the hydrogel sizes, and swelling pressure generation. Those parameters are important in this work in order to match the properties of a hydrogel tissue expander to stretch the GI tract tissues. The optimum swelling condition when reaching an equilibrium state (swelling ratio, rate, time) and pressure generation to produce the mechanical force needs to be considered the most.

Another limitation of the hydrogel tissue expander is swelling in an isotropic direction, meaning swelling happens in a 3D mode, identically in every direction. In plastic and reconstructive surgeries, unwanted tissue growth in one direction brings risks and inconvenience. The anisotropic hydrogel tissue expander is highly desirable in surgeries such as cleft palate defects, eyelid, or nasal construction. Former work in

this group successfully prepared the anisotropic hydrogel tissue expander by annealing the xerogel under its glass transition temperature and then cooling it under a compressive load [109]. Therefore, this method could also be applied in this work to create swelling in the desired direction.

2.3.1 Effect of Hydrophilicity/Hydrophobicity

The hydrophilicity/hydrophobicity ratio used in the preparation of hydrogel is crucial to determine the final property of the hydrogel. During swelling, the polymer network interacts with the polar solvent hence affecting the swelling rate and equilibrium swelling ratio. A hydrogel that has more hydrophilic groups on the polymer chains provide more binding sites for water molecules, while hydrophobic groups repel water molecule and act as a steric hindrance and preventing them from binding with a hydrophilic component [110]. VP/MMA hydrogels had been prepared using γ-irradiation together with increasing VP content from 5% to 85%. As a result, the equilibrium water content (EWC) was found to increase from 5% to 80% whether in the presence or absence of a cross-linker [111]. In the VP/HEMA (hydroxyl ethyl methacrylate) hydrogel system [112], the EWC was also increased from 40.4% to 85.4% when VP content was increased from 5% to 70% in the absence of a cross-linker.

2.3.2 The Microstructure of Hydrogel

The volume fraction of the polymer in the swollen state ($\upsilon_{2,s}$), the number of average molecular weight between cross-links ($\overline{M}_c$), and the correlation length between two adjacent crosslinks (ξ) are characteristics of the hydrogel microstructure

[113]. The volume fraction of the polymer in the swollen state represents the amount of liquid imbibed in the swollen gel and is described by [114]:

$$\upsilon_{2,s} = (\frac{D_0}{D_\infty})^3 \quad (2.1)$$

Where D_0 represents the diameter of the polymer in the xerogel and D_∞ is the diameter of the polymer in the fully hydrated states.

The number average molecular weight ($\overline{M}_c$) between crosslinks measure the degree of crosslinking and can be determined using the modified Flory-Rehner theory when using water as the swelling medium. The $\overline{M}_c$ for a non-ionic hydrogel is represented by the following equation [115].

$$\overline{M_c} = -\frac{\rho V_1(\upsilon_{2,s}^{\frac{1}{3}} - 2\upsilon_{2,s}f^{-1})}{[\ln(1-\upsilon_{2,s}) + \upsilon_{2,s} + \chi\upsilon_{2,s}^2]} \quad (2.2)$$

Where V_1 is the molar volume of water, ρ is the density of the dry hydrogel, f is the functionality of the crosslinking agent, and χ is the polymer solvent interaction parameter.

The low value of χ means a strong interaction between the polymer-water and weak interaction between hydrophobic groups of the polymer chains. The χ value could be calculated as [116]:

$$\chi = -\frac{\ln(1-\upsilon_{2,s}) + \upsilon_{2,s} + \upsilon_e V_1(\upsilon_{2,s}^{1/3} - 2\upsilon_{2,s}f^{-1})}{\upsilon_{2,s}^2} \quad (2.3)$$

Where υ_e is the effective crosslink density in the hydrogel and V_1 is the molar volume of water.

The correlation length or linear distance between two adjacent crosslinks or mesh size (ξ) provides a measure of the space available between the macromolecular chains of the hydrogel (Figure 2.17). This parameter depends on the degree of cross-linking, the chemical structure of the monomer, and external environments such as pH,

temperature, and ionic strength [114]. Typical ξ reported for biomedical hydrogels range from 5 to 100 nm in their swollen state [117], [118]. It could be determined using the following equation [119]:

$$\xi = Q^{-\frac{1}{3}} \, l \, (\frac{2\chi\overline{M_c}}{M_r})^{1/2} \qquad (2.4)$$

Where Q is the volume swelling ratio, l is the length of the bond along the polymer backbone (for vinyl polymer, 1.54 Å), χ is the polymer characteristic ratio, and M_r is the molecular weight of the repeating units.

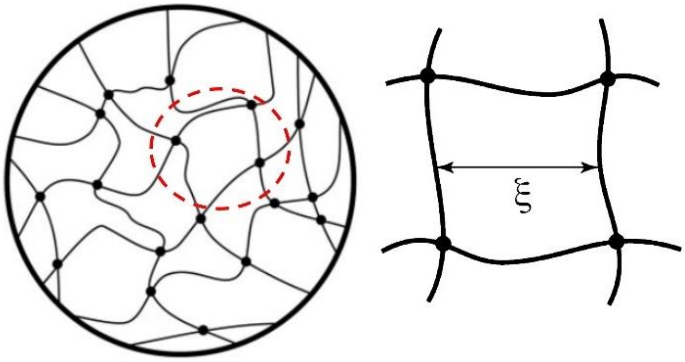


Figure 2.17 Definition of hydrogel ξ in the ideal crosslinked network [120]

Parameters in Equation (2.1) - (2.4) are related to each other to determine the swelling capacity of the hydrogel. For instance, changing the composition of crosslinkers and initiators will change the number of crosslinks per unit volume as well as the mesh size. A higher composition of crosslinker or initiator results in an increased number of crosslinks per unit volume (Figure 2.18). However, this leads to a decreased mesh size which means less effective space for water diffusion and less free volume for accommodating water molecules. Hence, more crosslinks also act as a disturbance for water diffusion leading to a decreased swelling rate and capacity by providing a stronger network thus improving the mechanical property of the hydrogel. PVP

hydrogels crosslinked with ethylene glycol dimethacrylate (EGDMA) with concentrations of 0.5 to 5.0 wt% were found that the EWC decreased from 95.7% to 77.4% [121]. VP/MMA hydrogels were prepared by using the same crosslinker with concentrations of 0.4% to 4% found the EWC decreased from 66.3% to around 48.1% [122]. Lee et al. [123] synthesized poly (2-hydroxyethyl methacrylate) (PHEMA) hydrogels and used an EDGMA crosslinker with concentrations of 0 to 40wt%. The results showed that the drug release rate was decreased by over 80%.

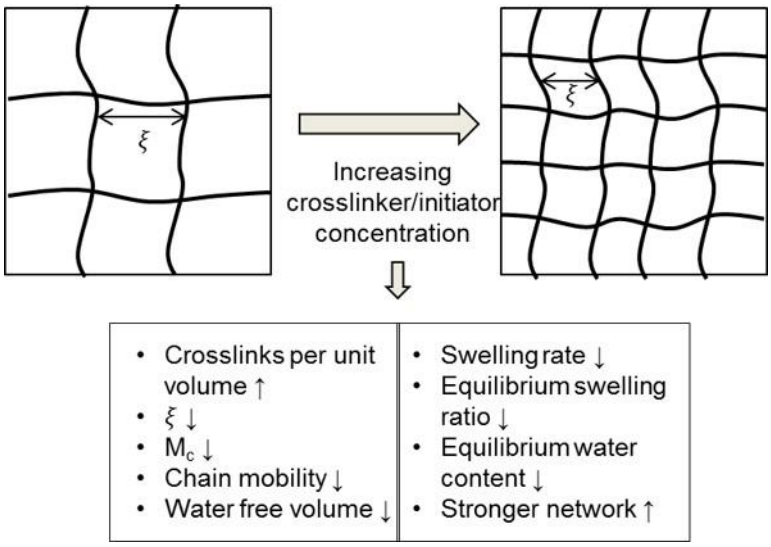


Figure 2.18 Effects of crosslinker/initiator modification on the number of crosslinkers per unit volume, volume swelling ratio, and mesh size

The porosity of hydrogels could be classified into four categories such as non-porous, micro-porous, macro-porous, and super porous hydrogels (Table 2.3) [124]. Non-porous gels have molecular-sized pores equal to the mesh size, ξ, 1-10 nm. The polymer chains are densely packed and provide strictly limited solute transport via the diffusion through free volumes. The pore size of micro-porous hydrogel is between 10-100 nm. Since the pore size begins to approach the size of the diffusing solutes, the solute transport occurs due to combination of molecular diffusion and convection of

water filled pores. Macro-porous gels have large pores, usually between 100-1000 nm. Super porous hydrogels (SPHs) size is in the range of several hundred micrometres [125], [126]. Most spherical pores inside the hydrogels are connected to form the open channel system, which acts as a capillary system causing rapid water uptake into the porous structure [127]. SPHs swell in water to an equilibrium state in a matter of a minute regardless of the size. Such fast swelling is due to the absorption of water by capillary force rather than by simple absorption [127], [128]. Conventional SPHs are characterized by fast swelling, a high swelling ratio, and weak mechanical properties. However, a new generation of SPHs was developed to improve their swelling ratio, and mechanical and high elasticity properties [125].

Table 2.3 Porosity of hydrogels related to the rate of swelling [129]

Porosity	**Size**	**Type of absorbed water**	**Swelling mechanism**	**Swelling rate**
Non-porous	1-10 nm	Mostly bound	Diffusion through free volumes	Very slow, sample-size dependent
Micro-porous	10-100 nm	Mostly bound	Combination of molecular diffusion and convection in the water-filled pores	Slow, sample-size dependent

Macro-porous	100-1000 nm	Mostly bound	Diffusion in the water-filled pores	Fast, sample size-dependent
Super-porous	High porosity with interconnected opened-cell structure	Mostly free	Capillary forces	Very fast, sample-size independent

2.3.3 Mechanisms of Hydrogel Swelling

Hydrogels can absorb and retain a large amount of water in their matrix, hence increasing their size and volume [91]. This process is known as the swelling of hydrogel. The mechanism of swelling is determined by the character of water in a hydrogel [85]. When a dry gel begins to absorb water, the first water molecules entering the matrix will hydrate the most polar, hydrophilic groups, leading to primary bound water. As the polar groups are hydrated, the network swells and exposes hydrophobic groups, which also interact with water molecules, leading to hydrophobically-bound water, or secondary-bound water. Primary and secondary bound water are often combined, and they are called total bound water. After the polar and hydrophobic sites have interacted with and bound water molecules, the network will imbibe additional water, due to the osmotic potential of the network chains towards infinite dilution, this is known as the ‘free’ or ‘bulk’ water and is assumed to fill the space between the network chains, and/or macropores or voids. Continuous swelling is opposed by the

covalent or physical crosslinks, leading to an elastic network retraction force. Thus, the hydrogel will reach an equilibrium swelling level.

Polymer swelling is driven by the osmotic pressure of the polymer network (π), which is counteracted by the elastic restoring force of the network (p) [130]. Thus, the swelling pressure (P) exhibited by the hydrogel is given by:

$$P = \pi - p \tag{2.5}$$

Equilibrium is obtained when $\pi = p$ and thus swelling pressure is zero. Penetrant diffusion is restricted by the three-dimensional polymer chain network, which can act as a physical 'barrier' to transport. Factors which increase either the mobility of the chains or the distance between them, enhance diffusion as predicted by the free-volume theory [131]. Swelling is also governed by additional factors including the crosslinking density, the ionic nature of the polymer network, and the nature of the swelling solvent [132]. Ionized moieties within the hydrogel tend to favour increased molecular interactions (*e.g.*, hydrogen bonding) with polar solvents and thus increase hydrophilicity and the degree of swelling. The swelling behaviour of ionic gels will also be influenced by the pH of the solvent. Therefore, an anionic hydrogel at low pH remains unionized, however, above its pK_a, the ionized groups result in increased electrostatic repulsion within the polymer network and increased hydrophilicity, thus resulting in an increased swelling ratio.

2.3.4 Kinetics of Hydrogel Swelling

The phenomenon of water sorption by a hydrogel depends mechanistically on the diffusion of water molecules into the gel matrix and subsequent relaxation of macromolecular chains of the hydrogels [133], [134]. The following possibilities might

arise and are divided into two basic categories: first, is the Fickian or Case I transport, which is classically seen in the rubbery state and polymer chains have higher mobility that allows easier penetration of the solvent [135]. Therefore, the solvent diffusion rate, R_{diff}, is slower than the polymer chain relaxation rate, R_{relax}, ($R_{diff}<<R_{relax}$) (Figure 2.19). In addition, a gel could be regarded as Fickian diffusion if it passes the following criteria such as the plot of F against $\sqrt{t}$ (Figure 2.20) is linear in its initial portion (generally 40-60% of equilibrium) and after the linear portion, the curve is concave to the $\sqrt{t}$ axis [136].

Secondly, it is non-Fickian diffusion, which is mostly glassy polymers. In this situation, the polymer chains are not adequately mobile to permit immediate penetration of water into the polymer core [137]. Depending on the relative rates of chain relaxation and diffusion, the non-Fickian diffusion is classified into two subsections: anomalous and case II transport [138]. The anomalous transport is observed when the diffusion and relaxation rate are comparable ($R_{diff}\approx R_{relax}$) [129]. It has been further categorized into three subclasses such as sigmoidal, pseudo-Fickian, and two-stage behaviours (Figure 2.20) [136]. The sigmoidal behaviour of the sorption curve shows an inflection point around F = 0.5. Pseudo-Fickian sorption curves show a small linear region resembling Fickian diffusion. The two-stage or dual-mode of sorption is characterized by initial rapid uptake, and the establishment of quasi-equilibrium, followed by a slow approach to final equilibrium. Case II transport is dominated when the diffusion is very rapid compared to relaxation ($R_{diff}>>R_{relax}$) (Figure 2.19), with relaxation occurring at an observable rate [129]. The mass uptake is proportional with time (Figure 2.20).

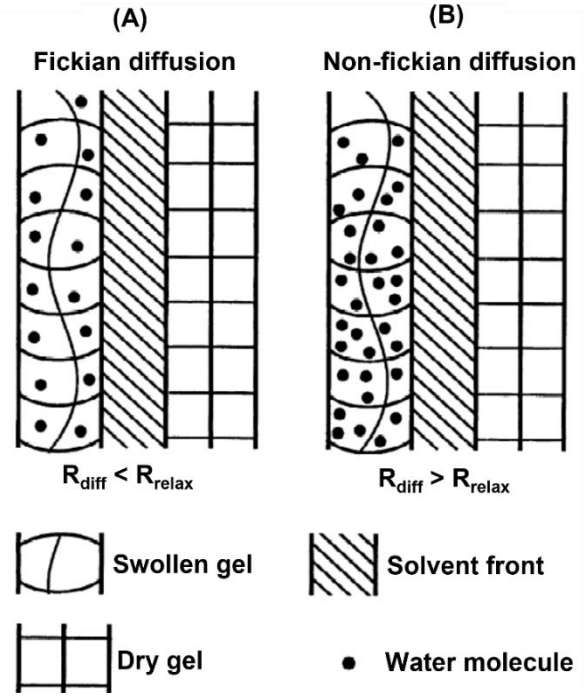


Figure 2.19 A model of Fickian and non-Fickian diffusion [139]

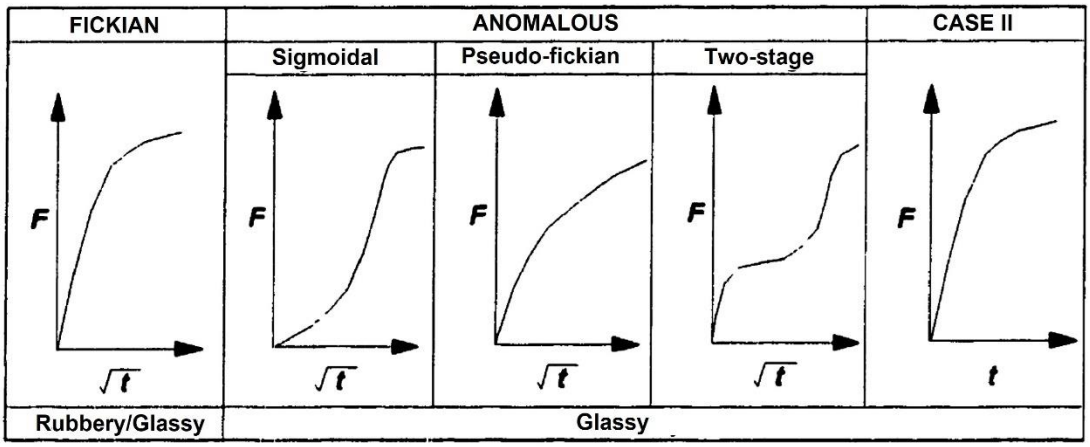


Figure 2.20 Swelling curves as indicators of transport types [140]

An empirical equation, the so-called power law equation, is commonly used to determine the mechanism of diffusion in polymeric networks [133], [141]:

$$F = \frac{M_t}{M_\infty} = kt^n \qquad (2.6)$$

Where, F is the fractional approach to equilibrium, M_t is the mass of the swollen gel at time t, M_∞ is the mass of the swollen gel at equilibrium, k is the empirical rate constant, and n is the diffusion exponent.

The diffusional exponent, n, is dependent on the geometry of the device as well as the physical mechanism of solute uptake [129]. The value of n could be obtained from the double logarithmic plot of water uptake (M_t/M_∞) and time (t) [139]. By determining the diffusional exponent, n, the information about the physical mechanism controlling solute uptake could be obtained [129]. For n = 0.5 indicates Fickian diffusion, when 0.5 < n < 1.0 indicates anomalous transport, and n=1 implies case II transport (Table 2.4) [142], [143]. Nevertheless, when the water penetration rate is much below the polymer chain relaxation rate, it is possible to record the n value below 0.5. This situation, which is still regarded as Fickian diffusion, is named as less Fickian behaviour [116].

Table 2.4 Exponent of n for various diffusion types [129]

Type of transport	**Diffusional exponent**
Fickian diffusion	0.5
Anomalous transport	0.5 < n < 1
Case II transport	1

The following Equation 2.7 is used to calculate the diffusion coefficient (D) [144]:

$$\frac{M_t}{M_\infty} = 4\left(\frac{Dt}{\pi r^2}\right)^{\frac{1}{2}} \quad (2.7)$$

Where r is the radius of the cylindrical hydrogel [145] and t is time.

2.3.5 Mechanical Properties of Hydrogel

The mechanical behaviour of hydrogels has long been recognized as fundamentally important. Hydrogels must have mechanical properties relevant to the desired application. Several ways of controlling the mechanical properties of hydrogels such as altering the comonomer composition, increasing or decreasing the crosslinking density, and changing the conditions under which the polymer is formed (Table 2.5) [146]. However, these changes in the polymer will affect not only the mechanical properties but also the swelling behaviour of hydrogel. There was an inverse relationship between the swelling capacity and the mechanical properties of the hydrogels.

Table 2.5 Several factors affecting the mechanical properties of hydrogels

Parameters	Descriptions	Ref
Monomer composition	• Increasing the stiffness of the backbone polymer by replacing acrylate with methacrylate • HEMA and MMA contributed to the mechanical strength of unswollen polymers • Increasing NVP from 5 to 60 wt% would decrease young's modulus from 0.8 MPa to 0.08 MPa	[112], [147]
Cross-linking density	• More than 5% crosslinking agent would give a significant mechanical strength • By increasing the allyl acrylate crosslinker fraction from 0.1% to 0.6 wt%, young's modulus increased from 0.1 to 1 GPa	[148], [149]

Polymerization condition (time, temperature, amount type of solvent)	• If a too large amount of solvent is used during the polymerization, the crosslinking agent will tend to form cycles rather than crosslinks, hence it will reduce the crosslink density, thus lowering the material strength. • Increasing the double bond conversion can lower the amount of residual soluble fraction and may increase the crosslink density. • Post-reaction treatments can also be effective in changing the network structure and the material strength • Thermally cycling the PVA hydrogels can alter the structure. By cycling the polymer, young's modulus was significantly increased from 20 kPa to 100 kPa	[150]
Degree of swelling	• The degree of swelling is inversely related to the material strength of a hydrogel. • The compressive modulus of swollen VP/MMA hydrogels decreased from 13.1 MPa to 0.15 MPa when the EWC was increased from 32.9% to 82.6% • The compressive modulus of VP/HEMA hydrogels was found to decrease from 220 kPa to 10 kPa when the equilibrium swelling ratio was increased from 8 to 80	[111], [151]

The general technique used to assess the mechanical properties of a hydrogel is the tensile testing, compression test, local indentation test with a probe- and frequency-based tests such as shear rheometric or dynamic mechanical analyzer (DMA) (Figure 2.21) [120]. The most common equipment used for the mechanical characterisation of materials is a Universal Testing Machine, which is capable of carrying out tension and compression testing. Most frames are uniaxial, in that motion is actuated and force measured along a single axis, although biaxial instruments have become increasingly common [152]. In tensile testing, two grips in the instrument hold a strip of the hydrogel, which is subjected to a tensile force [153]. In addition, a compression test technique involves placing the material between two plates and compressing it. The pressure applied to the surface of the hydrogel and the distance the hydrogel is compressed could be used to calculate the mechanical properties of the hydrogels. For both tension and compression testing, the load-displacement (F-x) data are converted to stress-strain (σ-ε) data using simple geometrical relationships [154] and Young's modulus, E and failure strength, σ_f are reported. Typical tests are done at a fixed rate until specimen failure. Due to the time-dependent nature of hydrogels, testing at a variety of strain rates might necessary (Figure 2.22) [155]. The specimen might be subjected to creep (extension at fixed load or fixed stress) or relaxation (load decrease at fixed deformation or strain) experiments (Figure 2.22).

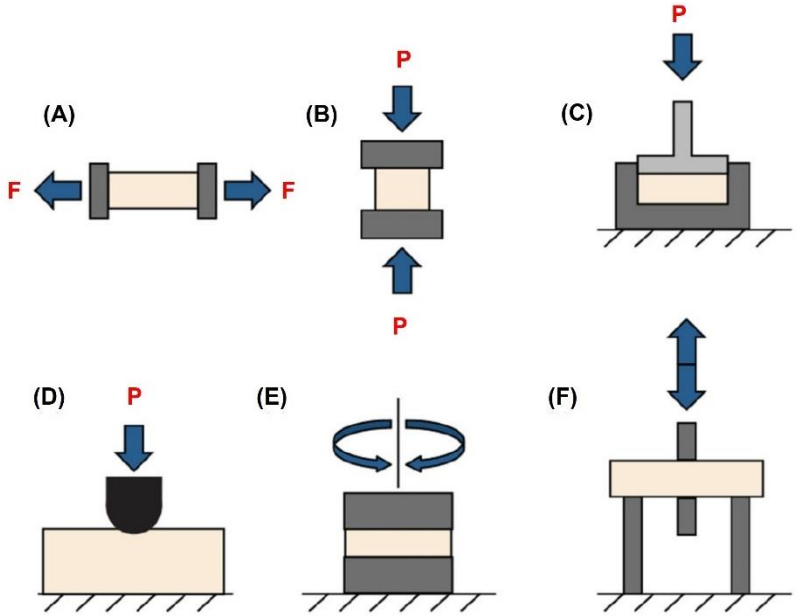


Figure 2.21 Schematics of different types of mechanical testing set-ups for testing hydrogel mechanical properties (A) Tension (B) Compression (C) Confined compression (D) Indentation (E) Shear rheometry (F) DMA three-point bending [120]

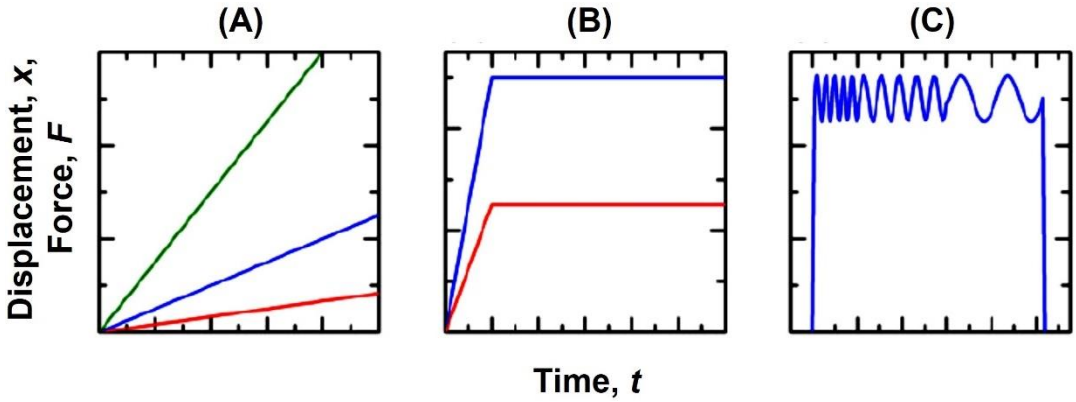


Figure 2.22 Mechanical test types of displacement-time (x-t) or force-time (F-t) for (A) Fixed rate for varying rates (B) Static creep or relaxation at fixed force or displacement and (C) Sinusoidal loading at varying frequency [120]

Analysis of elastic modulus, E could be simply interpreted from the slope of the linear, small strain, stress-strain (σ-ε) curve from a uniaxial tensile or compressive test. The stress-strain behaviour of hydrogels at their swelling equilibrium is elastomeric in

nature [132]. When in the xerogel state, the behaviour of thermoplastics will be dependent on the ambient temperature relative to its T_g. The relationship between the hydrogel compression modulus (E) and the effective crosslinking density (υ_e) of a polymer is given by the Davis-Huglin equation [121], [156]:

$$E = RT\upsilon_e{\upsilon_{2,s}}^{-1/3} \quad (2.8)$$

Where R is the universal constant (8.314 m^3.Pa.K^{-1}.mol^{-1}), T is the absolute temperature (in Kelvin) at swelling equilibrium, $\upsilon_{2,s}$ is the polymer volume fraction at the equilibrium state, and υ_e is the effective crosslink density in the hydrogel.

2.4 Structure, Properties, and Function of Gastrointestinal (GI) Tracts

Food is prepared for digestion by chewing and mixing saliva that contains water, mucus, electrolytes, and enzymes to facilitate the mechanical breakdown of food and begin carbohydrate digestion [157]. Partially digested food then passes through the pharynx into the esophagus, and then the stomach, small, and large intestine (Figure 2.23), during which digestion is affected by other organs, hormones, and nervous system effects.

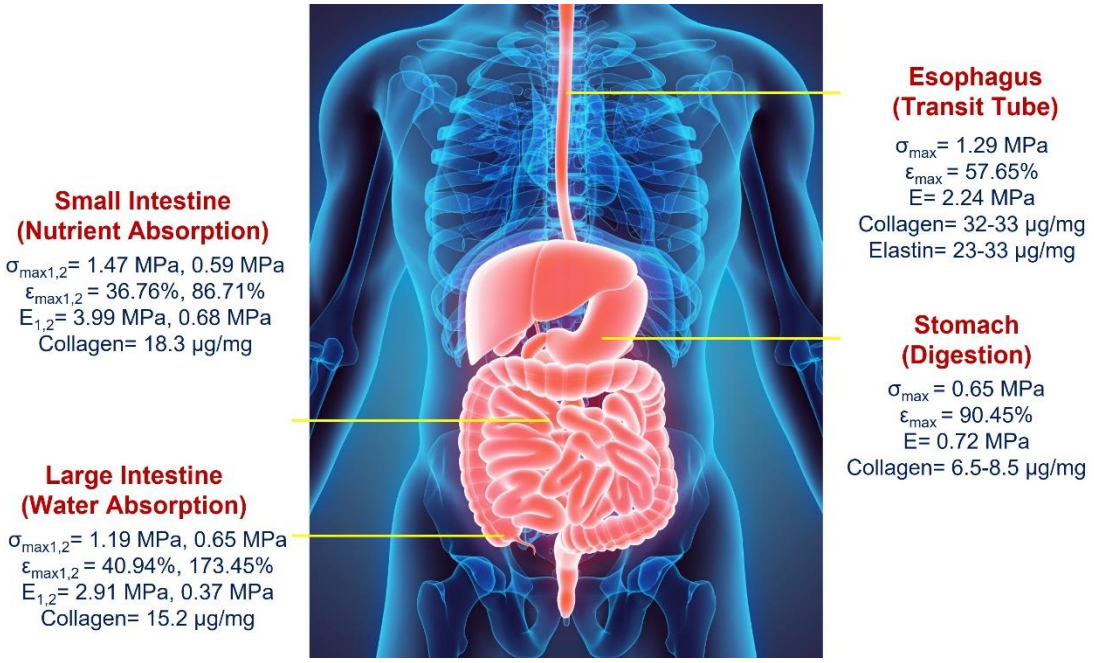


Figure 2.23 GI tract system consists of four major parts: esophagus, stomach, small intestine and large intestine

2.4.1 Esophagus

The esophagus is an expandable, normally closed muscular tube that connects the pharynx to the upper end of the stomach and measures about 25-30 cm in the adult [158]. It has an approximately cylindrical shape and a variable luminal diameter. This is surrounded by a wall, composed of four main layers i.e., the mucosa, submucosa, muscularis externa, and the adventitia (Figure 2.24) [159]. The mucosa layer is composed of connective tissue where collagen fibrils are organized according to a loose and random network. The submucosa plays a vital mechanical role in offering strong resistance to the deformation of the wall [160]. The major component of the submucosa is collagen [161]. Unlike mucosa which shows very fine collagen fibrils, submucosa has collagen fibrils organized in thick fibres arranged in a crisscross pattern (Figure 2.25). Two groups of collagen fibres are present: running in a

clockwise helix down the esophagus and in an anticlockwise helix. The fibres of both groups do not lie in different planes but intertwine extensively while crisscrossing each other [162]. Different values of the angle were reported in the literature, varying between 30˚ and 60˚ [160], [163]. The fibre orientation of mucosa-submucosa layers was significantly higher than in the muscle layer (α=60.5˚ for the mucosa-submucosa versus α=55.6˚ for the muscle) [164]. According to Schulze et al. [165], matrix components in the layers of the esophageal wall consist of collagen type I, collagen type III, collagen type V, collagen type IV, fibronectin, versican (chondroitin sulphate proteoglycan), and elastin. The collagen content of the opossum esophagus was reported about 65-104 µg/mg [166]. In the human esophagus, it was reported that the collagen and elastin contents were 32-33 µg/mg and 23-33 µg/mg, respectively [167].

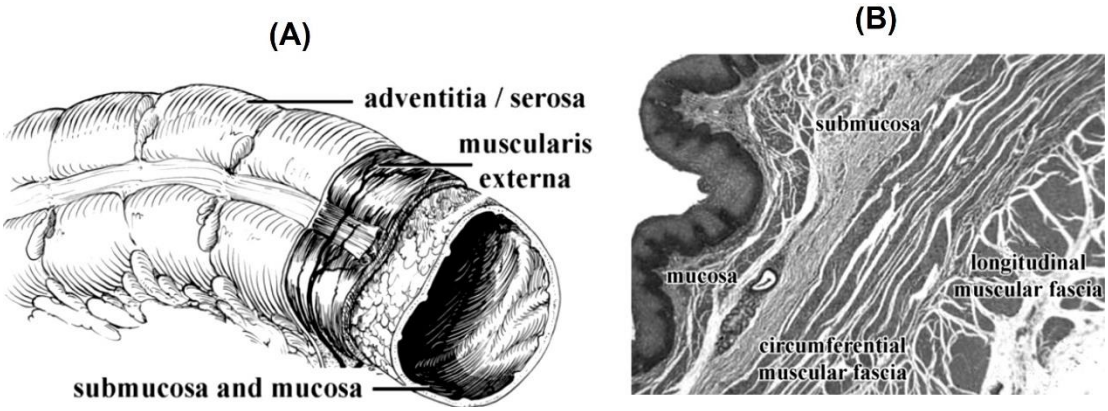


Figure 2.24 (A) Schematic representation of the histological configuration of esophagus (B) Optical microscope picture of an esophagus section [168]

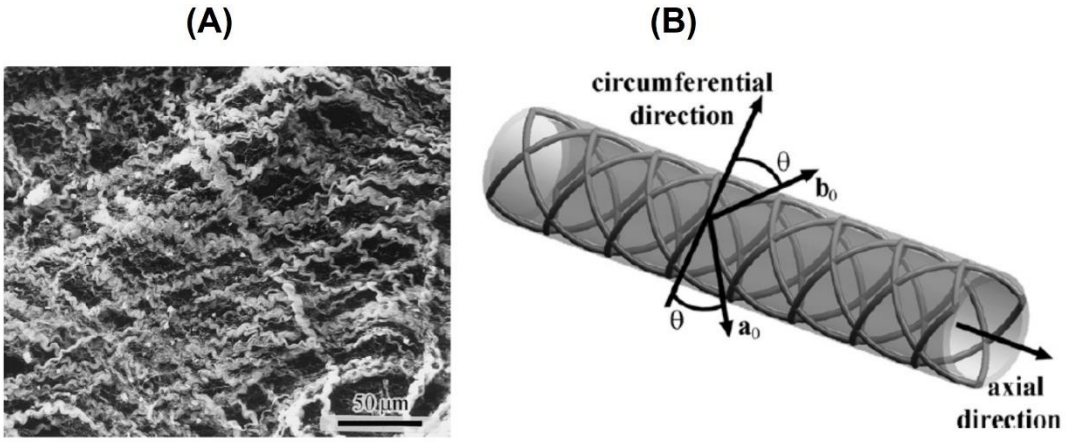


Figure 2.25 (A) SEM images of the distribution of collagen fibres within submucosa (B) Schematic representation of fibre arrangement [168]

Mechanical characteristics of human esophagus could be studied by analysing the stress and strain using a tensiometer. Results showed maximum stress and strain of 1.3 ± 0.5 MPa and 57.7 ± 13.4%, respectively [169]. The calculated elastic modulus in the linear stress-strain regime was 2.2 MPa. In addition, an experimental study in pigs showed the tensile strength and elongation at break values of the esophagus were 1.2 MPa and 180%, respectively [170]. The esophageal wall could be analyzed as a multi-layered anisotropic composite structure due to the specific orientation of reinforcing fibres. To quantify the anisotropy of the tissue, uniaxial tensile tests were conducted in pigs along with longitudinal and circumferential directions [163], [168]. When two layers of mucosa-submucosa and muscle were compared, the mucosa-submucosa layer showed significantly stronger than the muscle layer (3 MPa vs 1.1 MPa in the longitudinal direction and 2 MPa vs 0.7 MPa in circumferential) and more extensible than the muscle layer (2.6 vs 1.9 in longitudinal and 2.8 vs 2.5 in circumferential) [163]. Light microscopy disclosed that the esophageal wall and its layers contained more collagen (11-25%) than elastin (2.5-7.5%) in both directions, and elastin and collagen

contents were considerably higher in the longitudinal and circumferential sections of the mucosa-submucosa [171]. The directional differences in elastin content of both muscle layers were minimal, those in collagen content were more marked although with a less organized structure. In the adventitia, elastin was undulated and run primarily longitudinally. Collagen was similarly more continuous in that axis, but not to the extent of elastin.

2.4.2 Stomach

The J-shaped stomach lies below the diaphragm and has three divisions: the fundus, the body, and the antrum (Figure 2.26) [172], [173]. At the distal end of the stomach is the pyloric sphincter, which acts as a barrier between the stomach and the small intestine [174]. The stomach is temporary storage that mixes food (strong peristaltic contractions) with water and gastric juice to produce chyme, breaks food down physically and chemically, and controls the release of the chyme into the small intestine via regulation of the pyloric sphincter. The thickness of the stomach wall is around 3-7 mm and is comprised of four major layers such as mucosa, submucosa, muscularis, and serosa (Figure 2.26) [175], [176]. The serosa, or visceral peritoneum, is the outermost layer of the stomach. It consists of an inner layer of connective tissue and an outer layer of simple squamous epithelium. The muscularis of the stomach consists of three layers such as an outer longitudinal layer, a middle circular layer, and an inner oblique layer. In fundus, three layers blend and cannot be separated. Deep into the muscular layer are the submucosa and the mucosa, which are thrown into large folds called rugae when the stomach is empty. These folds allow the mucosa and submucosa to stretch, and the folds disappear as the stomach increases as it is filled.

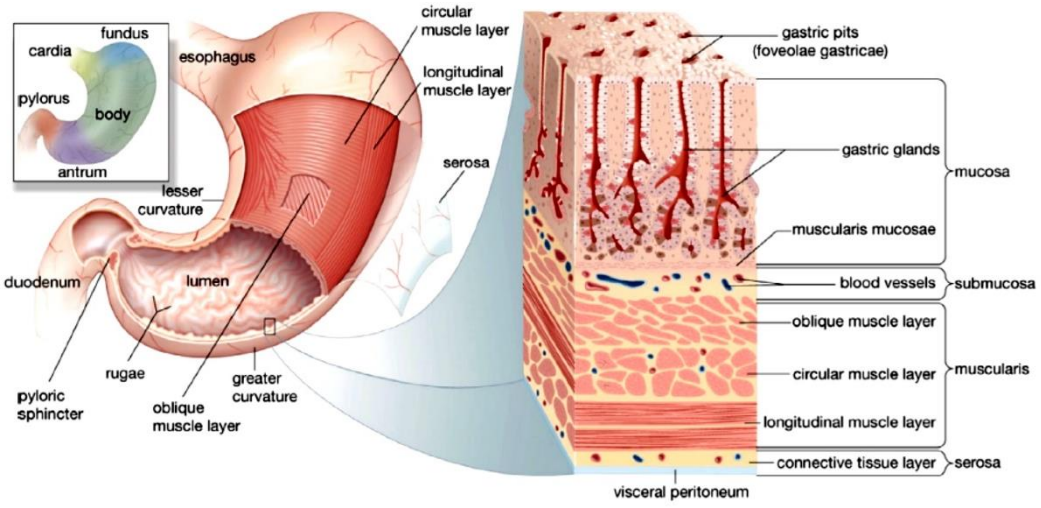


Figure 2.26 Structure of human stomach and gastric wall [177]

ECM of the gastric mucosa is composed of collagen, laminin, proteoglycan, elastin, fibronectin, and hyaluronic acid [178]. De Mello et al. [179], Gillessen et al. [180] and Shahin et al. [181] conducted a study on the expression of collagen types I, III, and IV in the gastric tissues. No differences were found in the expression of collagen types I, III, and IV within the fundic, corpus, or antral gastric regions. In marmosets, the expression of collagen types I and III was intense in the submucosa of the gastric wall [179]. In the lamina propria between the mucosal glands, however, collagen type I showed only mild staining, whereas collagen type III was detected by more intense staining in the gastric sections. This distribution pattern was similar to the normal human gastric pattern [180]. Collagen type III was more intensely expressed in the spaces between the gastric pits in the mucosa than collagen type I while type III exhibited the same staining intensity as collagen type I in the submucosa. In addition, collagen types I and III were also detected in the submucosa and lamina propria between the mucosal glands of rat gastric tissue [181]. Collagen type IV, the most abundant structural component in basement membranes [182], was intensely detected

not only around the mucosal glands and blood vessels within which basement membranes are presented [180] but also in the area surrounding the smooth muscle cells in the muscularis mucosa and muscular layers [179]. In normal rat gastric tissue, collagen type IV was detected in the lamina propria between the mucosal glands and the submucosa [181]. The collagen content in the human stomach was determined by the measurement of hydroxyproline. The data showed that the hydroxyproline content of human tissue was 6.5-8.5 µg/mg [183].

The biomechanical characterization of the stomach is important to study to understand the physiological function of gastric accommodation. In the investigation of the mechanical behaviour of the stomach, some studies in animals and humans measured pressure-volume relations for evaluation of tone, compliance, and tension in the gastric fundus by using a barostat [184]–[186]. The main assumption made in such studies the fundus was geometrically a sphere with uniform tension. In other words, it was assumed that the mechanical properties of the stomach in all directions and different layers were the same and that the wall was infinitely thin. However, other studies on the stomach had demonstrated the geometrical and structural complexity of the stomach and that the mechanical properties of the stomach were location-, direction-, and species-dependent [169], [187]–[190]. The mechanical properties of the human stomach were reported that the maximum stress and strain were 0.7 ± 0.2 MPa and 90.5 ± 23.6%, respectively, in the longitudinal direction and the maximum stress and strain were 0.5 ± 0.2 MPa and 99.6 ± 25.2 %, respectively, in transversal direction [169]. The Young's modulus was equal to 0.7 MPa and 0.5 MPa for longitudinal and transversal specimens, respectively.

The stress-strain properties of rat and rabbit stomachs in the longitudinal and circumferential directions were studied [188]. The rat gastric (longitudinal) was stiffer than the rabbit gastric specimen in all directions. The maximum stresses were recorded to be 50 and 30 kPa for rat stomach in the longitudinal and circumferential directions, respectively. However, the rabbit stomach showed the maximum stresses of 20 and 10 kPa when reached 50% strain in the longitudinal and circumferential directions, respectively. The mechanical characteristics of pig stomachs with different layers, locations, and directions were also studied [189], [190]. The maximum stress and strain of greater curvature samples of pig stomach were 0.0791 ± 0.0032 MPa and 2.281 ± 0.041 in the longitudinal direction and 0.041 ± 0.0025 MPa and 9.181 ± 0.062 in the circumferential direction, respectively [190]. Therefore, the tensile fracture stress value in the longitudinal direction was about twice as much as in the circumferential direction, while the fracture stretch ratio in the longitudinal direction was only about a third of that in the circumferential direction (Figure 2.27). The same pattern was observed for the smaller curvature stress-strain data.

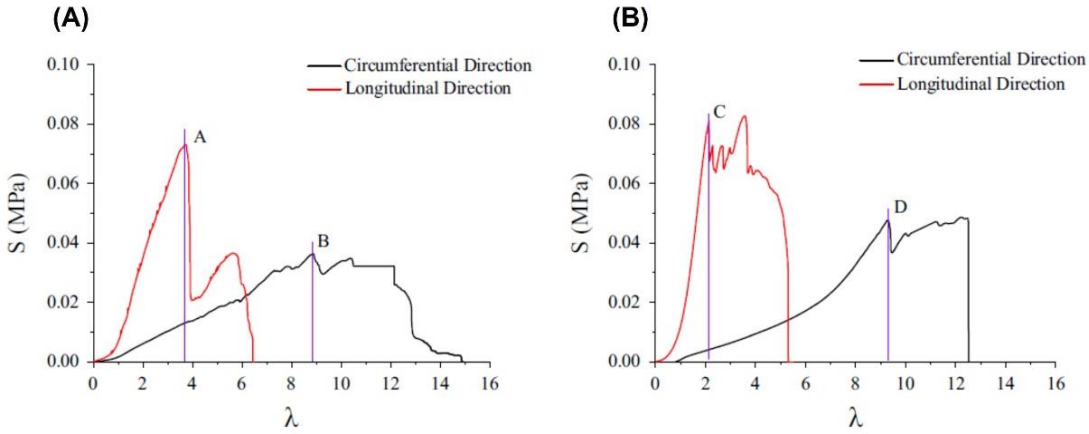


Figure 2.27 Tensile failure stress-stretch ratio curves of the stomach stripes at different orientations and locations (A) Smaller curvature (B) Greater curvature [190]

2.4.3 Small intestine

The small intestine is the site where most digestion and absorption take place [172]. This 6-meter tube (range: 4.6-9 m) extends between the stomach and the large intestine and has three subdivisions: the duodenum, the jejunum, and the ileum. The duodenum is the shortest section, on average measuring from 20-25 cm in length and this is the only part of the small intestines where Brunner's glands are present [191]. The jejunum constituting about two-fifths of the total length of the small intestine is about 2.5 m long and contains plicae circulars and villi to absorb the products of digestion. The ileum constituting three-fifths of the small intestine is about 3.5 m and it absorbs any final nutrients with major absorptive products being vitamin B12 and bile acids. Peyer's patches in the ileum have functioned as the immune surveillance system of the intestinal lumen and facilitate the generation of the immune response within the mucosa. Special anatomical features greatly increase the surface area for absorption, namely the circular folds of the inner surface of the intestine, villi, and microvilli or brush border. Altogether would increase the surface of the small intestine 600 times [192].

The intestinal wall is composed of four layers such as mucosa, submucosa, muscularis externa and serosa (Figure 2.28) [193]. Among these, the mucosa plays an essential role in digestion and absorption, whereas the submucosa acts as the skeleton of the intestine to integrate the internal mucosa and the external muscle layer. The muscularis contains two smooth muscle layers, a thin outer longitudinal layer that contracts, relaxes, shortens, and elongates the gut allowing food to move in one direction, and a thicker inner circular layer of smooth muscle that enables the gut to contract and break apart larger food particles. Nerves lie between these two layers and

allow these muscle layers to work together to propagate food in the proximal to distal direction. The serosa is the outside layer and consists of mesothelium and epithelium. The epithelial cells in the small intestine have a rapid renewal rate, with cells lasting for only 3-5 days.

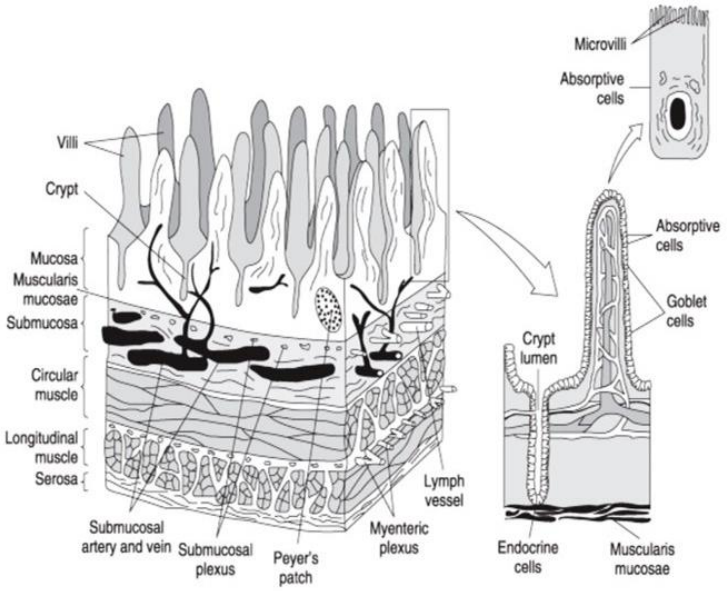


Figure 2.28 Structure of the small intestinal wall [194]

Most of the collagen types I and III of the intestinal wall are concentrated in the submucosa and only small amounts are found in the serosa and the two muscle layers [195]. Although collagen is rigid and nonelastic, the submucosa adapts to the various shapes of the intestinal lumen during peristalsis. This unique property has been explained by the diagonal arrangement of the collagen fibres [196], [197]. The main framework of the submucosa is composed of two arrays of interwoven collagen fibre bundles around the intestinal wall, one set in a clockwise direction, the other counter-clockwise helix (Figure 2.29) [198]. These two sets of helices, showing mirror-image symmetry, are oriented at a range of angle ±30-50˚ to the longitudinal axis of the intestine. These collagen fibre bundles generally measure about 5 μm in diameter, and

each collagen fibre consists of bundles of collagen fibrils about 60-80 nm in diameter. The fine network of the collagen fibrils is observed over the main framework. The fibrils might restore the crimp pattern of the large fibres after they have undergone small deformation [196]. It is also likely that these collagen fibrils play an important role in connecting adjoining external muscle layers to the main framework of the collagen fibres [198]. Thereby, muscle contraction force is transmitted to the skeletal framework of the submucosa to generate movement of the whole intestinal wall. The main ECM component of the small intestine is collagen type I with minor amounts of collagen types III, IV, V, and VI [199]. In addition, it also contains a variety of glycosaminoglycans (GAGs), including heparin, heparan sulfate, chondroitin sulfate, and hyaluronic acid [200]. Adhesion molecules such as fibronectin and laminin as well as various growth factors are presented in ECM small intestine [201]. The collagen contents were measured and the results were 3.9 ± 0.2 μg/mg, 2.5 ± 0.1 μg/mg, and 2.1 ± 0.1 μg/mg in the duodenum, jejunum, and distal ileum of pigs, respectively [202]. In addition, the collagen content in the human intestine was reported to be 18.3 μg/mg [203].

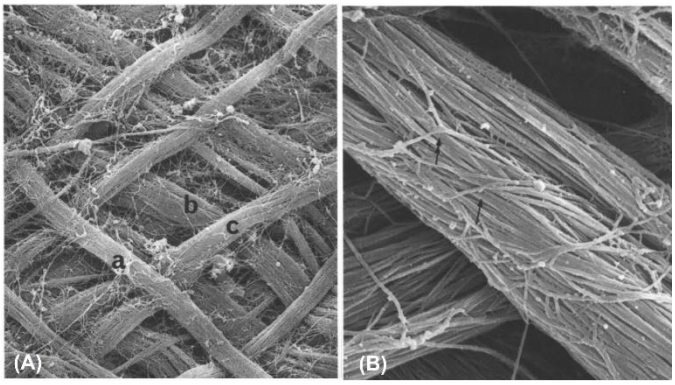


Figure 2.29 (A) Collagen fiber bundles with some branching and anastomosis (a,b,c) x300 (B) Collagen fiber composed of densely packed collagen fibrils (arrow) about 80 nm in diameter x9000 [198]

The mechanical properties of the human small intestine were studied by Egorov et al. [169]. The stress and strain values of the transversal sample of small bowel were 0.8 ± 0.3 MPa and 87.9 ± 22.9%. The axial specimens of the small intestine showed two values of maximum stress (Figure 2.30). The first stress maximum was nearly 2.5 times the second stress maximum. The first stress and strain maxima were 1.5 ± 0.5 MPa and 36.8 ± 10.8%, respectively. The value of the second stress maximum was 0.6 ± 0.4 MPa and the strain level corresponding to the second maximum was 86.7 ± 38.9%. The cause of two maximum stress in the axial direction was due to the heterogeneity of mechanical properties along with its layer thicknesses. In contrast, one maximum stress was generated in the transversal specimen because the adhesive connections between the intestinal submucosa and muscularis layers were strong. The mechanical stress-strain distribution of the pig's small intestine in different locations (duodenum, jejunum, and ileum) was also studied [202]. The stress-strain distribution and elastic modulus-strain distribution of the segments demonstrated that the duodenal wall was stiffer than the jejunal and the ileal walls. The elastic modulus values for duodenum, jejunum and ileum were 1.8 MPa, 1.1 MPa, and 1.0 MPa at strain levels of 0.6, 0.9 and 1.0 and maximum stress of 100 kPa. The mechanical properties might be associated with the differences in flow properties between the proximal and distal small intestines.

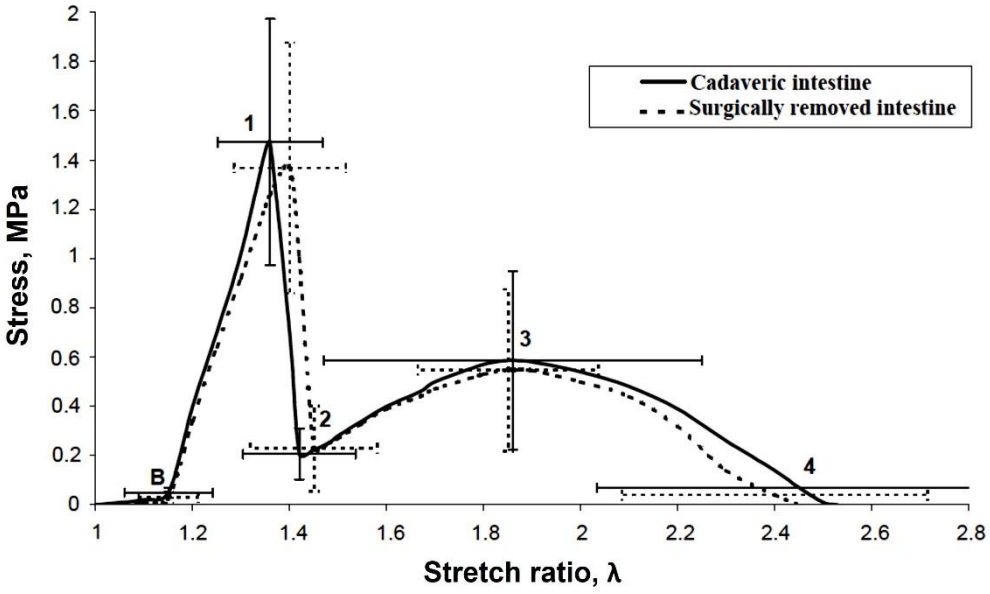


Figure 2.30 Mechanical testing of human cadaveric and surgically removed axial specimens of the small intestine at 2λ strain rate. B is the strain level at which a sharp increase of stress begins [169]

2.4.4 Large intestine

The horseshoe-shaped large intestine begins at the end of the ileum and ends at the anus. It consists of the colon (ascending, transverse, descending, and sigmoid), cecum, appendix, and rectum [172]. The large intestine is primarily a drying and storage organ whose major function is the reabsorption of water. The movement of the colon is more sluggish than those of the small intestine. While in the colon, chyme is converted to faeces. The large intestinal wall is made up of four main layers such as mucosa, submucosa, muscularis externa, and serosa (Figure 2.31) [204]. A loose network of collagen fibrils characterizes the structure of mucosa, while the submucosa is mainly composed of collagen fibres that are arranged according to two main helixes, a clockwise and an anti-clockwise one that runs down the colon structure [205]. The collagen contents in the rat and human large intestines were reported to be 5.07 ± 0.65

and 15.15 ± 0.13 μg/mg [206], [207]. Muscularis externa, contains two smooth muscular fibres, one in a longitudinal direction forming three thick bands known as taenia coli and another one in the circumferential direction. These layers contribute to the motility of the large intestine. The serosa forms a thin layer composed of loose connective tissue and a squamous epithelium that lines the overall tubular structure.

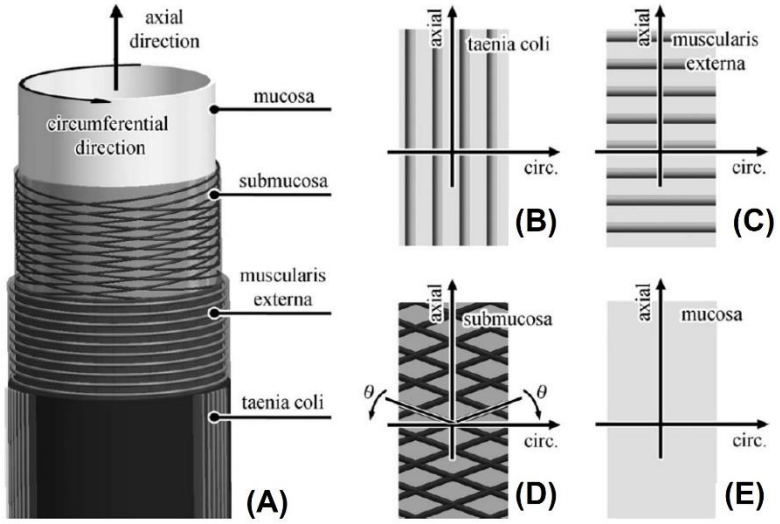


Figure 2.31 Schematic representation of colon structural configurations (A) Different distributions of fibrous elements characterize the different tissues leading to specific anisotropic properties (B) Muscular layer in the axial direction within taenia coli layer (C) Circumferential direction within muscularis externa layer (D) Submucosa layer (E) An overall isotropic configuration for mucosa [205]

Gao and Gregersen [208] examined the mechanical properties of the large intestine of rat. The longitudinal and circumferential stresses versus strain were then analyzed concerning the stiffness of the colonic wall. It was found that all the segments of the colon were stiffer in longitudinal than circumferential direction, from which the transverse colon was the stiffest segment in both directions (37.5 kPa). The exponential nature of the stress-strain curve helps to protect soft tissue from overdistension and

damage under high applied pressure inside the lumen. Egorov et al. [169] measured the mechanical properties of the human large intestine. The tensile tests were conducted in both axial and transversal directions. The results indicated that different layers of the large intestinal wall showed different mechanical properties in axial and transversal directions. The ultimate tensile strength and strain were 0.6 ± 0.2 MPa and 87.9 ± 27%, respectively, for transversal specimens. The calculated Young's modulus was 0.7 MPa. In the longitudinal specimens, they had two maxima curves very similar to the small intestine data. The first maximum stress and strain were 1.2 ± 0.3 MPa and 40.9 ± 12.5%, respectively. The calculated elastic modulus was 2.9 MPa. However, the second maximum stress and elastic modulus were significantly lower than the first data such as 0.7 ± 0.2 MPa and 0.4 MPa, respectively. However, the strain was almost two-fold higher such as 173.5 ± 47.9%. The mechanical behaviours of pig rectum under tensile (longitudinal and circumferential directions), compressive and shear stress was evaluated [209]. The results showed a significant difference in the linear modulus at different orientations. The resistance to deformation was found to be higher in circumferential than the longitudinal direction possibly due to the high number density of horizontal folds in the rectal wall with the characteristic width ranging from sub-μm level to sub-mm [210]. Sokolis et al. [211] examined a 3D constitutive model to mechanically analyze the multiaxial behaviour of the rat large intestine. These results from the inflation/expansion experiment strongly correlated to those of Gao and Gregersen, stating that all segments of the colon were stiffer in the longitudinal direction than circumferential direction, in which the transverse colon was the stiffest segment among all in both directions.

2.5 Summary

This chapter has discussed the inflammation condition in patients with Crohn's disease (CD). CD affects any part of the GI Tract, most commonly affecting the end of the small intestine (ileum) and the beginning of the colon. Surgical resection continues to play an important role in CD treatment, however, there are risks of recurrent disease and further resection. A progressive reduction in bowel length due to resection leads to the development of short bowel syndrome (SBS). Thus, management of SBS was developed and it required a combination of nutritional, medical, and surgical approaches. Despite all of the success, many complications might occur including sepsis, liver problems, fistulae formation, necrosis, staple line leakage, bowel obstruction, abscesses, and death. Intestinal lengthening using mechanical stretching (*distraction enterogenesis*) has been developed as a viable method to treat SBS. However, many of these methods introduce the complication risks such as infection, inflammation, and tissue obstruction. A self-inflating tissue expander has been explored and proved an exciting prospect with particular advantages in reconstructive surgery. VP and MMA hydrogels have a proven history as biomaterials and have a great combination of extraordinary chemical and physical properties. The morphology, mechanical properties, and function of the GI tract have been discussed and will be used as a reference parameter for the data analysis of the GI tract in this thesis.

Chapter 3: Experimental Procedures

3.1 Introduction

This chapter describes how the hydrogel was synthesized to produce various hydrogel compositions and sizes as well as how the hydrogels with different composition ratios were characterized by investigating the functional group (FTIR), microstructure (SEM), water contact angle (WCA), and mechanical properties. The mechanical properties of the hydrogel were investigated to determine the compressive modulus. The glass transition temperature (T_g) of hydrogels was measured using differential scanning calorimetry (DSC) and this temperature could be used to evaluate the optimal anisotropic processing temperature for the isotropic hydrogels. The swelling behaviour of VP/MMA hydrogels was investigated in DI water and PBS. This measurement was conducted to observe the effects of solvents on the swelling behaviour of hydrogels. The PBS solution most closely reflects the physiological milieu of human tissue fluid. The swelling pressure of hydrogels in DI water was also measured to determine the pressure generated from the hydrogels during swelling.

The GI tract tissues were obtained from Sprague Dawley (SD) rats. The tissue samples were prepared, washed, fixed, and dried to observe their morphology using SEM. The structure and the size of collagen fibre were the main focus of this thesis. The mechanical properties of the GI tract tissues were tested by Universal Tensile Machine (UTM) to determine the maximum stress and strain. The morphology of stretched tissue was observed by SEM to determine whether the arrangement of collagen fibre was significantly altered due to stretching.

The *ex vivo* study was conducted by applying various designs and sizes of hydrogel devices. When the hydrogel was immersed in the DI water, the hydrogel will expand and generate swelling pressure. Too little pressure would be insufficient to

cause significant expansion, whilst excessive pressure could result in tissue necrosis. The swelling pressure generated from hydrogel is crucial to predict probable clinical performance. An expander device can be used to stretch the tissues *in vivo*. The histology measurement was performed to observe the structure of the mucosa, crypt, and submucosa before and after lengthening with a hydrogel device.

3.2 Synthesis of VP/MMA Xerogels

N-Vinyl-2-pyrrolidinone (VP) and methyl methacrylate (MMA) were purchased from Sigma-Aldrich, United Kingdom. A 2,2'-Azobis (2-methylpropionitrile) (AIBN) and allyl methacrylate were supplied by Sigma, United Kingdom. VP/MMA xerogels were synthesized by adopting the procedure from Polymeric Siciences Ltd with some modifications in the purification step of the monomers, AIBN recrystalization, and addition of crosslinker and initiator concentrations. Figure 3.1 shows the polymerisation of VP/MMA xerogel. VP or MMA monomer was ditilled under vacuum before polymerisation reaction occurred to remove the sodium hydroxide (NaOH) or monomethyl ether hydroquinone (MEHQ) inhibitors. Firstly, the initial VP monomer with NaOH inhibitor was dried over calcium hydride (CaH_2) and distilled under vacuum. MMA contains monomethyl ether hydroquinone (MEHQ) was sequentially washed with an alkali solution, 5% sodium bisulfite ($NaHSO_3$) until the monomer became colourless and then washed with deionized water (DI) to remove residual alkali. Finally, dried over MMA with anhydrous calcium chloride ($CaCl_2$) followed by distillation in a nitrogen atmosphere at reduced pressure. Freshly distilled monomers were used for the synthesis of VP/MMA copolymer.

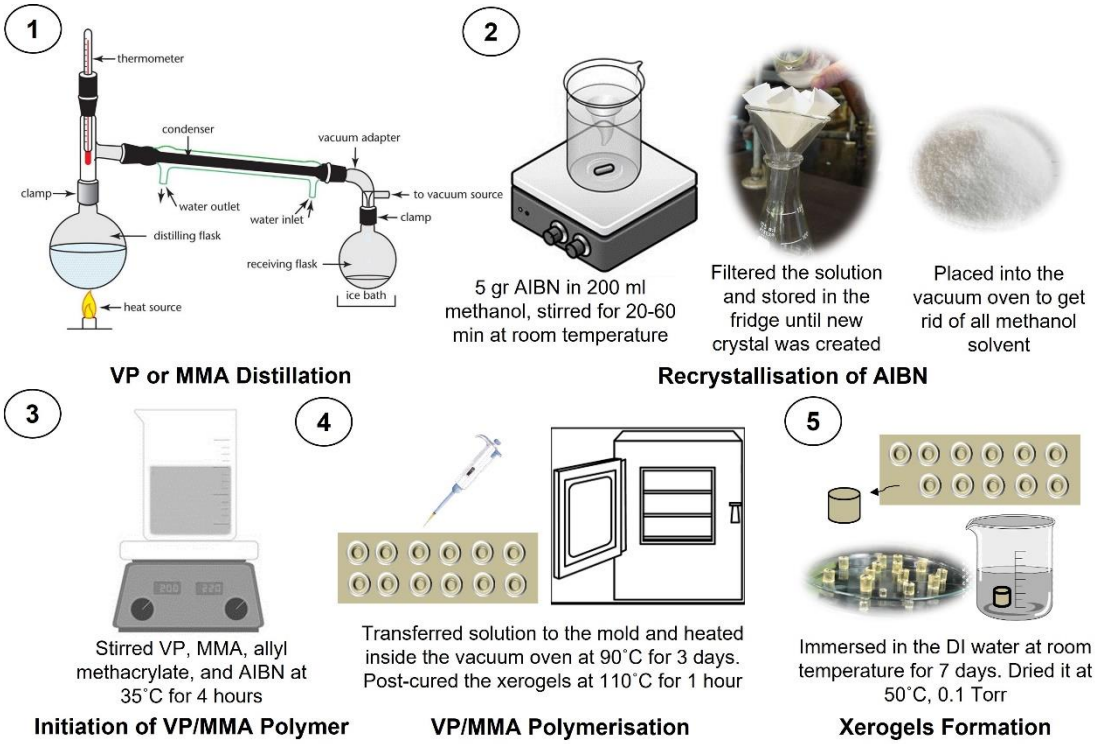


Figure 3.1 Polymerisation of VP/MMA until xerogels formed

AIBN was recrystallized using a methanol solution to reduce the risk of having impurities that corrupt the polymerisation process [212]. The polymerisation was carried out from VP and MMA monomers at the weight ratio of 95:5wt% (VP95), 90:10wt% (VP90), and 85:15wt% (VP85). Allyl methacrylate (0.3 wt%) was used as the crosslinker and AIBN (0.3 wt%) was used as the free radical initiator. In this study, the concentrations of crosslinker and initiator were increased compared to the crosslinking density (0.2wt%) used in the former work [108], [109]. The purpose is to obtain the optimum swelling properties to delay the expansion rate and swelling ratio, improve mechanical properties and increase the swelling force. Increasing the initiator concentration will decreases the size of the pores at a given polymerization temperature due to the increasing rate of polymerization [213]. In addition, increasing

the crosslinker content will increases formation of rigid copolymer chains and accelerates phase separation during the crosslinking process [214].

The VP and MMA monomers at various weight ratio were blended at 35˚C for 10 minutes. The crosslinker (allyl methacrylate) and initiator (AIBN) were then added to the mixture. The mixture was blended at 35˚C for 4 hours to ensure homogeneity. The mixture solution was poured into the cylindrical mould. The sizes of the hydrogel used in this study were 12mmD & 3mmL (A), 6mmD & 3mmL (B), 6mmD & 6mmL (C), 6mmD & 9mmL (D), 3mmD & 3mmL (E). The monomeric mixture was thermally polymerised in the vacuum oven at 90ºC for 3 days. Once curing was complete, the xerogel was post-cured by heating to 110ºC for 1 hour in order to remove any residual mechanical stress within the system. Prior to experimental use, the unreacted monomeric of the copolymer were extracted by immersing the copolymer in a bath of DI water at room temperature for 7 days (Figure 3.2) and the gels were dried at 50ºC in a vacuum oven at 0.1 Torr. The xerogel samples were then stored in an inert nitrogeneous atmosphere in lightproof airtight packages.

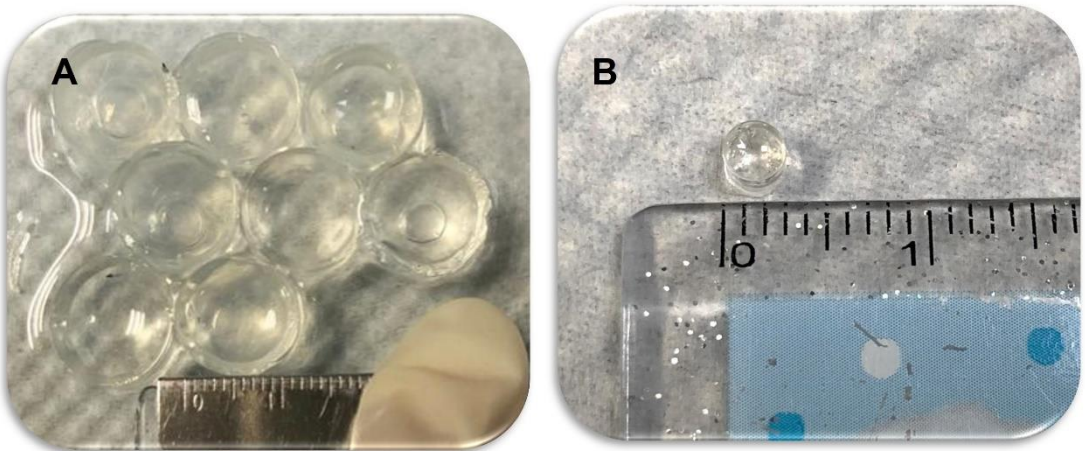


Figure 3.2 (A) Hydrogels washed in DI water for 7 days (B) Re-dried hydrogel sample

The free-radical crosslinking polymerization system for the production of copolymers includes VP or MMA monomer, crosslinker (allyl methacrylate), and initiator (AIBN). Figure 3.3 shows the breakdown of the AIBN into two free radicals and a nitrogen molecule. This occurs at 35˚C for 4 hours and the nitrogen gas diffuses out of the solution. As the free radicals are produced, they react with the NVP and MMA monomers to form further free radicals (Figure 3.4). When this free radical molecule is produced, it reacts further with MMA and NVP molecules to form three-dimensional network of polymer chains (called propagation), as shown in Figure 3.5. the reaction is terminated either by two of the molecules in Figure 3.5 combining, or through reaction of one molecule from Figure 3.5 reacting with a free radical produced in Figure 3.3. Crosslinking between the polymer chain occurs via the allyl methacrylate molecule, as seen in Figure 3.6.

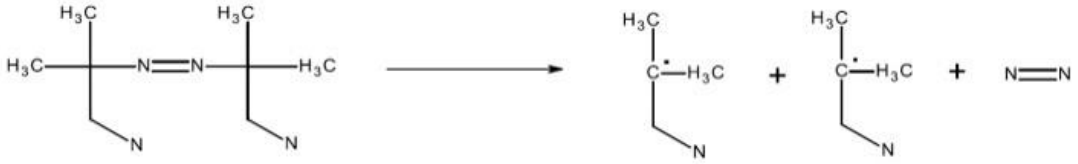


Figure 3.3 An AIBN molecule breaking into two free radical molecules and a nitrogen molecule



Figure 3.4 Initiation reaction where VP molecule reacts with a free radical (produced by the initiator) to form another free radical

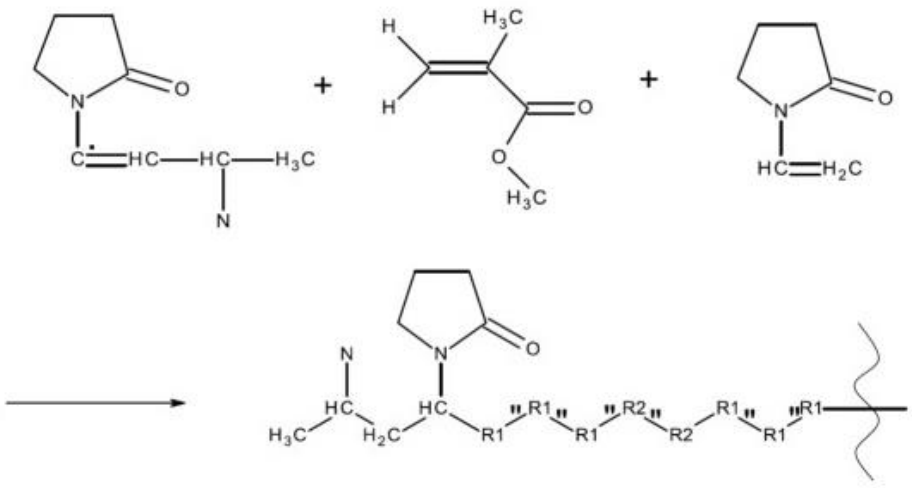


Figure 3.5 Propagation reaction where the free radical continuous to react with VP and MMA monomers to form a polymer chain. R1 represents the NVP component and R2 represents the MMA component

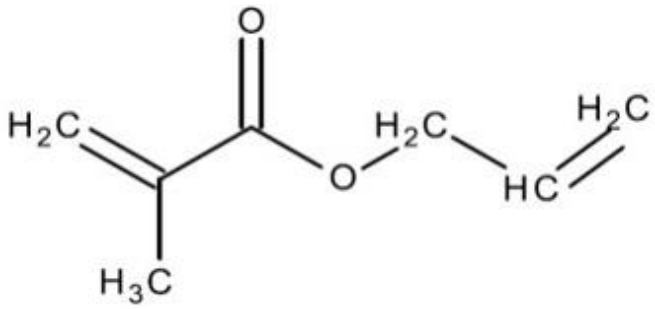


Figure 3.6 Allyl methacrylate molecules as a crosslinker

At the gel point, the polymer system changes from liquid to solid state. Continuing polymerization and crosslinking reactions will increase the amount of polymer mixture and the crosslinking density of the network. In VP/MMA copolymer system, there is a tendency for phase separation to occur into pure NVP regions and regions which are rich in MMA [215]. Small angle neutron scattering has previously been used on NVP/MMA copolymers (Polymeric Sciences, Ltd) and has shown that the polymer is block co-polymer in nature [216]. The first MMA phase separated and

intramolecularly crosslinked particles (nuclei) agglomerate into larger clusters. Continous reactions increase the number of clusters in the reaction system so that the polymer phase becomes continous. Thus, a system consisting of two continous phases. At high MMA contents (such as in the 85:15wt% VP/MMA), the nuclei are highly intramoleculary crosslinked thus creates an increasing of the effective crosslinking population so that the number of pores increases and the pore size decreases (it will be discussed in Chapter 4.2.4). The existence of MMA clusters or agglomerations in the copolymer structure obeserved by SEM showing cauliflowers-like structure [214].

3.3 Nuclear Magnetic Resonance (NMR)

The purity of monomers was investigated by using nuclear magnetic resonance (^{1}H-NMR, Bruker 500 MHz spectrometer). NMR instruments require 5mm tubes (Figure 3.7), where 5 mm refers to the outer diameter of the tube. The length of the NMR tube is 7-8 inches (17.8 or 20.3 cm). A 5-10 gram of distillate VP or MMA sample was dissolved in deuterated chloroform ($CDCl_3$) solvent. Mixed and transferred it into an NMR tube. An appropriate volume is 0.55 mL or 40-50 mm solution height in a 5 mm NMR tube. The polyethylene cap was then pushed fully onto the tube. 1H-NMR spectra of VP or MMA monomer were recorded and analyzed using MestreNova-Mestrelab software.



Figure 3.7 A 5mm NMR tube used for the NMR experiment

3.4 Fourier Transform Infra-Red (FTIR)

The chemical structures of the PVP, PMMA, and synthesized VP/MMA were investigated using Fourier Transform Infrared Spectroscopy (FTIR, Varian Excalibur FTS 3500), as shown in Figure 3.8. The absorbance spectra consist of 64 interferograms at 4 cm^{-1} resolution measured in the 4000-400 cm^{-1} mid-IR wavelength range. The experiment was conducted at room temperature. Firstly, the sample was placed on the top surface of the crystal. The sample surface must be flat, otherwise intimate contact between the sample and the attenuated total reflectance (ATR) crystal could not be obtained. When the sample was exposed to infrared radiation, the spectrum of the sample selectively absorbs radiation of specific wavelengths which causes the change of dipole moment of sample molecules. Consequently, the vibrational energy levels of sample molecules transfer from the ground state to the excited state. The intensity of absorption peaks is related to the change of dipole moment and the possibility of the transition of energy levels. The frequency of the absorption peak is determined by the vibrational energy gap. The spectrum of each sample, which took less than 2 minutes to acquire, was normalized. Duplicate independent measurements were taken on each sample. Between measurements, the attenuated total reflectance (ATR) surface was cleaned with a 70% ethanol solution.



Figure 3.8 FTIR Varian Excalibur FTS 3500 instrument

3.5 Water Contact Angle (WCA)

The static water contact angle was used to evaluate the surface wettability of the hydrogel. The Contact Angle Goniometer Sindatek Model 100SB instrument (Sindatek Instruments Co., Ltd.) was used for the measurement of contact angle. Sessile drop measurement is the most commonly used contact angle measurement method. In practice, a droplet was placed on the solid surface and an image of the drop was recorded. The static contact angle was then defined by calculating the included angle between the water droplet and the horizontal plane (Young-Laplace equation). In this study, the WCA of hydrogels at various composition ratios such as VP95, VP90, and VP85 were measured. Three water droplets were spread on the surface and the angles were analyzed by the device software.

3.6 Scanning Electron Microscope (SEM)

Hydrogels were prepared by immersing xerogels in DI water until equilibrium. Hydrogels were frozen at -80˚C for 24 hours and then freeze-dried to remove water absorbed within a gel. A small piece of hydrogels was cut with a sharp blade. A cross-section sample was attached by conductive adhesive tape (carbon tape) to a specimen holder. The edge of the sample was brushed with electrodag and coated with a thin gold layer (Bio-Rad Polaron Division). Then samples were inserted into the SEM microscope (Zeiss EVO MA10) and observed in a high vacuum at an accelerating voltage of 10 kV. Samples were observed at different locations and magnifications. The pore size, area, and volume of the hydrogels were analyzed and quantified using Image J software.

3.7 Compression Testing

The compressive Youngs Moduli of gels were measured using the same apparatus of the swelling force measurement. The experiment was conducted at a strain rate of 50 mm/min. Before measurement, hydrogels were measured and hydrated in DI water for 48 hours. Samples were taken out of the solution and any remaining surface water was removed using filter paper. The dimension of swollen gels was measured using digital callipers [± 0.01 mm]. The hydrogels were placed under a compression plate. Different scale loads were successively applied on the upper touch until a point was reached when the hydrogel could not support any more weight. The elastic modulus of hydrogels could be determined through the analysis of the stress-strain curve. Three tests were carried out for each composition and dimension of hydrogels.

3.8 Volume Swelling and Gel Fraction Measurement

The swelling behaviour of hydrogels with different compositions and sizes was observed by hydrating the dried gels in DI water at room temperature and PBS at 37˚C for 7 days. After being fully hydrated at a given time, samples were taken out of the solution and any remaining surface water was gently removed using filter paper. The expanded height and diameter of gels were measured using a digital calliper and weighed on a balance. The solution was changed with a fresh solution after each measurement. The mass and volume change of the hydrating samples were measured at a time interval. The swelling rate was observed from plots of increasing swelling ratio over-hydrating time. It could be quantified through volume (Q_v) and equilibrium (Q_∞) swelling ratio [116], [217]:

$$Q_v(\%) = \frac{V_s - V_d}{V_d}\ x\ 100\% \quad (3.1)$$

$$Q_\infty(\%) = \left[\frac{V_\infty - V_d}{V_d}\right] x\ 100\% \quad (3.2)$$

Where V_S is the volume of the swelled hydrogels at time t, V_d is the volume of the dried gels, V_∞ denotes the volume of the gels at equilibrium.

Gel fractions that indirectly reflected the copolymerization yields were estimated by measuring their insoluble part after immersion in DI water for 48 hours. The gel fraction was calculated as follows [218]:

$$Gel\ fraction\ (\%) = \frac{W_d}{W_i} x100 \quad (3.3)$$

Where W_d is the weight of the dried gel after extraction and W_i is the initial weight of the dried gel.

3.9 Swelling Force Measurement

The initial dimension of hydrogel was measured. Hydrogel samples were prepared and placed into a glass disc chamber. A fixed compression plate was placed on top of the hydrogel sample (Figure 3.9). DI water was filled into the chamber up to compression plate height. Initially, the force reading was zero. After additional solvent, the force reading began detecting the swelling force value. The uniaxial force collected was the force during hydrogel swelling against the fixed plate. Swelling force data were collected every second until an equilibrium was reached. The swelling force measurement was conducted using Densor Mayer Group apparatus which consists of a 3 kN load cell and a transducer meter (SM-100, Interface, USA). The swelling force was measured for different sample compositions and dimensions. After the swelling force was obtained, it could be used to analyze the swelling pressure.

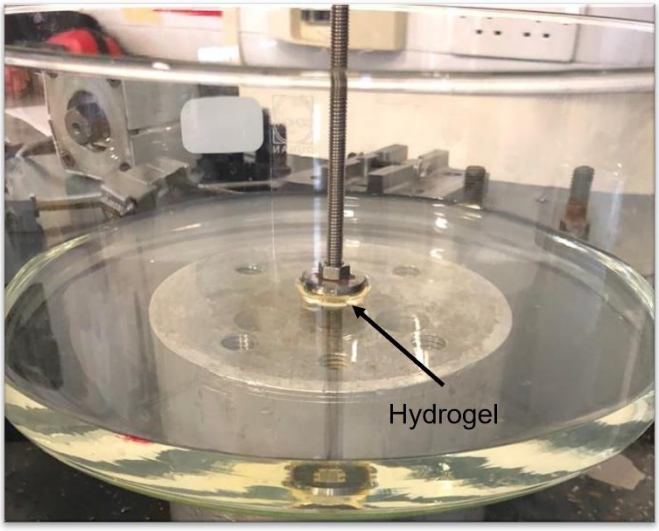


Figure 3.9 Swelling force measurement of hydrogels

3.10 Differential Scanning Calorimetry (DSC)

DSC (DSC7, Perkin Elmer, USA) measures the energy absorbed (endotherm) or produced (exotherm) as a function of time or temperature. DSC was applied to the

process involving a change in heat capacity, such as the glass transition. The indium calibration standard was used to calibrate DSC instruments. In DSC analysis, the powdered samples were prepared by crushing the xerogel in a pestle and mortar and weighing approximately 5-10 mg. The sample was placed in the bottom half of an aluminium DSC pan with the pan lid placed on top of the sample (Figure 3.10). The sample pan was aligned in the encapsulating press and the handle was pressed down to seal the aluminium pan. Both sample and empty reference pan were placed on small platforms within the DSC chamber. Thermocouple sensors lie below the pans. Samples were measured in the temperature range of 20-250˚C at 10˚C/min under a helium atmosphere. Data obtained from DSC measurements could be used for reference temperature of the anisotropic processing.

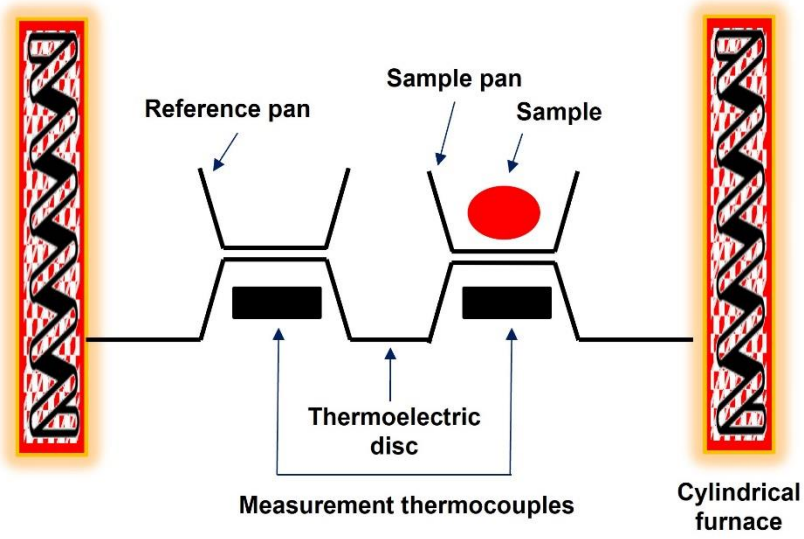


Figure 3.10 Schematic of the interior of DSC

3.11 Anisotropic Hydrogels

The anisotropic hydrogels were achieved by annealing the isotropic copolymer disc under pressure for a specified time using a manual hydraulic press (Specac Ltd,

Orpington, Kent, UK) fitted with thermostatically controlled heating plates (specifically designed and manufactured by Dr Drahosh Vesely) (Figure 3.11). This technique was chosen on account of its ease of operation and ability to precisely manipulate the degree of hydrogel compression and produce an anisotropic gel. The xerogels were heated to the range of T_g VP/MMA for 60 minutes before compressing at 100 MPa. The compressed gels were held constrained at this temperature for a further 60 minutes before allowing gels to cool to room temperature. Cooling took approximately four hours to reach room temperature. The ratio of the thickness of the uncompressed xerogel (l_0), to that of the compressed xerogel (l), defined as the compression ratio ($C = l_0/l$), was adjusted by use of a brass spacer with a thickness equal to the desired value of l. Thus, an isotropic gel has a nominal $C = 1$, whereas an anisotropic gel has a $C = 1.5$.

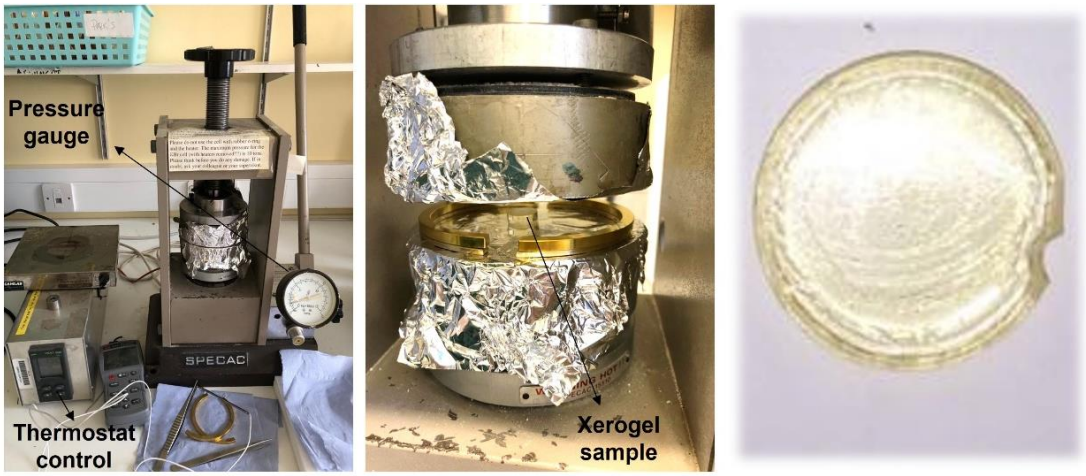


Figure 3.11 Thermostatically-controlled hydraulic press and anisotropic gel sample

3.12 Mechanical Testing of GI Tract Tissues

The dissection of the rats was conducted with the help of our collaborators (Thu Trang Nguyen and Prof. Ren-Jei Chung) from the National Taipei University of

Technology, Taiwan. Four males of Sprague-Dawley rats (BioLASCO Taiwan Co.) with the age of 3–4-week-old were anaesthetized by intraperitoneal injection of 0.15 ml mixture of Zoletil 50 (Virbac, Ltd., Taiwan) and Rompun 20 (Bayer Korea, Ltd.) with the ratio of 1:2. The rats were dissected and the organ segments such as esophagus, stomach, small and large intestine were taken (Figure 3.12 a). Each part of the segment was cut longitudinally and circumferentially. Samples were washed in PBS solution and stored at 4˚C before being used. The mechanical properties of samples were tested using a universal material tensile machine (Yang Yi Technology, Co. Ltd, Taiwan). It has a maximum load of 1.98 kN. Both ends of the sample were wrapped with sandpaper to prevent tissue slippage. The sample was placed between the tensile clamps and vertically aligned from the upper clamp (the fixed grip) to the lower clamp (the grip in charge of applying tension) (Figure 3.12 B & C). This alignment ensured the specimen avoided side loading or bending during the test. After securing the sample, the tensile tester machine started to pull the sample at speed of 50 mm/min. It would take several minutes for the sample to fracture. A stress-strain curve generated from this measurement was used to analyze the mechanical behaviour of the sample. The parameters of the samples for tensile test measurement could be listed in Table 3.1.

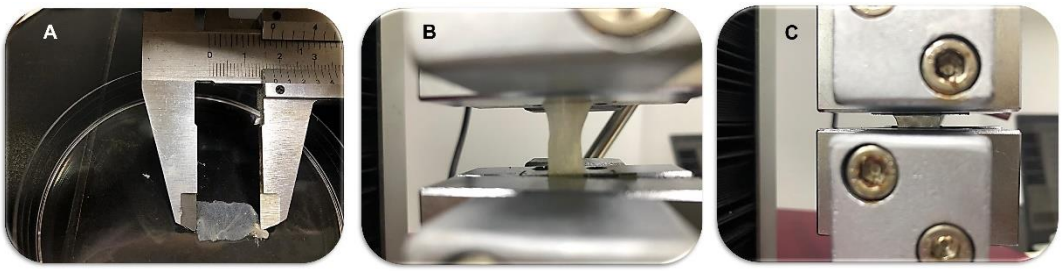


Figure 3.12 (A) Tissue sample (B) Tensile test in longitudinal and (C) Circumferential directions

Table 3.1 Parameter of the tissue samples for tensile test measurement

Samples	Cutting Direction	Length (mm)	Width (mm)	Thickness (mm)	V (mm/min)
Esophagus	Longitudinal	15	2*	-	50
Stomach	Longitudinal	15	10	2	
	Circumferential	5	20	2	
Small intestine	Longitudinal	20	5	1	
	Circumferential	4	15	1	
Large intestine	Longitudinal	20	10	1	
	Circumferential	4	15	1	

* Diameter of the samples

3.13 SEM of GI Tract Tissues

The morphology of GI tract tissues such as esophagus, stomach, small and large intestines without or with stretching, were observed using Ultra High-Resolution SEM (Regulus 8100, Hitachi) at an accelerating voltage of 10 kV. Before SEM scanning, samples were washed in PBS solution for one hour and fixed for 4 hours with 2.5% glutaraldehyde in 0.1 M sodium cacodylate buffer at pH 7.4. After fixation, samples were washed three times at room temperature in 0.1 M sodium cacodylate buffer at pH 7.4 for periods of 15 minutes. Samples were dehydrated in increasing ethanol concentrations from 30%, 50%, 70%, 90%, 95%, and 100%. Then samples were immersed in hexamethyldisilazane (HDMS) (Sigma-Aldrich, USA) for 15 minutes. Samples were air-dried overnight and coated with gold (JEOL JFC-1600).

3.14 *Ex vivo* Study

Hydrogel with a composition ratio of 85:15wt% VP/MMA was chosen in this study. This hydrogel composition was chosen because it could produce stronger mechanical force compared to other compositions (refer to the evidence in Chapter 4, Figure 4.37 & Table 4.18). The sizes of the hydrogels chosen in this study were 3mmD & 3mmL (0.028 gr), 2mmD & 2mmL (0.011 gr), and 1mmD & 1mmL (0.002 gr) (Figure 3.13 B). Two stainless steel (SS) plates with an approximate length of 18 mm were used as support to attach the hydrogel devices (Figure 3.13 A). The small intestine sample was passed through the hole (D= 6 mm) on both sides of the SS plates and securely tightened with the metal plate using a suture. For the *ex vivo* study, several methods had been tried to stretch the intestine. Firstly, one hydrogel was attached in the middle of the short SS plate (L= ~10 mm) while the intestine was attached to the bottom of the plate through the hole (Figure 3.14 A). Secondly, two hydrogels were attached to both sides of the SS plate (top and bottom position) while the two intestine samples were also clamped in both sides of the holes (Figure 3.14 B). However, all those methods failed to prove the expander device can be used for *ex vivo* study due to hydrogel buckling and the force was not adequate to push the plate, thereby the intestine was not stretched. The hydrogel swelled but the intestinal length remained the same. Therefore, modification of the method needs to be developed to solve the problem. The two hydrogels were attached to the SS plate (Figure 3.13 B). The one intestine sample was inserted through the hole located in the middle of the plate and the tissue was clamped together with an SS plate by using 4-0 coated Vicryl suture (Polyglactin 910 suture, Ethicon J494G) or cyanoacrylate adhesive (Vetbond 3M). The hydrogel expander device was immersed together with the intestine in PBS for 7 days.

When the intestine length was changed as the hydrogel swelled, the change will be measured as a function of time.

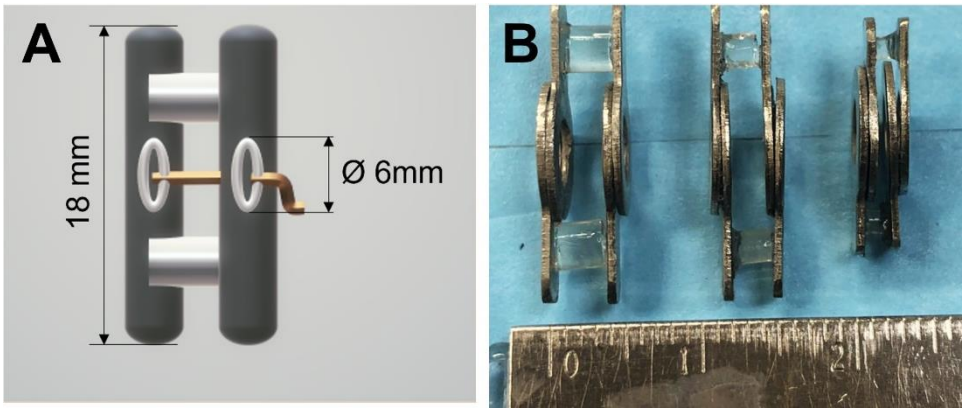


Figure 3.13 (A) Design illustration of hydrogel expander device consists of an SS plate, two hydrogels, and one intestine sample in the middle (B) The hydrogel expander device at different sizes used for *ex vivo* study

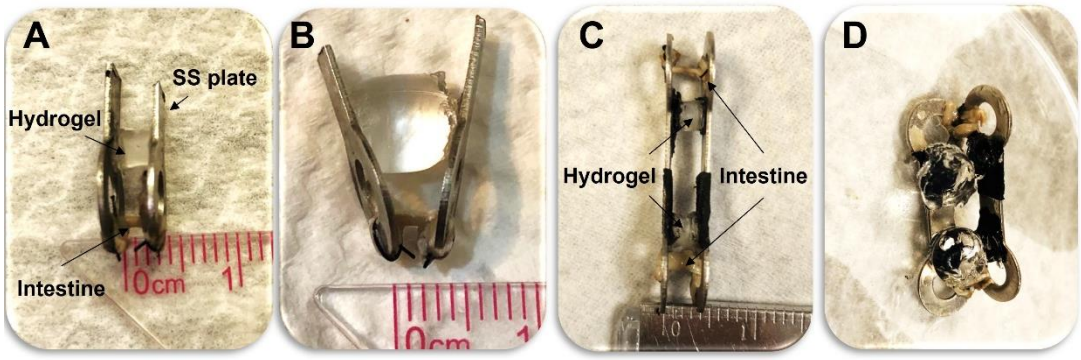


Figure 3.14 The failed design of the hydrogel expander device used to stretch intestines (A,B) First (C,D) Second method in the condition (A,C) Before (B,D) After stretching

3.15 *In vivo* Study

Biocompatible materials upon implantation show a normal acute inflammation reaction and then rapidly heal into a passive state wherein the implant is surrounded by a thin, uniform fibrous capsule in which multinucleated giant cells and other inflammatory cells are generally absent [219]. VP has been widely used in biomedical applications because of its good biocompatibility and non-toxicity [220]. The biocompatibility of MMA is well documented [221]. It was used to create the first intraocular lens[1] and is the principal constituent of orthopaedic bone cement [222], [223]. The biocompatibility of poly (MMA-*co*-NVP) was studied by Wiese et al. to evaluate potential cytotoxicity, mutagenicity, and foreign body reactions using the cell lines MRC-5 and P3X63 Ag8 653 (Ag8) [219]. *In vitro* tests revealed high biocompatibility in VP/MMA hydrogels and no toxicity was observed. Mutagenicity tests revealed a negligible mutation rate in the hydrogel expander which means hydrogel does not appear to contribute to mutagenic processes. There was no sign of foreign body reaction in the hydrogel expander device such as the formation of multinucleated giant cells or monocyte proliferation. From these results, there was a high biocompatibility of the VP/MMA hydrogel expander, which might be favourable for this study.

The in vivo study was done with the help of the National Taipei University of Technology and Taipei Medical University, in Taipei, Taiwan. Sprague-Dawley (SD) rats are all male with the age between 3–4-week-old and purchased from BioLASCO Taiwan Ltd. Animals were acclimatized for a minimum of one week before experimentation and had ad libitum access to standard chow and water at all times. All

[1] Sir Harold Ridley (1906-2001) implanted the first intraocular lens at St Thomas' Hospital in 1949. He chose PMMA following observations made during World War II that wounded Royal Air Force pilots who sustained penetrating eye injuries involving Perspex splinters from their aircraft cockpit failed to mount a response to the intraocular foreign body

procedures were performed after obtaining approval from the Institutional Animal Care and Use Committee of Taipei Medical University, under document number LAC20210130. All animal experiments were conducted under the Taiwan Code of Practice for the Care and Use of Animals for Scientific Purposes. The experiment was divided into three groups such as normal, isolated-control, and stretched-intestine. The 'isolated control' segment is the area of the small intestine that was attached to the metal plate without the hydrogel. The 'stretched-intestine' is the area of the intestine that was attached to the metal plate with hydrogel on it. The anesthesia was conducted by intraperitoneal injection of a 0.15 ml mixture of Zoletil 50 (Virbac, Ltd., Taiwan) and Rompun 20 (Bayer Korea, Ltd.) with a ratio of 1:2. The abdomen area was shaved and cleaned with an alcohol swab. Before surgery was performed, all surgical tools were sterilized in an autoclave chamber (HL-320, Han Lien International Corp., Taiwan). The surgery was done under sterile conditions inside an operation fume. A 2 cm midline incision was made and the ligament of Treitz was identified. The health segment of the small intestine was inserted through the metal plate hole of the hydrogel device (Figure 3.15). Both left and right sides of the intestine near the metal plate were sutured using 4-0 coated Vicryl (Polyglactin 910 suture, Ethicon J494G) and/or glued with cyanoacrylate adhesive (Vetbond 3M). The original length and diameter of the intestine were measured. The intestine was then returned into the abdominal cavity, and the abdominal wall and the skin were closed using a 4-0 coated Vicryl (Polyglactin 910) suture (Ethicon J494G). The surgical area was cleaned with NaCl 0.9% saline solution and iodine. The rat recovered immediately after surgery. Free access to a liquid diet of Ensure (Abbot Laboratories) and water were given to rats. Throughout the postoperative period, any sign of pain or abnormal behaviour of the rat was

monitored and recorded. On postoperative days 1 and 7, the rat was sacrificed, and the change in length and diameter was measured. The distended segment of the intestine was then placed into 10% buffered formalin for 24 hours. Cross-sections of the intestine were cut into 5µm sections and were stained with Hematoxylin and Eosin (H&E), Immunofluorescence (IF) CD31, and Van-Gieson staining. All staining experiments were carried out with the help from Taipei Institute of Pathology, Taiwan.

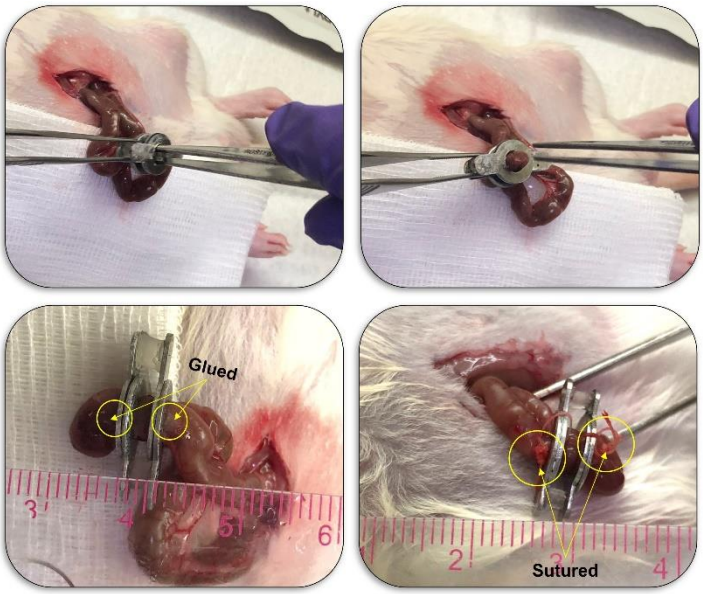


Figure 3.15 Photograph of the intestine during implantation with a hydrogel device

3.16 Statistical Analysis

Statistical analysis was conducted with GraphPad Prism 9. Statistical significance for all results was determined by one-way ANOVA or two-way ANOVA. Turkey's tests were performed whereby $p<0.05$ was considered to be statistically significant. Data were represented as average ± standard error.

3.17 Summary

The ability to accurately manipulate hydrogel swelling by tailoring either the composition ratios of VP/MMA, sizes of the hydrogels, or the anisotropic hydrogel, can be achieved to provide the desired swelling functionality of the expander device. Knowing the mechanical properties and morphology of the hollow organs of the GI tract appears to be important to understand the structure and arrangement of collagen fiber. Maximum stress-strain data of GI tract samples can be used as a parameter to determine the proper design of a hydrogel device. Finally, *ex vivo* and *in vivo* studies were performed to investigate the safety of the hydrogel device and the efficiency of intestinal lengthening.

Chapter 4: Characterizations, Swelling Behaviour Studies, and Mechanical Properties of Self-Inflating Hydrogels Expanders

4.1 Introduction

This chapter describes the characteristics of isotropic and anisotropic hydrogels, the swelling behaviour of both the isotropic and anisotropic hydrogels at various composition ratios and sizes, and the swelling behaviour of isotropic hydrogels in different solvents (*i.e.*, DI water and PBS). The chemical structure of the VP or MMA monomer was investigated by Nuclear Magnetic Resonance (NMR) spectroscopy. The purity of the monomers before and after distillation was compared and calculated using the relative quantification method. The functional group of the various compositions of VP/MMA hydrogels was analyzed by Fourier Transform Infrared (FTIR) spectroscopy to confirm whether the new synthesis method would significantly alter the chemical structure of the polymers.

The wettability of the isotropic hydrogel was measured by water contact angle to determine the hydrophilicity or hydrophobicity of the polymer. The microstructure of the hydrogel was observed by a Scanning Electron Microscope (SEM). From the SEM results, the size of the pore was analyzed using Image-J software. The mechanical properties of the hydrogels were measured by the Universal Testing Machine in order to determine the elastic modulus of the xerogels (dry gels) and hydrogels (wet gels). These data were then used to determine the crosslinking density of the polymer.

The effects of various composition ratios and sizes on swelling behaviour of both isotropic and anisotropic hydrogels were examined. In addition, the effects of different solvents on isotropic swelling behaviour were also investigated. The phosphate-buffered saline (PBS) solution most closely reflects the physiological environment of human tissue fluid. The nature of the diffusion kinetics in both DI

water and PBS solution were elucidated and their importance was discussed. It was apparent that the hydrogel was used for *in vivo* study to stretch the intestine, hence the maximal swelling pressure generated by the hydrogel is crucial for this application. When the pressure is too little, it will be insufficient to cause significant expansion, whilst excessive pressure could result in tissue necrosis. *In vivo* application was further explored using a Sprague-Dawley (SD) rat model in Chapter Five.

4.2 Characterization of Hydrogels

4.2.1 Chemical Structures and Purities of the Monomers

The ^{1}H-NMR spectrum of VP is shown in Figure 4.1. The NMR spectrum of VP shows peaks at 7.0 ppm, 4.4 ppm, 3.5 ppm, 2.5 ppm, and 2.1 ppm. The peak at 7.26 ppm belongs to chloroform solvent, this peak is far downstream due to the highly deshielding the proton of chloroform experiences because of extremely electronegative chlorine atoms attached to the carbon (CH_3Cl). The peak at 7.0 ppm is associated with the methyne proton (=CH−) underneath the pyrrolidone ring due to the highly polar nature of the carbon-nitrogen bond as well as the electron-withdrawing effects of the carbonyl carbon in the pyrrolidone ring. These two factors create the most deshielded environment of all protons involved. The peak at 4.4 ppm is associated with the methylene proton (−CH_2−) of the carbon adjacent to the methyne proton. These protons are located farther away from the carbonyl group in the pyrrolidone ring as well as from the carbon-nitrogen bond. The series of peaks from 3.5 to 2.1 ppm are associated with the six protons in the pyrrolidone ring as they are the least deshielded of all protons involved in the structure since they are more electropositive. Peaks at 5.4, 1.3, and 0.03 ppm have a strong indicator that VP solution

containing NaOH inhibitors and dimers as impurities. The ^{1}H-NMR spectrum of MMA is shown in Figure 4.2. The NMR spectrum of MMA shows peaks at 6.1 ppm, 5.5 ppm, 3.7 ppm, and 1.9 ppm. There are two peaks signal at 6.1 ppm and 5.5 ppm showing the presence of vinyl (CH_2=CHR) in MMA. A peak signal around 3.7 ppm indicates the presence of methoxy protons (O−CH_3). The peak signal at 1.9 ppm indicates the methyl proton (−CH_3) of the MMA present.

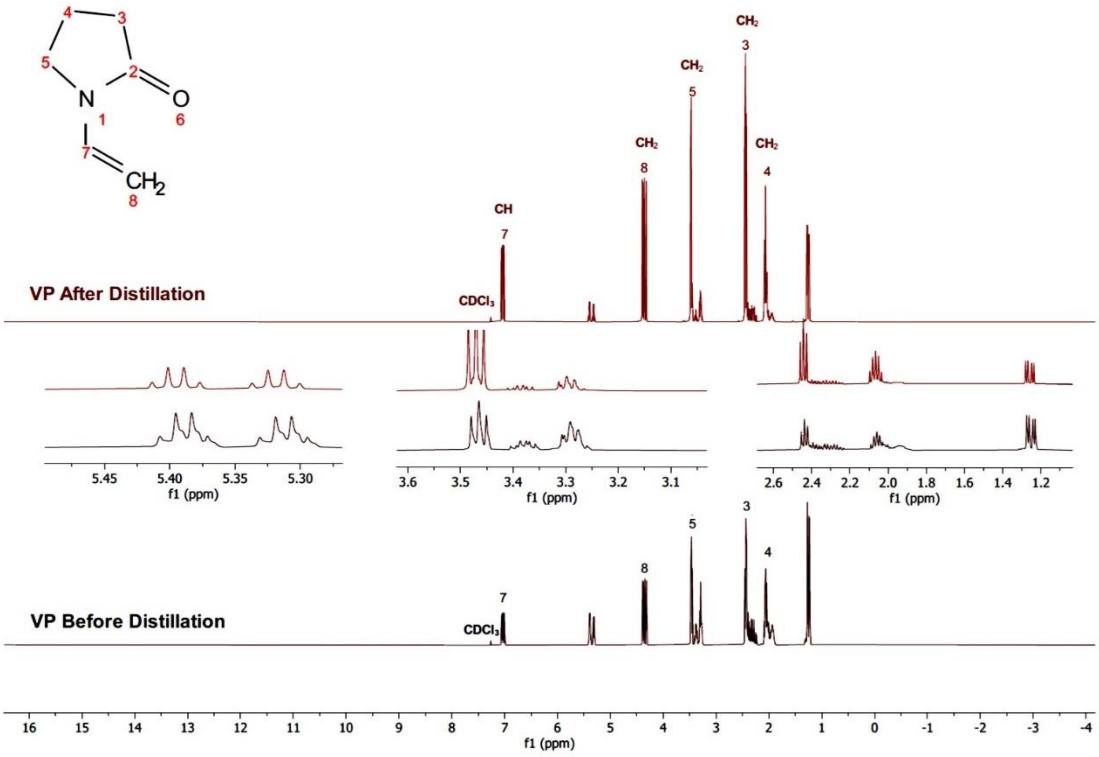


Figure 4.1 NMR spectrum of VP before and after distillation

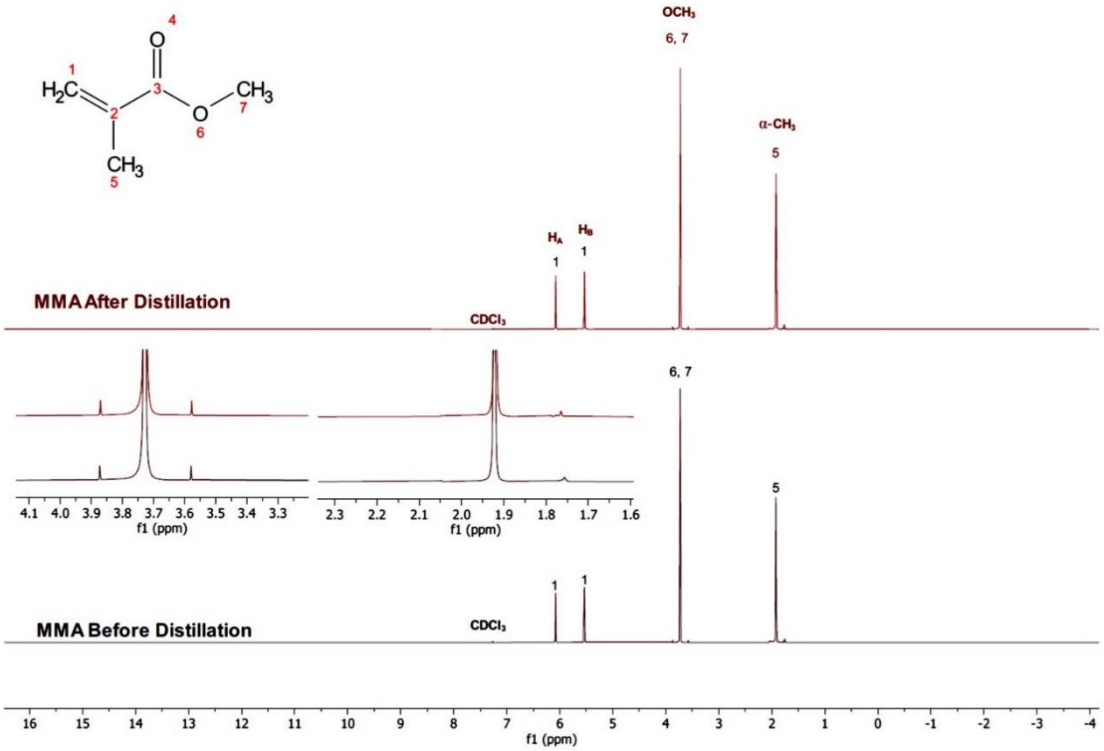


Figure 4.2 NMR spectrum of MMA before and after distillation

In this study, the relative quantification (100%) NMR method is applied to determine the purity of the monomer. It involves a calculation that establishes the proportionality between Mw, n, lnt_t of the target analyte (t), lnt_u of the impurities [224]. It uses the total measure of all signals as the basis for the 100% calculation. The key of purity calculation using 100% method is the normalization of the integrals to the number of protons giving rise to them, leading to normalized integrals for one proton ($nlnt\ [per1H]$). The calculation of purity (P), is as follows:

$$P(\%) = \frac{nlnt_t \,.\, Mw_t}{nlnt_t \,.\, Mw_t + \sum_1^u nlnt_u \,.\, Mw_u} x100 \qquad (4.1)$$

Where $nlnt_t$ and $nlnt_u$ are integral values normalized to ^1H for target molecules and impurities, respectively. Mw_t and Mw_u are the molecular weight of target molecules and impurities, respectively.

Figure 4.3 shows the percentage of purity values of VP and MMA monomers before and after distillations. The purity of VP monomer after distillation is significantly increased compared to the condition before distillation (91.7 ± 1.4 % versus 82.6 ± 3.4 %). The purity of the MMA monomer after distillation shows a similar value to the VP monomer. The purity of the MMA after distillation increased up to 92.1 ± 2.3 % compared to before distillation (84.8 ± 3.0 %). The 100% qNMR method has two important advantages [224]. First, it does not require precise weighing of the sample, and this will eliminate analytical errors resulting from inconsistent weighing or inadequate balances. The second advantage of the 100% method lies in the demand it places on the analyst to assign all signals of a qNMR spectrum.

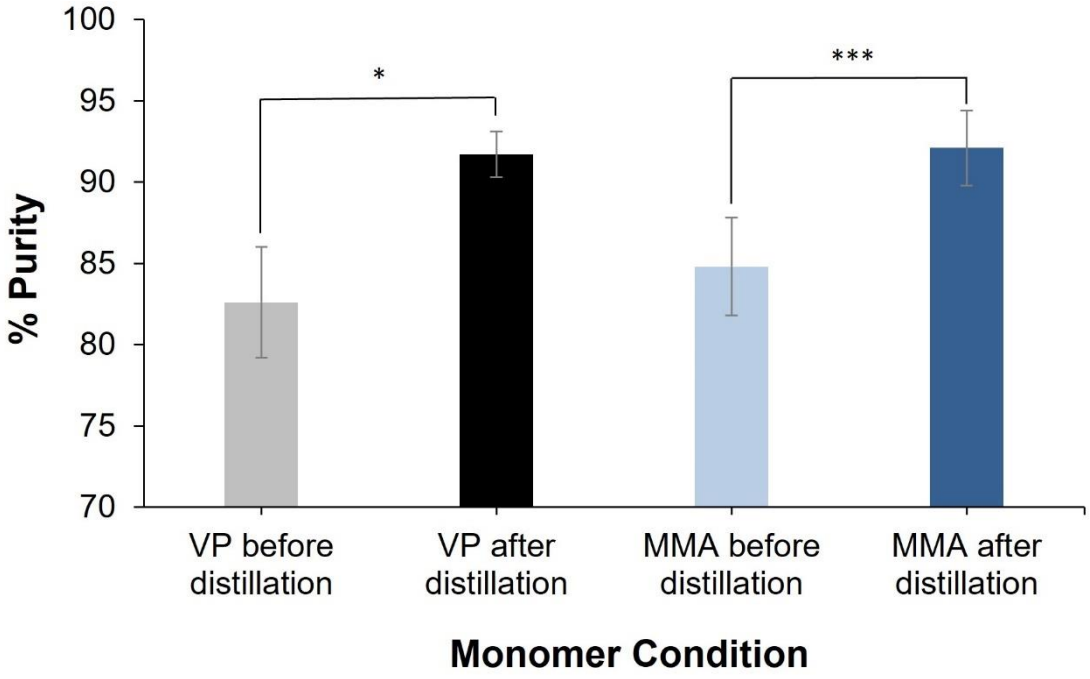


Figure 4.3 % Purity of VP and MMA monomers before and after distillation. Note: Data is expressed as mean (n=3) ± SD, *$p \leq 0.05$, ***$p \leq 0.001$

4.2.2 Functional Group of VP/MMA Copolymers

FTIR spectroscopy is used to investigate the polymeric structure and possible interaction among the functional group in polymer complex systems. When a molecule absorbs infrared light, it undergoes a spectroscopic transition from a lower to an upper vibrational energy level. The energy will be absorbed when infrared light of the same energy as a vibrational transition impinges upon a molecule [225]. The corresponding decrease in light energy at the absorption wavenumber gives rise to a peak in the measured spectrum of the molecule. The peak positions in an infrared spectrum thus disclose the vibrational energy levels of the functional group in a molecule, and when infrared spectra are analyzed, the peaks are assigned to specific vibrations of specific functional groups. The peak position is determined by the force constant, hence the strength of the chemical bond of the molecule, and the mass of the two atoms composing the bond [226]. As the force constant goes up the peak position increases. This means strong chemical bonds have higher peak positions than weak chemical bonds. The molecules with heavy atoms in them have lower wavenumber peaks than molecules with light atom.

Different functional groups can have peaks at about the same position and to distinguish the peaks of different functional group from each other is from the peak heights and peak widths. Peak heights in an infrared spectrum are determined by Beer's law, including absorptivity, pathlength, and concentration [4], [5]. Polar functional groups will have large dipole moments, will frequently have vibrations for which $d\mu/dx$ ($d\mu$ is the change in dipole moment, dx is bond length) is large, and will have intense peaks. Nonpolar functional groups will have large dipole moments, will frequently have vibrations for which $d\mu/dx$ is small, and will have infrared that are

weak or even non-existent. The peak widths are determined by the strength of the intermolecular interactions for the two compounds [225]. When intermolecular interactions are strong, the strength of the intermolecular bonds varies over a wide range giving rise to a large number of energy states. Each of these states will absorb infrared light at a number of slightly different wavenumbers, giving rise to broad peaks.

Figure 4.4 shows the FTIR spectra of the VP/MMA copolymers at 85:15wt% (VP85), 90:10wt% (VP90), and 95:5wt% (VP95). The spectra of PVP and PMMA are also demonstrated in this figure. The characteristic peaks of pure PVP are observed at 2358 cm^{-1} and 1656 cm^{-1} corresponding to C−N stretching and C=O stretching vibration (Table 4.1), respectively [229], [230]. The peaks at 2947 cm^{-1} and 2920 cm^{-1} are ascribed to asymmetric CH_2 stretching ring and symmetric CH_2 stretching chain, respectively [231]. The peaks at 1421 cm^{-1} and 1168 cm^{-1} are corresponding to C-H bending and C-N stretching [232], [233], respectively. The peaks at 1284 cm^{-1} and 1269 cm^{-1} are corresponding to CH_2 rocking and CH_2 wagging, C-N stretching. The stretching frequency at 1720 cm^{-1} corresponds to the C=O stretching of pure PMMA (Table 4.2) [234]. The vibrational frequency at 1483 cm^{-1} and 1441 cm^{-1} of PMMA are assigned to $-CH_2$ scissoring and $-CH_2$ symmetric deformation [235]. The peaks at 1435 cm^{-1}, 1240 cm^{-1} and 750 cm^{-1} are corresponding to $-CH_3$ asymmetric bending, C−O stretching, $-CH_2$ twisting and rocking vibration of PMMA, respectively [236]. A stretching vibration is occurred when there is a continuous change in the interatomic distance along the axis of the bond between two atoms. Bending vibrations include wagging, twisting, rocking, and scissoring are a change in the angle occurring between two bonds.

The most frequently performed observations to confirm the complexation of the copolymers are variation in intensity of the bands, shifting of the bands with respective to the MMA content and appearance of new bands due to presence of MMA content in the VP polymer. The sharper band at 1656 cm^{-1} (C=O pyrrolidone) decreases in its intensity as the MMA concentration increases and VP content decreases (Figure 4.4 c). The 1421 cm^{-1} (C-H), 1284 cm^{-1} (CH_2), and 1269 cm^{-1} (CH_2, C-N) are also found to decrease with the increase in MMA content. The complexation of the VP polymer with MMA leads to the carbonyl stretching vibration of PMMA at 1720 cm^{-1} (in Figure 4.4 a) attached to the carbonyl group of PVP at 1656 cm^{-1} (in Figure 4.4 b). It is seen as a shoulder to the VP spectra and the peak is broadened in the VP85 (85:15wt% VP/MMA). The PMMA peaks at 1240 cm^{-1} and 750 cm^{-1} shows increasing its intensity in the copolymer system with higher MMA concentration. The shift in band positions is also observed, which confirms the complexation. In pure PVP, C=O related peak at 1656 cm^{-1} shifts to 1651-1649 cm^{-1} when MMA is added to the VP system. The asymmetric and symmetric CH_2 stretching shift from 2947 cm^{-1} to 2951 cm^{-1} and 2920 cm^{-1} to 2922 cm^{-1}, respectively. The vibration band at 2358 cm^{-1} shifts to 2364 cm^{-1} in VP85 and VP90. The bands at 1284 cm^{-1} and 1269 cm^{-1} shift to 1286 cm^{-1} and 1273 cm^{-1}, respectively, when MMA content is increased. The C-N stretching absorption band at 1168 cm^{-1} shifts to 1170 cm^{-1} in VP90 and VP95. The band at 844 cm^{-1} of VP/MMA blend shifts to 848-846 cm^{-1} when MMA is introduced to the system. The other PVP peaks in copolymer blend are not showing band shift.

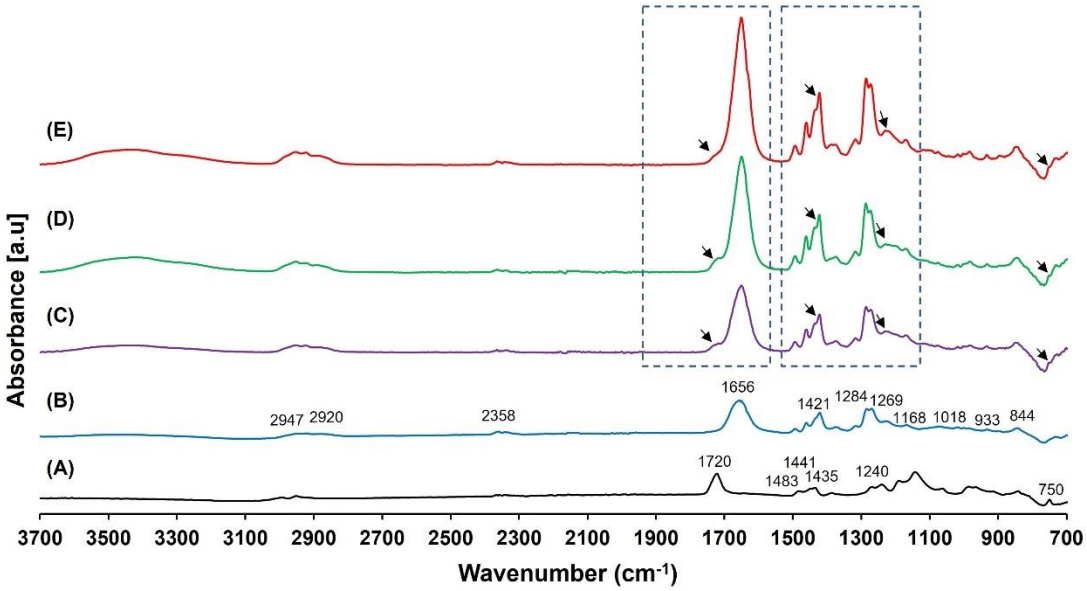


Figure 4.4 FTIR spectra of (A) pure PMMA (B) pure PVP (C) VP85 (D) VP90 (E) VP95

Table 4.1 Vibrational frequencies observed in the FTIR spectra of 100% PVP

Wavenumber	**Band Assignment**
2947 cm^{-1}	Asymmetric CH_2 stretching, ring
2920 cm^{-1}	Symmetric CH_2 stretching, chain
2358 cm^{-1}	C−N stretching
1656 cm^{-1}	C=O stretching
1421 cm^{-1}	C−H bending
1284 cm^{-1}	CH_2 rocking
1269 cm^{-1}	CH_2 wagging, C-N stretching
1168 cm^{-1}	C-N stretching
1018 cm^{-1}	C−C, CH_2 rocking
933 cm^{-1}	C−C bonding
844 cm^{-1}	CH_2 bending

Table 4.2 Vibrational frequencies observed in the FTIR spectra of 100% PMMA

Wavenumber	**Band Assignment**
1720 cm^{-1}	C=O stretching
1483 cm^{-1}	CH_2 scissoring
1441 cm^{-1}	CH_2 symmetric deformation
1435 cm^{-1}	CH_3 asymmetric bending
1240 cm^{-1}	C−O stretching
750 cm^{-1}	CH_2 twisting and rocking vibration

4.2.3 Wettability and Surface Energy

Measurements of contact angle have been used in the study of wettability and surface energy. The contact angle (CA) is defined as the angle between the solid surface and a tangent, drawn on the drop surface, passing through the triple point atmosphere-liquid-solid (Figure 4.5) [237]. The contact angle can be calculated from Young's equation (Equation 4.2). A small contact angle is observed when the liquid spreads on the surface (complete wetting), while a large contact angle is observed when the liquid beads on the surface (non-wetting).

$$cos\theta_c = \frac{\gamma_{sv}-\gamma_{sl}}{\gamma_{lv}} \quad (4.2)$$

Where γ_{sv} is the surface free energy of solid, γ_{sl} is the interfacial tension between a liquid and solid, γ_{lv} is the surface tension of the liquid, and θ_c is the contact angle formed between a pure liquid and the surface of the solid.

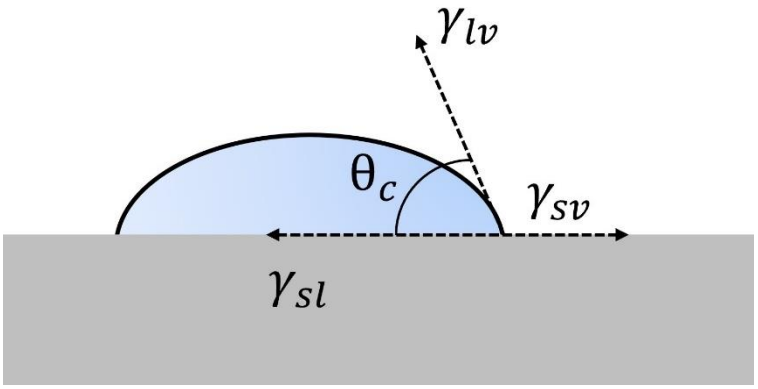


Figure 4.5 Contact angle and interface energies

The contact angles of VP/MMA hydrogels were measured and analyzed from camera data on software. Figure 4.6 demonstrates the effect of various VP/MMA composition ratios on the contact angle (CA). The CA values of VP85, VP90, and VP95 are 65.8˚ ± 5.4, 55.7˚ ± 3.0, and 37.4˚ ± 1.6, respectively. Hydrogel with higher VP concentration is significantly lower the CA. In biomaterial and tissue engineering, a contact angle of less than 65˚ (θ<65˚) is categorized as a hydrophilic surface, whereas a contact angle greater than 65˚ (θ>65˚) is categorized as a hydrophobic surface [238]. The CA of the VP had been reported to be 26.8˚ [239]. VP had been used to modify the surface properties of the material by demonstrating a significant decrease in the CA on the surface of glass ionomer cement [233]. VP modified poly (vinylidene fluoride) (PVDF) membrane produced a hydrophilic surface and then significantly reduced the CA [240]. The pure PVDF membrane exhibited strong hydrophobic characteristics with a CA of 80.9˚. After 10wt% PVP was added to the membrane, the CA decreased to 65.1˚ and the hydrophilicity was enhanced. In addition, the effect of VP composition on the CA of PVA/PVP blend membranes decreased from 42.4˚ to 36.5˚ when VP content increased from 0% to 100% [241].

The hydrophilicity of VP/MMA hydrogels is increased due to higher VP concentration tends to form strong hydrogen bonding between the cyclic amide group and carbonyl group to the water protons [242]. The hydrophilic domains can support localized hydrophilic spheres that increase the bipolar-bipolar forces between the matrixes. However, the addition of MMA concentration will increase the contact angle and indicates the surface is hydrophobic [243]. PMMA has a WCA of merely 67.8˚-72.5˚C [244], [245]. Since MMA is more hydrophobic than VP polymer, its presence in the hydrogel system causes the hydrophilicity reduced. The CA of HEMA/MMA increased from 18˚ to 77˚ when MMA content was increased from 1% to 99% [246].

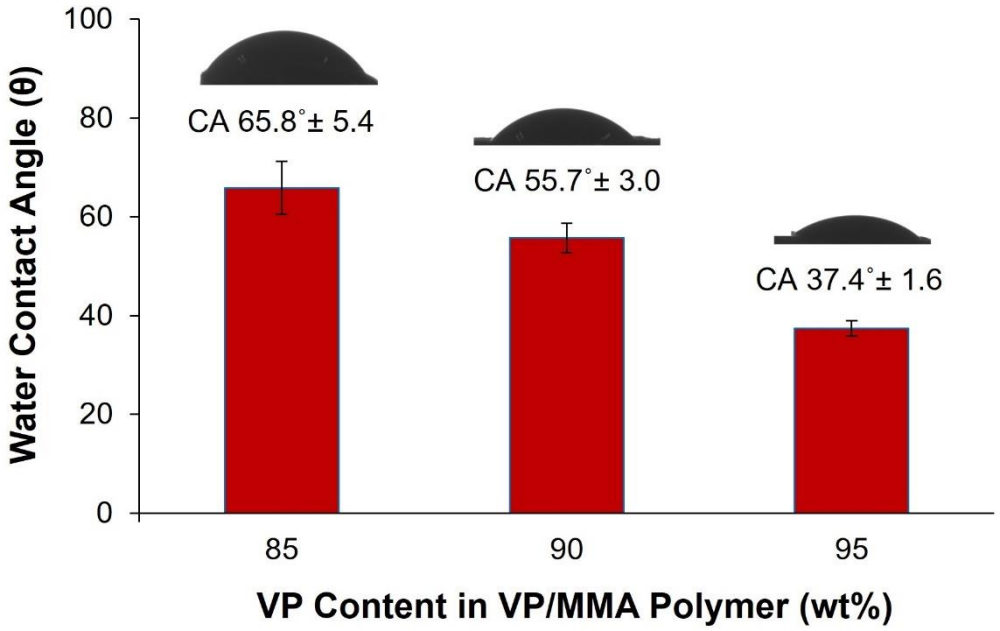


Figure 4.6 Effect of VP/MMA compositions on the water contact angle

It is agreed that the measurement of contact angle on a given solid surface is the most practical way to obtain surface energies [247]. Dupré equation can be used to relate interfacial tension and the interactions between the solid and liquid. Interaction is generally described by the work of adhesion, W_{sl}, which represents the work which

must be done to separate the two phases, or the energy released in wetting. The equation can be written as:

$$\gamma_{sl} = \gamma_l + \gamma_s - W_{sl} \quad (4.3)$$

Where $\boldsymbol{\gamma_s}$ is the surface energy of the solid and $\boldsymbol{\gamma_l}$ is the surface tension of the liquid.

The combination of Equations 4.2 & 4.3 gives the Young-Dupré equation in the form:

$$W_{sl} = \gamma_l (1 + cos\theta) \quad (4.4)$$

Equation 4.4 shows that contact angle is a thermodynamic quantity, which can be related to the work of adhesion and interfacial free energy terms. The work of adhesion for a liquid-solid combination of various VP/MMA compositions could be listed in Table 4.3. Assume the surface tension of the liquid (water) is 72.8 mN/m [248]. When the contact angle (θ) value is small, the W_{sl} is high and considerably energy must be spent to separate the solid from the liquid. On the other hand, as contact angle (θ) increases from 37.4˚ to 65.8˚, W_{sl} decreases, which means less work needs to be done to completely separate water drops from solid surface. Surfaces with small work of adhesion have small amounts of polar group on the surface.

Table 4.3 Contact angle and work of adhesion of VP/MMA hydrogels at various composition ratios

Hydrogels Composition	Contact Angle (θ)	Work of Adhesion (mN/m)
VP85	65.8˚ ± 5.4	102.5 ± 6.2
VP90	55.7˚ ± 3.0	113.8 ± 3.1
VP95	37.4˚ ± 1.6	130.7 ± 1.2

4.2.4 Microarchitecture of Hydrogels

Microarchitectures of VP/MMA hydrogels at various composition ratios are demonstrated in Figure 4.7. The SEM images show a sponge-like network structure. It suggests that the effect of various composition ratios of VP/MMA causes remarkable changes in the porous structure and pore size. The analysis of the pore size distribution by the ImageJ software shows the increasing tendency of pore size with increasing VP concentration. Table 4.4 summarizes the pore size, area, and volume of the VP/MMA hydrogel samples. The VP95 hydrogel demonstrates a highly porous structure with an average pore size of 27.5 ± 4.4 μm. Decreasing the size of the pore is most visible in the hydrogel at the highest concentration of MMA. The network structure is more compact and denser but rougher. It is measured that the pore size of VP90 and VP85 are 19.1 ± 3.7 μm and 13.3 ± 1.7 μm, respectively. The pore size of all hydrogel samples in this study lies in the range of 10-30 μm and can be categorized as super porous hydrogels (SPHs) due to their sizes being in the range of several micrometres with the characteristic of high porosity and interconnected opened-cell structure [125], [126].

The pore areas of all hydrogel samples were evaluated according to the SEM images using the ImageJ software. The pore areas of VP95, VP90, and VP85 are 328.5 ± 78.9 μm^2, 111.8 ± 28.2 μm^2, and 57.7 ± 12.3 μm^2, respectively (Table 4.4). Assuming that the porous structure of the hydrogel is equivalent to hemisphere shape, the pore volume was calculated according to the volume of the hemisphere ($V=\frac{2}{3}\pi r^3$). The pore volumes of VP95, VP90, and VP85 are 4816.9 ± 1554.2 μm^3, 2482.8 ± 964.9 μm^3, and 676.9 ± 253.1 μm^3, respectively (Table 4.3). The pore volume of the higher VP hydrogel significantly increases. The porous structure facilitates the permeation of

water, which allowed water to penetrate the inner structure. As a result of the absorption of water, the space in the networks of hydrogels is increased. However, the reduction of the pore volume is due to the presence of the hydrophobic MMA which acts as a barrier to water diffusion leading to lower water uptake. The microstructure of the hydrogels accurately describes the pore structure in its native equilibrium swollen state, which will be verified in Section 4.3.

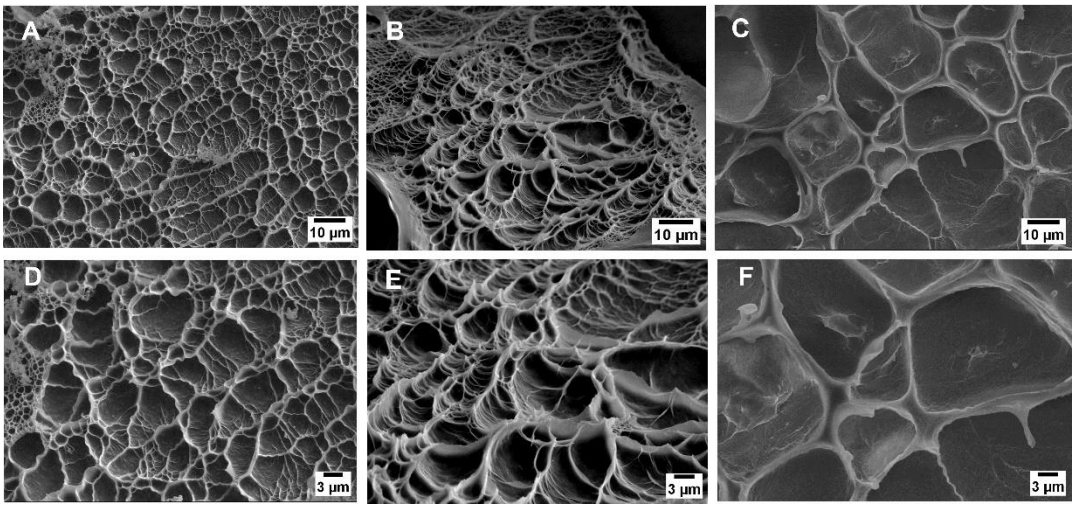


Figure 4.7 SEM images of freeze-dried VP/MMA hydrogels (A-D) VP85 (B-E) VP90 (C-F) VP95 with magnifications of (A-C) 1000x (D-F) 2000x

Table 4.4 Effect of composition ratios on the pore size, area, and volume of the hydrogels

Composition Ratio	Pore Size (µm)	Pore Area (μm^2)	Pore Volume (μm^3)
VP85	13.3 ± 1.7	57.7 ± 12.3	676.9 ± 253.1
VP90	19.1 ± 3.7	111.8 ± 28.2	2482.8 ± 964.9
VP95	27.5 ± 4.4	328.5 ± 78.9	4816.9 ± 1554.2

4.2.5 Mechanical Properties of Hydrogels

As a self-inflating tissue expander, the hydrogel is required to meet the criteria of being highly expandable, controllable, and capable of withstanding compressive pressure. It is very important to maintain the mechanical integrity and original shape of the hydrogel during swelling, especially when used to stretch the intestine. For instance in skin tissue expansion application, the moduli of hydrogels are supposed to be similar to those of human living tissues in the range between 0.1 kPa and 50 MPa [249], [250]. In this study, the mechanical properties of VP/MMA xerogels and hydrogels at various compositions were measured in dry and wet (after 48 hours of immersion) conditions under static compression. The sizes used in this study were 3mmD & 3mmL. Figures 4.8 shows the stress-strain curves of VP85, VP90, and VP95 xerogels (dry state) and hydrogels (wet state). As shown in the curve, the VP/MMA polymers display nonlinear stress-strain relationships. The stress-strain curves of dry gels are located to the left, indicating that those samples are the stiffest, whereas the curves for the hydrogels show a rapid decrease in stiffness, indicating it is the softest. As the percentage of the VP content decreases (VP85), the stress-strain curve shifts to the left, indicating that those samples are the stiffest.

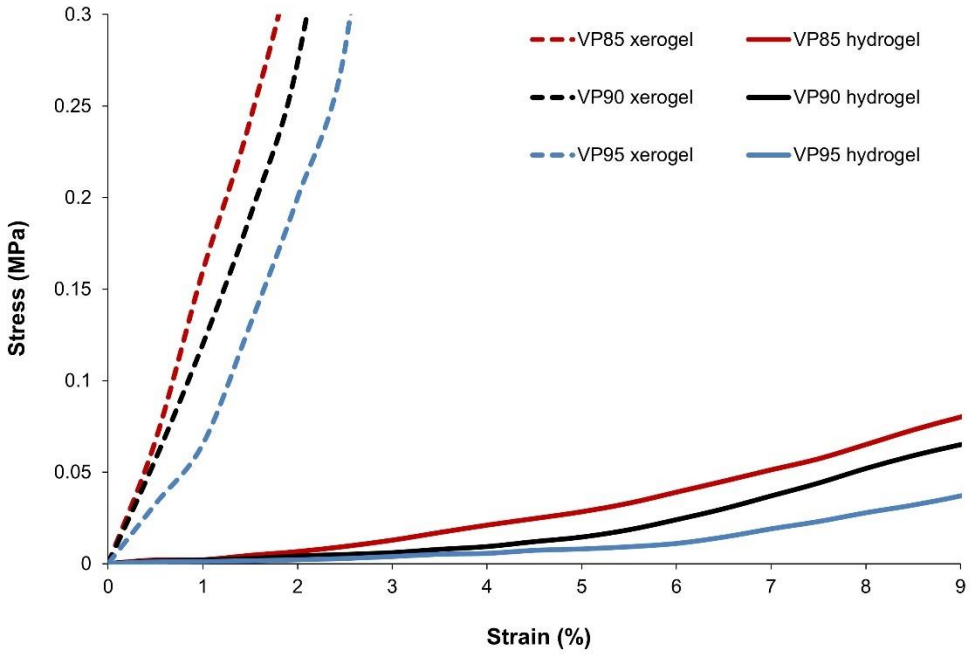


Figure 4.8 Compressive stress-strain curve of xerogels (dry state) and hydrogels (wet state) at various VP/MMA composition

The Young's modulus or elastic modulus (E) of hydrogel is a critical property to understanding its mechanical behaviour. It can be determined from the slope of the initial linear region of the stress-strain curve. The effects of VP/MMA composition on the elastic modulus of xerogel (dry) and hydrogel (wet) samples are summarized in Table 4.5. The Young's modulus of VP85, VP90, and VP95 xerogels in a dry state are 4.3, 3.9, and 3.6 MPa, respectively. It has been reported that the Youngs modulus of PVP and PMMA are ~2.4 GPa and ~2.8 GPa, respectively [251], [252]. The Young's modulus of VP/MMA in this study is lower than xerogels (dry gels) of PVP and PMMA. It might be due to polymers absorb water from water vapour in environmental air, thereby the modulus tends to decrease. The absorbed water could work as a plasticizer [253].

The dry hydrogel was immersed in DI water for 48 hours and the elastic modulus of the hydrogel was measured. Compared with dry gel, the elastic modulus of hydrogel decreases due to softening effect. Firstly, the network strands of the xerogel will maintain the elastic modulus, by the time of swelling it leads to the reduction of the modulus. Water molecules could act as a plasticizer in the swollen hydrogel network. The presence of water provides more flexibility for the mobility of the chain. Hence, the net effect is that the gel modulus will decrease after hydrogel swelling. By considering the effect of swelling pressure (P) of the wet samples, young's modulus of the hydrogels can be calculated using a combination of the stress (σ_1) divided into the strain (ε) as stated in the following equation:

$$E = \frac{(\sigma_0 + P)}{\varepsilon} \tag{4.5}$$

Table 4.5 summarizes young's modulus of VP/MMA hydrogels at various composition ratios. The Young's modulus of VP85, VP90, and VP95 hydrogels (wet state) are 47.3 kPa, 38.8 kPa, and 21.4 kPa, respectively. Decreasing VP concentration while increasing MMA composition (VP85) results in an increase in the slope of the stress-strain curve and therefore, the Youngs modulus and the stiffness. The higher MMA concentration produces more hydrophobic bonding among the methacrylate chain. The inherent modulus difference of the two component polymers is one of factors that would contribute to the modulus. The young's modulus of PMMA polymer has been reported higher than modulus of VP [252]. With increasing the MMA concentration in the copolymer system, the modulus elasticity will significantly increase due to dominancy of PMMA rigid chain. More rigid chains should be more prone to forming phase separation from the polar chain. The MMA will form clusters to increase the effective crosslinking population, hence the density of crosslinking

increased. The crosslinking density of the hydrogels is related to the swelling ratio. The higher crosslinking density would lead to a lower swelling ratio. Therefore, the water content of the hydrogel will decrease in polymer with higher MMA composition (Chapter 4.3.1). The differences in pore structure also contributed to the mechanical properties of hydrogel. The hydrogel structure with more MMA composition having smaller pore size compared than hydrogel with more VP concentration (Chapter 4.2.4). A smaller pore has higher modulus (stiffness) than that with larger pore size.

Table 4.5 Young's modulus of xerogels (dry condition) and hydrogels (wet condition) of different VP/MMA composition

Gel Condition	Composition	Young's Modulus (E)
Xerogel (dry)	VP85	4.3 ± 0.4 MPa
	VP90	3.9 ± 0.1 MPa
	VP95	3.6 ± 0.5 MPa
Hydrogel (wet)	VP85	47.3 ± 1.3 kPa
	VP90	38.8 ± 2.4 kPa
	VP95	21.4 ± 0.9 kPa

The elastic modulus or Young's modulus of the hydrogel can be related to the crosslinking density [121], [151], [254]. With an increase in the crosslinking between network chains, the hydrogel tends to become stiffer. The effective crosslinking density of the VP/MMA hydrogels was calculated from Equation 2.8. Table 4.6 summarizes Young's modulus and crosslinking density of hydrogels at various VP/MMA compositions. Increasing content of MMA from 5 to 15wt% would increase

both the effective crosslink density, υ_e, and young's modulus (E). This behaviour could be described by the decrease in water uptake from having more hydrophobic material within the gel. Hydrophobic bonding is shown to make a significant contribution to the high modulus or rigidity of the gel [156]. Modification of the hydrogel using a hydrophobic monomer had been reported to enhance the mechanical properties of the material [255]. The increased hydrophobic bonding contributes to the effective crosslinking density (υ_e). Poly (methyl methacrylate-*b*-methacrylic acid) was synthesized and characterized using ^{1}H-NMR to check for line broadening, a sign of self-assembly had occurred [256]. The hydrogel was measured at different D_2O concentration, and the result showed a sudden broadening of the backbone methyl of poly (methyl methacrylate) (PMMA) with increasing D_2O. The broadening effect was due to the hydrophobic PMMA aggregates together and forms the core of the micelle. MMA clusters might lead to stronger hydrophobic interactions and contributed to increasing the effective crosslinking density. Yokota *et al* [257]. employed an experimental approach (^{13}C-NMR) to study VP/MMA xerogels swollen in water. The structure proposed from their analysis was one in which VP and MMA constitute separate domains within the gel and specifically with regard to hydrogels, it was suggested that the MMA-rich domains might contain a rigid disordered crystalline region that contributes to effective crosslinking. It was observed from the literature that the hydrophobic MMA component did not give rise to ^{13}C resonances even at 90˚C (the glass-transition temperatures of uncross-linked syndiotactic or atactic PMMA being at 105˚C [258]), therefore the MMA might contain a crystalline region.

Table 4.6 Elastic modulus and effective crosslinking density of various VP/MMA composition ratio

Composition	Elastic Modulus (kPa)	Crosslinking Density (mol/m^3)
VP85	47.3 ± 1.3	8.7 ± 0.3
VP90	38.8 ± 2.4	7.0 ± 0.3
VP95	21.4 ± 0.9	3.8 ± 0.2

The mechanical properties of the hydrogels at various sizes were measured. The fixed composition ratio of 85:15wt% VP/MMA was used. The stress-strain curves of hydrogel samples are shown in Figure 4.9. It shows that the stress-strain curves differed in each sample. The hydrogel sample with the largest diameter is located to the left, however, the smallest diameter is tended to shift to the right. When the swollen hydrogel is compressed by the plate, the gel would change its shape or deformed. The plate exerts a force on the gel and the gel restores its initial shape because the hydrogel is elastic. The elastic property of the hydrogel is quantified by Youngs's modulus (*E*), and this modulus describes the relationship between the stress applied to the gel and the strain that the hydrogel shows through deformation. There is a swelling pressure effect involved in this measurement due to hydrogel being tested in the wet condition. Young's modulus is measured as the result of stress contribution from the compressive measurement and swelling pressure to the compressive resistance of polymer gels. The Young's modulus is calculated using Equation 4.5 and the results are summarized in Table 4.7. It shows that the elastic modulus does not significantly change with a variation of hydrogel sizes and the value is in the range of 47.3-48.6 kPa.

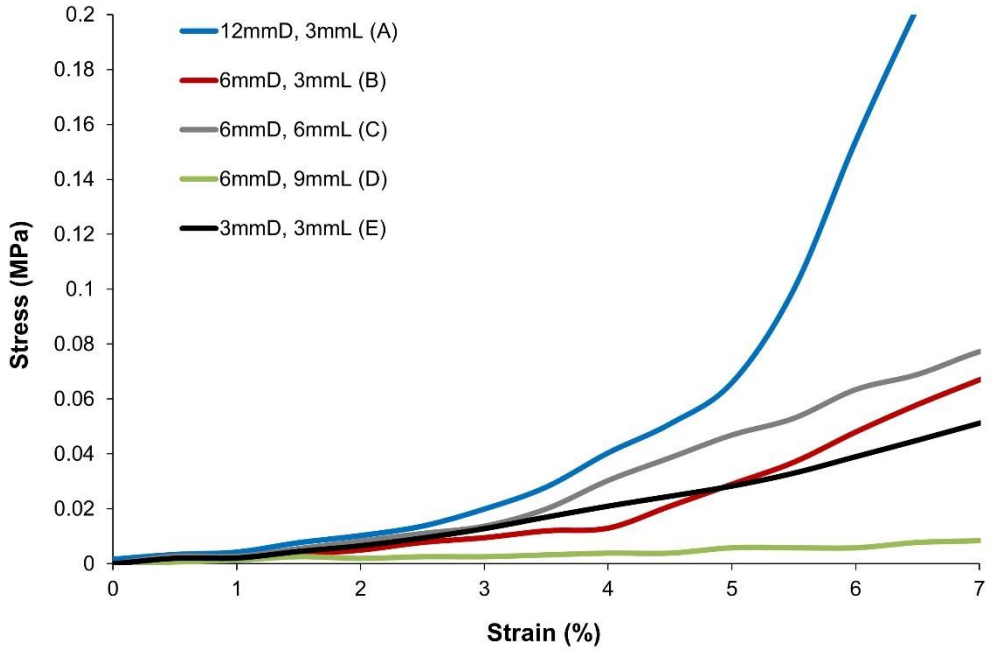


Figure 4.9 Stress-strain curves of VP/MMA hydrogels at various sizes

Table 4.7 Elastic modulus of VP85 hydrogel at various hydrogel sizes

Sample	Diameter (mm)	Length (mm)	Area (mm^2)	Volume (mm^3)	Elastic Modulus (kPa)
A	12	3	113.04	339.12	48.6 ± 1.5
B	6	3	28.26	84.78	47.7 ± 1.4
C	6	6	28.26	169.56	47.6 ± 2.6
D	6	9	28.26	254.34	1.6 ± 0.5*
E	3	3	7.07	21.21	47.3 ± 1.3

*Sample fails due to buckling

The hydrogel with a size of 6 mm in diameter and 9 mm in length fails to produce the right stress-strain values due to the sample buckling (Figure 4.10). The occurrence of buckling means that there is a limit to the shape of swelling gel. Understanding the

effect of the load applied on the gel during compression on the occurrence of buckling might offer an insight on critical limits in terms of the device design. The hydrogel buckles and fails once the critical load has been reached. The buckling phenomenon was investigated by Euler who derived the formula shown in Equation (4.6), where F is the maximum load allowed, n is the numerical factor allowing for end conditions (0.69), E is the elastic modulus, and L is the effective length of the cylindrical hydrogel and I is the moment inertia [259].

$$F = \frac{n\pi^2 EI}{L^2} \tag{4.6}$$

$$I = \frac{\pi d^4}{64} \tag{4.7}$$

Radius of gyration, r, is a useful to estimate of the stiffness of column and it represents the distribution of the cross-sectional area around its geometric central axis. In this case, the radius gyration is assumed to be equal to the radius of hydrogel.

$$r = \sqrt{\frac{I}{A}} \tag{4.8}$$

The critical stress, σ_{cr}, can be calculated if the cross-sectional area is known:

$$\sigma_{cr} = \frac{F}{A} = \frac{n\pi^2 EI}{AL^2} \tag{4.9}$$

$$\sigma_{cr} = \frac{n\pi^2 E}{(L/r)^2} \tag{4.10}$$

The ratio of effective length to the radius (L/r), is the slenderness ratio. It is of considerable importance when investigating the ability of a hydrogel to withstand a load without buckling. Table 4.8 shows the sizes and slenderness ratio used in this study. Four distinct slenderness ratios were chosen and three samples of each were fabricated.

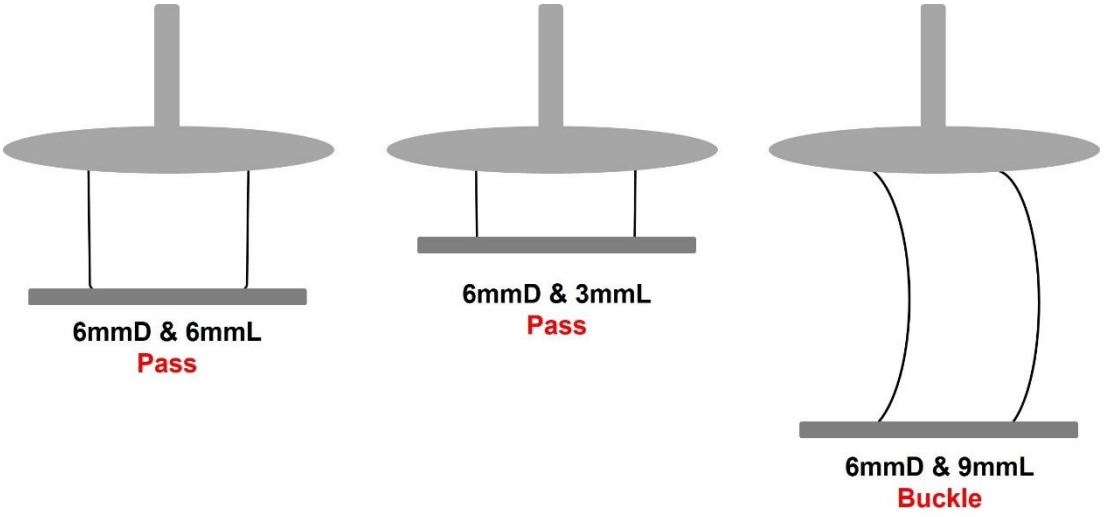


Figure 4.10 Illustration showing the samples with sizes of 6mmD and 9mmL buckled during the compression test

Table 4.8 Samples size and slenderness ratio used in this study

Sample	Radius (r)	Length (L)	Slenderness Ratio (L/r)
12mmD, 3mmL (A)	6 mm	3 mm	0.5
6mmD, 3mmL (B)	3 mm	3 mm	1
6mmD, 6mmL (C)	3 mm	6 mm	2
6mmD, 9mmL (D)	3 mm	9 mm	3
3mmD, 3mmL (E)	1.5 mm	3 mm	2

The critical or maximum stress of hydrogels at different sizes is calculated from Euler's formula (Equation 4.10). The critical stress is plotted in Figure 4.11 as a function of slenderness ratio. This will provide information about a visible range of maximum stress that needs to be allowed to design the hydrogel so that the hydrogel will not lead to buckling. The maximum stress that obtained from the compression test is also plotted in Figure 4.11. The sample is annotated as fail or buckle when the stress

value obtained from experiment exceeds the critical of Euler's formula. The slenderness ratio (L/r) must lie in the range of 0.5-2. The hydrogel with the slenderness ratio above 2 experiencing buckled. It is due to the experimental stress is larger than the critical stress ($\sigma_{experiment} > \sigma_{euler}$). For instance, the sample with a slenderness ratio 3.0, after calculated, will have critical stress (σ_{euler}) of approximately 1.2 kPa, however, the stress obtained from the experiment (8.4 kPa) exceeds the maximum stress obtained from Euler's formula, therefore the sample failed or buckled.

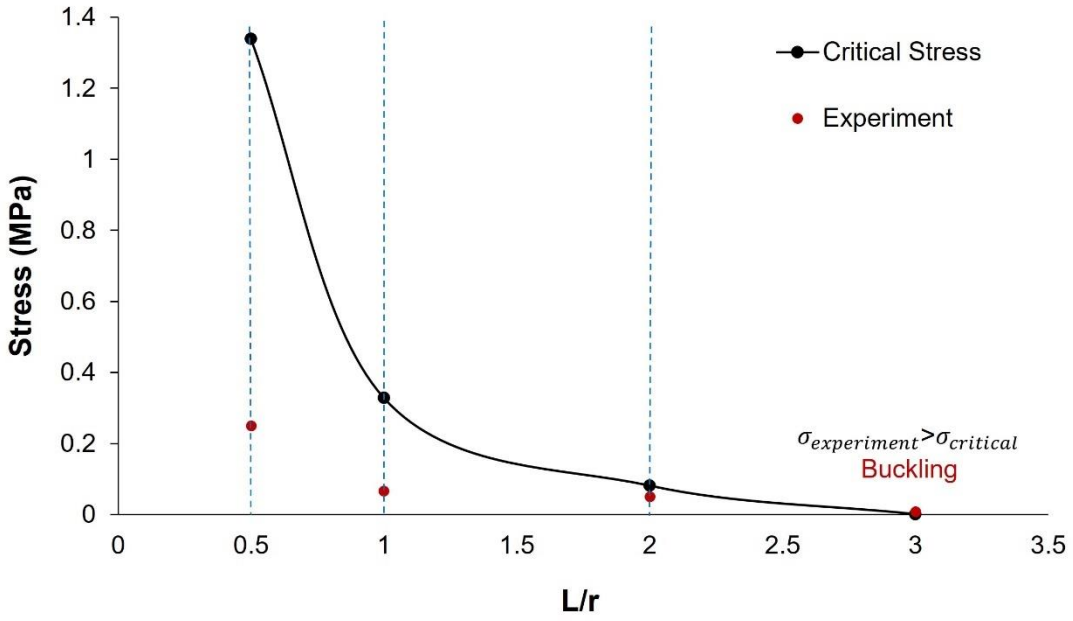


Figure 4.11 Maximum allowable stress showing line drawn from Euler's formula (black curve line) and stress data from experiments (red dot)

4.2.6 Glass Transition Temperature

The glass transition temperature (T_g) is defined as the temperature of amorphous polymers at which increased molecular mobility results in significant changes in thermal properties. Beyond this transition temperature, the polymer has sufficient energy to allow long-range molecular motion, thereby increasing the degree of

rotational freedom [260]. Below T_g, the physical properties of polymers change to those of a glassy state, and above T_g, they behave like rubbery materials, hence the T_g is sometimes referred to as the 'softening point'. In the case of binary mixtures, the glass transition of compatible polymers occurs in a temperature region that is intermediate between the transition temperature regions of each of the pure amorphous phases. The most common approach for estimating the compositional dependence of the T_g value remains the use of the Gordon-Taylor (G-T) equation [261]:

$$T_{g,mix}=\frac{w_1 T_{g,1}+kw_2 T_{g,2}}{w_1+kw_2} \quad (4.11)$$

$$k=\frac{\rho_1 T_{g,1}}{\rho_2 T_{g,2}} \quad (4.12)$$

Where, $w_{1,2}$, $T_{g,1,2}$, and $\rho_{1,2}$ are the weight fraction, glass transition temperatures, and densities of the two components, respectively. This approach is based on the assumptions of ideal mixing.

The T_g and density values of pure PVP and PMMA are 178˚C and 1.25 g/cm^3 and 105˚C and 1.17 g/cm^3, respectively [258]. The predicted T_g values for the various compositions of VP/MMA xerogels are calculated from the G-T equation and the results are demonstrated in Figure 4.13. The T_g values of VP/MMA of various composition ratios are 160.3˚C, 165.0˚C, and 171.7˚C for VP85, VP90, and VP95, respectively. It is found that the Gordon-Taylor equation describes the dependence of the glass transition temperature on the composition of the copolymers very well. The increasing of the VP concentration causes the $T_{g,\,mix}$ to increase. It is dominantly affected by high molecular weight, thus the $T_{g,\,mix}$ increases close to the T_g of PVP. The addition of MMA is lowering the T_g and the lower T_g helps to soften the polymer backbone and improves the segmental movement of the polymer chain [262].

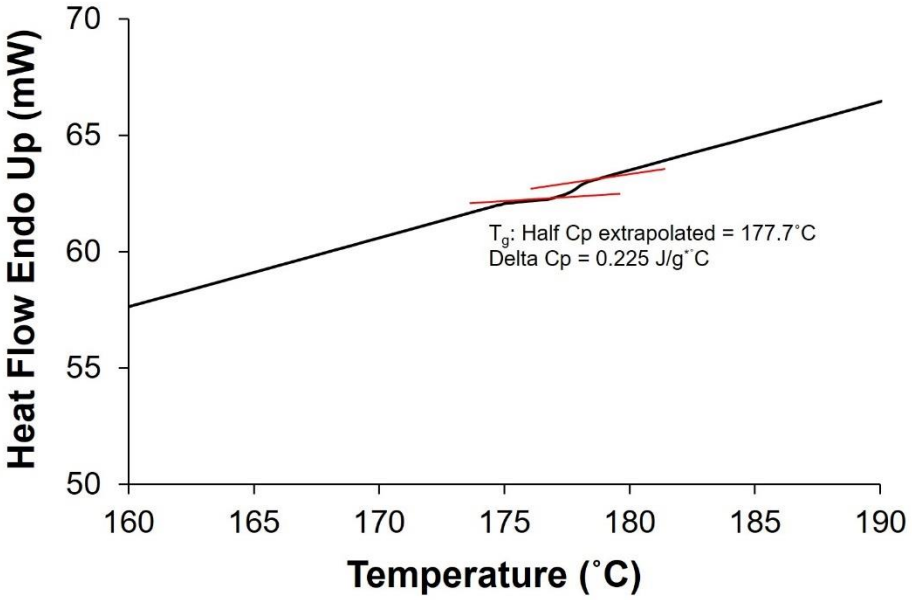


Figure 4.12 DSC spectrum of VP95 xerogel showing the glass transition temperature is taken as the middle of the sloped region

Figure 4.12 shows the result from the DSC measurement of the VP95 gel. The DSC curve exhibits the inclined region of the endothermic peak at a temperature of 177.7˚C and the temperature is taken as T_g. It results in a kink in the heat versus temperature plot due to a change in heat capacity. The heat capacity (C_p) of xerogel is higher above T_g. At the molecular level, the chain in the amorphous (i.e., disordered) region, where chain motion is frozen, gains enough thermal energy to begin sliding past one another at a noticeable rate around T_g. Figure 4.13 shows the summary of T_g values at various VP/MMA composition ratios obtained from DSC measurement. T_g transitions are seen at 156.9˚C ± 12.8, 164.8˚C ± 3.7, and 170.9˚C ± 5.6 for the composition of VP85, VP90, and VP95, respectively. These experiment and predicted values are entirely consistent assuming a miscible mixture of VP and MMA monomers in the VP/MMA polymer complexes. Interestingly, the glass transition temperature for

the VP85 is lower than the predicted value. This might be related to a residual monomer in the extractable portion of the xerogel which would act as a plasticizer and thus lower the T_g. The experiment T_g values are critical as this represents the anisotropic processing temperature. Only at the T_g and above do the polymer chains have sufficient mobility to allow molecular realignment and thus produce the required anisotropic properties.

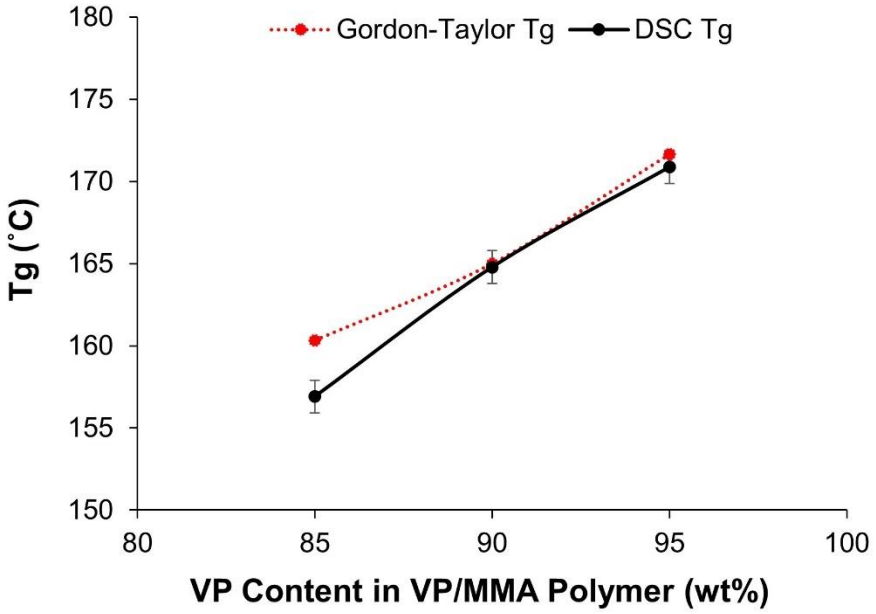


Figure 4.13 T_g values of various VP/MMA compositions obtained from G-T equation and DSC measurement

4.3 Swelling Behaviour Study of Hydrogels

4.3.1 Volume Swelling and Diffusion of Hydrogels in DI Water

The swelling process of hydrogel was photographed by the camera as a function of time (Figure 4.14). After being immersed in water, the gel starts to swell in the radial direction. There was a continuous decrease of internal diameter (D_{int}) and increase in external diameter (D_{ext}) versus time, which indicates that the wetting front advances towards the centre. At the initial stage, the unswollen core constrains the

swelling region and thus leads to cusp-like pattern formation on the surface. The second stage occurs when the d_{int} is near zero, the core is broken (Figure 4.15), and the gel shrinks in the radial direction while swelling in the axial direction. This phenomenon is described as a shrinking intermediate during the swelling process. The last stage is the gel re-swelling in the radial direction. The complicated patterns disappear eventually with the final homogeneous equilibrium state. In the condition of free swelling, the water could penetrate into hydrogel from all directions such as the top, bottom, and side surfaces. The hydrogel swelled freely (isotropic swelling) and stretched in all three dimensions ($\lambda_r=\lambda_\theta=\lambda_z=\lambda f_{ree}$). However, in the swelling force experiment, the hydrogel swelled under constraint condition. There was no water ingress through the top and bottom surfaces of hydrogel. The stretch in the axial direction is minimal and can be assumed to deform with no axial deformation ($h_0=h_1$, $\lambda_z=1$).

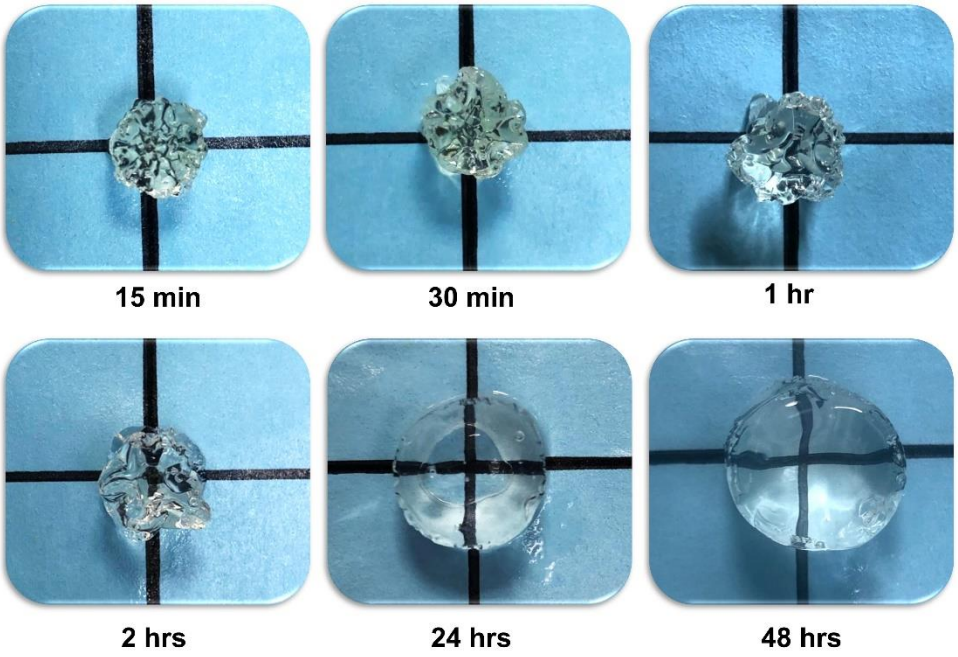


Figure 4.14 Photograph of the swelling process of the hydrogel as a function of time

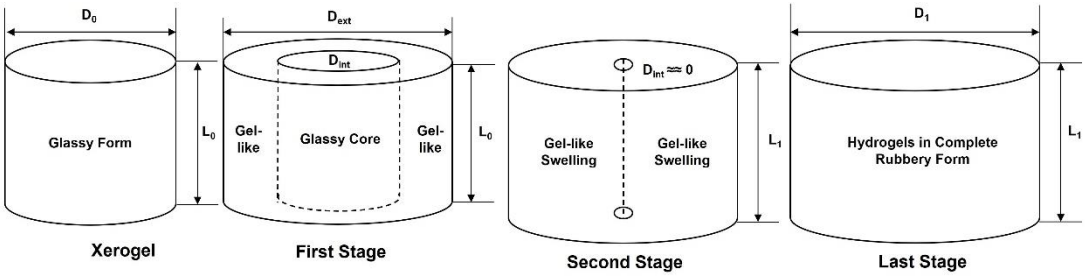


Figure 4.15 Schematic illustration of the shape changes hydrogel sample from initial to equilibrium stage upon the free swelling condition in DI water

4.3.1.1 Effect of Chemical Composition on the Swelling

The network content of the polymer is called the gel fraction. The determination of hydrogel composition ratio has a significant impact on the gel polymerisation by chemical crosslinking method and it would determine the amount of gel fraction. Figure 4.16 shows the gel fraction of VP/MMA hydrogels as a function of VP concentration in the copolymer system. It demonstrates that the gel fraction is dependent on the copolymer composition. As the VP concentration increases, the gel fraction increases. These results suggest that the presence of VP with MMA enhanced the gelation process of the copolymer.

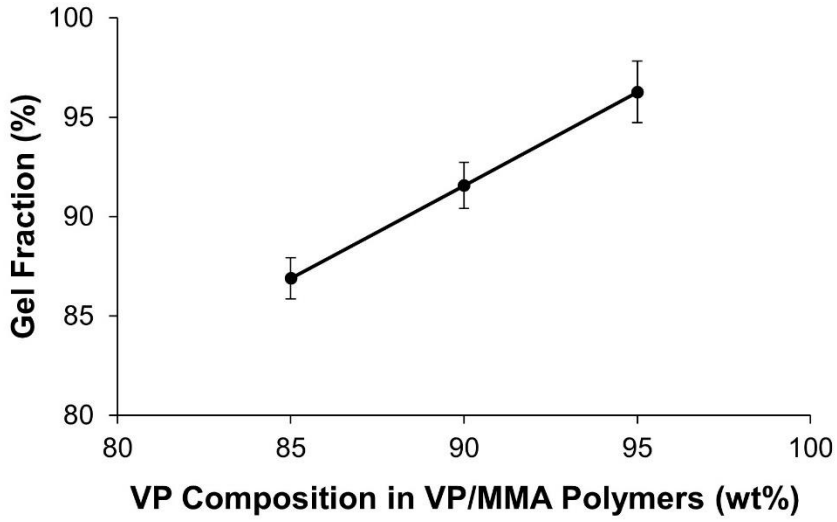


Figure 4.16 Effect of polymer composition ratio on the gel fraction

Varying the VP/MMA monomer ratios used in the hydrogel preparation is an important factor to determine the final property of the hydrogel network. In this study, three different composition ratios of VP/MMA such as 85:15 (VP85), 90:10 (VP90), and 95:5 (VP95) were chosen. The size chosen in this study was 3mmD & 3mmL. Figure 4.17 shows the effect of VP/MMA composition on the volume swelling ratio versus time. At the initial stage, the swelling ratio quickly increases up to a certain value. It continuously increases slowly until the swelling capacity reaches the equilibrium condition. Swelling of hydrogel with higher VP concentration (VP95) reaches up to 9.7 ± 0.5 within the first 24 hours. However, increasing MMA concentration significantly lower the swelling rate. In the first 24 hours, the volume swelling ratio only reaches up to 7.7 ± 0.4 and 6.8 ± 0.1 for VP90 and VP85, respectively. The swelling rate is related to the water uptake of fluid into a network of the polymer. The initial swelling rate (%/h) of hydrogel is 92.0 ± 2.0 which is faster in VP95, then significantly decreased to 59.8 ± 3.4 in VP85 (Figure 4.18). VP95 hydrogel is highly hydrophilic that preferably attracts and binds with water. The first water molecules to enter the xerogel matrix will bind the most polar hydrophilic groups, leading to ‘primary bound water [85]. In addition, the significant mobility of VP polymer chains might cause fast swelling in VP95.

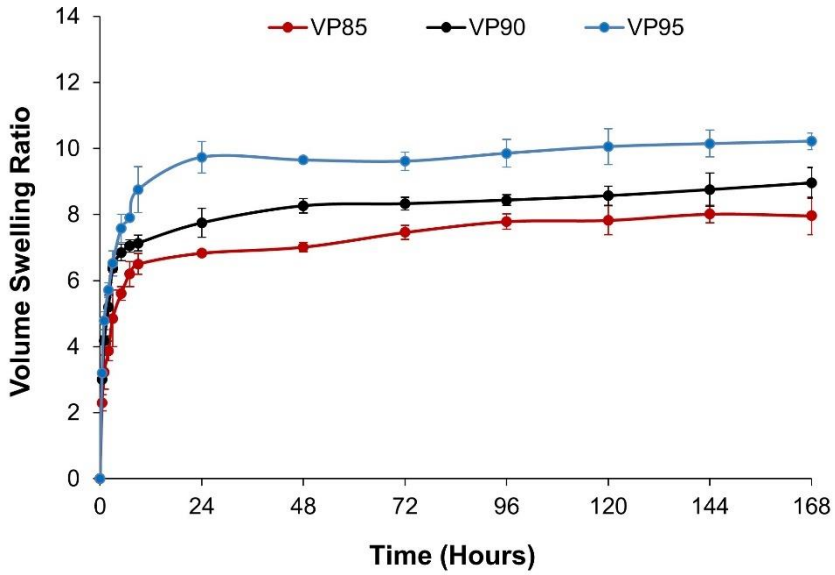


Figure 4.17 Volume swelling ratio of VP/MMA hydrogels at various composition ratios

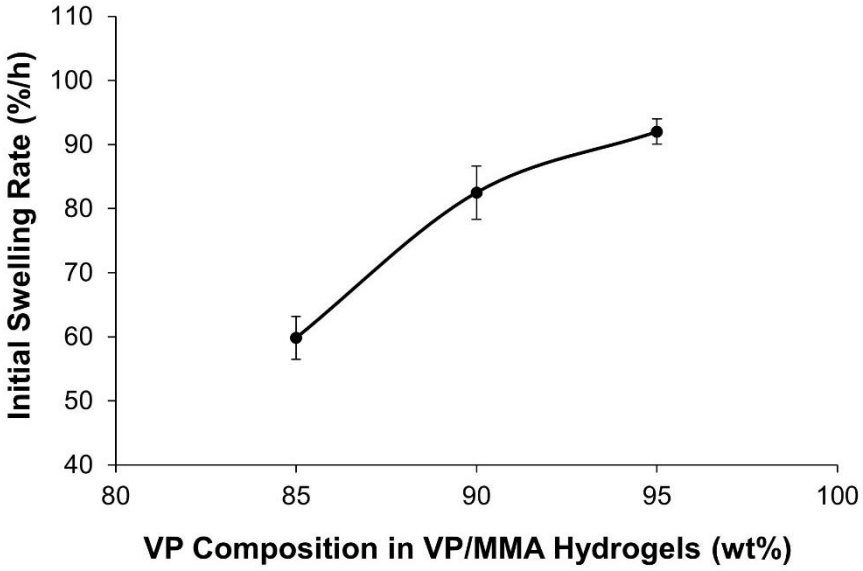


Figure 4.18 Initial swelling rate of VP/MMA hydrogel at various compositions as a function of time

At equilibrium condition, the volume swelling ratios of VP85, VP90, and VP95 is 8.0 ± 0.3, 9.0 ± 0.5, and 10.2 ± 0.3, respectively (Figure 4.19). VP95 has higher

equilibrium volume swelling than other hydrogels. It might be due to the higher pore size network structure (Section 4.2.4) to enlarge the volume uptake of water into the hydrogel. The equilibrium swelling ratio is significantly decreased with increasing MMA weight fraction, while the time taken to reach the equilibrium condition is longer. In this study, the swelling rate of the VP90 hydrogel is slower compared to the commercial sample. The initial swelling rate of VP90 in the commercial sample was 96%/h [108] versus 82.5%/h in this study. This might be due to the sample size used in this study being smaller than the commercial sample, hence the swelling rate in this study is slower.

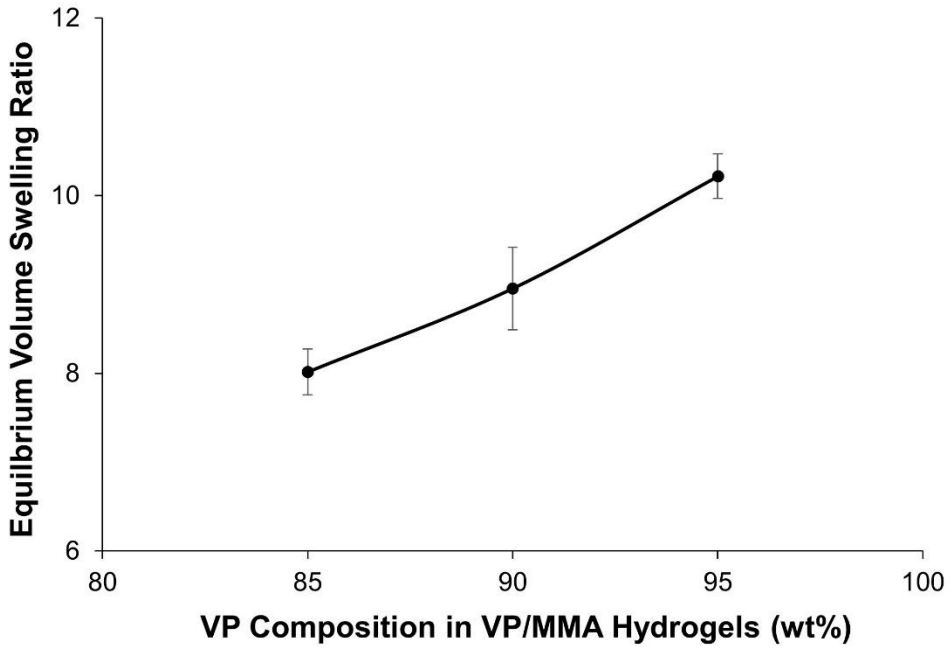


Figure 4.19 Equilibrium swelling ratio as a function of VP composition

The swelling ratio of the hydrogels could be affected by the change in monomer ratio, i.e., hydrophobicity/hydrophilicity. It is characterized by its water contact angle via young's equation (Section 4.2.3) and according to the water contact angle test result, VP is regarded as a highly hydrophilic polymer. The presence of a

hydrophilic group in VP has a positive effect on the swelling of the VP/MMA hydrogel system. This is due to the hydrophilic polymer networks being more thermodynamically favourable with water. Water is able to form a hydrogen bond with the carbonyl oxygen atom of the lactam ring of VP. The maximum two water molecules are able to be coordinated at one O-atom of a functional hydrophilic group [263]. There is a significant reduction in the swelling capacity when hydrophobic MMA is introduced to VP/MMA complexes. A hydrophobic network tends to clump up together with hydrophobes (non-polar molecules) rather than distributing itself in a water medium, hence allowing MMA molecules to have minimal contact with water to create 'secondary bound water'. This behaviour could be explained by using the thermodynamics of hydrophobic interactions. When MMA is immersed in water, hydrogen bonds between water molecules will break to make room for the hydrophobic group, however, water molecules do not react with the hydrophobic group. This is considered an endothermic reaction because when bonds are broken, heat is put into the system. Water molecules that are distorted by the presence of the MMA will create new hydrogen bonds and form an ice-like cage structure called a clathrate cage (Figure 4.20) around the hydrophobic group. This orientation makes the hydrophobic system more structured with a decrease in the total entropy of the system, therefore $\Delta S < 0$. In this case, the change in enthalpy (ΔH) of the system is insignificant in determining the spontaneity of the reaction (mixing of hydrophobic molecules and water) because the change in entropy is large. A large negative value of ΔS causes the value of ΔG will turn out to be positive ($\Delta G = \Delta H - T\Delta S$). A positive ΔG indicates that the mixing of the MMA hydrophobic and water molecules is not spontaneous.

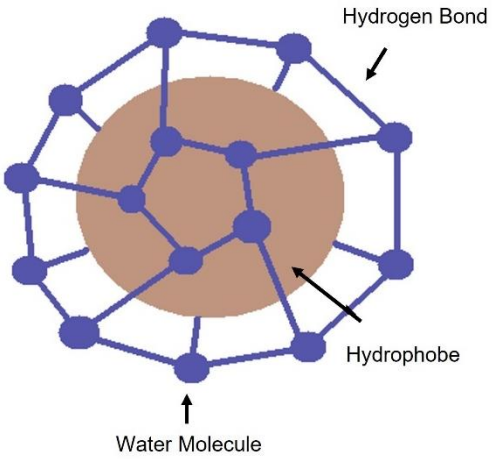


Figure 4.20 A clathrate cage structure around the hydrophobe

The diffusion behaviour of solvent into the VP/MMA hydrogel is important to study to understand the mass transport and parameters that can control the swelling rate. The Power Law (Equation 2.6) was used to determine the mechanism of diffusion in the polymeric network. Figure 4.21 shows the plot of water uptake in Equation (2.6) as an indicator of diffusion transport type. Equation (4.13) shows the natural logarithm of equation (2.6). The diffusion exponent (n) for the material is calculated as the gradient of a log plot of the linear portion of the water uptake as a function of time (Figure 4.22).

$$\ln\left({}^{M_t}/_{M_\infty}\right) = lnk + nlnt \qquad (4.13)$$

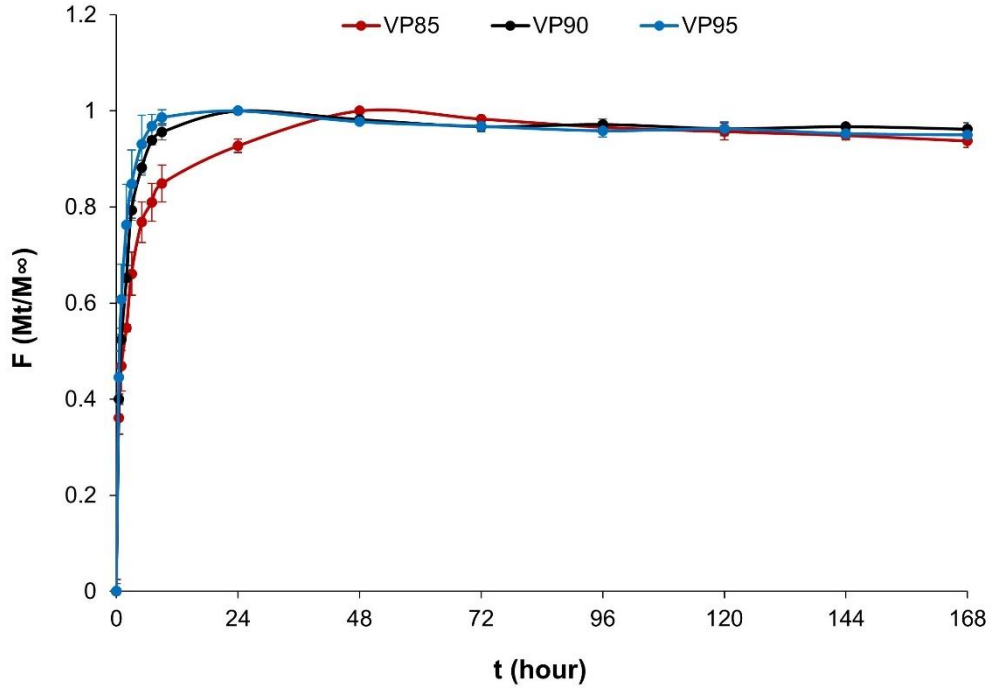


Figure 4.21 Water uptake of various composition ratios of VP/MMA hydrogel as a function of time

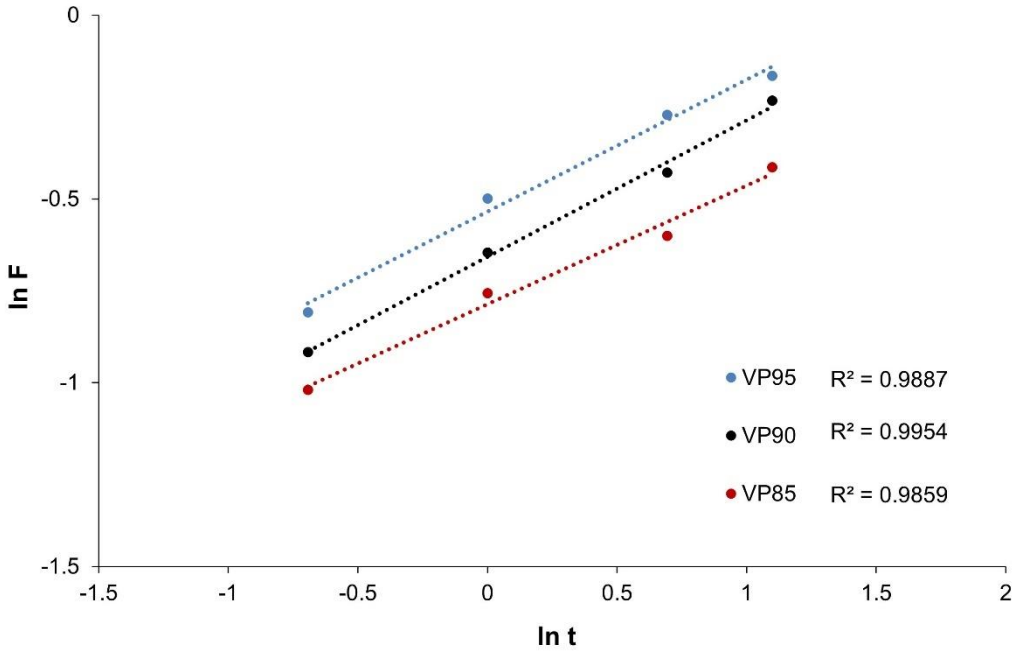


Figure 4.22 Natural logarithm of water uptake as of function of ln t

The mean value of diffusion exponent (n) is obtained and summarized in Table 4.9. For cylindrical shapes polymer, an n = 0.5 indicates Fickian diffusion, an n > 0.5 indicates anomalous transport, and n = 1 implies case II transport [129]. In this study, VP95 has an n value of around 0.5 which characterizes Fickian diffusion. The solvent sorption in this hydrogel is relatively fast due to rapid molecular relaxation, and therefore a diffusion-controlled process. In this condition, polymer chains will have higher mobility that allows for easier penetration of water [135]. It refers to the solute transport process in which the water diffusion rate is much slower than the polymer chain relaxation rate ($R_{diff} < R_{relax}$). Diffusion into glassy polymers is typically relaxation controlled, however, the plasticising effect of the penetrant molecule on the polymer matrix has the ability to alter the diffusion dynamics towards a diffusion-controlled (Fickian diffusion) whereby the rate-limiting step to sorption is the Brownian motion of the penetrant molecule itself [131].

The VP85 and VP90 hydrogels show diffusion exponents (n) of 0.79 and 0.66, indicating an anomalous diffusion (non-Fickian), which means the rate of water diffusion (R_{diff}) and that of polymer chain relaxation (R_{relax}) are comparable ($R_{diff} \approx R_{relax}$) [264]. Kaplan investigated the diffusion of water into the isotropic PVP hydrogels and found it to exhibit non-Fickian behaviour [265]. Interestingly, as the crosslinking density of the PVP system increased, the transport of water became increasingly non-Fickian (with a greater diffusion exponent). In this study, the transfer of diffusion mechanism to non-Fickian (anomalous transport) in VP85 and VP90 is believed to be a result of MMA weight fraction which will bring more hydrophobic bonding. Thus, the effective crosslinking density is increased (Table 4.6), leading to restricted chain mobility and a change in the diffusion mechanism. The decreased

chain mobility will later contribute to a decreased diffusion coefficient, which will be confirmed in Table 4.10.

Table 4.9 The diffusion exponent (n) and the diffusion mechanism of VP/MMA

VP/MMA Composition	Diffusion Exponent (n)	Transport Type
VP85	0.79	Anomalous transport
VP90	0.66	Anomalous transport
VP95	0.53	Fickian diffusion

The diffusion coefficient clearly shows the rate at which diffusing substance is transported through a cross-section of a system. Derived from Fick's second law of diffusion, the diffusion coefficient (D) could be calculated using Equation 2.7 [144]. This is an early time approximation that measures the swelling of the first 60% of solvent uptake, *i.e.*, $0 \leq F \leq 0.6$ [133]. Table 4.10 shows the diffusion coefficient (D) values of VP/MMA hydrogels. The diffusion coefficients of VP/MMA hydrogels are 5.7 x 10^{-7}, 9.2 x 10^{-7}, and 13.2 x10^{-7} cm^2/s for VP85, VP90, and VP95, respectively. Figure 4.23 shows the diffusion coefficient (D) as a function of VP concentration. The VP85 has a smaller D value compared with VP90 and VP95. The decrease in D is also believed to be a result of the increased hydrophobicity and steric hindrance of MMA. The polymer volume fraction ($\upsilon_{2,s}$) is also calculated from Equation (2.1) and it is shown in Table 4.10. Diffusion coefficient of VP85 decreases following with an increase $\upsilon_{2,s}$,. These results suggest that $\upsilon_{2,s}$ is an essential factor to control the diffusion behaviour of water molecules in hydrogels. In other words, the existence of the polymer prevents the diffusion of water molecules.

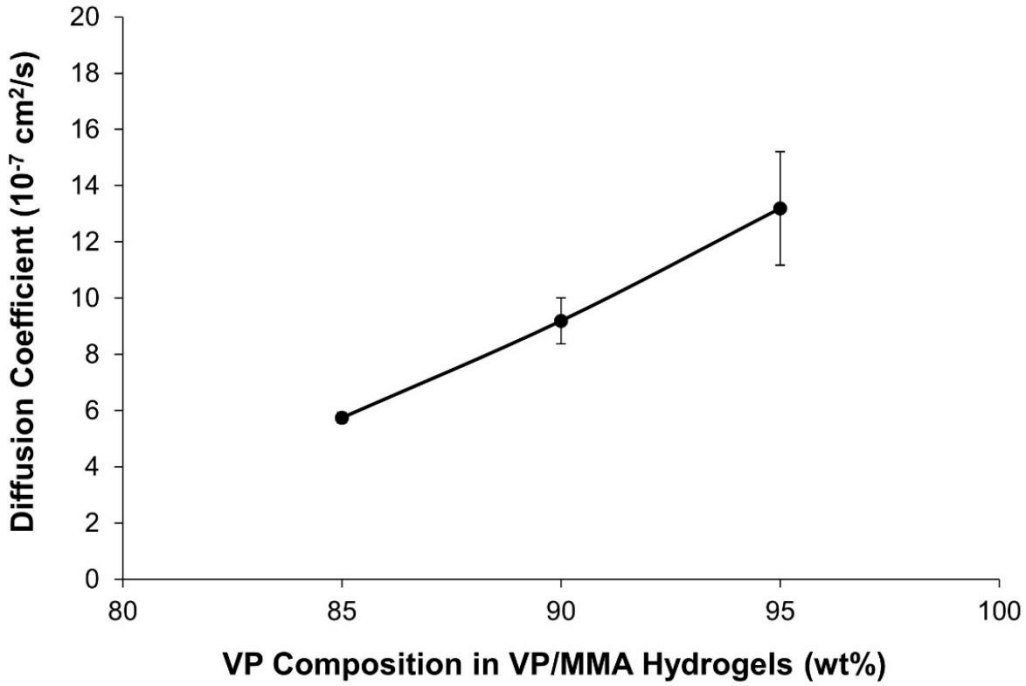


Figure 4.23 The diffusion coefficients of hydrogels as a function of VP composition

It had been reported that the diffusion coefficient is acutely sensitive to the polymer crosslinking density [266]. The effective crosslinking density (υ_e) is calculated using Equation (2.8) and it can be summarized in Table 4.10 [121], [156]. When 5wt% to 15wt% MMA is introduced to the VP/MMA hydrogel system, the crosslinking density increases from 3.8 to 8.7 mol/m^3 (Figure 4.24). This is due to the increased hydrophobic bonding between MMA domains. It had been reported that the crosslinking density of VP/MMA copolymer hydrogels increased from 0.9 mol/m^3 to 34.0 mol/m^3 when the MMA weight fraction was increased from 5% to 30% while the crosslinker content remained at 0% [267]. Increasing crosslinking density causes a reduction in diffusion coefficient (D) on account of reduced chain mobility and reduced free volume within the matrix. The restricted chain mobility means that the chain relaxation takes a longer time, and more energy is needed for the water to

transport into the hydrogel network. The increase in crosslinking density also corroborates with the increase in polymer volume fraction ($\upsilon_{2,s}$) (Table 4.10). The greater value of effective crosslink density in the hydrogel results in restrained mobility of the water molecule entering the polymer network, hence the volume fraction of the hydrogel is also increased.

Table 4.10 The diffusion coefficient and volume fraction of VP/MMA hydrogels

VP/MMA Composition	**Diffusion Coefficient (cm^2/s)**	**Volume Fraction ($\upsilon_{2,s}$)**	**Crosslinking Density (mol/m^3)**
VP85	5.7×10^{-7}	0.094 ± 0.005	8.7 ± 0.3
VP90	9.2×10^{-7}	0.091 ± 0.007	7.0 ± 0.3
VP95	13.8×10^{-7}	0.083 ± 0.003	3.8 ± 0.2

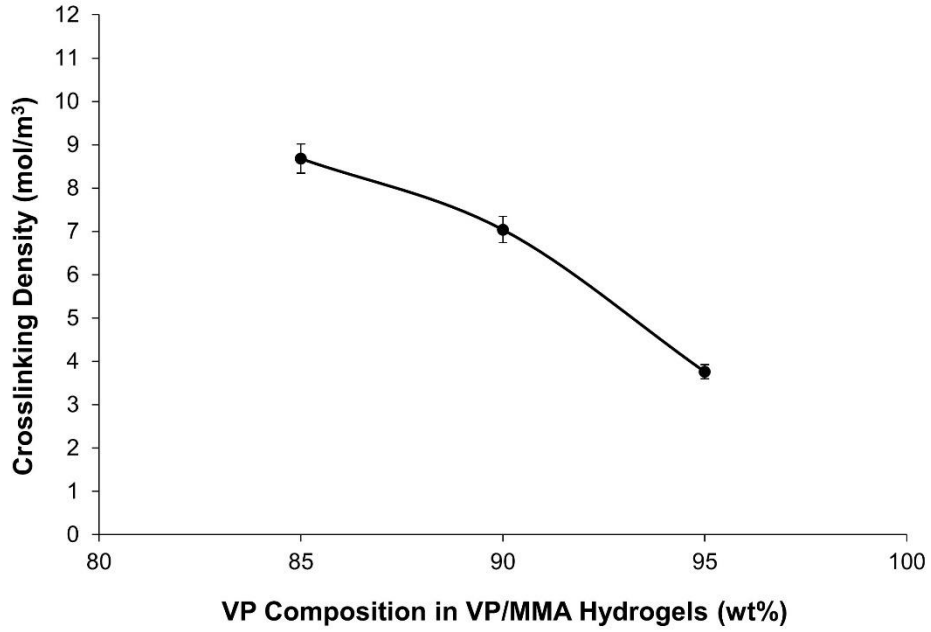


Figure 4.24 Effective crosslinking density as a function of VP composition

The average molecular weight between consecutive crosslinks ($\overline{M_c}$) is another structural parameter characterising the 3D network structure of the polymer. It can be calculated using Equation (2.2) [115]. Table 4.11 shows the average molecular weight ($\overline{M_c}$) of VP/MMA hydrogel at various composition ratios. The average molecular weight between crosslinking is affected by the concentration of VP (Figure 4.25). This parameter is also directly related to the effective crosslink density (υ_e). When the effective crosslinking density increased, it would significantly decrease the molecular weight between crosslinks (M_c), which indicates a significant reduction in an average distance between two adjacent crosslinks or mesh size (ξ) (Table 4.11). Decreasing in mesh size (ξ) results in reduction of free volume between the macromolecular chains, which then become less accessible water molecules to penetrate the hydrogel. This condition would decrease the equilibrium volume swelling.

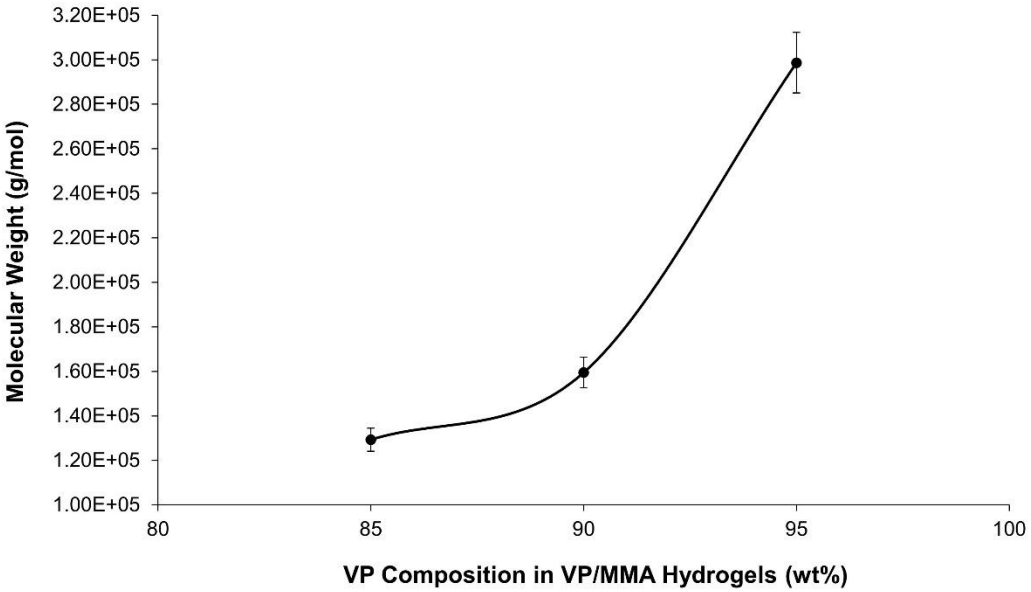


Figure 4.25 Molecular weight between crosslinks as a function of VP/MMA composition ratios

The mesh size (ξ) has been long predicted to scale the volume fraction ($v_{2,s}$) of a swollen hydrogel. The relationship between ξ and $v_{2,s}$ roughly agreed with the well-known scaling relationship in Equations (4.14) and (4.15):

$$\xi \sim {v_{2,s}}^{-3/4}, \text{when } v_{2,s} \leq 0.01 \quad (4.14)$$

$$\xi \sim {v_{2,s}}^{-1/2}, \text{when } v_{2,s} \geq 0.01 \quad (4.15)$$

In this study, the polymer volume fraction ($v_{2,s}$) is reported $v_{2,s} \geq 0.01$, hence the calculated correlation length or mesh size (ξ) is plotted as a function of ${v_{2,s}}^{-1/2}$ (Figure 4.26). It shows that the correlation length of VP/MMA hydrogels with varied VP composition fits well with the scaling law. This show that the experimental data from the swelling behaviour is well described by the scaling law.

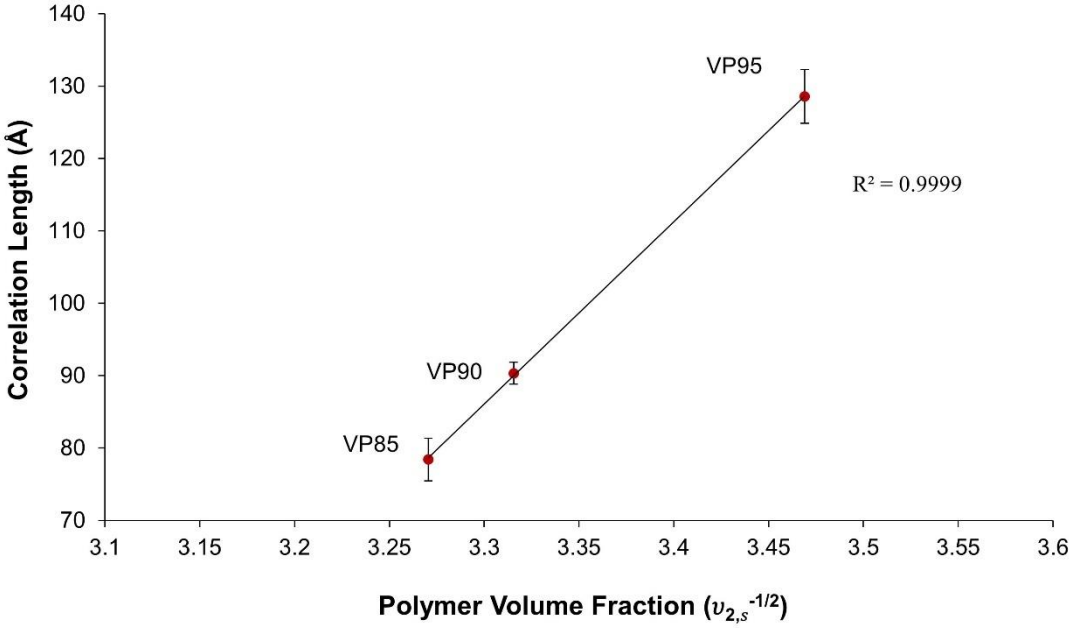


Figure 4.26 Calculated correlation length (ξ) as a function of the volume fraction ($\boldsymbol{v_{2,s}^{-1/2}}$) of the swollen VP/MMA hydrogels

The ability of polymer networks to absorb water depends on the interaction between water molecules and polymer chains. According to the Flory-Huggins theory,

χ takes a higher value if the interaction between polymer and water is weak. A more hydrophobic network has a higher χ. The polymer-solvent interaction parameter (χ) of VP/MMA hydrogels at swelling equilibrium could be calculated using Equation (2.3) [116]. The calculated polymer-solvent interaction (χ) of VP/MMA hydrogel at various composition ratios is demonstrated in Table 4.11. Hydrogels show polymer-solvent interaction parameter (χ) values are above 0.5 (χ>0.5). An increase χ value from 0.531 to 0.538 with a decrease in VP composition from 95wt% to 85wt% indicates weak interaction between the polymer and water, which also means the strong interaction between hydrophobic groups of the polymer chains. An increase in χ supports the explanation that hydrophobicity is increasing with MMA concentration, leading to a decreased initial swelling rate (%/h), equilibrium swelling ratio, and diffusion coefficient (D).

Table 4.11 Structure characterization parameters of VP/MMA hydrogels with varied VP composition ratios

Composition	$\boldsymbol{v_e}$ **(mol/m^3)**	$\boldsymbol{v_{2,s}}$	$\boldsymbol{\chi}$	$\boldsymbol{\overline{M_c}}$ **(g/mol)**	**ξ (Å)**
VP85	8.7 ± 0.3	0.094 ± 0.005	0.539	1.3 x 10^5	78.4 ± 2.9
VP90	7.0 ± 0.3	0.091 ± 0.007	0.537	1.6 x 10^5	90.3 ± 1.5
VP95	3.8 ± 0.2	0.083 ± 0.003	0.532	3.0 x 10^5	128.6 ± 3.7

4.3.1.2 Effect of Hydrogel Size on the Swelling Behaviour

In this study, a hydrogel with VP/MMA 85:15 wt% (VP85) was used to investigate the effect of hydrogel size on swelling behaviour. Various hydrogel sizes

used in this study are shown in Table 4.12. The hydrogel with the largest surface area and volume is labelled as A sample and the smallest surface area and volume of the hydrogel is labelled as E sample. The size of the hydrogel has significantly affected the swelling capacity induced by heterogeneous swelling and buckling instabilities.

Table 4.12 Sizes of the VP/MMA hydrogel used in this study

Sample	Diameter (mm)	Length (mm)	Area (mm^2)	Volume (mm^3)
A	12	3	113.04	339.12
B	6	3	28.26	84.78
C	6	6	28.26	169.56
D	6	9	28.26	254.34
E	3	3	7.07	21.21

Figure 4.27 shows the volume swelling of VP/MMA hydrogels at various sizes versus time. All hydrogels show a rapid increase of volume swelling at the initial state. The sharper the curve behaves in the beginning, the faster the hydrogel swells in the water. At the time (t), the swelling gets slower to an asymptotic value and finally reaches the equilibrium condition. At the equilibrium state, the hydrogel with a larger volume (D=12 mm, L= 3mm) produces a higher volume swelling as it provides a bigger space for water to penetrate inside the network chain. Figure 4.28 shows the volume swelling ratio of VP/MMA hydrogels at various sizes. According to the results, water tends to occupy almost similar swelling capacity when the hydrogel with the same length and composition is introduced into the polymer system.

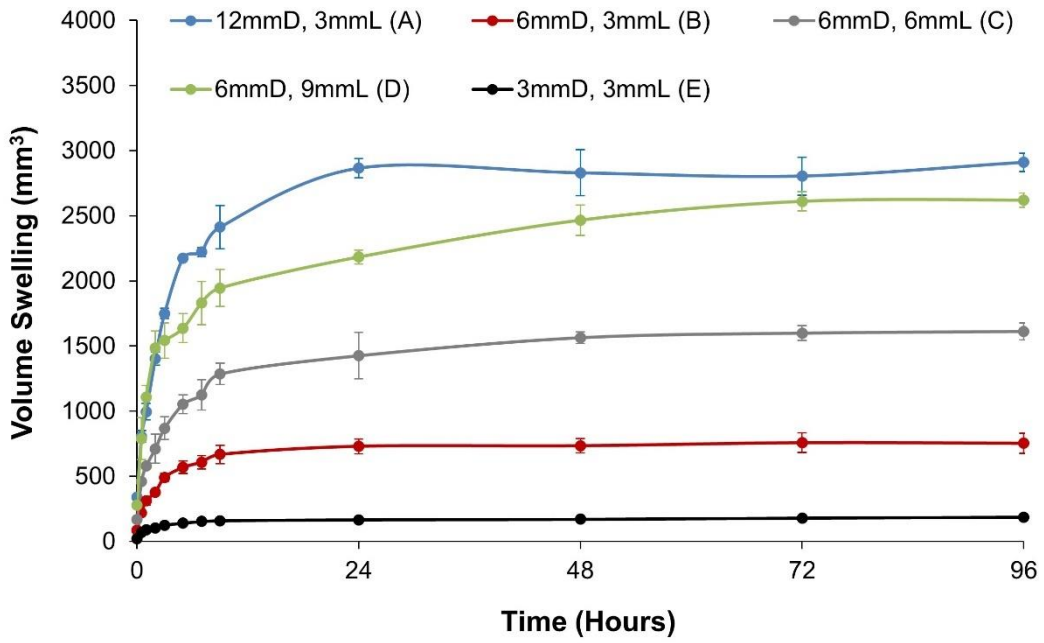


Figure 4.27 Volume swelling of the hydrogel at various sizes plotted as a function of time

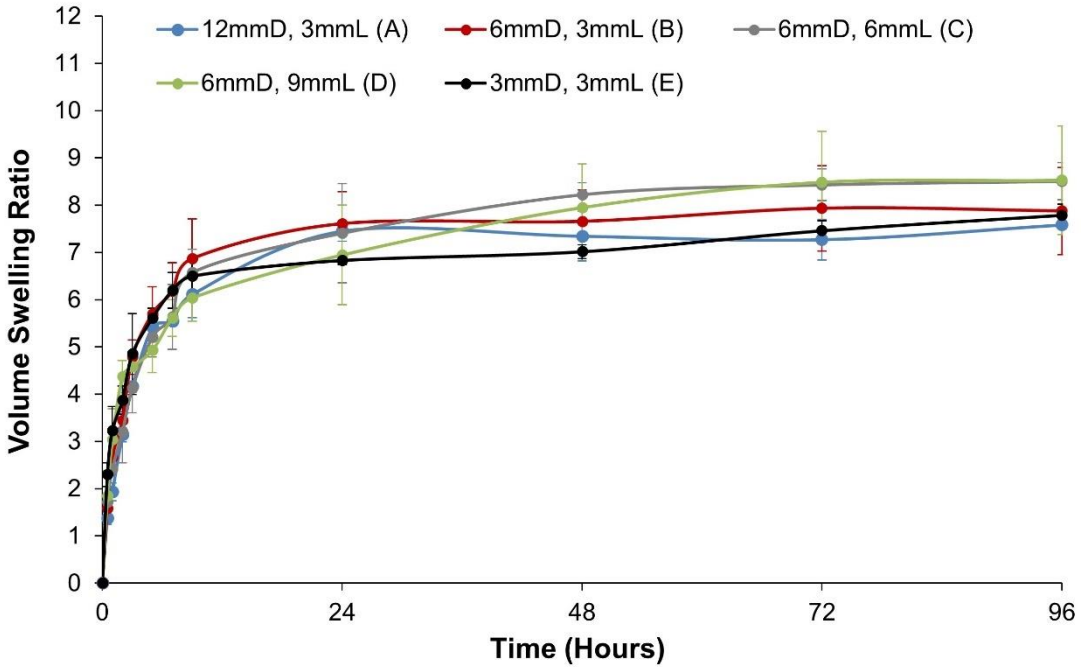


Figure 4.28 Volume swelling ratio of various hydrogel sizes as a function of time

Figure 4.29 demonstrates the initial swelling rate of hydrogels at various sizes. The swelling rate is calculated as the linear slope region of the swelling curve. The hydrogel with the largest volume (D= 12mm, L= 3mm) produces the fastest initial swelling rate (76.9%/h). However, the smallest volume (D=3mmD, L=3 mm) shows a swelling rate reduction of 59.8%/h (Table 4.13). At the initial stage, the wetting towards the centre and the gel starts to swell in the radial direction (most significantly near the two edges), while the centre part of the hydrogels is constrained with a little deformation in the length direction. As a result, the hydrogel with a larger diameter swells faster due to water easily penetrating through the edge surface, while hydrogel with a smaller diameter and longer length demonstrate a slower rate. Figure 4.30 shows the equilibrium swelling ratio of hydrogels at various sizes. The hydrogel with a longer length has a slightly higher equilibrium volume swelling ratio (Table 4.13). This is due to the extension of the end deformation in the y-direction scales with the length of the hydrogel.

Table 4.13 Effect of hydrogel sizes on the initial swelling rate and equilibrium swelling ratio

Diameter (mm)	**Length (mm)**	**Volume (mm^3)**	**Initial Swelling Rate (%/h)**	**Equilibrium Swelling Ratio**
12	3	339.12	76.9 ± 0.1	7.6 ± 0.2
6	3	84.78	68.2 ± 8.9	7.9 ± 0.9
6	6	169.56	63.4 ± 3.9	8.5 ± 0.4
6	9	254.34	65.9 ± 4.5	8.5 ± 1.2
3	3	21.21	59.8 ± 3.4	7.8 ± 0.2

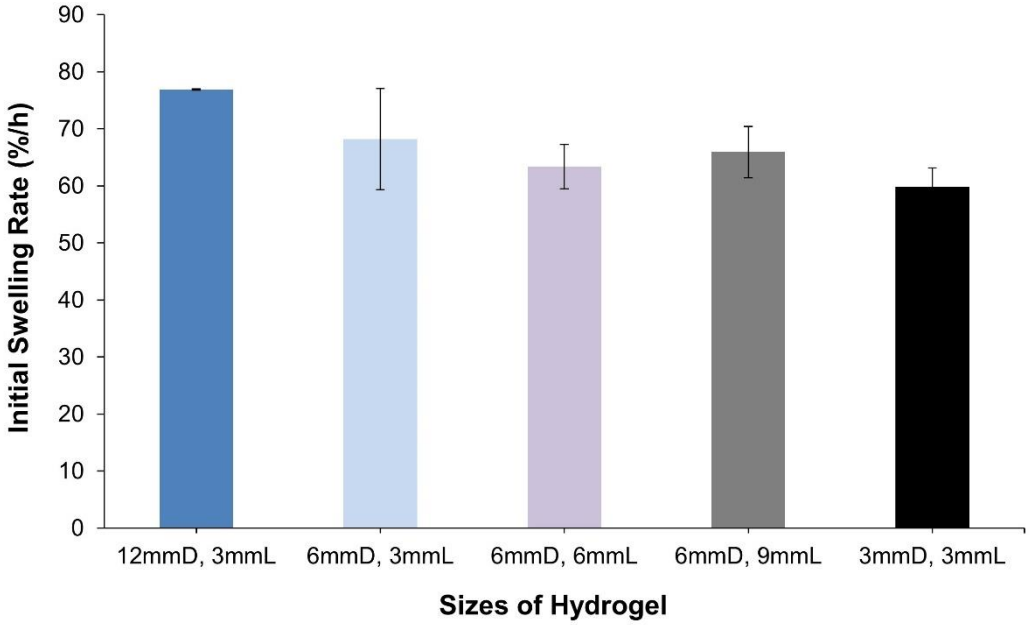


Figure 4.29 Initial swelling rate of VP/MMA hydrogel at various sizes

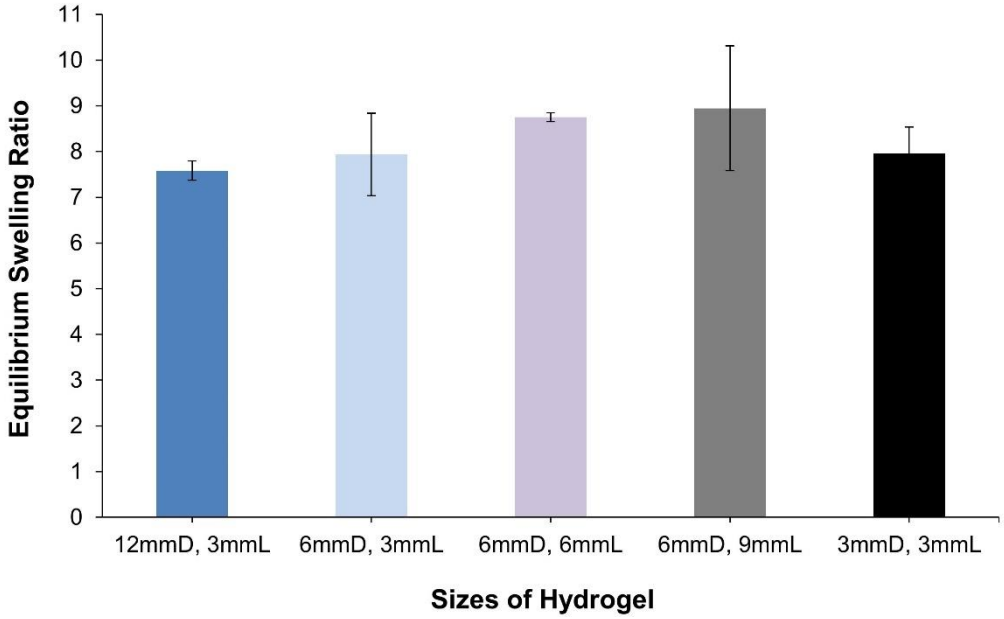


Figure 4.30 Equilibrium volume swelling ratio of VP/MMA hydrogel at various sizes

When a glassy hydrogel is brought into contact with water, water diffuses into the hydrogel, and the hydrogel swells. Diffusion involves the migration of water into pre-existing or dynamically formed spaces between hydrogel chains whereas swelling

of the hydrogel involves a larger scale segmental motion resulting in a bigger separation between hydrogel chains [268]. Equations (2.6) and (4.13) were used to determine the nature of the diffusion of water into hydrogels. The plot of Equation (2.6) is shown in Figure 4.31. Equation 4.13 shows the natural logarithmic of Equation (2.6). The value of diffusion exponent (n) was calculated as the gradient of the curve, and it is shown in Figure 4.32.

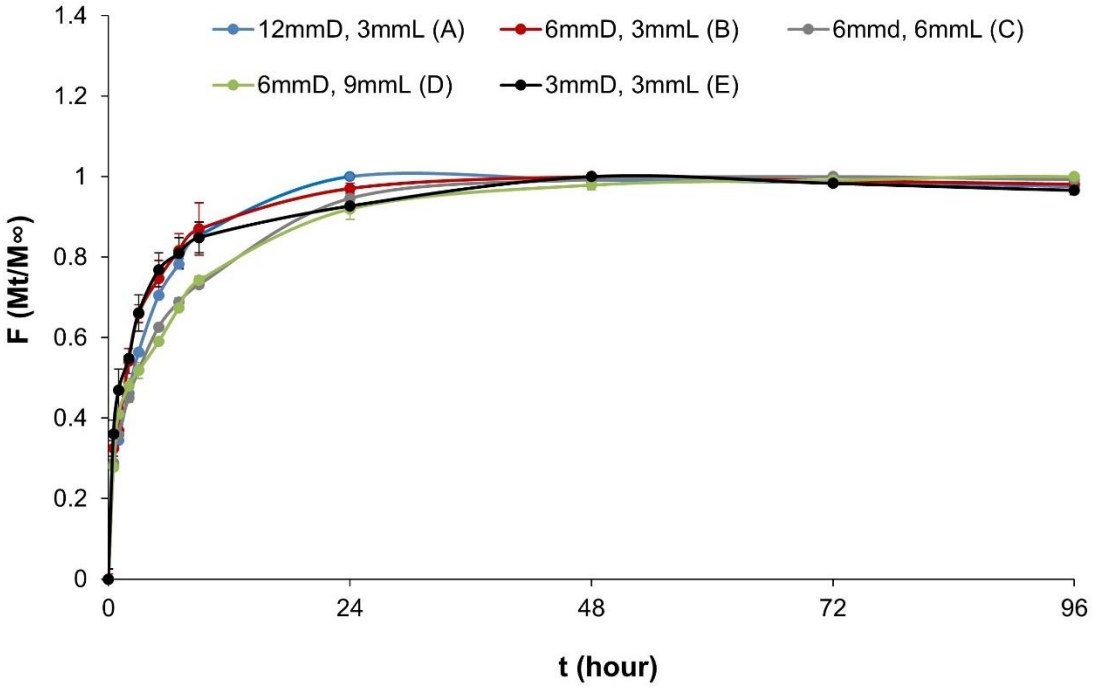


Figure 4.31 Water uptake of various hydrogel sizes as a function of time

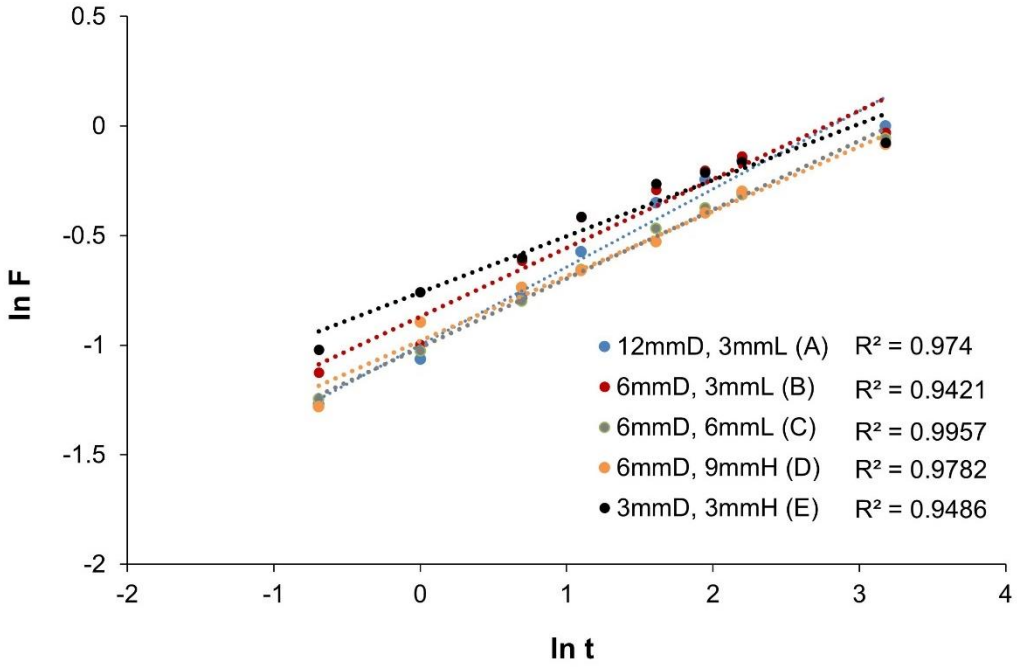


Figure 4.32 Natural logarithmic water uptake at various hydrogel sizes as a function of time

Alfrey *et al*. demonstrated that penetrant uptake is dependent on two processes such as the diffusion of the penetrant into the polymer and the relaxation of the polymer chains in response to the penetrant [143]. Table 4.14 shows that the diffusion exponents (n) of hydrogels at different sizes ranging from 0.79 to 1. This follows a "non-Fickian" diffusion behaviour on account of having a diffusion exponent (n) > 0.5 [269]. Most hydrogel samples are showing the characteristics of anomalous diffusion which occurs in the transition region between cases I and II when the diffusion and relaxation rates are comparable [270]. However, the hydrogel with the size of 12mmD & 3mmL demonstrates the characteristic of case transport II (n=1). The characteristic of case II diffusion is when the diffusion is very rapid compared to polymer relaxation ($R_{diff} > R_{relax}$) [271]. As the diameter of the hydrogel increased, the distance from the centre to the surface of the sample is also increased. At xerogel stage, the hydrogel is in the

glass structure. During swelling, the water diffuses into polymer network through the exposed surface, eventually reaching a high enough concentration to cause the polymer region to swell and become rubbery. Subsequently, the outer edges of the gel expanded outward from the centre line of the sample, as a sharp front between rubbery and glassy regions moved towards the centre of sample. Hydrogels with larger diameter, at the first 60% of swelling, the hydrogel is partially expanded. The presence of a glassy core in partially swollen hydrogel acts as a constraint to swelling. Therefore, the polymer relaxation process is slower.

Diffusion is a process whereby matter is spontaneously transported from one region of a system to another as a result of random molecular motion. The diffusion coefficients (D) of the VP85 hydrogels at various sizes were calculated using Equation 2.7 and the D values can be summarized in Table 4.14. D value increases when the diameter of the hydrogel increased. As the diffusion is very rapid at the initial stage, it will significantly affect the diffusion coefficient (D). The diffusion coefficient shows similar trend with the initial swelling rate results (Table 4.13), which shows at the beginning of swelling the hydrogel with the larger diameter would swell faster. As a significant chain relaxation must occur for the water molecules to penetrate the polymer network, some water must be diffusing into the sample to allow this chain rearrangement. Hence, the diffusion coefficient increased. However, a decrease in the D value is observed when the hydrogel diameter decreased. As the size of the sample is smaller, the local densification of the macropores might cause the reduction in the diffusion coefficient value. The hydrogel with the same diameter size shows almost the same value of diffusion coefficient (D). It might indicate that variation of hydrogel diameter seems to have less effect on the diffusion values.

Table 4.14 The diffusion exponent, type of diffusion, and diffusion coefficient of VP/MMA hydrogel at various sizes

Diameter (mm)	Length (mm)	Diffusion Exponent (n)	Diffusion Mechanism	Diffusion Coefficient (D)
12	3	1.00	Case II	5.7×10^{-6}
6	3	0.90	Anomalous	1.9×10^{-6}
6	6	0.96	Anomalous	1.5×10^{-6}
6	9	0.96	Anomalous	1.7×10^{-6}
3	3	0.79	Anomalous	0.6×10^{-6}

4.3.2 Volume Swelling and Diffusion of Hydrogels in PBS

4.3.2.1 Effect of Composition Ratio on Swelling

All hydrogels were prepared with an identical polymer size of 6mmD & 6mmL as this study aimed to compare the influence of two different solvents on polymer swelling. Hydrogels with a composition ratio of VP/MMA 85:15, 90:10, and 95:5 were immersed in DI water at room temperature and PBS at 37˚C. The results are quantified through the volume swelling ratio analysis, as shown in Figure 4.33 plotted as a function of time. The hydrogel based on the more hydrophilic VP monomer such as VP95 is more swelled in PBS and DI water. In contrast, as the MMA increases, the hydrogels are less able to swell. There is a significant reduction in the volume swelling ratio when VP85 is introduced in the VP/MMA system.

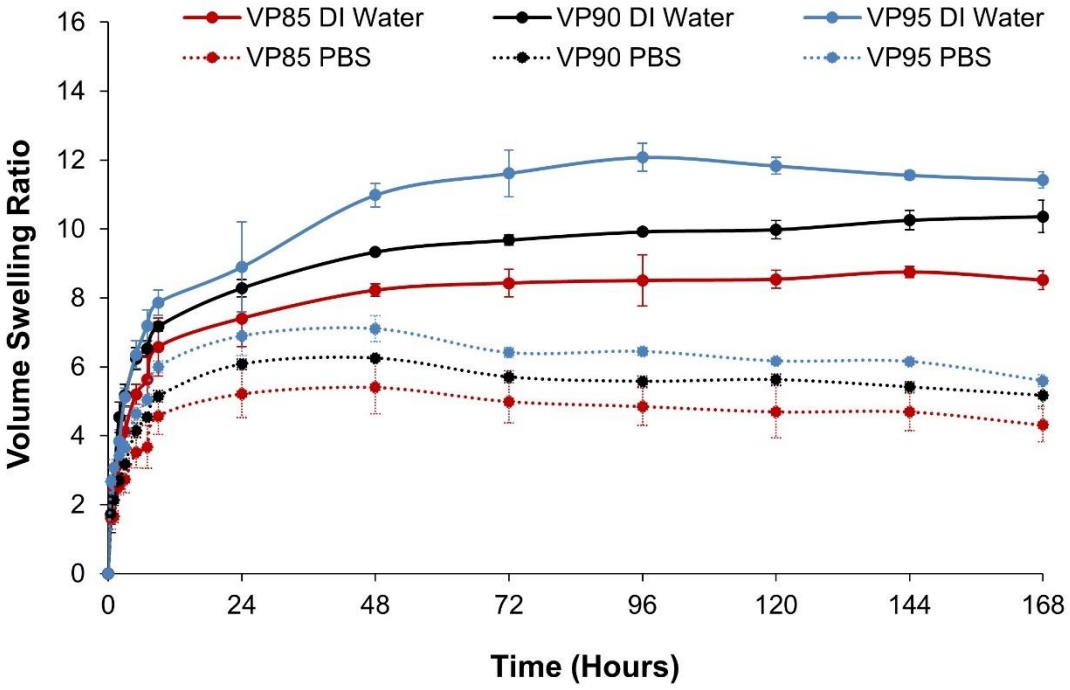


Figure 4.33 Volume swelling ratio of VP/MMA hydrogels at various composition ratios as a function of time swelled in DI water at room temperature and PBS at 37˚C

The type of solvent has an important influence on hydrogel swelling. Since water has the greatest osmotic potential, it will facilitate a faster swelling rate and the greatest degree of swelling at equilibrium (Table 4.15). In this study, PBS solution was used to simulate a representative biological environment. PBS solution contains Na^+ and K^+ cations, which interact with the polar groups of vinyl pyrrolidone thus diminishing the degree of swelling by reducing the osmotic potential [219]. The hydrogel experiences a significant decrease in the swelling ratio.

Table 4.15 Initial swelling rate and equilibrium volume swelling ratio of 6mmD, 6mmL hydrogel at various compositions swelled in DI water at room temperature and PBS at 37˚C

Solution	Composition	Initial Swelling Rate (%/h)	Equilibrium Volume Swelling Ratio
DI Water	VP85	63.7 ± 6.6	7.6 ± 0.2
	VP90	86.7 ± 4.6	10.4 ± 0.5
	VP95	96.3 ± 6.8	12.1 ± 0.4
PBS	VP85	40.7 ± 5.5	5.4 ± 0.8
	VP90	47.8 ± 0.9	6.3 ± 0.1
	VP95	53.8 ± 3.5	7.1 ± 0.4

The diffusion exponent (n) is calculated using Equation 4.13. Table 4.16 shows the diffusion exponent (n) of VP/MMA hydrogels at various composition ratios swelled in PBS and DI water. All hydrogel samples have diffusion exponent values in the range of $0.5 < n < 1.0$, which indicates that the hydrogel shows the 'anomalous diffusion' behaviour, where water penetration is partially controlled by the viscoelastic relaxation of the polymer chain [264]. The rate of water diffusion (R_{diff}) and that of polymer chain relaxation (R_{relax}) are comparable. The diffusion exponent (n) of hydrogel swelled in PBS is lower compared to when hydrogel swelled in DI water. PBS solution produces a slower diffusion rate due to it contains Na^+ and K^+ cations that will form a 'hydration-shell', which acts to disrupt the intermolecular structure of the surrounding bulk water [272]. The diffusion coefficient (D) is calculated using Equation 2.7 and is shown in Table 4.16. Increased hydrophilicity leads to an increase

in the diffusion coefficient (D). The diffusion coefficient (D) of hydrogels swelled in PBS is slightly lower compared to hydrogels swelled in DI water, following the swelling ratio result. The effect of solvents on swelling behaviour is important to study. Cations are introduced in the solvents when the hydrogel is swelled in PBS. This ionic shielding (Figure 4.34) prefers to interact with the polar group in the hydrophilic chain of VP which disrupt the binding between the hydrophilic chain and water, hence it is unable to effectively increase the swelling. As a result, compared to pure water, the presence of cations in PBS solution not only reduced the maximum swelling ratio, but also the rate at which this value is attained.

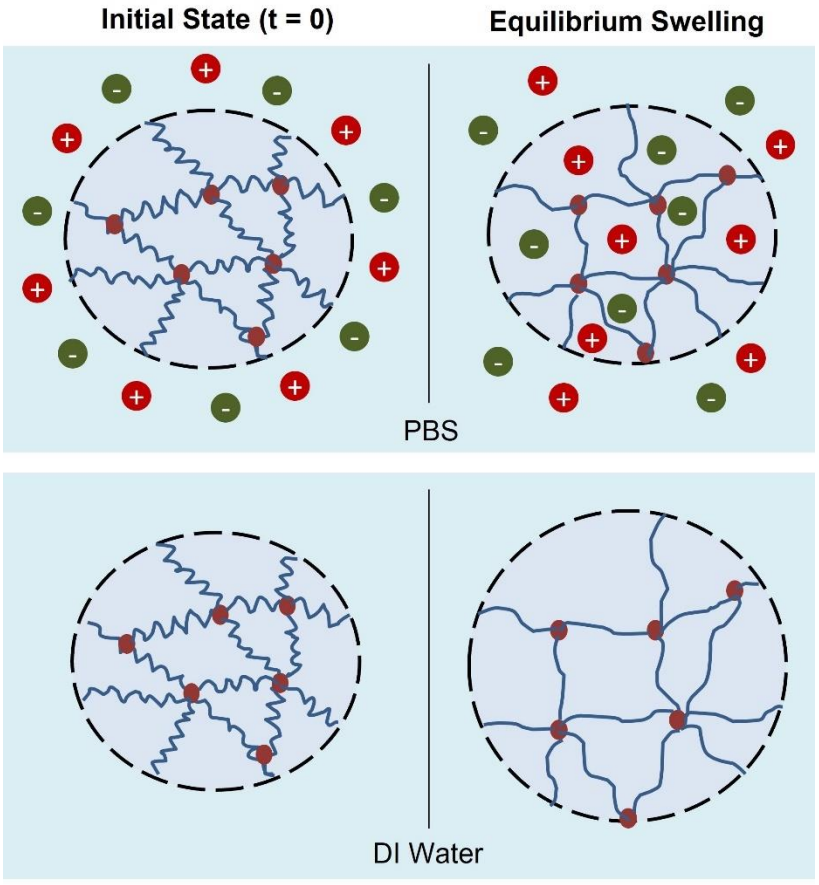


Figure 4.34 Illustration of hydrogel swelling in PBS and DI water at the initial stage (t=0) and equilibrium

Table 4.16 Diffusion exponent and diffusion coefficient of hydrogels at various composition ratios swelled in DI water at room temperature and PBS at 37˚C

Solution	Composition	n	Transport Type	Diffusion Coefficient (cm^2/s)
DI Water	VP85	0.96	Anomalous	1.5×10^{-6}
	VP90	0.95	Anomalous	1.6×10^{-6}
	VP95	0.93	Anomalous	1.8×10^{-6}
PBS	VP85	0.78	Anomalous	0.9×10^{-6}
	VP90	0.77	Anomalous	1.5×10^{-6}
	VP95	0.75	Anomalous	1.8×10^{-6}

4.3.2.2 Effect of Hydrogel Sizes on Swelling

Figures 4.35 shows the volume swelling of VP85 hydrogel at various sizes such as 12mmD & 3mmL (V= 339.12 mm^3), 6mmD & 3mmL (V= 84.78 mm^3), 6mmD & 6mmL (V= 169.56 mm^3) swelled in DI water at room temperature and PBS at 37˚C. Hydrogel with a bigger volume (12mmD, 3mmL) ideally would produce a greater swelling capacity when immersed in both solvents (PBS and DI water). It could provide spaces to accommodate the solvents to penetrate the network structure. Figure 4.36 demonstrates the volume swelling ratio of various hydrogel sizes expanded in PBS and DI water. All hydrogel sizes swell to almost similar volume ratios, which means the change of hydrogel sizes slightly contributes to the volume swelling behaviour.

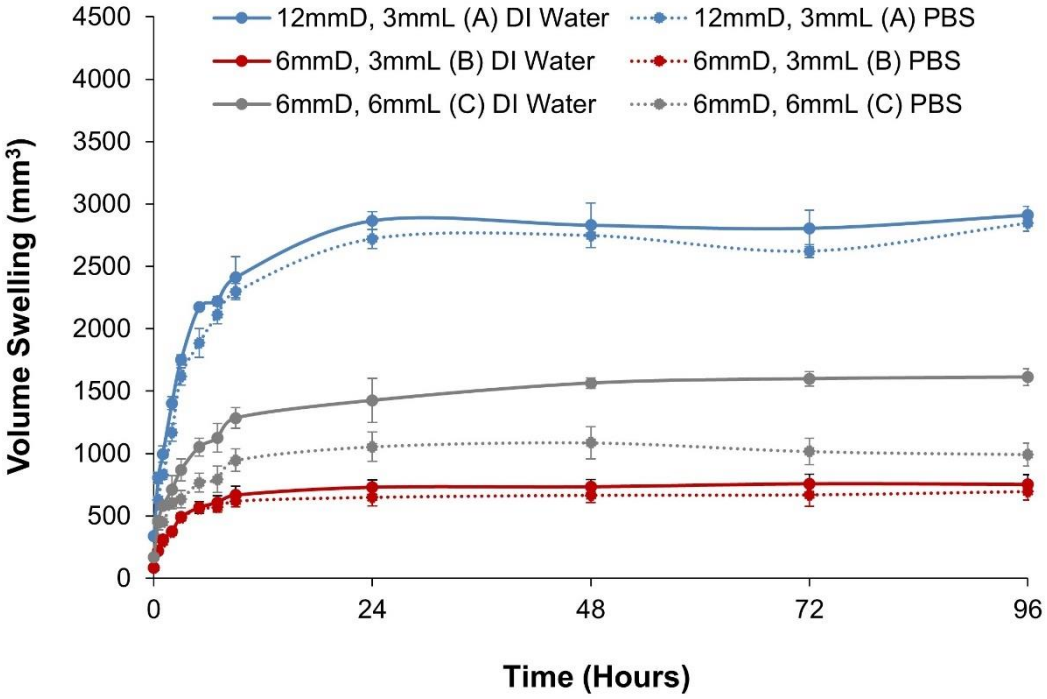


Figure 4.35 Volume swelling of VP/MMA hydrogels at various hydrogel sizes immersed in DI water at room temperature and PBS at 37˚C as a function of time

The swelling behaviour of VP/MMA hydrogels at various sizes is also investigated in PBS at 37˚C. PBS solution was the most commonly chosen swelling medium to model hydrogel behaviour in biomedical applications [273]. The result shows that the swelling behaviour of all hydrogels in PBS solution is slightly lower compared with the swelling in DI water (Figure 4.36). The swelling ratio decreases after 72 hours in PBS but then increased again thereafter until 96 hours. Ionic strength is known to affect the swelling of the neutral hydrogel since the presence of an ion established within the gel at equilibrium will inevitably cause the gel to swell or shrink [274]. According to the traditional theory of osmotic pressure of salt solutions, the osmotic pressure of a salt solution can be calculated by the equation $\Pi = iRTc_s$, where c_s is the molarity of the solute, and i is the Van Hoff factor, or the number of moles of

solute in solution, which is two for NaCl. This equation gives PBS, which is ~0.15*M* NaCl, the osmotic pressure of over 7 atm [275]. The ions in PBS can move freely into the hydrogels, quickly reducing the difference between the osmotic pressures of the hydrogels and the surrounding solution.

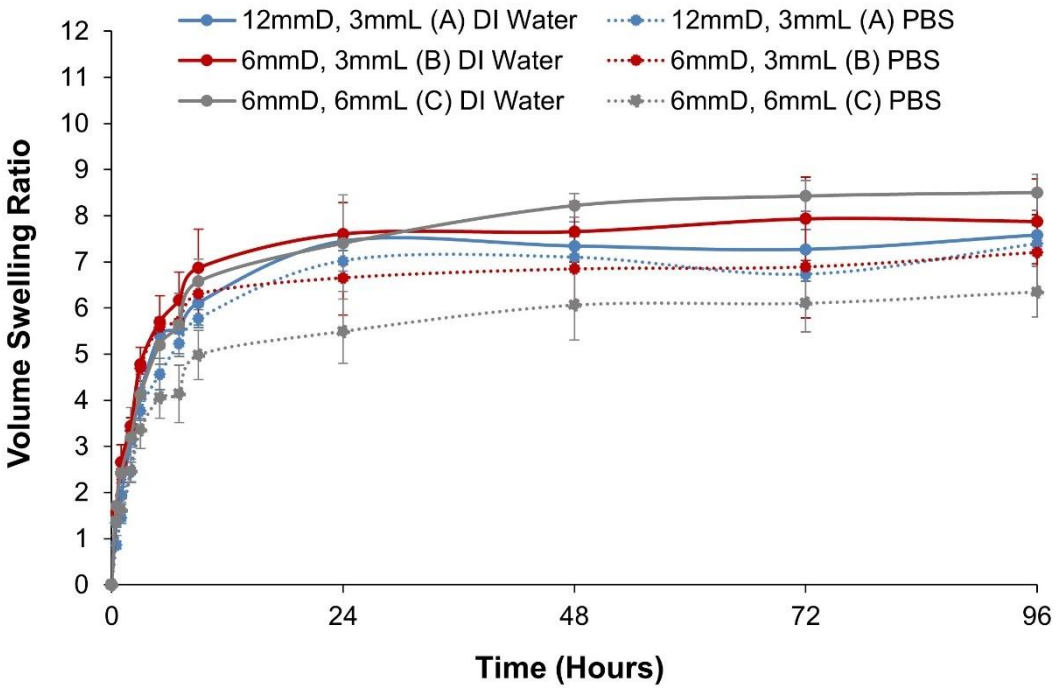


Figure 4.36 Volume swelling ratio of VP/MMA hydrogels at various sizes immersed in DI water at room temperature and PBS at 37˚C as a function of time

The diffusion kinetics of VP/MMA hydrogels at various sizes swelled in PBS are determined the same way as described in the previous section. Table 4.17 summarizes the diffusion exponent (n) and diffusion coefficient (D) of VP/MMA hydrogels with sizes of 12mmD & 3mmL (V= 339.12 mm^3), 6mmD & 3mmL (V= 84.78 mm^3), and 6mmD & 6mmL (V= 169.56 mm^3) swelled in DI water and PBS. The diffusion exponent is calculated from the gradient of the plotted curves in Equation 4.13. All hydrogel samples have n > 0.5 and n=1 which correspond to non-Fickian

diffusion behaviour [269]. The non-Fickian diffusion (anomalous and case II) means the macromolecular relaxation dominates penetrant transport. Hydrogels swelled in PBS with the sizes of 6mmD & 3mmL and 6mmD & 6mmL are showing n values between 0.5 and 1, which belongs to the characteristic of anomalous diffusion. Hydrogel with the size of 12mmD and 3mmL which swelled in PBS shows the characteristics of case II transport that are similar to hydrogel swelled in water. The diffusion coefficients (D) are calculated from Equation 2.7. The diffusion coefficient decreases as the volume of the hydrogel decreases. When the hydrogels are swelled in PBS, the diffusion coefficient (D) is lower than the hydrogels swelled in water. These patterns are similar to the decrease of swelling capacity with an increase in ionic concentration. It often results from a charge effect of the additional cations, leading to a decreased osmotic pressure between the polymer network and the external solution [276]. The swelling of the hydrogels is depressed which causes to decrease in the diffusion coefficient (D).

Table 4.17 The diffusion exponent (n) and the diffusion coefficient of VP/MMA hydrogels at various sizes immersed in DI water at room temperature and PBS at 37˚C

Solvent	Size	n	Transport Type	D (cm^2/s)
DI Water	12mmD, 3mmL (A)	1.00	Case II	5.7×10^{-6}
	6mmD, 3mmL (B)	0.90	Anomalous	1.9×10^{-6}
	6mmD, 6mmL (C)	0.96	Anomalous	1.5×10^{-6}
PBS	12mmD, 3mmL (A)	1.00	Anomalous	5.2×10^{-6}
	6mmD, 3mmL (B)	0.87	Anomalous	1.8×10^{-6}
	6mmD, 6mmL (C)	0.78	Anomalous	0.9×10^{-6}

4.4 Swelling Force and Swelling Pressure of the Hydrogels

The force of expanding hydrogels was measured using a Densor Mayer Group instrument. Samples were placed under a compression plate attached to the load cell. Swelling is constrained and the gel generates a swelling force (F). In this study, a hydrogel with the size of D=3 mm & L= 3mm is chosen by considering the effect of composition ratios on the swelling force. Figure 4.37 plots the swelling force of various VP/MMA composition ratios as a function of time. It shows an initial sharp force peak at 0-1 hour before a noticeable decrease. The appearance of a sharp peak at the initial stage is due to the rapid relaxation on the hydrogel surface which forms a stress boundary between gel-like material and a glassy unsolvated core. As the surface absorbs more water, the glassy core is broken, and the gel is rapidly softened. In this stage, the swelling force is controlled by water transport and the expansion of the gel. An asymptotic swelling force for all hydrogel samples is observed after 115 hours of expansion attaining values between 4.2-4.9 N (Table 4.18). The more hydrophobic the

polymer (VP85), the greater the maximum swelling force. VP85 has a higher crosslinking density causing hydrogel to become stiff and swell less. However, a decrease in the swelling force is observed in the hydrogel with higher swelling. It had been reported in the literature that the blocking force of PNIPAm hydrogel increased with increasing crosslink density, while the free swelling decreased [277]. However, a contradictory result had been reported by Khare et al which showed that the more hydrophilic the polymer network the higher the maximum swelling force due to an increase of ionic content [278].

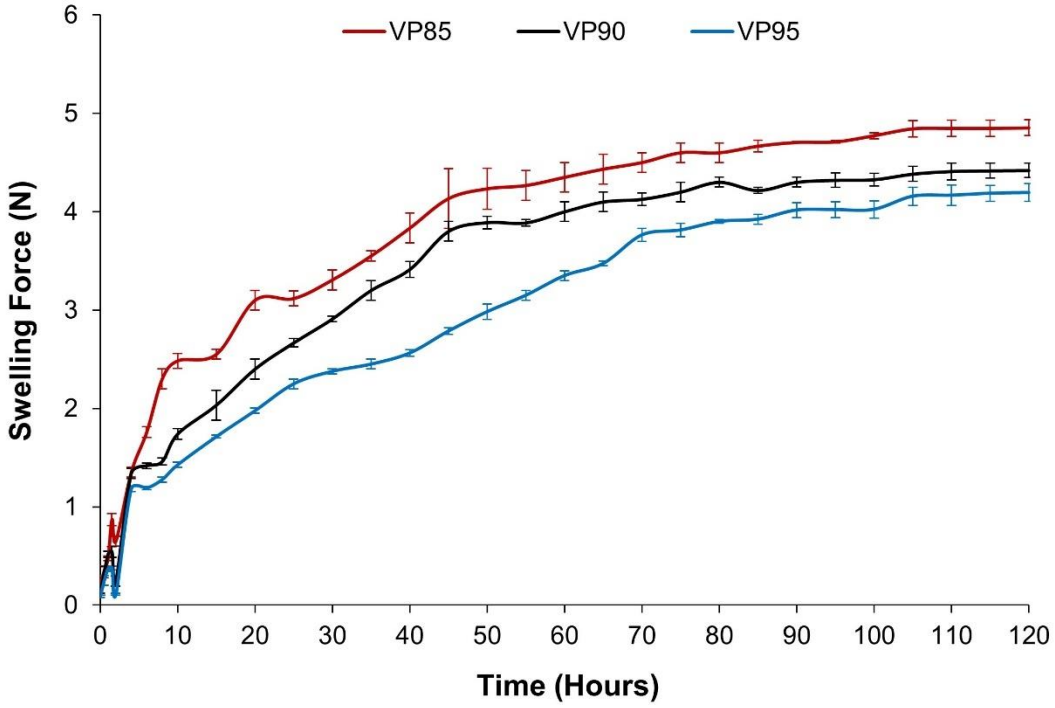


Figure 4.37 Swelling force of VP/MMA hydrogels at various composition ratios as a function of time

During hydrogel swelling, once the hydrophilic and hydrophobic sites have bound water molecules, further imbibition of water is driven by the osmotic pressure of the polymer network (π), which is counteracted by the elastic reaction force of the

network (p) [130], thus resulting the swelling pressure (P). The swelling pressure of the hydrogel could be regarded as the pressure that is required to prevent hydrogel from swelling [279]. At equilibrium, the swelling pressure is zero and hence $\pi = p$. In this study, the swelling pressure can be calculated using Equation 4.16. As the hydrogel is being constrained by the compression plate, therefore swelling in the axial direction would be limited and the length remains unchanged.

$$P(t) = \frac{F(t)}{V(t)} x\ l_0 \qquad (4.16)$$

where $F(t)$ is the force at the time, t, $V(t)$ is volume swelling at the time (t) and L_0 is the initial length.

Table 4.18 Swelling force, swelling pressure, and volume swelling ratio of various VP/MMA composition

Composition	Swelling Force (N)	Swelling Pressure (kPa)	Swelling Ratio
VP85	4.9 ± 0.08	77.9 ± 4.8	8.0 ± 0.3
VP90	4.4 ± 0.07	68.3 ± 6.8	8.9 ± 0.5
VP95	4.2 ± 0.09	49.9 ± 4.0	10.2 ± 0.3

Figure 4.38 shows the swelling pressure of VP/MMA hydrogels at various VP compositions as a function of time. Similar to the swelling force result, the curve shows an initial sharp peak at 0-1 hour. It is due to the hydrogel being still dominated by the glassy structure at the centre "core." The hydrogels continuously swell until the swelling pressure reaches an asymptotic value at 120 hours. For the VP95 composition, the swelling pressure achieves a value of 49.9 kPa (Table 4.18). By comparing with VP85, the swelling pressure increases to the value of 77.9 kPa. The swelling pressure

is increased by almost 1.5-fold with decreasing VP composition. Therefore, the hydrogel with less VP composition will be more effective to generate the swelling pressure due to increasing stiffness from hydrophobic MMA over water-soluble hydrophilic VP content. The highest swelling pressure is recorded in VP85, however, the equilibrium volume swelling ratio shows the lowest value *i.e.*, 8.0 ± 0.3 (Table 4.18). There is an inverse relationship between the volume swelling ratio and the swelling pressure of the hydrogel affected by the composition (Figure 4.39).

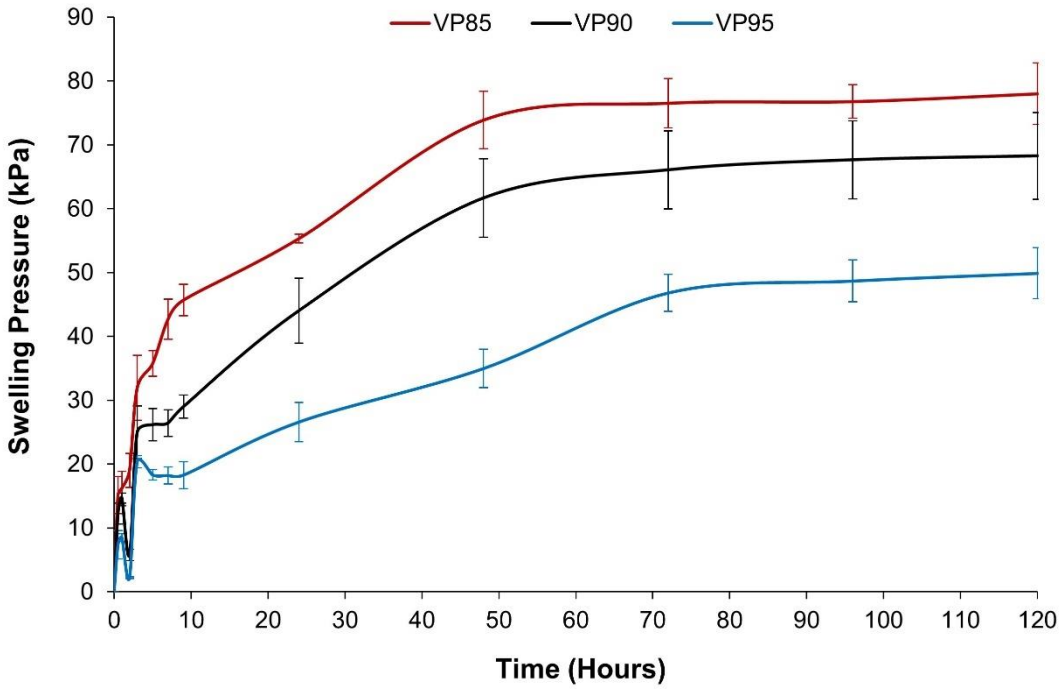


Figure 4.38 Swelling pressure of various composition VP/MMA hydrogels as a function of time

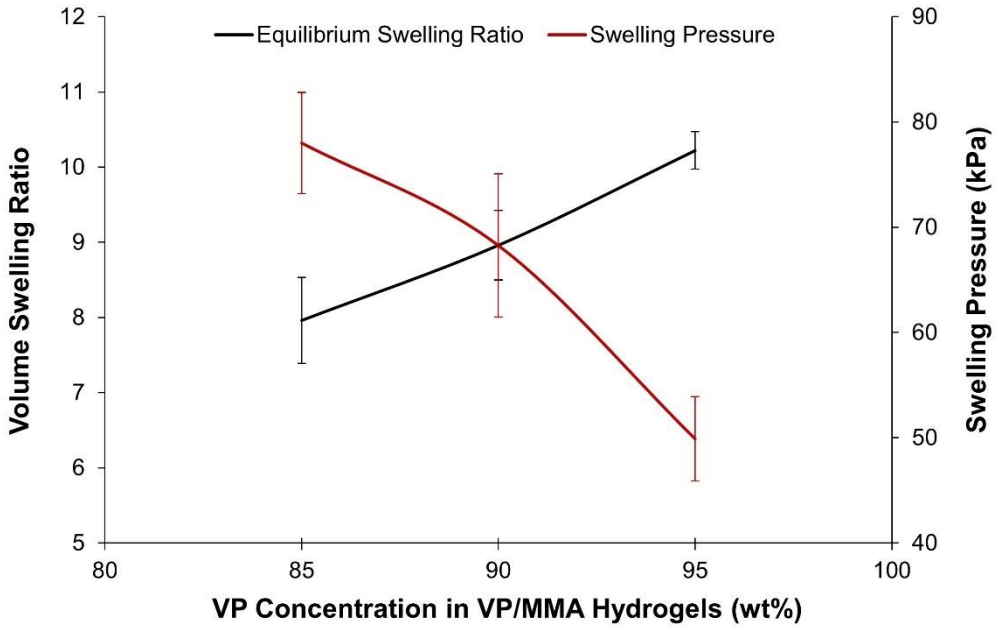


Figure 4.39 Inverse relationship between volume swelling ratio and swelling pressure of hydrogels at the various VP/MMA composition

For non-ionic hydrogel, the swelling pressure originates from the total osmotic pressure inside the gel and the elastic deformation of the polymer network. Elastic pressure (p) was estimated from elastic modulus measurement by using Equation 4.17. This model was adopted from the Gaussian chain model to describe the mechanical behaviour of the polymer network [277]:

$$p = G\left(1 - \frac{1}{\lambda_f{}^2}\right) \tag{4.17}$$

$$\mathrm{G} = \frac{E}{2\,(1+\upsilon)} \tag{4.18}$$

$$\lambda_f = \frac{r}{R} \tag{4.19}$$

Where G is the shear modulus of the gel in the swollen state, λ_f is swelling ratio, E is the elastic modulus, υ is Poisson's ratio (assume the value is 0.5), r is the radius of swelling gel, and R is the radius of the dry gel.

The elastic pressures of various VP/MMA composition ratios are shown in Table 4.19. VP/MMA composition significantly affects the elastic pressure. Higher MMA concentration means more crosslinking density resulting stiffer polymer networks. The mechanical properties of hydrogels will affect the magnitude of elastic pressure. The elastic pressure increases as MMA composition and stiffness increase. The osmotic pressures (π) of all hydrogel samples at 48 hours of swelling were calculated from swelling pressure (P) and elastic pressure (p) by Equation 2.5 ($P = \pi - p$). The results are shown in Table 4.19. The osmotic pressure of VP85, VP90, and VP95 are 86.4 kPa, 71.9 kPa, and 40.7 kPa, respectively. The osmotic pressure is contributed by the structural properties of the hydrogel. The swelling pressure of the hydrogels is dominated by the significant contribution of the osmotic pressure of the polymer network.

Table 4.19 Swelling pressure, osmotic pressure, and elastic contractile force of VP/MMA hydrogels at various VP compositions measured at 48 hours of swelling

VP Composition	Swelling Pressure (kPa)	Osmotic Pressure (kPa)	Elastic Pressure (kPa)
VP85	73.9 ± 4.5	86.4 ± 4.7	12.5 ± 0.3
VP90	61.7 ± 6.1	71.9 ± 5.6	10.3 ± 0.8
VP95	34.9 ± 2.9	40.7 ± 3.2	5.8 ± 0.2

In this study, the swelling pressure is a function of elastic modulus. Figure 4.40 shows the linear relationship between the elastic modulus and swelling pressure of hydrogels after 48 hours swelled in DI water at room temperature. The swelling

pressure of VP/MMA hydrogel reaches almost twice the elastic modulus value. Increasing the elastic modulus is incorporated with the increase in the swelling pressure. The presence of MMA monomer in the copolymer system contributes to produce denser network structure through the process called phase separation, which leads to greater crosslinking density of the network and results in increasing the number of micropores. Thus, increasing the crosslinking density in the copolymer creates rigidity of the structure (denser hydrogel), thereby contributing to the higher elastic modulus. Therefore, MMA plays an important role in giving a significant contribution to the mechanical properties of the hydrogels.

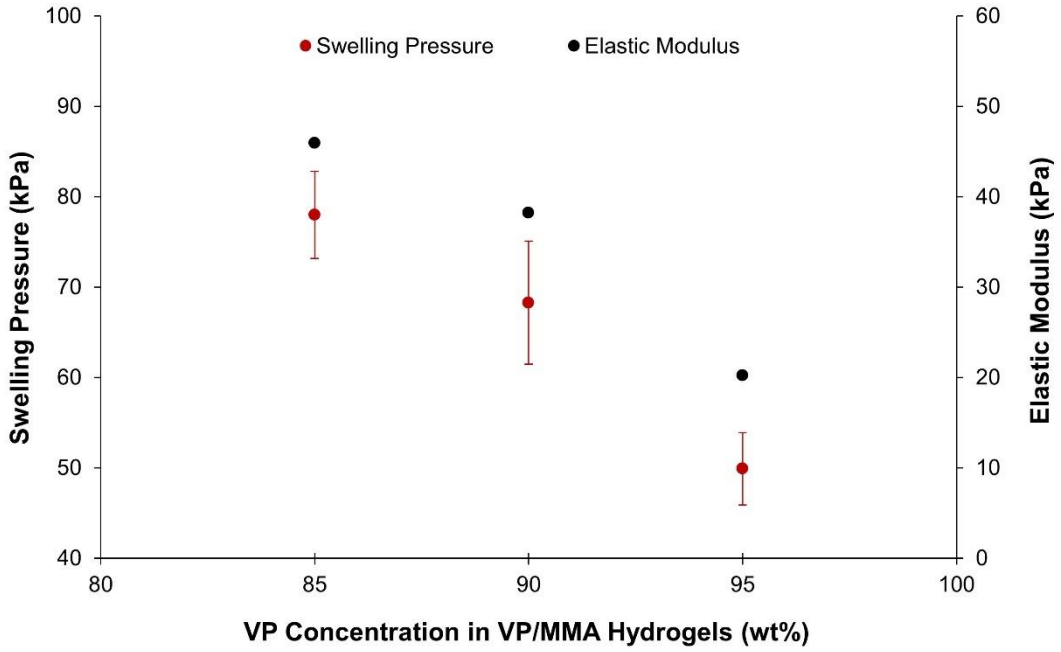


Figure 4.40 Linear relationship between the swelling pressure and elastic modulus of hydrogel samples as a function of VP concentration

Figure 4.41 shows the swelling force of the VP/MMA hydrogels at various sizes plotted as a function of time. VP85 composition was used in this study. The result shows that modifying the initial surface area (A_0) of the hydrogel provides a greater

contribution to the swelling force value. There is a linear increase in swelling force with increasing surface area of the hydrogels. The force could increase by almost 3-fold when the surface area changes from 7.07 to 113.04 mm^2. As the diameter of the hydrogel increases twice from 6 mm to 12 mm, the surface area is significantly altered, thereby contributing to a 2-fold increase in the swelling force. However, when the diameter is fixed (such as 6 mm in diameter) but the initial height varies (such as 3 mm, 6 mm, and 9 mm), the swelling force values remain constant. Therefore, the swelling force relative to the size is important.

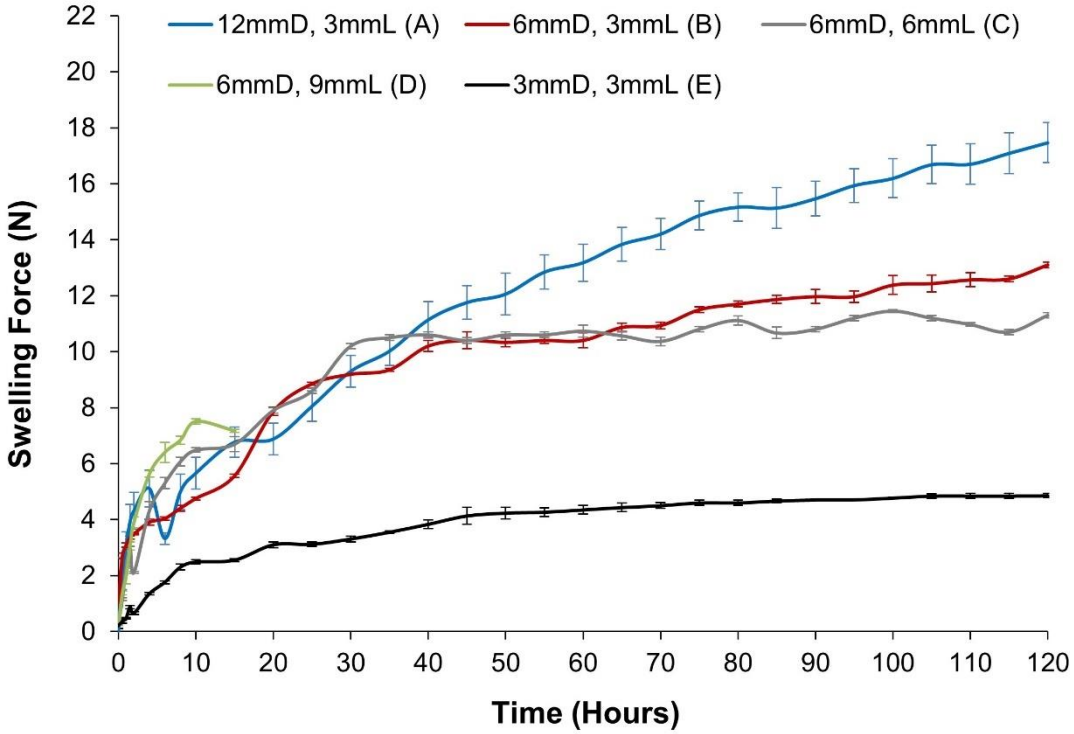


Figure 4.41 Swelling force of various sizes of VP/MMA hydrogels as a function of time

Figure 4.42 shows the swelling pressure of hydrogels at various sizes. The result shows that the swelling pressure increases with a decrease in the surface area of the hydrogels. The surface area provides a significant contribution to the swelling

pressure according to Equation 4.16. The swelling pressure is calculated from the recorded swelling force (F) over the contact surface area (A). For example, if the force acts over a bigger swelling area, it will produce a lower value of swelling pressure, however, the highest swelling pressure is owned by the hydrogels with the smallest surface area (D=3mm, L=3mm). Designing hydrogels with the same surface area will produce a similar swelling pressure value, although the diameter and height of the hydrogels are varied. The pressure generated from the different surface areas could be illustrated in Figure 4.43.

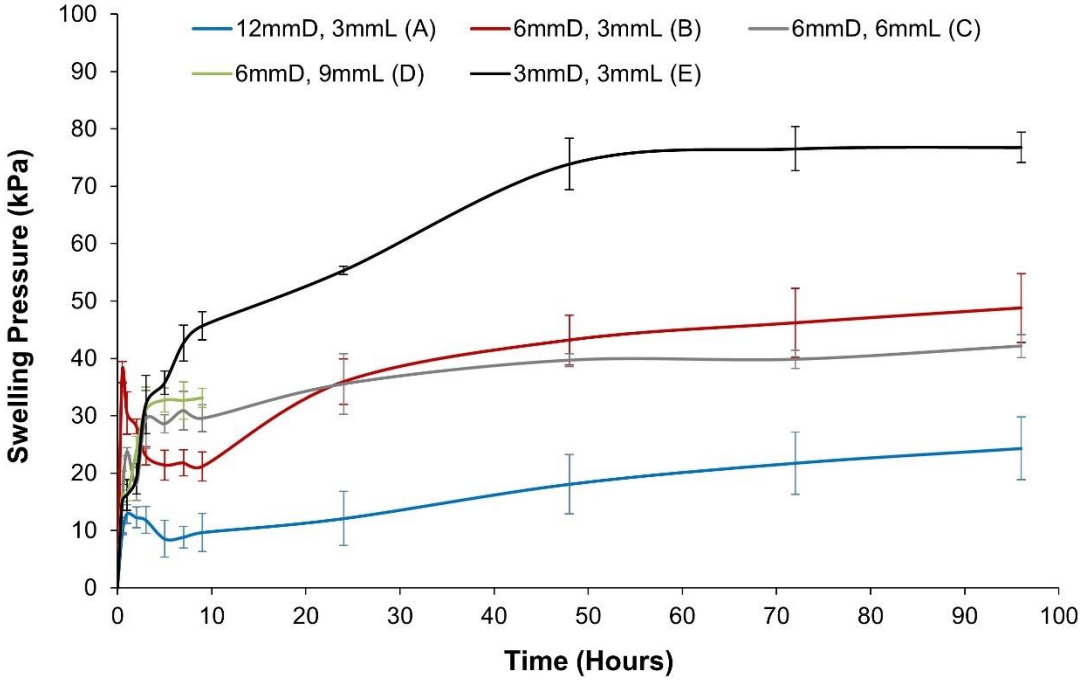


Figure 4.42 Swelling pressure of VP/MMA hydrogels at various sizes as a function of time

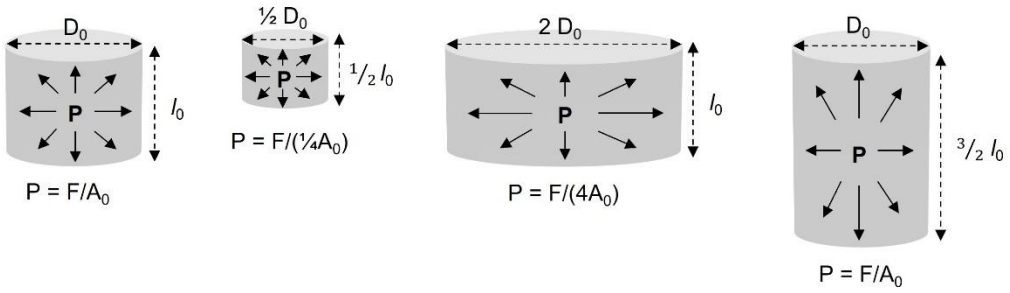


Figure 4.43 Illustration of the swelling pressure generation obtained from various surface areas of hydrogels

Table 4.20 summarizes the maximum swelling force and swelling pressure of various hydrogel sizes at 96 hours of swelling. The swelling force and pressure could not be linear due to area dependence. The swelling force increased from 4.7 N to 15.9 N with the increasing surface area from 7.07 mm^2 to 113.04 mm^2, respectively. However, the swelling pressure decreases from 76.8 kPa to 24.3 kPa when the surface area and diameter increase. It is due to the swelling pressure being diverted to the sideway, resulting in decreasing value of swelling pressure. When the surface area has the same value, the swelling force and swelling pressure show almost similar values. Therefore, it can be summarized that the variation of the surface area especially the diameter of the hydrogel significantly contributed to the swelling behaviour and mechanical properties of hydrogels compare to the influence of height.

Table 4.20 Effect of hydrogel sizes on the swelling force and the swelling pressure

Diameter (mm)	**Length (mm)**	**Area (mm^2)**	**Swelling Force (N)**	**Swelling Pressure (kPa)**
12	3	113.04	15.9 ± 0.6	24.3 ± 5.4
6	3	28.26	11.9 ± 0.2	48.8 ± 6.0
6	6	28.26	11.2 ± 0.1	42.1 ± 2.0
6	9	28.26	N/A	N/A
3	3	7.07	4.7 ± 0.1	76.8 ± 4.8

* Sample fails at 9 hours of swelling due to sample buckling

The elastic pressure was calculated by using Equation 4.17. Table 4.21 summarizes the value of elastic pressure as a function of hydrogel sizes. The elastic retractive force of hydrogel with the same composition does not significantly change with size. The osmotic pressure was estimated using Equation 2.5. The results of osmotic pressure at 48 hours of swelling are summarized in Table 4.21. The hydrogels were analyzed using the same VP/MMA composition ratio. It shows that the osmotic pressure significantly changes with size. Hydrogels with the same diameter produce similar osmotic pressure (52.5-55.3 kPa). Hydrogels with smaller sizes produce more osmotic pressure than larger sample sizes.

Table 4.21 Effect of hydrogel sizes on the swelling pressure, osmotic pressure, and elastic contractility (at 48 hours of swelling)

Sizes	Swelling Pressure (kPa)	Osmotic Pressure (kPa)	Elastic Contractility (kPa)
12mmD, 3mmL	18.1 ± 5.2	30.6 ± 5.6	12.5 ± 0.5
6mmD, 3mmL	43.2 ± 4.4	55.3 ± 4.9	12.1 ± 0.6
6mmD, 6mmL	39.7 ± 1.1	52.5 ± 1.7	12.8 ± 0.7
6mmD, 9mmL*	N/A	N/A	N/A
3mmD, 3mmL	73.9 ± 4.5	86.4 ± 4.7	12.5 ± 0.3

* Sample fails at 9 hours of swelling due to sample buckled

4.5 Anisotropic Hydrogels

The anisotropic hydrogel was formed by annealing hydrogel under pressure for a specified time using a hydraulic press equipped with thermostatically controlled heating plates. The xerogels were heated to the polymer glass transition temperature (156.9˚C ± 12.8 for VP85, 164.8˚C ± 3.7 for VP90, and 170.9˚C ± 5.6 for VP95) for 60 minutes. The xerogels were compressed at 100 MPa while the temperature was held on the samples during loading for 60 minutes (refer to Chapter 3.11). A 60-minute heating phase was necessary in order to ensure the entire specimen had attained its T_g prior to compression, otherwise, material fragmentation would inevitably occur. However, a prolonged heating phase would result in excessive oxidation of the polymer, with the resulting xerogel becoming discoloured and brittle. After heating, the xerogels were allowed to cool to room temperature. The deformation ratio of the anisotropic gel ($C = l_0/l$) is equal to 1.5.

The final form of the anisotropic hydrogel is a gel that will restore most of its geometry once swelled. Force was stored within the hydrogel in the axis of compression, and this would create an anisotropic swelling behaviour where swelling direction could be controlled [109]. The ability to control the direction of swelling makes anisotropic hydrogel suitable for biomedical applications. The microarchitecture of anisotropic hydrogels was observed, and it is shown in Figure 4.44. The oriented network structure slightly changes induced by mechanical anisotropy. The sponge-like structure of anisotropic hydrogels is more elongated than isotropic gels. The elongated structure can be measured from the aspect ratio (length to diameter ratio). It shows that the aspect ratio of the anisotropic hydrogels is higher than isotropic gels (Table 4.22). The volume space of the interconnected-wall network structure is deeper than isotropic gels. These findings suggest that there is a permanent structural change when the hydrogels are modified from isotropic to anisotropic models. This change is due to the alignments of polymer chains that occurred during compression near the glass transition temperature (T_g).

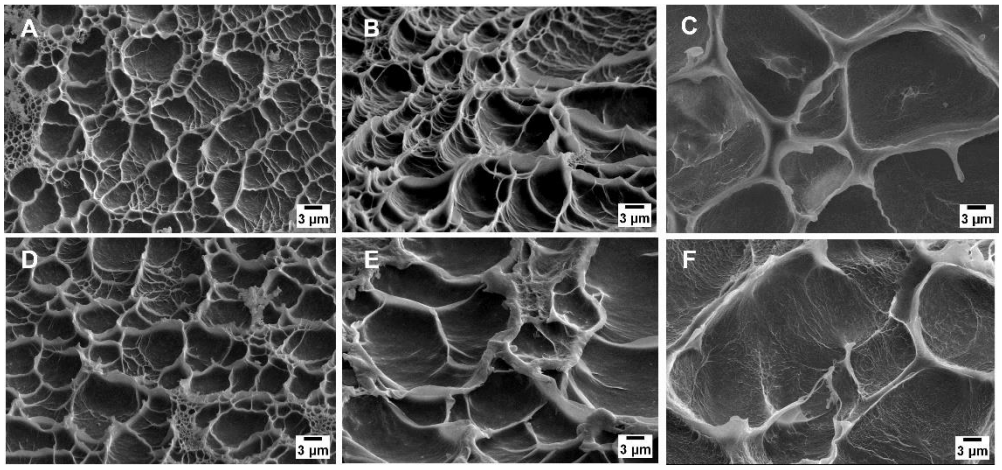


Figure 4.44 SEM image of freeze-dried VP/MMA swollen gels (A-C) Isotropic and (D) Anisotropic at composition ratios of (A, D) VP85 (B, E) VP90 (C, F) VP95 at a magnification of 2000x

Table 4.22 Length to diameter ratios of isotropic and anisotropic polymer structure at various VP/MMA compositions

Conditions	Composition	Aspect Ratio (Length/Diameter)
Isotropic	VP85	1.15 ± 0.10
	VP90	1.20 ± 0.11
	VP95	1.24 ± 0.13
Anisotropic	VP85	1.21 ± 0.18
	VP90	1.34 ± 0.17
	VP95	1.68 ± 0.48

The pore size and pore area of anisotropic gels were analyzed using ImageJ processing software. Table 4.23 shows the pore size, area, and volume of isotropic and anisotropic hydrogels at various VP/MMA compositions. The pore sizes of isotropic and anisotropic VP95 hydrogels are 27.5 ± 4.4 μm and 29.2 ± 4.5 μm respectively. In addition, the pore areas of isotropic and anisotropic VP95 hydrogels are 328.5 ± 78.9 μm^2 and 349.9 ± 53.6 μm^2, respectively. By assuming the volume of the hemisphere ($V=\frac{2}{3}\pi r^3$), the pore volume of hydrogel was calculated. The pore volumes of isotropic and anisotropic VP95 hydrogels are 4816.9 ± 1554.2 μm^3 and 5056.3 ± 1425.2 μm^3, respectively. From these results, the anisotropic and isotropic hydrogels are showing little difference in the porous structure. However, the anisotropic hydrogels have a slightly bigger pore size compared with isotropic gels. By comparing various VP compositions, the isotropic VP85 hydrogel shows a smaller pore size (13.3 ± 1.7 μm), pore area (57.7 ± 12.3 μm^2), and pore volume (676.9 ± 253.1 μm^3) among other samples. In both isotropic and anisotropic VP85 gels, the network structure is more

compact and denser. However, increasing VP concentration leads to a greater porous structure. The significant improvement in the pore size, area, and volume of anisotropic VP90 hydrogels are 20.9 ± 6.1 µm, 117.6 ± 46.0 μm^2, and 2665.2 ± 853.4 μm^3, respectively.

Table 4.23 Pore size, area, and volume of isotropic and anisotropic VP/MMA hydrogels at various composition ratios

Conditions	**Composition**	**Pore Size (µm)**	**Pore Area (μm^2)**	**Pore Volume (μm^3)**
Isotropic	VP85	13.3 ± 1.7	57.7 ± 12.3	676.9 ± 253.1
	VP90	19.1 ± 3.7	111.8 ± 28.2	2482.8 ± 964.9
	VP95	27.5 ± 4.4	328.5 ± 78.9	4816.9 ± 1554.2
Anisotropic	VP85	14.0 ± 1.3	58.5 ± 8.8	685.2 ± 213.1
	VP90	20.9 ± 6.1	117.6 ± 46.0	2665.2 ± 853.4
	VP95	29.2 ± 4.5	349.9 ± 53.6	5056.3 ± 1425.2

4.5.1 Volume Swelling and Swelling Kinetic of Anisotropic Gels

4.5.1.1 Effect of Chemical Composition on the Swelling of Anisotropic Gels

The swelling behaviour of anisotropic hydrogel was studied by investigating the volume swelling and length swelling ratios. The size of hydrogel used in this study is 3mmD and 3mmL in the condition before compression and 4mmD & 1.5mmL in the condition after compression. The effect of composition on the anisotropic hydrogels was also investigated. Figure 4.45 shows the volume swelling ratios of isotropic and anisotropic hydrogels at various VP composition ratios plotted as a function of time.

There is little difference between the volume swelling ratio for isotropic and anisotropic hydrogels of equivalent VP concentration. It is also confirmed by the microstructure result in Figure 4.44. The volume swelling ratio of anisotropic hydrogel has slightly greater compared with the isotropic hydrogels. The bigger pore volume provides more space to let the water fill the network structure of the VP/MMA hydrogel system. The isotropic gels could expand 2-2.5 times from its initial dimension. It swells in all directions, resulting in a significant increase in radius and length. The reason for a similar change in radius and length is due to the nature of the modulus of gel to maintain its shape in order to minimize the shear energy, resulting in isotropic swelling [280]. In contrast, the anisotropic hydrogels preferred swelling in one direction, hence the final volume swelling is only affected by length change. The anisotropic gel showed expansion up to 4-5 times in the direction parallel to the compression (y-direction).

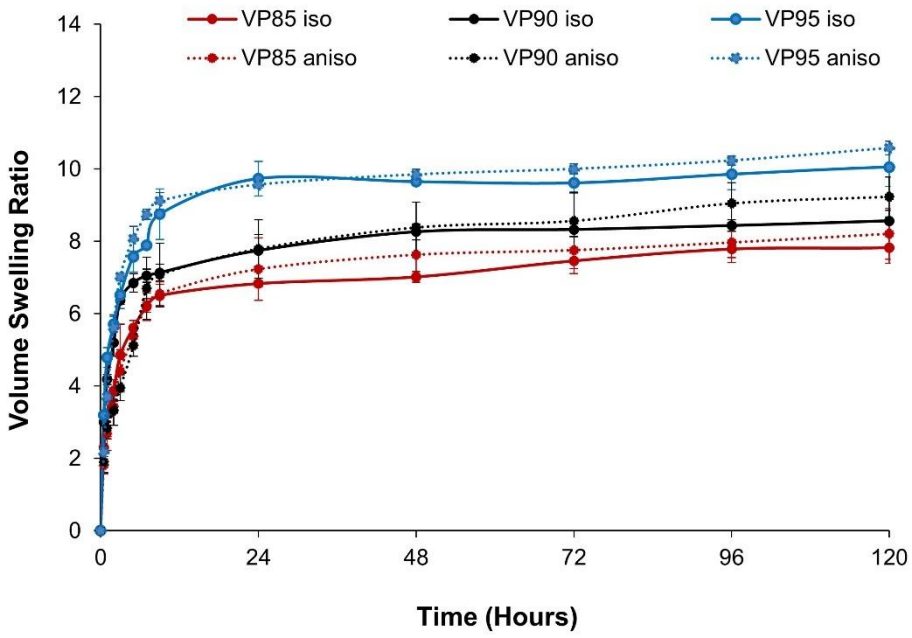


Figure 4.45 Volume swelling ratio of isotropic and anisotropic VP/MMA hydrogels at various composition ratios versus time

Figure 4.46 shows the length swelling ratio of isotropic and anisotropic hydrogels at various composition ratios as a function of time. The obvious length changes occurred in the anisotropic hydrogel, especially in the initial 24 hours. At equilibrium conditions, it shows that the length swelling ratio of anisotropic hydrogel is almost 4-fold greater than isotropic hydrogel. Previous works showed that the anisotropic hydrogels of 9:1 VP/MMA swollen up to 800% in height, but the diameter almost remained unchanged [108]. The hydrogels preferred swelling in parallel to the compression direction [109]. In this study, the VP/MMA hydrogels swell up to 315-392% in the length direction. It is smaller compared to the previous study due to the smaller hydrogel size used in this study.

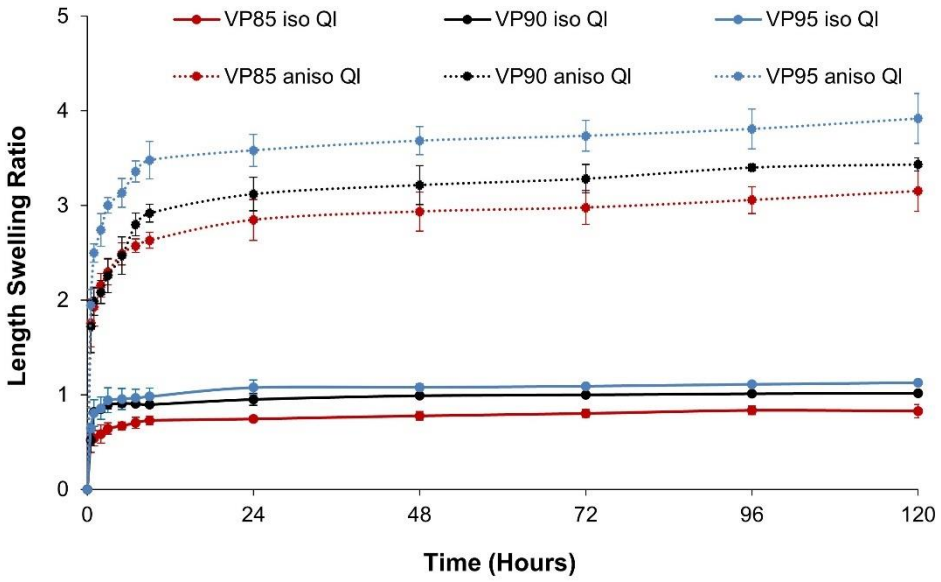


Figure 4.46 Length swelling ratio of isotropic and anisotropic VP/MMA gels at various composition ratios plotted as a function of time

Table 4.24 summarizes the equilibrium volume, length, and radius swelling ratio of isotropic and anisotropic VP/MMA hydrogels at various composition ratios. At equilibrium swelling conditions, the length swelling ratio of anisotropic hydrogel

is significantly increased compared with the isotropic hydrogel, however, it is noted that the change of the hydrogel radius is insignificant. The shape deformation of the anisotropic hydrogels mainly took place in length rather than radius. A nearly 315-392% of length increase is investigated, followed by a 49-54% expansion in the radius. The equilibrium volume swelling ratio of anisotropic hydrogels is a multiplication between the length and radius of the gels. Due to the decreasing radial expansion in anisotropic gels, the equilibrium volume swelling ratio is almost similar compared to the equivalent isotropic gels.

Table 4.24 Equilibrium volume, length, and radius swelling ratios of isotropic and anisotropic VP/MMA hydrogels at various composition ratios

Hydrogels	**Compositions**	**Volume Swelling Ratio**	**Length Swelling Ratio**	**Radius Swelling Ratio**
Isotropic	VP85	8.0 ± 0.3	0.9 ± 0.06	1.2 ± 0.04
	VP90	8.9 ± 0.5	1.0 ± 0.01	1.2 ± 0.06
	VP95	10.2 ± 0.3	1.1 ± 0.03	1.3 ± 0.03
Anisotropic	VP85	8.1 ± 0.3	2.6 ± 0.19	0.5 ± 0.01
	VP90	9.1 ± 0.6	3.4 ± 0.05	0.5 ± 0.05
	VP95	10.8 ± 0.4	3.9 ± 0.26	0.6 ± 0.02

Table 4.25 summarizes the diffusion exponent (n) and diffusion coefficient (D) of isotropic and anisotropic hydrogels at various composition ratios. The diffusion coefficient (D) and exponent (n) for each VP/MMA hydrogel were calculated from the linear portion of the swelling curves, taken only from the initial 60% increase in mass

swelling ratio. Both isotropic and anisotropic VP85 and VP90 hydrogels are categorised as having anomalous transport diffusion due to the n value being between $0.5 < n < 1$. This type of diffusion occurred when the diffusion rate of water (R_{diff}) and that of polymer chain relaxation (R_{relax}) are comparable ($R_{diff} \approx R_{relax}$) [264]. Both isotropic and anisotropic VP95 hydrogels demonstrate Fickian diffusion (n=0.5) which solvent sorption in this hydrogel is relatively fast due to rapid molecular relaxation, and therefore a diffusion-controlled process. In this condition, polymer chains will have higher mobility that allows for easier penetration of water [135]. For anisotropic hydrogel, the diffusion exponent (n) is lower than the isotropic gels due to a faster relaxation rate. The diffusion coefficient (D) of anisotropic hydrogel is slightly higher than the isotropic gel which means that the anisotropic gel generates a faster diffusion rate to reach the equilibrium expansion. This behaviour is expected since the bigger pore volume structure would increase the diffusion of water. It might be due to increasing expansion in one-direction (parallel to the compression direction).

Table 4.25 Diffusion exponent (n) and the diffusion coefficient (D) of isotropic and anisotropic hydrogels of various VP/MMA composition ratios

Hydrogels	**Compositions**	**n**	**Transport Type**	**D (cm^2/s)**
Isotropic	VP85	0.79	Anomalous	5.7×10^{-7}
	VP90	0.66	Anomalous	9.2×10^{-7}
	VP95	0.53	Anomalous	13.8×10^{-7}
Anisotropic	VP85	0.71	Anomalous	7.6×10^{-7}
	VP90	0.63	Anomalous	9.8×10^{-7}
	VP95	0.54	Anomalous	14.4×10^{-7}

4.5.1.2 Effect of Sizes on the Swelling of Anisotropic Gels

The variation of hydrogel sizes of the anisotropic hydrogel also gives significant contribution to the swelling behaviour. In this study, VP/MMA hydrogel with a composition ratio of 85:15wt% (VP85) was used to investigate the effect of hydrogel sizes on the swelling study. The sizes of the hydrogel before compression are listed in Table 4.12. Figure 4.47 shows the effect of various sizes of both isotropic and anisotropic hydrogels on the volume swelling ratio as a function of time. When the sizes are varied, water tends to occupy almost the same ratio of volume capacity. As the hydrogel reaches a similar ratio at equilibrium, it means the variation of hydrogel sizes will less contribute to the change of volume swelling ratio. There is little difference between the volume swelling ratio for isotropic and anisotropic hydrogels of equivalent VP/MMA composition (Table 4.24). Although soft and rubbery at T_g, the gels were slowly cooled to room temperature during which the polymer returned to its glassy state. The elastic stress stored during the cooling process is the main mechanism of anisotropic swelling. As this internal stress gets higher it is evident that the gel network, which is stretched in radial directions, is also permanently deformed in alignment with compression plates. This is why the anisotropic gels do not expand to the same volume swelling ratio.

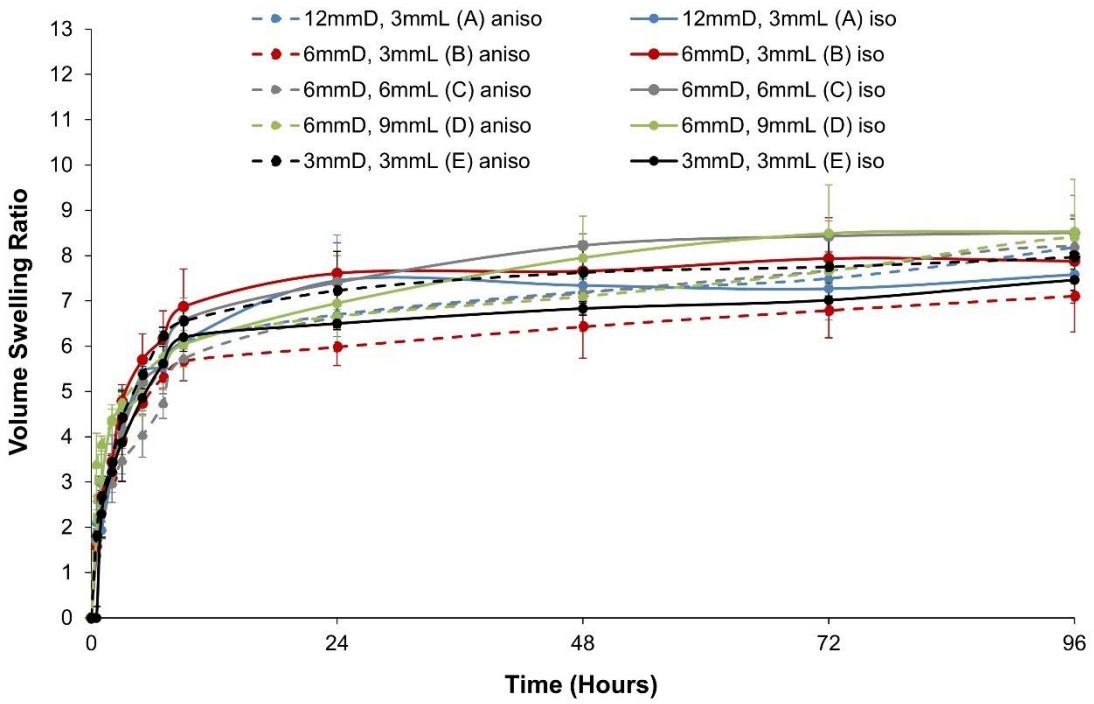


Figure 4.47 Volume swelling ratio of isotropic and anisotropic gels at various sizes as a function of time

The advantage of anisotropic gel is the ability to swell in a preferred direction. The length of the initial gel is thinner as a result of compression. According to Swan et al., the modification of the isotropic gel through compression under heat treatment will create a device that can ideally expand in one direction, increasing the swelling in one dimension from 3 times to 15 times in length [109]. Figure 4.48 shows the length swelling ratio of both isotropic and anisotropic gels at various sizes as a function of time. The anisotropic gels swell up to 305-369% in length while the radius can only expand about half of their original size (Table 4.26). The isotropic gels show the expansion in all directions most significantly in the radius direction while the length only shows expansion up to 76-104%.

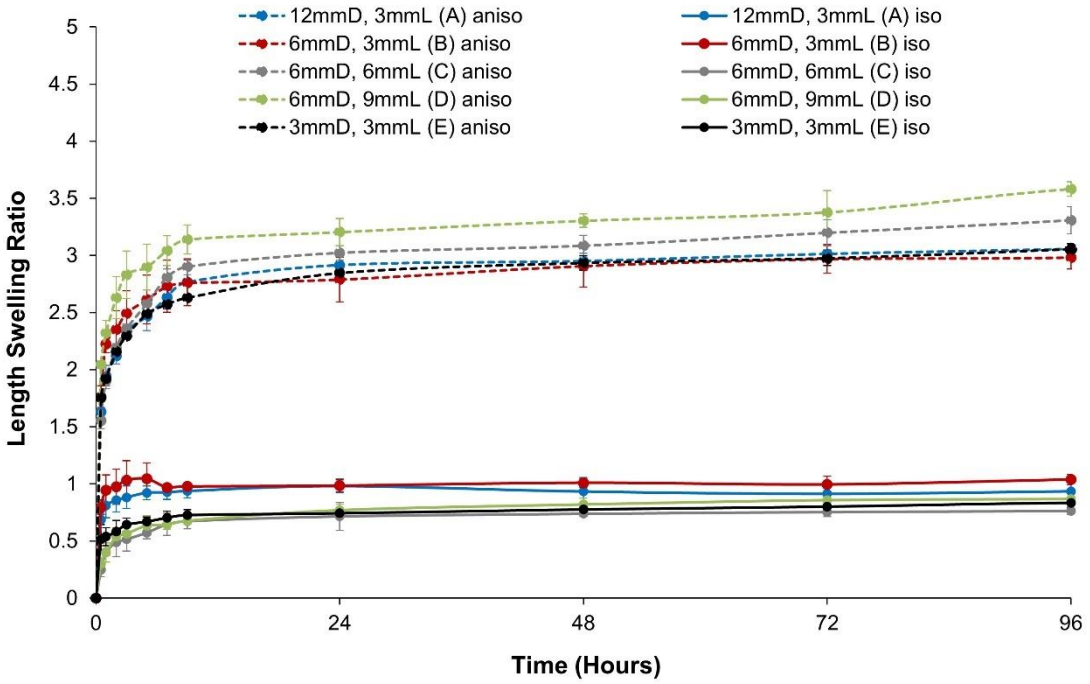


Figure 4.48 Length swelling ratio of isotropic and anisotropic hydrogels at various hydrogel sizes against time

Table 4.26 Equilibrium volume, length, and radius swelling ratio of isotropic and anisotropic gels at various sizes

Hydrogels	**Sizes**	**Volume Swelling Ratio**	**Length Swelling Ratio**	**Radius Swelling Ratio**
Isotropic	12mmD, 3mmL (A)	7.6 ± 0.2	0.9 ± 0.08	1.1 ± 0.02
	6mmD, 3mmL (B)	7.9 ± 0.9	1.0 ± 0.05	1.1 ± 0.16
	6mmD, 6mmL (C)	8.5 ± 0.4	0.8 ± 0.03	1.3 ± 0.03
	6mmD, 9mmL (D)	8.5 ± 1.2	0.9 ± 0.01	0.9 ± 0.47
	3mmD, 3mmL (E)	7.8 ± 0.2	0.8 ± 0.05	1.2 ± 0.01

Anisotropic	12mmD, 3mmL (A)	8.2 ± 1.1	3.1 ± 0.11	0.5 ± 0.08
	6mmD, 3mmL (B)	7.4 ± 1.1	3.1 ± 0.16	0.4 ± 0.07
	6mmD, 6mmL (C)	8.2 ± 0.6	3.3 ± 0.11	0.5 ± 0.03
	6mmD, 9mmL (D)	8.5 ± 0.2	3.7 ± 0.12	0.4 ± 0.03
	3mmD, 3mmL (E)	7.9 ± 0.6	3.1 ± 0.14	0.5 ± 0.02

By comparing the water uptake between the isotropic and anisotropic hydrogels, the diffusion exponent (n) and diffusion coefficient (D) of hydrogels are investigated. The diffusion exponent (n) for each VP/MMA hydrogel was calculated from the linear portion of the swelling curves, taken only from the initial 60% increase in mass swelling ratio. Both isotropic and anisotropic hydrogels at various sizes are showing characteristics of anomalous diffusion that occurs in the transition region between cases I and II when the diffusion and relaxation rates are comparable. However, both isotropic and anisotropic gels with a bigger volume (12mmD, 3mmL) is showing the characteristic of case II transport (n=1). The characteristic of case II diffusion whereby diffusion is very rapid compared with the relaxation process ($R_{diff} > R_{relax}$) and macromolecular relaxation governs penetrant transport [271].

The diffusion coefficients (D) of both isotropic and anisotropic VP85 hydrogels at various sizes were calculated using Equation 2.7 and D values can be summarized in Table 4.27. The largest volume of hydrogel produces a higher diffusion coefficient value. As the diffusion is very rapid at the initial stage (n=1, case II transport), it significantly affects the diffusion coefficient (D). The hydrogel with the same diameter shows almost the same diffusion coefficient value. It indicates that variation of diameter gives less contribution to the diffusion of the hydrogel. The

decrease in the D value is believed to be a result of a decrease in the hydrogel volume. The diffusion coefficient (D) of anisotropic gel is slightly higher than that of isotropic gels which means that the anisotropic gel generates a faster diffusion rate to reach the equilibrium expansion.

Table 4.27 Diffusion exponent, type of diffusion, and diffusion coefficient of isotropic and anisotropic gels at various sizes

Conditions	**Sizes**	**n**	**Transport Type**	**D (cm^2/s)**
Isotropic	12mmD, 3mmL (A)	1.00	Case II	5.7×10^{-6}
	6mmD, 3mmL (B)	0.90	Anomalous	1.9×10^{-6}
	6mmD, 6mmL (C)	0.96	Anomalous	1.5×10^{-6}
	6mmD, 9mmL (D)	0.96	Anomalous	1.7×10^{-6}
	3mmD, 3mmL (E)	0.79	Anomalous	0.6×10^{-6}
Anisotropic	12mmD, 3mmL (A)	1.00	Case II	5.9×10^{-6}
	6mmD, 3mmL (B)	0.93	Anomalous	2.1×10^{-6}
	6mmD, 6mmL (C)	0.97	Anomalous	1.6×10^{-6}
	6mmD, 9mmL (D)	0.95	Anomalous	1.7×10^{-6}
	3mmD, 3mmL (E)	0.71	Anomalous	0.8×10^{-6}

4.5.2. Swelling Force and Swelling Pressure of Anisotropic Gels

When anisotropic gel swells, the swelling behaviour is observed until it reaches an equilibrium swelling. It is possible that the swelling of anisotropic gel is the result of the restoring the relaxation of the polymer chain after being compressed in the y-

direction to attain the shape memory property and isotropic swelling process which is due to the swelling pressure contributed by the osmotic pressure and the elastic retraction force. Figure 4.49 shows the swelling force of isotropic and anisotropic hydrogels at various composition ratios as a function of time. The VP/MMA with a lower VP concentration (VP85) has a greater swelling force. The swelling force recorded from anisotropic hydrogel is higher compared to isotropic gels. The swelling force of anisotropic gel is between 9.4-18.3 N. The increasing of the swelling force in the compressed gel is due to force relaxation and the stored force is restored during swelling.

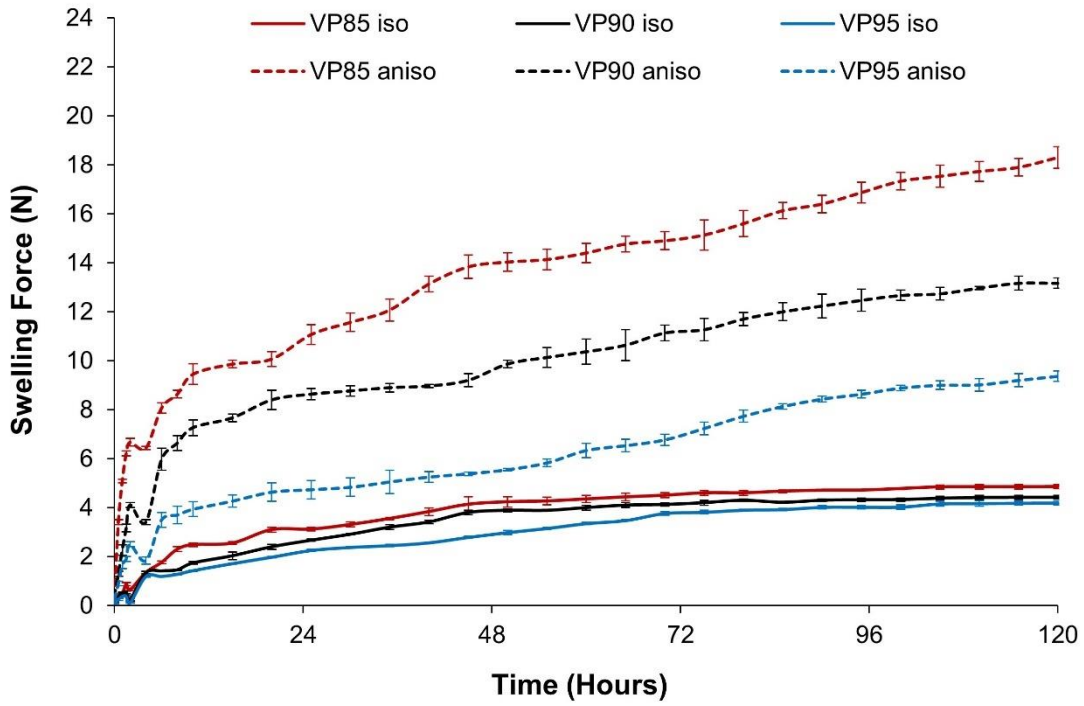


Figure 4.49 Swelling force of isotropic and anisotropic hydrogels of various composition ratios as a function of time

The swelling pressure can be calculated using Equation 4.16. As the hydrogel is being constrained by the compression plate, therefore swelling in the axial direction

would be limited and the length remains unchanged. Figure 4.50 shows the swelling pressure of both isotropic and anisotropic hydrogels at various composition ratios as a function of time. Similar to previous swelling force and swelling pressure results in Chapter 4.4, the hydrogel with less VP concentration (VP85) would effectively generate swelling pressure compared to hydrogel with more VP concentration (VP95). It shows that the swelling pressure of VP85 anisotropic gel reaches maximum values of 133.8 kPa which is almost 2-fold higher than isotropic gel (Table 4.28). This pressure is not recommended to apply for *in vivo* study due to the pressure exceeding the total maximum stress of the small intestine (Chapter 5). It might damage the tissue, thus resulting in tissue necrosis.

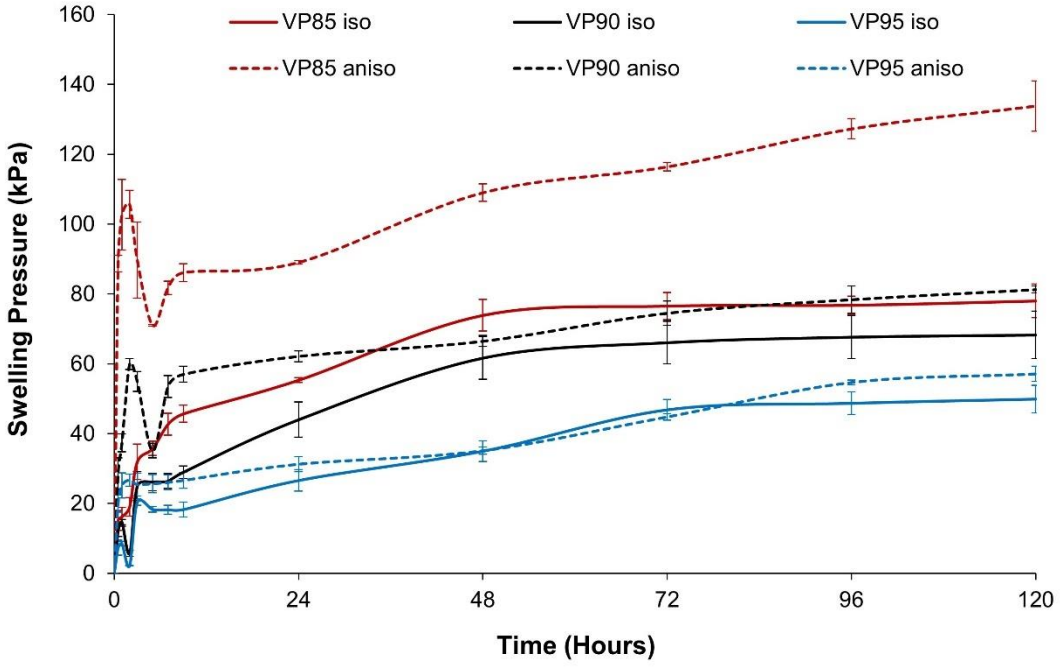


Figure 4.50 Swelling pressure of isotropic and anisotropic VP/MMA hydrogels of various composition ratios swelled as a function of time

Table 4.28 Maximum swelling force and swelling pressure at 120 hours for both isotropic and anisotropic hydrogels at various composition

Condition	Composition Ratio	Swelling Force (N)	Swelling Pressure (kPa)
Isotropic	VP85	4.9 ± 0.08	77.9 ± 4.8
	VP90	4.4 ± 0.07	68.3 ± 6.8
	VP95	4.2 ± 0.09	49.9 ± 3.9
Anisotropic	VP85	18.3 ± 0.44	133.8 ± 7.2
	VP90	13.2 ± 0.21	81.3 ± 1.0
	VP95	9.4 ± 0.21	57.1 ± 2.2

Figures 4.51 & 4.52 show the swelling force and swelling pressure of both isotropic and anisotropic hydrogels at varied sizes as a function of time. Modifying the sizes and processing conditions significantly affects the swelling force and pressure values. There is a linear increase in swelling force with increasing surface area and/or volume of the hydrogels, as previously explained in Chapter 4.4. However, the swelling pressure and surface area are showing an inverse relationship ($P = \frac{F}{A}$). The gels with the same area and diameter would generate almost similar swelling force and pressure values although the length of the hydrogel is varied. The anisotropic gels demonstrate a higher swelling force and pressure compared to isotropic gels. The compression process in initial structural anisotropy results in a larger swelling pressure. The swelling pressure changes start with a quick increase followed by a peak value, a decrease, and finally a slight increase or stabilisation. The swelling pressure of anisotropic gel is in the range of 36.9-133.8 kPa (Table 4.29).

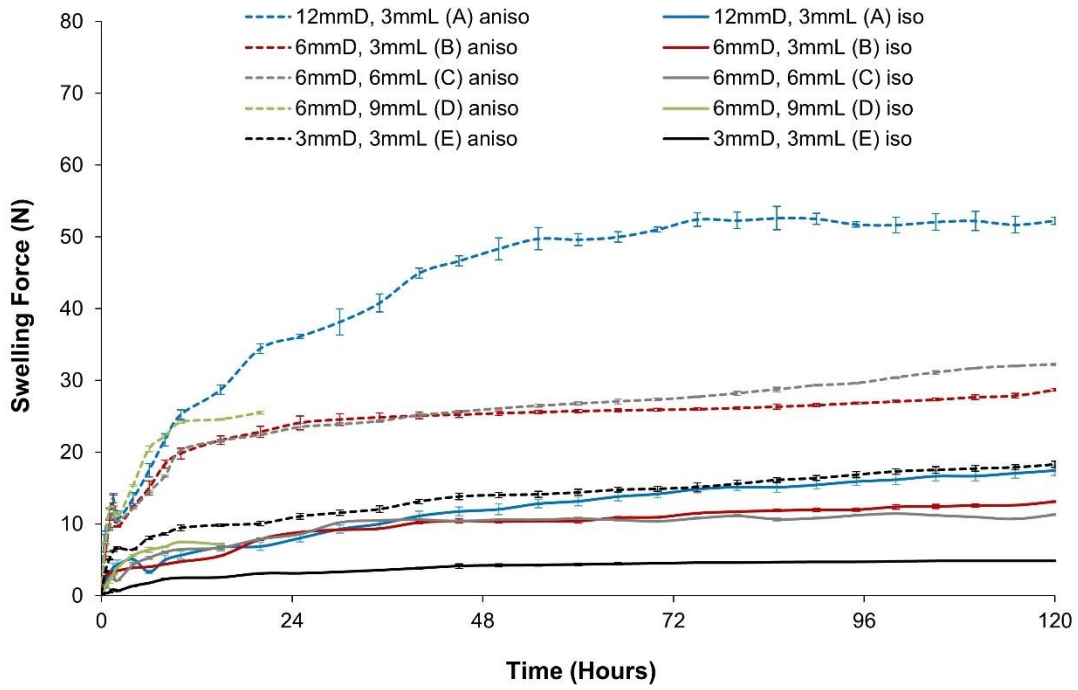


Figure 4.51 Swelling force of isotropic and anisotropic hydrogels at various sizes plotted as a function of time

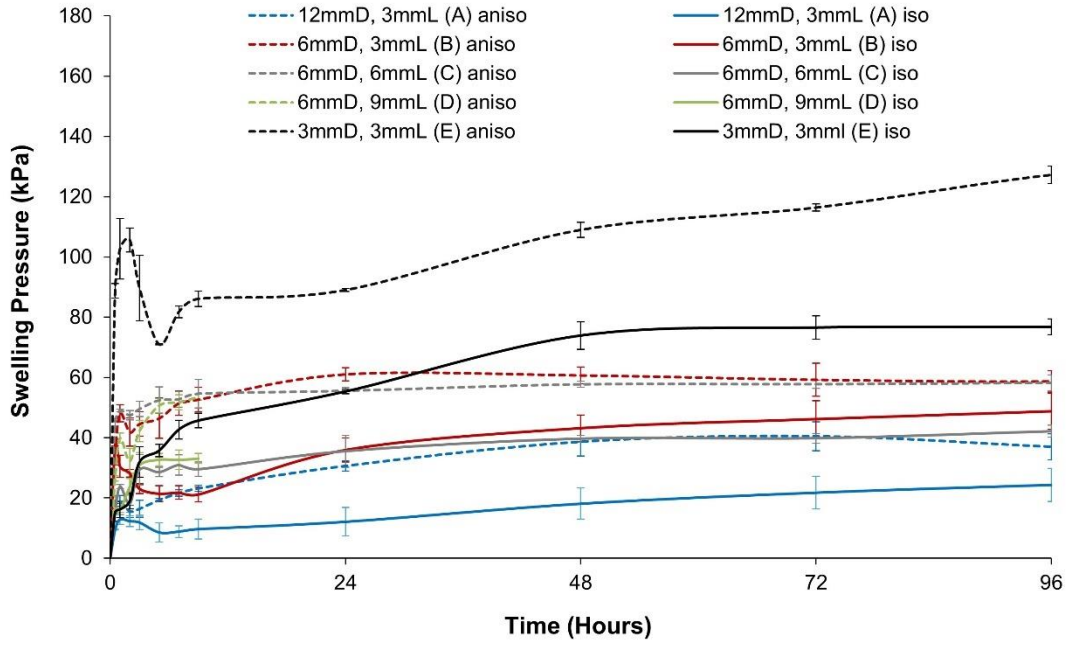


Figure 4.52 Swelling pressure of isotropic and anisotropic VP/MMA hydrogels at various sizes as a function of time

Table 4.29 Maximum swelling force and swelling pressure of isotropic and anisotropic hydrogels at various sizes

Condition	Size	Swelling Force (N)	Swelling Pressure (kPa)
Isotropic	12mmD, 3mmL (A)	15.9 ± 0.6	24.3 ± 5.4
	6mmD, 3mmL (B)	11.9 ± 0.2	48.8 ± 6.0
	6mmD, 6mmL (C)	11.2 ± 0.1	42.1 ± 2.0
	6mmD, 9mmL (D)*	N/A	N/A
	3mmD, 3mmL (E)	4.7 ± 0.1	76.8 ± 4.8
Anisotropic	12mmD, 3mmL (A)	51.7 ± 0.4	36.9 ± 4.3
	6mmD, 3mmL (B)	26.8 ± 0.2	58.7 ± 3.6
	6mmD, 6mmL (C)	29.6 ± 0.1	58.2 ± 2.6
	6mmD, 9mmL (D)*	N/A	N/A
	3mmD, 3mmL (E)	18.3 ± 0.4	133.8 ± 7.2

*Hydrogel sample buckled

4.6 Summary

The different compositions of VP/MMA hydrogel as a self-inflating tissue expander were used in the range of 85-95wt% VP. The swelling ratios were decreased, and the elastic moduli were increased for gels with more MMA composition. The decrease in swelling ratio is due to more hydrophobic groups which can decrease the absorption of solvent. The hydrophobicity of MMA had been proven from the water contact angle results (θ>65˚). When the surface is more hydrophobic, the work of adhesion and the interfacial tension properties are lower. The low interfacial tension

property would reduce the tendency of proteins in body fluid to absorb and unfold upon absorption. The hydrogel with more MMA composition produces phase separation during synthesis resulting in a microstructural change in the hydrogel. The pore size decreased but the number of interconnected pores increased. The network structure is more compact due to increasing the effective-crosslinking population. The rigid network structure could contribute to the improvement of mechanical properties The swelling force and swelling pressure of hydrogels were measured in the hydrogel of different compositions. The results showed that the hydrogel with more MMA composition and higher modulus elasticity would generate more swelling force and pressure than gel with more VP content. The gel elasticity and network structure are two important parameters in force generation. In this study, the swelling pressure is a crucial feature in the hydrogel, and it should be sufficient to stretch the intestine while not causing tissue obstruction.

The hydrogels were also designed in different sizes (12mmD, 6mmD, and 3mmD). The volume swelling ratio of hydrogels at equilibrium showed similar swelling capacity when the hydrogel with the same length is introduced. The hydrogels with a longer length (6mmD & 9mmL) showed a slightly higher equilibrium swelling ratio. This is due to the extension of the end deformation in the y-direction scales with the length of the hydrogel. The modulus elasticity of the hydrogels at various sizes was measured. It showed that the elastic modulus was not significantly changed with a variation of sizes. The swelling force and pressure of hydrogels were also measured in different sizes. The increasing initial surface area of the hydrogel provided a significant contribution to the swelling force generation. However, the swelling pressure decreased as the initial surface area increased. Designing hydrogels with the

same surface area generated similar swelling pressure, although the diameter and height were varied. The hydrogel with the smallest size (3mmD & 3mmL) was chosen in this study for *ex vivo* and *in vivo* studies. The hydrogel could produce the highest swelling pressure (77.9 kPa) and that pressure is important to be able to stretch the intestine.

The anisotropic hydrogels were manufactured by heat treatment and compression. The hydrogels were heated at the glass transition temperature (T_g) which was obtained from the DSC measurement. The volume swelling ratio of anisotropic hydrogel was slightly higher than isotropic gels. The anisotropic gels swelled significantly in length compared to isotropic gels. The swelling pressure of the anisotropic hydrogel was measured which showed larger force generation due to force relaxation and the stored force was restored during swelling. The hydrogel with more MMA concentration would effectively generate swelling pressure. The maximum swelling pressure of 85wt% VP was 133.8 kPa which was almost 2-fold higher than isotropic hydrogel. This pressure was found too big for *in vivo* study due to it exceeding the maximum stress of the small intestine (it will be discussed later in Chapter 5).

Chapter 5: Properties of GI Tract Tissues and Intestinal Lengthening Studies

5.1 Introduction

A primary objective of this research is the applicability of VP/MMA hydrogel self-inflating tissue expander to lengthen and naturally grow the intestine tissue. In order to determine device efficacy *in vivo*, a suitable animal model was required. The Sprague-Dawley (SD) rat was chosen as the animal model for this study. It was chosen based on several criteria such as it is most widely used for biomedical research [281], [282]; their anatomical, physiological and genetic similarity to humans; there is considerable expertise at Taipei Medical University in the management of rats; a rat is relatively cheap to purchase and to maintain. In this study, a male rat was chosen. The gastrointestinal tract tissues such as esophagus, stomach, small intestine, and large intestine were taken in order to study the biomechanical tensile properties of the tissues, the morphology of tissues was also observed to investigate the major structural component that constitutes the tissues, and finally, the effectiveness of the swelling pressure generated from hydrogel tissue expander was investigated through *ex vivo* and *in vivo* studies whether it can successfully lengthen the intestine.

5.2 Mechanical Properties of GI Tract

The mechanical properties of GI tracts (*e.g.*, esophagus, stomach, small, and large intestine) are important to study to understand their physiology and function, as well as their ability to withstand deformation. The mechanical properties of GI tract tissues show properties of both elastic solid and viscous fluid (viscoelastic). A typical stress-strain curve of the tissue generated from the mechanical test is non-linear. The tissue is behaving as an elastomer, with a characteristic initial ‘toe region’ related to uncrimping of the collagen fibres as the stress is applied. The failure point normally

resulted from sample rupture. The maximum stress-strain value can be used as a reference value to choose a design of the hydrogel as a self-inflating tissue expander. In this study, the mechanical properties of the Sprague Dawley (SD) rat's esophagus, stomach, small, and large intestine were examined uniaxially. Due to the anisotropic properties of the tissue, the tissues should consider the stress in the longitudinal (axial) and circumferential (hoop) directions. Figures 5.1-5.4 show the stress-strain behaviour of the GI tract samples. The maximum stress and strain values of each sample are summarised in Table 5.1. For all specimens, curves with one maximum are generated in both directions, the longitudinal specimen produces higher maximum stress than in the circumferential direction, however it could not withstand intensive deformation for a long duration.

The esophagus is an important part of the GI tract that performs the function of transferring food bolus from the pharynx to the stomach. A study analysing the strain and the stress borne by the rat esophagus (in which the esophagus has been taken as a homogeneous layer) has been conducted. Results depict the maximum stress of 0.7 MPa and maximum strain of 58% of the esophagus tested in the longitudinal direction. The Young's modulus of the rat esophagus is calculated to be 1.7 ± 0.3 MPa (Table 5.1). The esophagus is the stiffest among other organs. Compared to the human esophagus, the mechanical property of the rat esophagus is significantly lower. It had been reported that the maximum stress and strain of the human esophagus are 1.3 MPa and 57.7%, respectively [169]. The circumferential sample of the esophagus fails to perform the test due to a very short specimen causing difficulties to install the sample to the clamp.

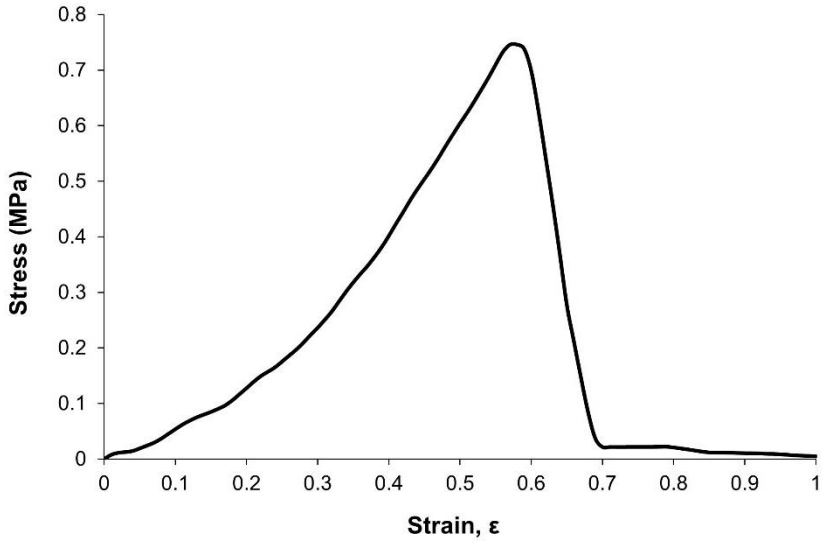


Figure 5.1 Stress-strain curve of rat longitudinal specimens of esophagus

The stomach is an expanded section of the digestive tube between the esophagus and the small intestine. The major functions of the stomach are storage reservoir, substantial chemical and enzymatic digestion particularly proteins, vigorous contraction of gastric smooth muscle, mixing and grinding food with gastric secretions and delivering the food into the small intestine for further digestion [283]. The stomach has a complex geometry and is mechanically anisotropic. In this study, the mechanical properties of the stomach at different cutting directions were examined and the uniaxial stress-strain relationship of the stomach tissues is shown in Figure 5.2. The stress-strain curve differed between the specimen obtained in different directions. In the longitudinal specimen, the maximum stress and strain are reported to be 63.9 kPa and 63%, respectively (Table 5.1). In the circumferential specimen, the maximum stress and strain are 31.9 kPa and 202%, respectively. The elastic moduli of longitudinal and circumferential rat stomachs are 196 kPa and 25.7 kPa, respectively (Table 5.1). According to Murtada et al. [284], the orientation of smooth muscle myofilaments had a strong influence on the mechanical properties of the stomach. The mechanical testing

result of human axial and transversal stomachs was estimated at 0.6 MPa and 0.5 MPa for maximum stress values and 90.5% and 99.6% for destructive strain values, respectively [169]. The mechanical properties of the porcine stomach at different orientations and locations were also investigated [190]. The results showed that at smaller curvatures the longitudinal and circumferential samples had maximum stress and strain of 72.8 kPa and 238% as well as 36.5 kPa and 885%. At the greater curvature, the maximum stress and strain values were almost similar to the smaller curvature. Comparing with the values obtained from the human and porcine stomachs, it clearly shows that the strain of rat stomach is in between both values. The rat stomach functions largely as a food reservoir and is usually never empty, hence it is more stretched than that of the human stomach.

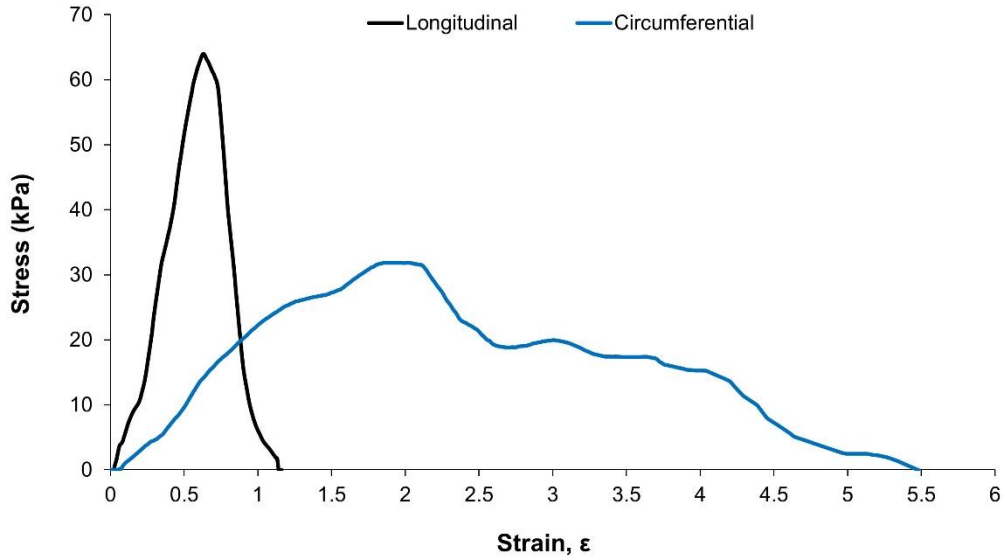


Figure 5.2 Stress-strain curves of rat longitudinal and circumferential specimens of stomach

The small intestine has the function to transport, digest, and absorb nutrients [285]. It comprises the duodenum, jejunum, and ileum. To understand the small

intestine's mechanical behaviour, it is necessary to know the stress-strain distribution of the tissues. The stress-strain distributions of the small intestine in the longitudinal and circumferential directions are shown in Figure 5.3. The maximum stress and strain values of the longitudinal small intestine are 78.9 kPa and 26%, respectively (Table 5.1). However, the stress and strain in the circumferential direction are 27.5 kPa and 147%, respectively. The compressive modulus of the longitudinal and circumferential small intestine samples is estimated at 525.4 kPa and 33 kPa, respectively. The longitudinal specimen firstly began to fracture, and the required stress is about twice as much as the circumferential direction, while the strain in the longitudinal direction is smaller than that of the circumferential specimen. These results indicate that the small intestine tissue could be resistant to tensile deformation in the circumferential direction. The longitudinal stress of the small intestine tissue is parallel to the direction of collagen fibres, hence the maximum stress and stiffness in the longitudinal direction are higher than that in the circumferential direction under the same strain.

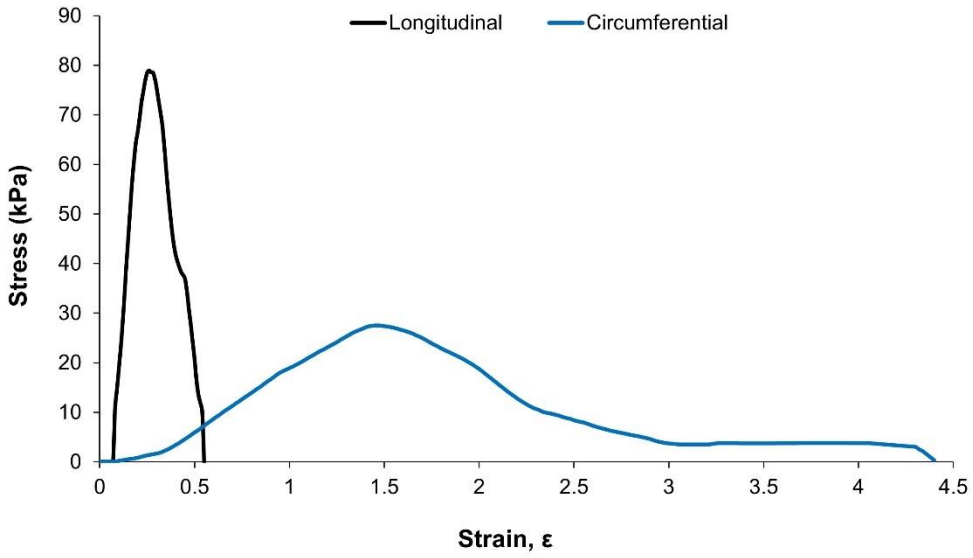


Figure 5.3 Stress-strain curves of rat longitudinal and circumferential specimens of the small intestine

The large intestine receives liquid chyme from the terminal ileum [208]. Water is gradually absorbed from the chyme along the length of the large bowel and the chyme turns into a more solid faecal mass. The faeces enter the rectum after storage in the distal colon and are evacuated whenever convenient. The distribution of stress-strain along the large intestine of the rats in different orientations is shown in Figure 5.4. Longitudinal stress is significantly greater than stress in circumferential direction, indicate of wall stiffening in the longitudinal direction. It is reported that the maximum stress and strain for the longitudinal large intestine are 50.6 kPa and 32%, respectively, and 31.3 kPa and 183% for circumferential direction, respectively (Table 5.1). The compressive modulus for both longitudinal and circumferential directions are 169 kPa and 28.7 kPa, respectively. The increased circumferential compliance reflects the function of the large intestine, that is storage and propagation of faeces, whereas the higher longitudinal stiffness helps to keep the intestinal intact.

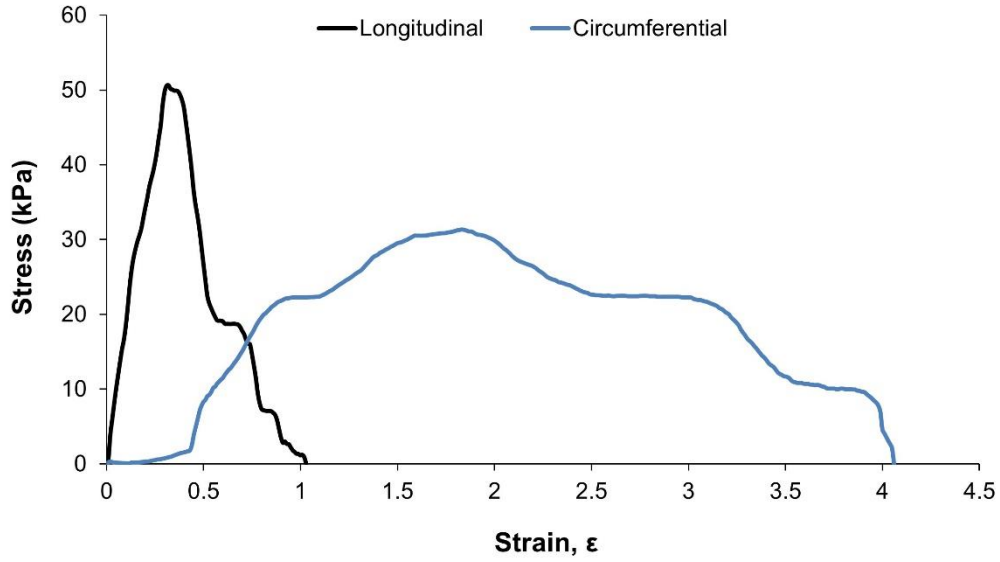


Figure 5.4 Stress-strain curves of rat longitudinal and circumferential large intestine specimens

The elastic modulus of the GI tract tissues is obtained from the linear region of the stress-strain curve. The longitudinal and circumferential stresses and the increment elastic modulus as a function of strain are exponential by nature. The greater elasticity in the circumferential direction compared to the longitudinal direction is uniquely suited to the physiological function of the GI tract tissues which necessitates changes in diameter rather than length during bolus transport. In this study, the stiffest organ among other tissues is the longitudinal esophagus. The mechanical properties of the esophagus are important to its function because the esophagus is subjected to changes in wall stress and strains caused by the passage of boli and the action of peristalsis. A stiffer esophagus might be important to prevent the esophageal wall from overstretching when the bolus pressure is higher than the normal level. The softer wall of the stomach could increase compliance and it is suitable to accommodate the large volume of the bolus that enters the stomach over a short time. Similarly, the muscle contraction and antral peristalsis knead and mix solid or liquid food within the stomach, and the contraction provides the force required to move the food into the bowels at a controlled rate. The mechanical properties of the small intestine are affected by the contribution of the longitudinal and circular muscle layers. They play an important role in the digestion and absorption of nutrients. The circumferential muscle layer promotes the mixing of the content, in contrast, the longitudinal muscle layer mainly produces forward transit with relatively little mixing. The large intestine has two major functions such as extraction of water and electrolytes from the fluid contents of the lumen and control of defecation. The large intestinal wall is much more elastic than the small intestine. The stiffness of the intestine is related to the collagen content as well as the size and arrangement of collagen fibers. It had been reported that

collagen content in the human large bowel is smaller compared to the small bowel [203], [207]. An increase in the amount of elastin in the large intestine would therefore increase the distensibility of the bowel wall [286].

Table 5.1 Stress-strain parameters of various GI tissues in longitudinal and circumferential directions

Specimen	Tissues	Strain	Maximum Stress	Young's Modulus
Longitudinal	Esophagus	58%	0.7 ± 0.1 MPa	1.7 ± 0.3 MPa
	Stomach	63%	63.9 ± 18.7 kPa	196.0 ± 24.2 kPa
	Small intestine	26%	78.9 ± 18.8 kPa	525.4 ± 58.6 kPa
	Large intestine	32%	50.6 ± 12.4 kPa	169.0 ± 29.2 kPa
Circumferential	Stomach	202%	31.9 ± 9.6 kPa	25.7 ± 6.3 kPa
	Small intestine	147%	27.5 ± 7.1 kPa	33.0 ± 4.6 kPa
	Large intestine	183%	31.3 ± 8.1 kPa	28.7 ± 7.1 kPa

5.3 Morphology of GI Tract Tissues

The wall of the GI tract is composed of four layers such as mucosa, submucosa, muscle, and serosa layers [157]. Each layer of the GI tract is highly specialized and endowed with characteristic mechanical properties. The submucosa is a layer of dense connective tissue positioned between the interior mucosa and the exterior muscle layers. It gives mechanical strength and structural integrity to the GI tract wall and thereby acts as the skeleton. The major structure of the submucosa is type-I (70-80%) and type-III collagen (20-30%) [161]. It has been suggested that type-I and type-III

collagens form separate networks of large and small fibres [287]. It is unlikely that elastin plays a significant role in the mechanical properties of the GI tract due to the amount of elastin being a very small percentage of the weight compared to collagen [288], [289].

Figure 5.5 shows the morphology of the esophagus, stomach, small, and large intestine tissues. SEM images show the arrangement of collagen fibre bundles of different tissues. The fibres show a three-dimensional wavy array and crimped pattern. The wavy structure pattern is due to the helical of the individual fibres. During the normal peristaltic activity of the intestine, the waviness of the collagen fibres acts as an elastic sleeve for smooth muscle contractions. The mark of the collagen fiber bundle and collagen fibril is shown in Figure 5.6. The diameter of the collagen fiber and fibril was analyzed using image-J software. The collagen fiber diameter of esophagus, stomach, small, and large intestines are 6.2 µm, 4.1 µm, 4.4 µm, and 3.9 µm, respectively (Figure 5.7 A). At higher magnifications, it shows that the large fibres are enmeshed in a fine network of small randomly oriented fibres. This network is composed mainly of a single fibril and/or thin bundles of a few fibrils. The collagen fibril diameter of esophagus, stomach, small, and large intestines are 62.7 nm, 47.3 nm, 54.1 nm, and 45.8 nm, respectively (Figure 5.7 B). It had been reported that the collagen fibre diameter of the small intestine in 3-week-old rats was 4-5 µm [196], [198] and the small fibre (fibril) was about 0.2 µm in diameter [196], however, another study, reported that the bundles of collagen fibrils of 3-week-old rats intestine were about 50-80 nm in diameter [198], [290]. Large collagen fibres could provide strength and might be load-bearing, while the function of the fibrils might be to hold the large fibres together in different layers and transfer stresses from one fibre to another. The small

fibre network may also have an important role in restoring the crimp pattern of the large fibres after they have undergone small deformations.

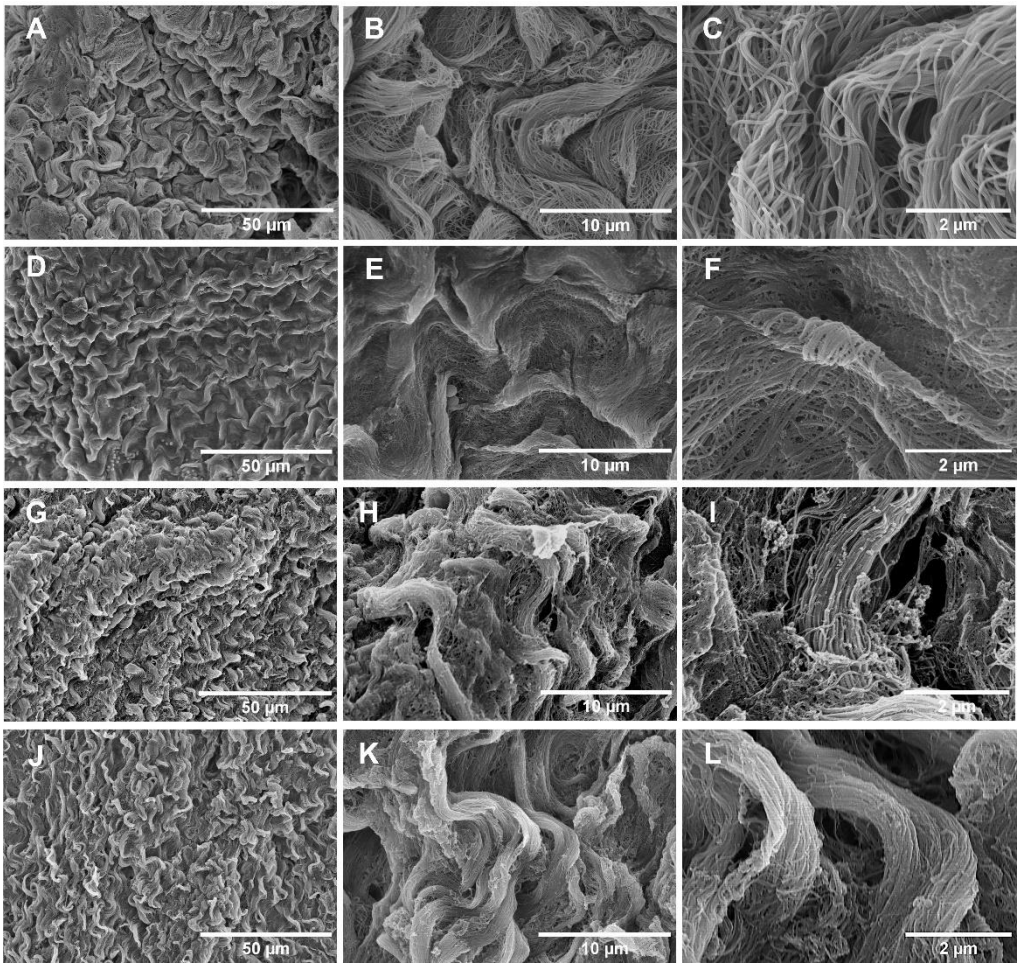


Figure 5.5 SEM images of GI tract tissues (A-C) Esophagus, (D-F) Stomach (G-I) Small intestine (J-L) Large intestine at a magnification of 1000x, 5000x, and 20,000x, respectively

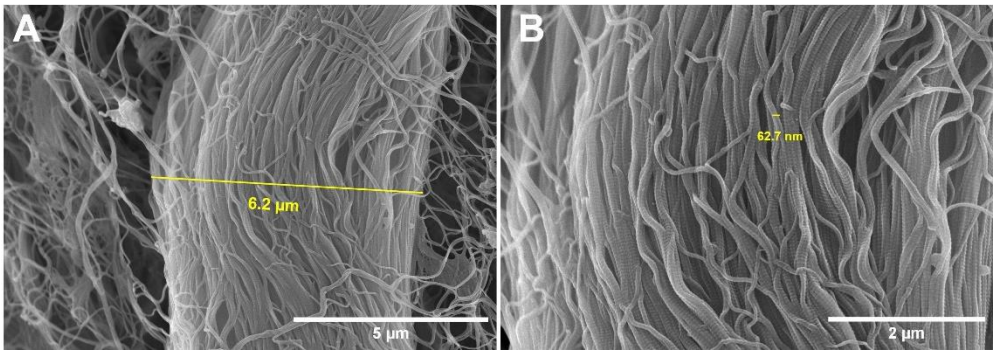


Figure 5.6 Diameter of (a) Collagen fiber and (b) Fibril bundles in the tissue

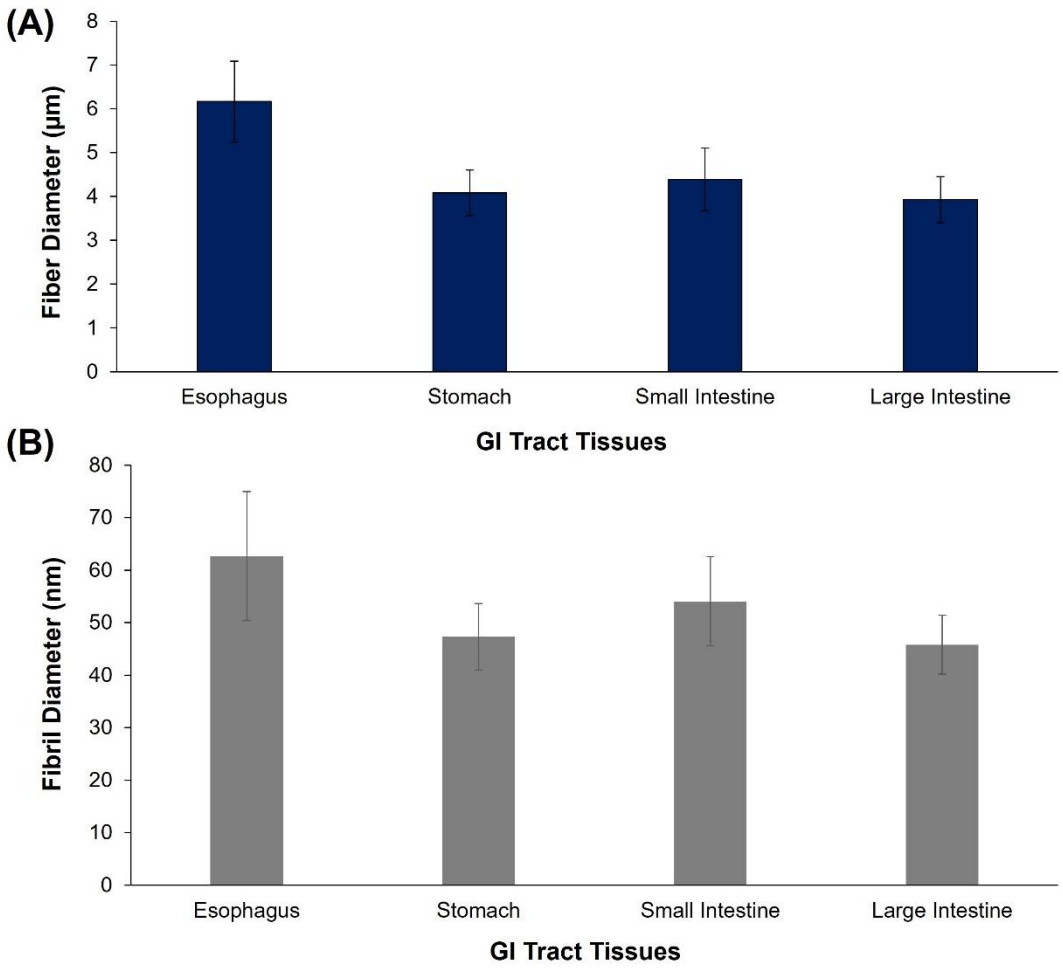


Figure 5.7 (A) Collagen bundles and (B) Fibrils diameter of esophagus, stomach, small intestine, and large intestine

The differences in the mechanical behaviour of GI tract tissues are expected due to the differences in the structure, e.g., the orientation and configuration of collagen fibres. To study the correlation between the microstructure and mechanically the effects of tensile deformation, the longitudinal small intestine sample was stretched from 0 to 50% strain. The microstructure of the intestine is observed in SEM and demonstrated in Figure 5.8. Initially, at 0% strain, it shows undulating fibres and crimps patterns in register. The shape of undulation fibres is represented by a wave that is slightly tilted at a crimp angle (θ_1) of 31.3˚ (Figure 5.9). The undulations of the

collagen fibres in the intestine are smoother than the undulations in tendon fibres, and cannot be represented by a planar zigzag model [291]. The uniaxial stress is applied to the unstretched intestine resulting in gradual uncrimping and reorientation of wavy collagen fibres until the fibres are completely straightened. These fibres are biaxially oriented e.g., one running in a clockwise helix down to the intestine and the other running in an anticlockwise helix. The biaxial angle varies approximately +30˚ and -30˚ in the longitudinal direction [197]. The orientation of the collagen fibres is important for the flexibility of the submucosa, which has to allow deformation of the intestinal wall [198]. With this arrangement, despite the nonelastic nature of the collagen fibres, the submucosa can make provision for a variable lumen by a simple change of the angle formed by diagonal collagen fibres.

Application of longitudinal stress to the intestine results in the straightening of the wavy fibres while maintaining their biaxial orientation. It is shown that the presence of partly stretched fibres in one direction compared to the stretched-out fibres in the other is due to preferential extension in one direction. The crimp angle (θ_1) decreases according to the degree of stretching. The measured crimp angle decreases (θ_1) approximately at 31.3˚ to 22.2˚ as the longitudinal strain increases from 0% to 50% (Table 5.2). The strain in the fibre direction necessary to straighten the fibres can be calculated from crimp parameters θ' and θ" (Figure 5.10) and the ratio of length through the following relationships:

$$l_0 = l_0' cos\theta_0' + l_0" cos\theta_0" \quad (5.1)$$

$$l = l' cos\theta' + l" cos\theta" \quad (5.2)$$

$$\varepsilon = \frac{\Delta l}{l_0} = \frac{(l' \cos\theta' + l" \cos\theta") - (l_0' \cos\theta_0' + l_0" \cos\theta_0")}{l_0' \cos\theta_0' + l_0" \cos\theta_0"} \quad (5.3)$$

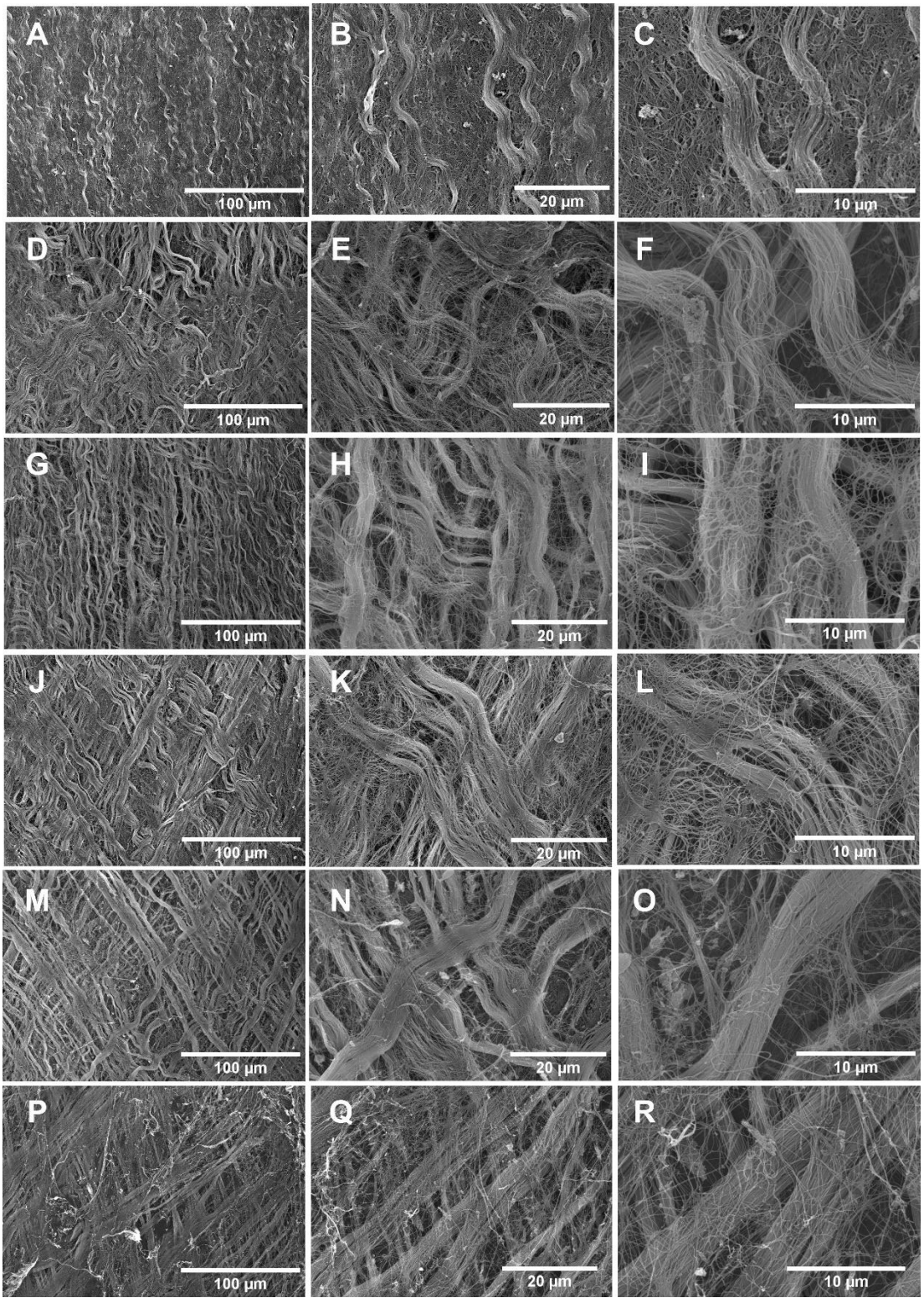


Figure 5.8 SEM images of small intestine after stretched with (A-C) 0% (D-F) 10% (G-I) 20% (J-L) 30% (M-O) 40% (P-R) 50% strain

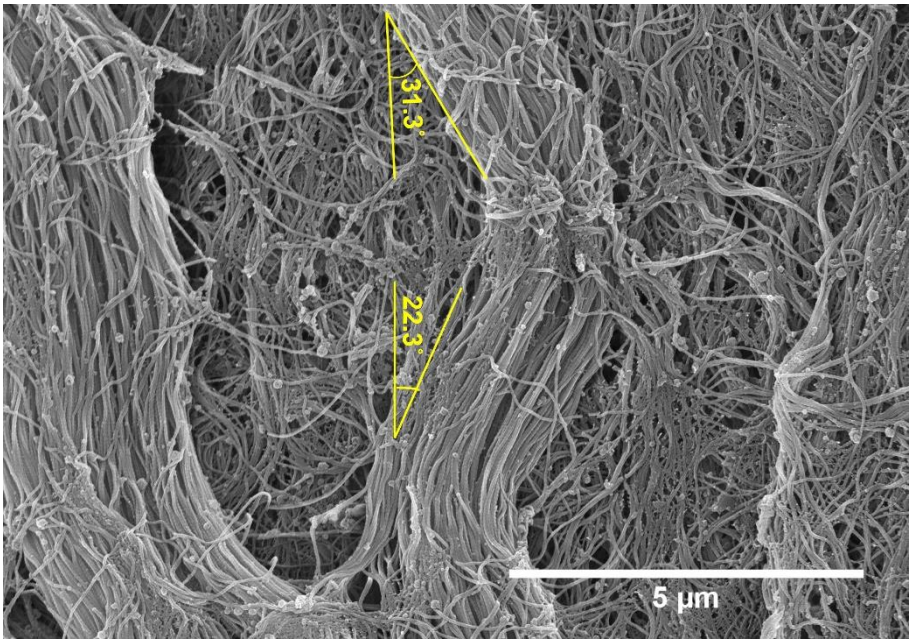


Figure 5.9 Crimp angle (θ_1) of undulations collagen fibre at 0% strain

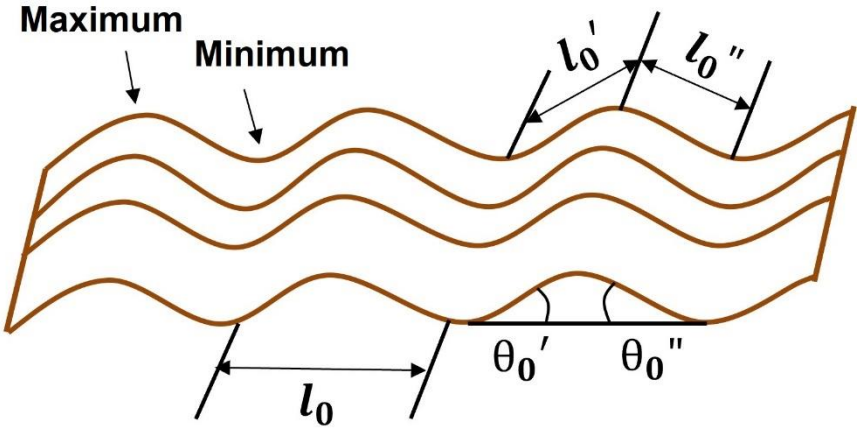


Figure 5.10 Illustration of tilted wave configuration of collagen fibres in the small intestine

Table 5.2 Strain, length, and crimp angle of the fibres

ε	Calculated ε	l' (μm)	l'' (μm)	θ' (°)	θ'' (°)
0%	0%	6.9 ± 1.1	6.4 ± 0.9	31.3 ± 2.8	22.3 ± 3.6
10%	10.7%	7.4 ± 0.5	7.2 ± 1.2	29.6 ± 2.7	24.7 ± 2.2
20%	20.4%	8.1 ± 0.8	7.9 ± 1.1	28.2 ± 3.5	26.6 ± 2.5
30%	30.0%	8.9 ± 0.7	8.3 ± 1.2	27.9 ± 2.5	24.9 ± 3.1
40%	39.9%	9.9 ± 2.0	8.5 ± 1.5	24.6 ± 2.6	28.3 ± 3.3
50%	50.9%	10.4 ± 0.7	9.4 ± 1.6	22.4 ± 3.6	29.0 ± 3.8

The submucosa collagen fibres provide the intestine with sufficient structural integrity and strength. The organisation of the collagen fibres and the stress response are responsible for the highly anisotropic mechanical properties of the intestine. The gradual uncrimping of the crimped collagen fibres and decrease of the angle between fibres is associated with the toe region observed in stress-strain curves.

5.4 Intestinal Lengthening Studies

5.4.1 *Ex vivo* Study

An *ex vivo* study was carried out to ensure that the hydrogel was successfully applied before doing *in vivo* study to stretch the intestine. VP85 (VP/MMA 85:15wt%) cylindrical hydrogel with a slenderness ratio (L/r) of 2 was chosen for this study based on several criteria such as the swelling pressure of hydrogel not exceeding the maximum stress of intestinal tissue (P < 78.9 kPa), the swelling pressure is adequate to stretch the intestine (42.1-73.9 kPa), slower swelling rate and lower strain value, and good mechanical properties. Due to the small size of the rat intestine, the hydrogel

would need to be designed to have a small size. Hence, the hydrogels with the size of 3mmD, 2mmD, and 1mmD were chosen for *ex vivo* study. The intestine samples were obtained after the rats were dissected. The dissection of the rats was carried out by Thu Trang Nguyen (National Taipei University of Technology). The hydrogel devices together with the intestine were immersed in PBS at room temperature to observe the change in intestinal length as a function of time. Two hydrogels were attached at both ends of the metal plate. The intestine was glued and/or sutured in the holes locates in the middle of the metal plate. The length of the intestine with the hydrogel in place was measured. Figure 5.11 shows the photograph of intestinal length after being stretched with various hydrogel sizes on days 0, 1, and 7 respectively. The hydrogel with sizes of 3mmD & 3mmL and 2mmD & 2mmL show a significant increase in the length (almost 2-folds from the initial length), however, stretching the intestine using 1mmD & 1mmL hydrogel is not effective. It shows that the hydrogel is almost not swelling, hence the swelling pressure is not capable to push the metal plate as well as stretching the intestine. Figures 5.12 and 5.13 show the change in the intestinal length and lengthening ratio as a function of time after being stretched with three different hydrogel sizes. The hydrogel size of 3mmD & 3mmL and 2mmD & 2mmL show a rapid lengthening in the first 12 hours with a value of lengthening ratios are 1.1 and 0.9, respectively, then slowly increase until the lengthening reaches the equilibrium state. At equilibrium, the length of the intestine after lengthening and lengthening ratio is estimated to be 7.0 mm and 1.3 for hydrogel sizes of 3mmD & 3mmL, respectively. In addition, for the hydrogel with a smaller size (2mmD & 2mmL), the final length and lengthening ratio are decreased to 4.5 mm and 1.2, respectively.

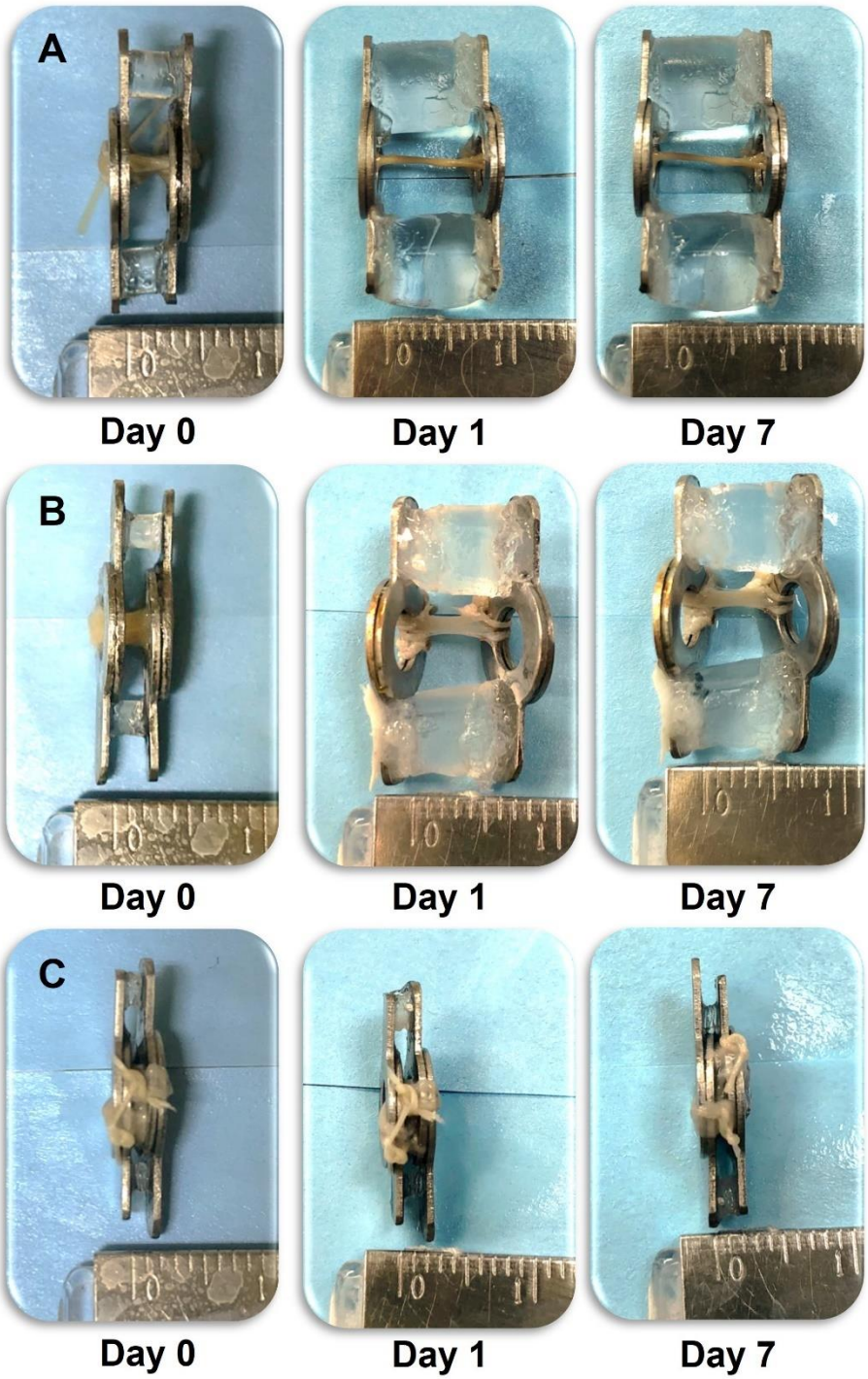


Figure 5.11 Photograph of intestinal lengthening using hydrogel sizes of (A) 3mmD & 3mmL (B) 2mmD & 2mmL (C) 1mmD & 1mmL observed at day 0, 1, and 7, respectively

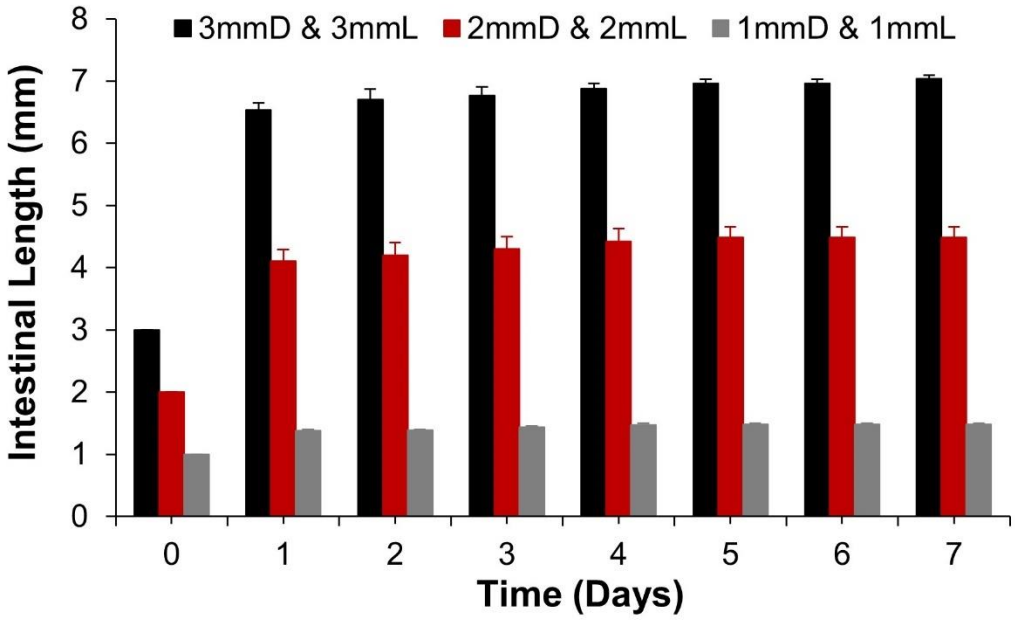


Figure 5.12 *Ex vivo* study showing a change of intestinal length after being stretched with three different hydrogel sizes as a function of time

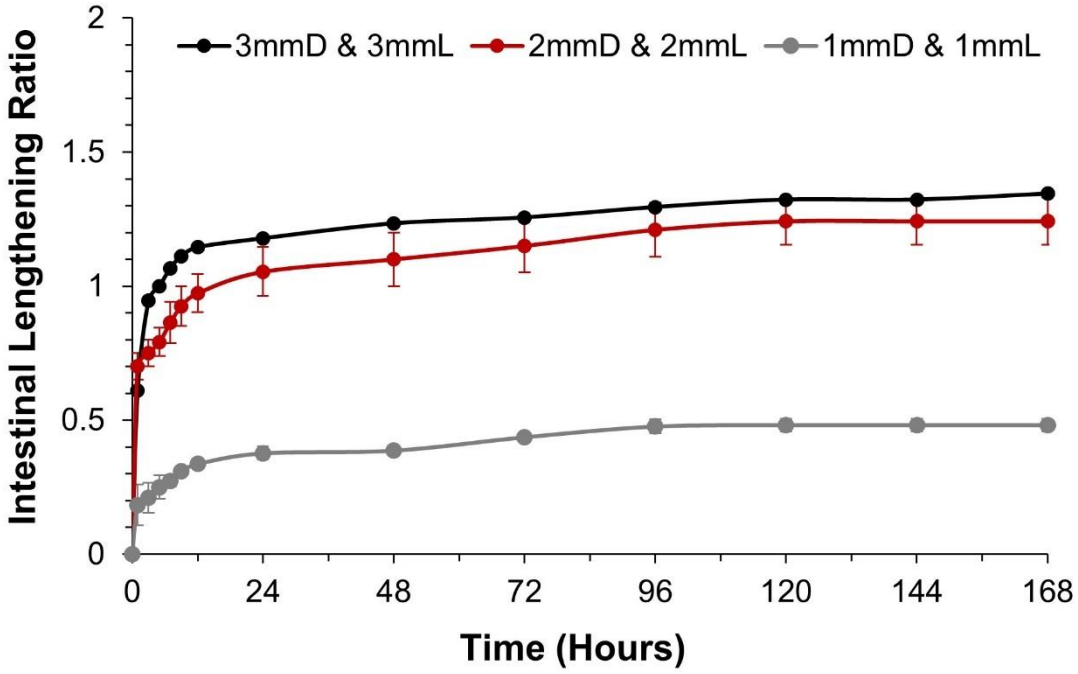


Figure 5.13 Intestinal lengthening ratio after the intestine is stretched with three different hydrogel sizes as a function of time

5.4.2 *In vivo* Study

In vivo study was carried out in Taipei, Taiwan. It collaborated with the National Taipei University of Technology (NTUT) and Taipei Medical University (TMU). Self-inflating VP/MMA (85:15wt%) hydrogel expanders were designed and synthesized in NTUT for *in vivo* use. Two individual hydrogels were attached to the SS plate in order for that device could be located in the small intestine area. The sizes of hydrogel used in this study were 3mmD & 3mmL and 2mmD & 2mmL. Hydrogels were transferred to TMU for device sterilizations and animal experiments. Hydrogel devices were first double-sealed within sterilization pouches. The hydrogels were sterilized in a steam autoclave and under ultraviolet (UV) light. In order to constrain the hydrogel during the autoclaving process and prevent polymer distortion, a bespoke brass mould was designed for the 10-mm diameter cylinder. The hydrogels fitted within a cylindrical recess within the base plate and were firmly sealed within the mould using a bolted lid. Once autoclaved, the hydrogel was readily expelled via a small purge hole machined in the base of the mould. The mould-autoclaved hydrogel retained its original dimensions and had identical swelling properties to the non-sterilized hydrogel.

The animal experiment was conducted at Taipei Medical University in accordance with guidelines for the care and use of animals. The surgical experiment was carried out with the help of my colleague, Thu Trang Nguyen (National Taipei University of Technology). *In vivo* procedure was carried out after obtaining approval from the Affiliated Institutional Animal Care and Use Committee (IACUC) under document number LAC20210130. Firstly, a hydrogel with the size of 3mmD and 3mmL was implanted inside the rat body but outside the intestine. After observing the

condition of rat on day 4, the rat was experiencing moderate pain (Figure 5.14). When the pain is scalable, it categorizes as a rat grimace scale of "1". It showed a significant change in their facial expression such as closing the eyelid (narrowing of orbital area), flattening and elongation of the bridge of the nose, flattening of the cheeks, ear curling inwards and angled forward to form a 'pointed' shape. After the rats were sacrificed, it was found that their intestines (n=3) were swollen, and their stomach was filled with full of fluid. The condition is known as ascites, and it develops as a result of portal hypertension. The intestinal blood flow could not be compromised when the intestine stretches too fast and/or too far. The initial intestinal length is 3 mm and after being stretched with a hydrogel device the length increases to 7 mm. There is a significant change in strain (133.3%) and the strain value is exceeded the maximum strain of the small intestine (longitudinal direction). It had been reported that the strain beyond physiological limits may lead to alteration of cell function such as tissue necrosis and/or apoptosis as well as tumour formation [292]–[295].

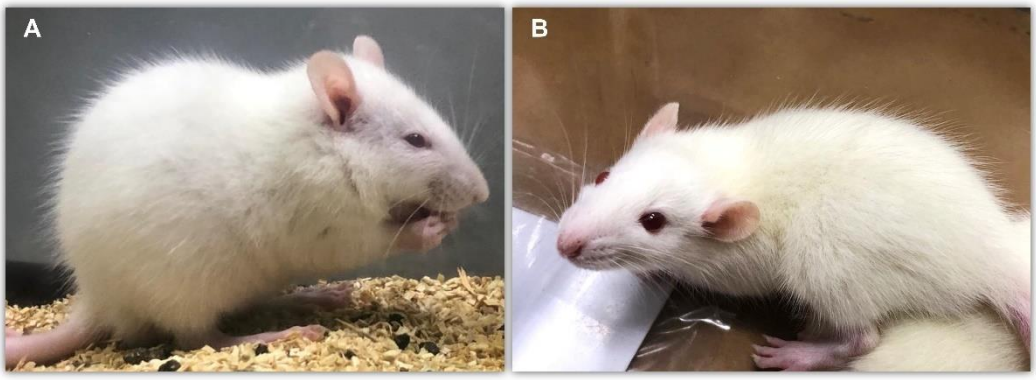


Figure 5.14 (A) Rat condition on day 4 after the intestine was stretched with 3mmD & 3mmL hydrogel device (B) Normal rat condition

Due to the above reason, the hydrogel with the size of 2mmD & 2mmL was finally chosen in this study. There are two ways to attach the small intestine to the

metal plate. The first method was applying cyanoacrylate adhesive (medical glue) on the left and right sides of the metal plate and sticking to both ends at isolated intestinal length. This method was chosen due to the cyanoacrylate adhesive had been used in cardiac surgery [296]. After surgery, the rats were observed day by day. On day 4, all rats including the isolated-control and the stretched-intestine groups died. The 'isolated control' group is the area of the small intestine that was attached to the metal plate without the hydrogel and the 'stretched-intestine' is the area of the intestine that was attached to the metal plate with hydrogel on it. The rats died due to the wall structure of their intestine changing from originally viscoelastic to becoming a stiffer wall. It would cause intestinal tissue damage and cell death due to a reduction of blood flow to the intestine (bowel necrosis), hence the intestine is unable to meet the normal function of metabolic demands.

It was observed that there was a significant change in length and diameter when the intestine was stretched using a hydrogel device (Figure 5.15). Upon the removal of the hydrogel device, the loss of tension allowed the lengthened intestinal segment to recoil. The results of final length and diameter are summarized in Figure 5.16. In the stretched-intestine group, the initial length and diameter were 2.1 ± 0.1 mm and 2.9 ± 0.3 mm, respectively. After being stretched with the hydrogel, the length and diameter were doubled to 4.9 ± 0.1 mm and 4.0 ± 0.4 mm, respectively. Comparing the initial and the final length and diameter of the stretch segment, the significant difference is $p \leq 0.0001$. There was an obvious change in the diameter of the stretched intestine due to accumulation of intestinal secretions. In the isolated-control group, the length of the intestine on days 0 and 4 shows no significant difference. However, the diameter of the isolated control on days 0 and 4 shows a significant change ($p \leq 0.001$). Initially,

the diameter of the intestine on day 0 was 3.2 ± 0.07 mm. On day 4, the intestine was inflamed, and the diameter changed to 4.3 ± 0.08 mm with hydrogel in place.

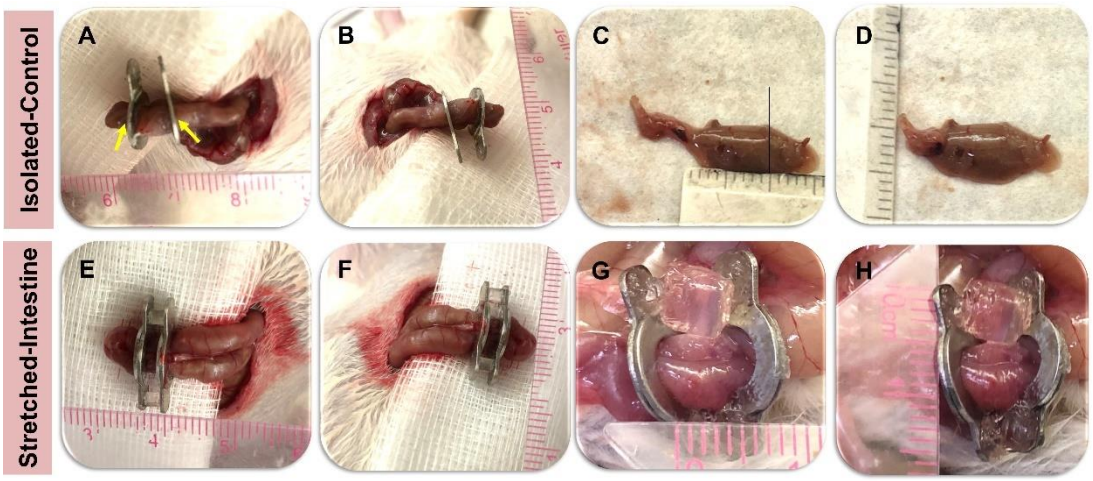


Figure 5.15 Photograph of isolated-control and stretched-intestines attachment to the metal plate using biomedical grade cyanoacrylate adhesive (yellow arrow) at (A, B, E, F) day 0 and (C, D, G, H) day 4, respectively

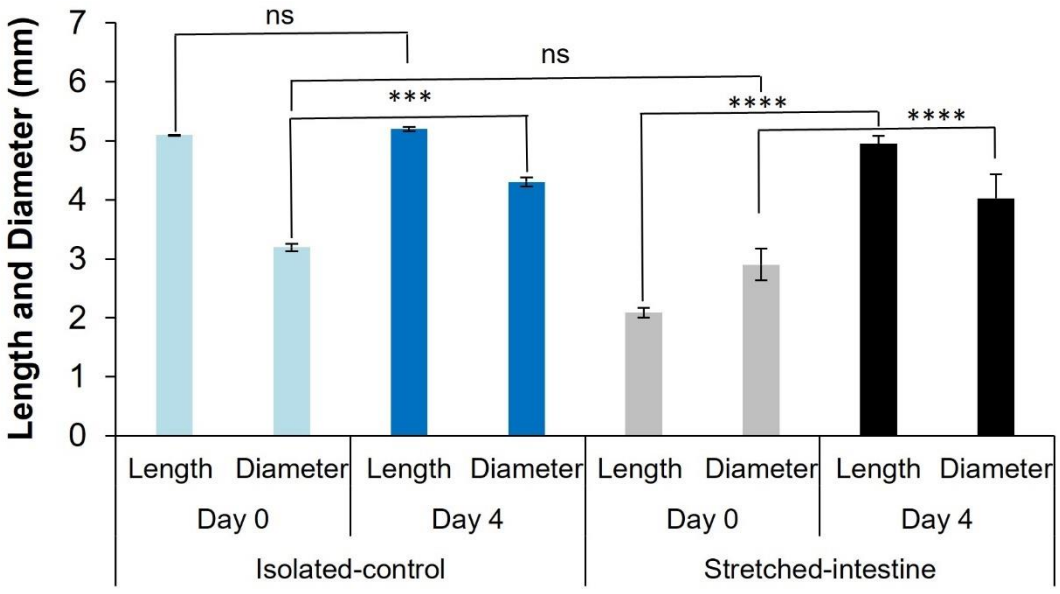


Figure 5.16 Significant change in length and diameter of an isolated-control segment and stretched-intestine at day 0 and day 4 after hydrogel devices removal. Note n=4, *** $p \leq 0.001$, **** $p \leq 0.0001$, ns $p > 0.05$ (Turkey's test)

Understanding the morphology change of both isolated-control and stretched-intestine, the tissue segments were observed using H&E staining (Figure 5.17). The H&E staining experiment was carried out with the help of the Taipei Institute of Pathology, Taiwan. The morphologies of both samples show loss of tissue integrity and thickened muscle layer. In isolated-control intestinal segment displays crypt loss, epithelial barrier breakage, and a sign of edema (black arrow) in the intestinal mucosa, as well as submucosa layer damage. The stretched intestine shows denudation of the small intestinal villi and patchy loss of crypts. The remaining crypts have epithelial cells with cytoplasmic depletion (crypt "withering"). The epithelial barrier is also found to breakage in the stretched segment. The morphology of both intestines shows that the ischemic injury is prominent. Intestinal ischemia occurs when blood flow to the intestine decreases due to a blocked artery. The loss of blood flow to the intestines could damage intestinal tissue and lead to death.

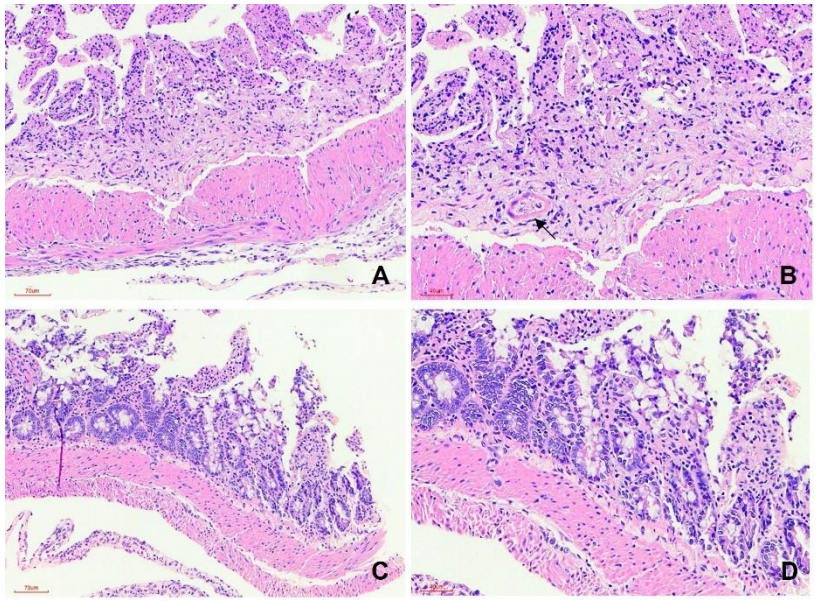


Figure 5.17 H&E-staining of (A-B) isolated-control and (C-D) stretched-intestinal segments attached to a metal plate using cyanoacrylate adhesive observed on day 4 with magnifications (A,C) 17x and (B,D) 26x

The second method used in this study to prevent the intestine from moving was using sutures. The intestine was folded and inserted through the metal plate hole. A needle was initially inserted through the intestinal serosa wall and sutured. A needle and suture passed through the metal plate hole and tightened with a metal plate. This method is useful for marking the initial length and the final length of the intestine after being stretched with hydrogel. The rats were observed on days 1 and 7 post-surgery. Figure 5.18 shows the photographic images of isolated-control and stretched-intestine from unlengthened condition to 1 and 7 days after implantation with a hydrogel device. In the isolated-control group, it shows that there was a significant change in the diameter from day 1 until day 7 due to wall inflammation. The diameter increased by almost 2-fold, but the length of the intestine remains the same. In the stretched-intestine, the final length of the intestine was significantly increased from the initial length of the intestine. The hydrogel device successfully lengthened the intestine through a mechanism called mechanotransduction. The hydrogel employs force during swelling in the biological environment to stretch or deform the intestine and activate the biochemical signals of the cell, thereby a certain amount of length and cell growth could be obtained [76].

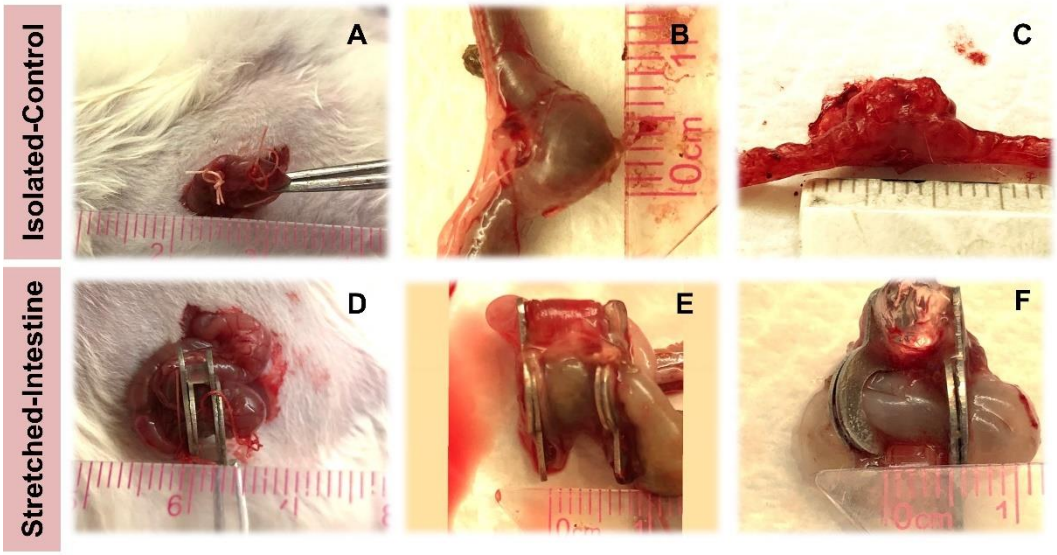


Figure 5.18 Photograph of an isolated-control and stretched-segment of rat intestine observed at (A, D) Day 0, (B-E) Day 1, (C, F) and Day 7

Measurements of the final length, diameter, area, and weight of the intestines were taken upon the removal of hydrogel expander device. The extended intestinal segment was allowed to recoil partially due to the tension has been released. There was a possibility of reduced relaxed length when hydrogel is removed. For clinical application, it is essential that the lengthened intestinal segment retain its length and function after hydrogel expander removal. Figure 5.19 shows a measurement diagram of intestinal length, diameter, weight, and surface area of both isolated-control and stretched-segment rat intestines on days 0, 1, and 7. On day 0, the mean lengths of the isolated-control and stretched-intestine are 5.9 mm and 2.3 mm, respectively (Table 5.3). On days 1 and 7, the lengths of the stretched-intestine increased to 5.0 mm and 5.2 mm, respectively, 122.6% and 129.2% increase in length ($p \leq 0.0001$). Austad et al. reported that increased length was a result of cellular proliferation [297]. Further study will require to carry out for the restoration of the lengthened intestinal segment

back into the gastrointestinal tract to allow the intestine to relax after the mechanical force has been removed. The new relaxed length after the hydrogel removal will be measured in the further study. The isolated-control intestine demonstrates no significant change in length. The final lengths are 6.0 mm and 6.1 mm after observed on days 1 and 7, respectively. The diameter of the stretched-intestine group was also expanded but not as obvious as in the isolated-control intestine (Table 5.3).

In addition to length, the growth is accessed by measuring the bowel weight and surface area of the intestine. The total intestinal weights of the stretched intestine are 178.6% and 207.1% heavier than the unlengthened intestine (Table 5.3). In contrast, the isolated-control segment shows no significant increase in weight on days 1 and 7 (0.7 gr vs 0.4 gr). The increase in bowel weight is in similar proportion to the increase in length. The surface area of the stretched segment has significantly greater than the unlengthened isolated control ($p \leq 0.0001$). Intestinal tissue mass per square centimetre of the surface area did not differ between stretched-intestinal segment and isolated-control groups (Table 5.3; $p > 0.05$), demonstrating that the observed intestinal lengthening is actual tissue growth, instead of merely redistribution of tissue. Mechanical stretch on tissue is related to several physiological phenomena such as cellular growth enhancement and/or expansion with significantly higher vascularity of expanded tissue [298]. In summary, the hydrogel has successfully lengthened the intestine.

Table 5.3 Assessment of tissue condition in both isolated-control and stretched-intestinal groups showing the length, diameter, weight, and surface area of the intestines after immediate hydrogel removal

	Day	**Isolated-Control**	**% Change**	**Stretched-Intestine**	**% Change**
Length (mm)	0	5.90 ± 0.14	-	2.26 ± 0.11	-
	1	6.05 ± 0.21	2.5%	5.03 ± 0.21	122.6%
	7	6.13 ± 0.04	3.9%	5.18 ± 0.18	129.2%
Diameter (mm)	0	3.04 ± 0.05	-	3.18 ± 0.13	-
	1	5.53 ± 0.25	81.9%	3.83 ± 0.29	20.4%
	7	5.58 ± 0.11	83.6%	4.01 ± 0.18	26.1%
Weight (g)	0	0.38 ± 0.02	-	0.14 ± 0.01	-
	1	0.71 ± 0.03	86.8%	0.39 ± 0.03	178.6%
	7	0.74 ± 0.01	94.7%	0.43 ± 0.02	207.1%
Surface Area (cm^2)	0	0.56 ± 0.01	-	0.22 ± 0.01	-
	1	1.04 ± 0.02	85.7%	0.60 ± 0.03	172.7%
	7	1.09 ± 0.03	94.6%	0.65 ± 0.02	195.5%
Mass per Unit Area (g/cm^2)	0	0.67 ± 0.05	-	0.64 ± 0.08	-
	1	0.68 ± 0.03	1.5%	0.65 ± 0.09	1.6%
	7	0.68 ± 0.02	1.5%	0.66 ± 0.05	3.1%

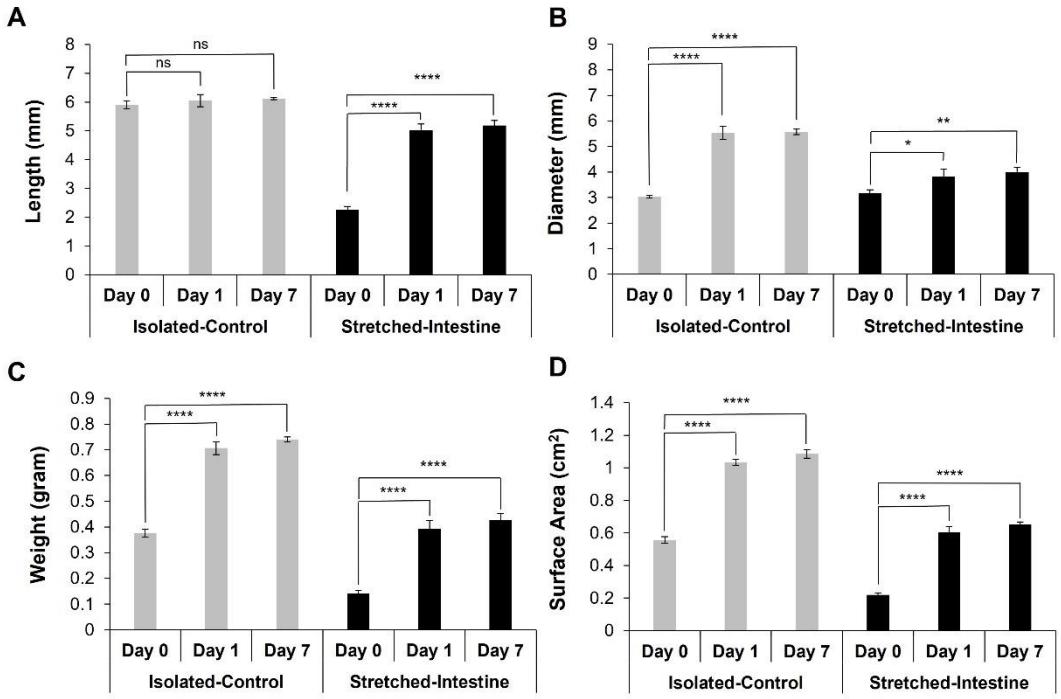


Figure 5.19 Measurement of (A) Intestinal length (B) Diameter (C) Weight, and (D) Surface area of both isolated-control and stretched-intestine on days 0, 1, and 7. Note n=4, ns $p > 0.05$, *$p \leq 0.05$, **$p \leq 0.01$, ****$p \leq 0.0001$

To identify the cellular changes that were occurring in response to the external tension, the basic histological components of the intestine, including total mucosal thickness, crypt depth, and villous height were evaluated. Figure 5.20 shows the H&E staining of the normal, isolated-control, and stretched intestine observed on days 1 and 7 with the attachment using the suture method. In addition to macroscopic growth, the muscular thickness of the isolated-control and stretched-segment rat intestines demonstrate marked hypertrophy and are 68% and 62% thicker than the normal intestine (Figure 5.20). These findings are not specifically due to the application of tension as both the isolated-control and stretched-intestinal segments are showing thicker layers than the normal intestine. Muscularis thickening might occur as a result

of surgical procedures. The change in the muscularis layer may pose significant problems for future use, therefore future models might need to address these issues changes. The crypt depth is markedly increased in the stretched-intestinal segment versus the isolated-control intestine, but it shows no significant difference when compared to the normal intestine (Figure 5.20). A greater thickness of crypt depth might indicate cell movement and proliferation. These observations suggest that the swelling force imparted by the hydrogel results in cellular proliferation. BrdU staining has shown a significant increase in epithelial proliferation in segments subjected to mechanical distraction [59], [67], [71], [72]. In addition, the villous height of the stretched intestine is significantly increased from day 1 to day 7 and compared with isolated-control and normal intestines (Figure 5.20). It is likely from exposure to alimentary nutrition.

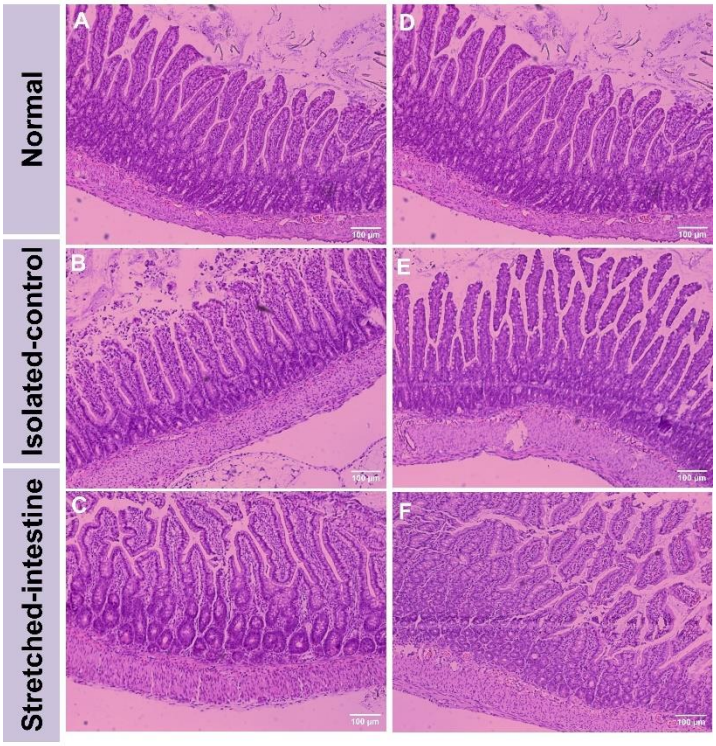


Figure 5.20 H&E staining of normal, isolated-control, and stretched-intestinal segments observed on (A-C) Day 1 and (D-F) Day 7

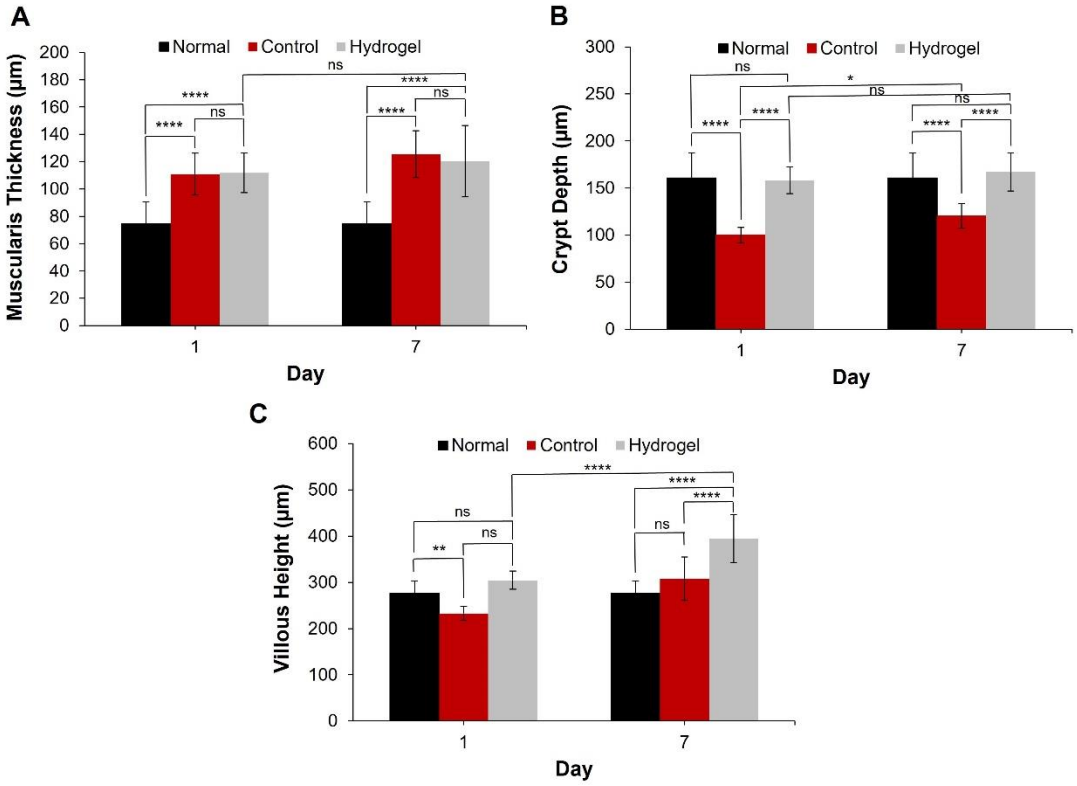


Figure 5.21 Summary of histological measurement showing muscular thickness, crypt depth, and villous height in normal, isolated-control, and stretched-intestine on days 1 and 7. Note n=4, ns $p > 0.05$, *$p \leq 0.05$, **$p \leq 0.01$, ****$p \leq 0.0001$

It is known that cells can sense mechanical forces as a result of signals transmitted from extracellular matrix to intracellular biochemistry [299]. Alteration of histological appearance in response to mechanical (swelling) force is due to the cells changing their phenotype and their surrounding ECM [300]. Mechanical (swelling force) is transmitted and the fibroblasts receive the signals and prepare to proliferate (Figure 5.22) [301]. The ECM plays an important role in strain-induced cell proliferation [302]. The force transmitted through the ECM leads to the deformation of the matrix, followed by alteration of the plasma membrane and adhesion complexes [303]. The transmembrane protein integrin communicates with both ECM and

cytoplasmic proteins such as talin, paxillin, and vinculin. The binding of talin to the integrin cytoplasmic tail induces a conformational change from an inactivated to an activated state with an increased affinity for the ECM [304]. Upon the activation of integrins, the β subunit complexes with numerous structural and signalling proteins form a focal adhesion kinase (FAK) to provide both physical link between integrin-adhesion receptors and the actin cytoskeleton, as well as sites of signal transduction into the cell interior [305], [306]. The activated FAK then activate signal transduction pathways that coordinate cell proliferation [76]. FAK works in a complex with α-actinin and Rac to promote cell motility and growth [307], [308]. It has been previously demonstrated that Rac1 signalling pathway activates AKT through p38MAPK [309], [310]. FAK is potentially using these two pathways to promote intestinal epithelial cell (IEC) growth and reduce apoptosis during mechanotransduction. It has been demonstrated that FAK promotes both MEK/ERK and PI3-AKT signalling pathways [311], [312]. AKT activation downstream of PI3K has a role in inhibiting apoptosis.

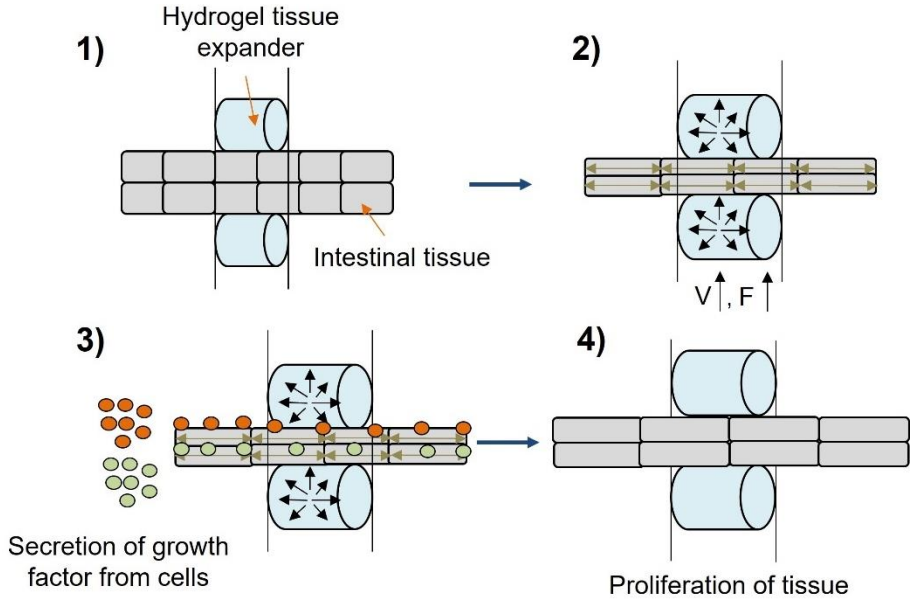


Figure 5.22 Illustration of tissue stretching by using hydrogel expander device activated cell proliferation

The Verhoeff-Van Gieson staining experiment was carried out with the help from Taipei Institute of Pathology, Taiwan. Figure 5.23 shows the morphology of isolated-control and stretched-intestinal segments on days 1 and 7, respectively, stained using the Verhoeff-Van Gieson method. There are no significant elastic fibres (elastin) found in the structure of the intestinal wall. Serious signs of fibrosis in both intestines are not found in this study. Both intestines display appreciable amounts of van Gieson's pink-stained collagen fibres in the submucosa layer. Figure 5.24 shows the thickness of the collagen layer in the submucosa region of the isolated-control intestine and stretched-intestinal segments on days 1 and 7, respectively. On day 1, the isolated-control intestine shows a thickened collagen layer compared to the isolated-control on day 7 ($p \leq 0.01$). The stretched intestine also has a similar pattern ($p \leq 0.05$). This is because of the post-surgery effect that causes the intestinal wall inflamed, thereby increasing the collagen content. The inflammatory mediator plays an important role in the adaptation of tissue to external mechanical force. To adapt to a changing environment, the ECM is remodelled. Fibroblast is a major driver of ECM remodelling. Fibroblast produces and secretes collagen. Therefore, this finding suggests that the activation of inflammatory pathways is important for the physiological rise in collagen synthesis that is seen in with mechanical loading of intestinal tissue. On day 7, it is found that the thickness of the collagen layer decreases in both intestines.

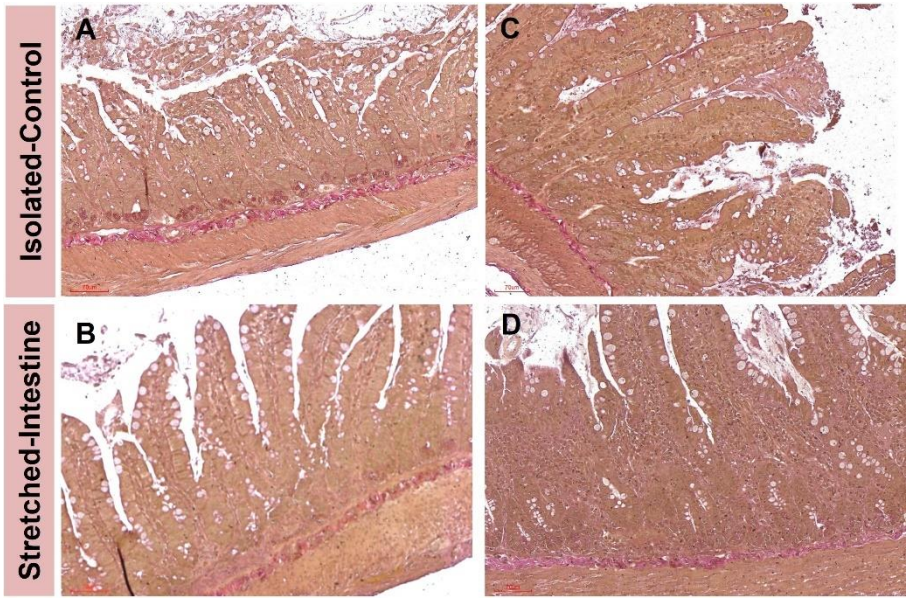


Figure 5.23 Verhoef-Van Gieson staining of isolated-control and stretched-intestinal segments on (A-B) Day 1 and (C-D) Day 7, respectively, at 17x magnification

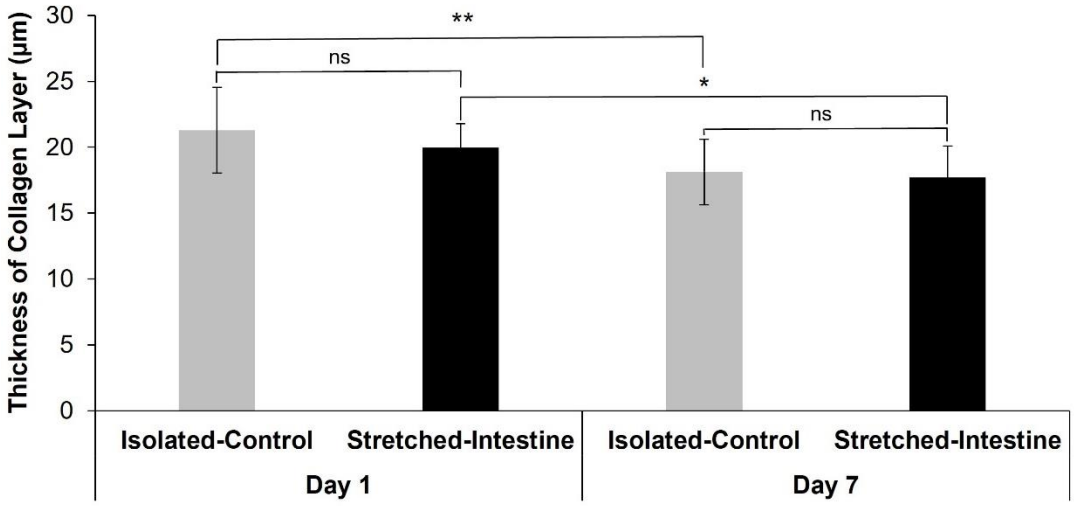


Figure 5.24 Thickness of collagen in the submucosa layer of the isolated-control and stretched-intestinal segments on days 1 and 7, respectively. Note: ns $p > 0.05$, *$p \leq 0.05$, **$p \leq 0.01$

The immunofluorescence CD31 staining was carried out with the help from Taipei Institute of Pathology, Taiwan. The platelet-endothelial cell adhesion molecule-1 PECAM-1 (CD31) is expressed in the junction area of endothelial cells and the surface of human platelets, where it is supposed to mediate the transmigration of leukocytes into the gut [313], [314]. It is also expressed as a mark of inflammation. Figure 5.25 shows the immunohistochemistry CD31 staining of normal, isolated-control and stretched-intestinal segments on days 1, and 7, respectively. The CD31 expression, which is involved in the transmigration of leukocytes into the mucosa, is not found in the normal intestine. In contrast, CD31 is highly expressed in the isolated-control and stretched intestine, but most significant in the isolated-control segment. The degree of CD31 expression is involved in the early phases of inflammation [315]. Due to inflammation being found in both intestines, it might be coming from the surgical suture procedure. Therefore, an alternative safely method needs to find to solve the problem.

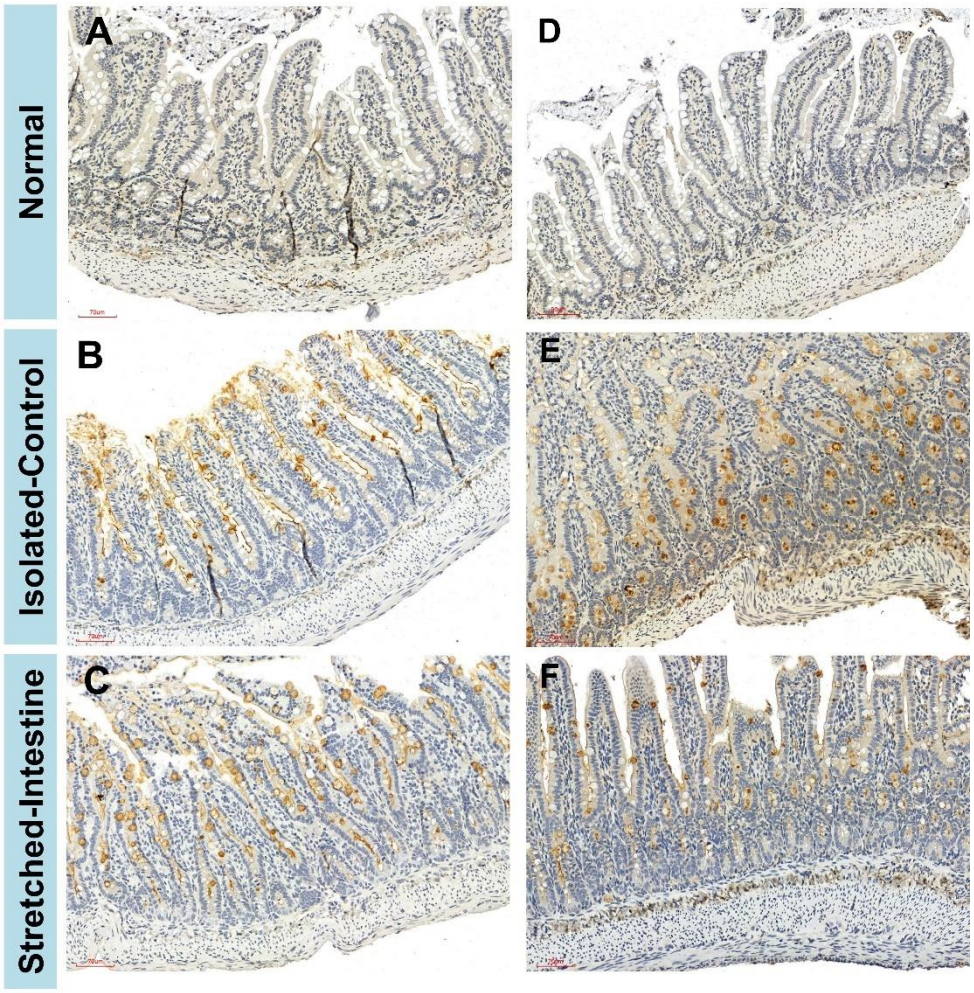


Figure 5.25 Immunohistochemistry for PECAM-1 (CD31) staining in the normal intestine, isolated-control, and hydrogel-stretched intestine on (A-C) Day 1 and (D-F) Day 7, respectively, at 17x magnification

5.5 Summary

This chapter demonstrates the morphology and mechanical properties of the gastrointestinal tract tissues. However, the main discussion in this chapter is the small intestine tissue. The maximum stress and strain of the small intestine are 78.9 kPa and 26%. These values are useful as a parameter to choose the design of the hydrogel for *ex vivo* and *in vivo* studies. The morphology of the small intestine under strain

conditions is observed and it links to the stress-strain curve. Initially, the collagen fibres show undulating and crimp patterns in register. After the intestine was stretched, the initial region of the stress-strain curve was termed the 'toe' region. In the toe region the rate of stress with respect to strain ($d\sigma/d\varepsilon$), steadily increases until it reaches a constant value. The toe region of the stress-strain curve corresponds to the straightening of the crimped fibre while maintaining the biaxial orientation (+30˚ and -30˚ in the longitudinal direction). The following linear region of the stress-strain curve is related to the elastic extension of the fibre.

The maximal *ex vivo* pressure of VP85 with the hydrogel sizes of 2mmD & 2mmL and 3mmD & 3mmL would be sufficient to expand the small intestine. However, the clinical implication and hydrogel maximal *in vivo* swelling pressure need to be confirmed. Finally, the VP85 hydrogel with the size of 2mmD & 2mmL is chosen and the intestine was sutured to the metal plate. The intestine could be successfully lengthened using a hydrogel device. Histological image of stretched-intestine shows a significantly greater muscularis thickness, crypt depth and villous height which indicates tissue growth. Therefore, the hydrogel tissue expander has the potential value as a prototype device to be applied in other reconstructive indications of GI tract tissue. However, the implant method needs to be carefully considered and the inflammation issue needs to be addressed in future studies.

Chapter 6: Conclusion

6.1 Thesis Conclusion

VP/MMA hydrogels had been successfully prepared using the chemical crosslinking method. The concentrations of crosslinker and initiator used in this study were higher (0.3wt%) compared to the concentrations used previously in the former work in this group (0.2wt%). The purpose is to obtain the desired mechanical and swelling properties of the hydrogels specifically for this application. The hydrogel was post-cured at 110˚C to remove residual stress that will have the potency to disturb and cause failure during the swelling process. Hydrogels were synthesized with various composition ratios and sizes. The results suggested that introducing the hydrophobic MMA to the system would decrease the swelling rate and equilibrium volume swelling ratio. The greater value of equilibrium swelling was also affected by the greater initial surface area and volume of the hydrogels. The swelling pressure of hydrogel had an inverse relationship with the volume swelling. As two pressures contributed to the total swelling pressure, the elastic force tends to balance the free energy of mixing between polymer and solvent. The higher the VP, the lower the swelling force as well as the swelling pressure. The swelling pressure of the hydrogels was size-dependent. The greater the initial volume and surface area, the higher the swelling force. However, the same surface area did not significantly change the swelling force. Due to the swelling pressure being a function of force over a surface area, the greater surface area provides smaller swelling pressure. Swelling media also played an important factor in this study. The swelling in DI water at room temperature and PBS at 37˚C were chosen. There was a significant reduction in the swelling capacity when PBS was introduced as a swelling media. It was due to the ionic contribution that limited penetration of water to the polymeric network structure. Anisotropic hydrogels were also synthesized and

the result shows that the volume swelling ratio is slightly increased compared to isotropic gels. When compared to the length change, the length significantly increased 4-5 times in the desired direction.

The mechanical properties of GI tract tissues were also conducted to understand the properties and morphology of the tissues before the hydrogel device was implanted into the organ. The measurement in longitudinal and circumferential directions was conducted using a uniaxial tensile test. The longitudinal samples had a higher value to withstand high stress compared to circumferential directions. However, the circumferential directions could withstand the deformation. The mechanical properties of GI tract tissue were related to the real function of the organ in normal conditions. The morphology of GI tract tissues showed a wavy and crimped collagen fibre. After being stretched, the collagen fibres were uncrimped and straightened out. The *ex vivo* experiment was conducted to simulate hydrogel swelling to achieve lengthening of the small intestine before being implanted in the real body. Considering the hydrogels would be implanted in small animals, the hydrogels with small sizes were chosen. *Ex vivo* results showed a significant lengthening of the small intestine when stretched using hydrogels with sizes of 2mmD & 2mmL and 3mmD & 3mmL. However, *in vivo* study showed an unsatisfactory result for the hydrogel with the size of 3mmD & 3mmL, therefore the hydrogel with a size of 2mmD & 2mmL was finally chosen for further analysis. The hydrogels have successfully lengthened the intestine and the mechanotransduction mechanism might induce tissue growth. The muscularis thickness, crypt depth, and villous height were increased, however, there was still a problem with inflammation. The problem might be caused by the suture technique or procedure during the attachment of the intestine to the metal plate. Therefore, a better

technique to secure the intestine from moving still needs to have further investigation. In this study, we report the first successful application of force using a hydrogel device to induce length and growth in the rat intestine.

6.2 Future Work

The following future works are recommended to further build upon the work presented in this thesis such as:

1. With respect to the mechanical and swelling properties of the isotropic and anisotropic hydrogel, the elastic modulus of the hydrogel needs to be measured over time from 0 hours to an equilibrium state condition. The elastic pressure (p) of the hydrogel can be calculated and the mechanism of swelling that contributes to the total swelling pressure (P) can be studied in more detail.
2. The rate of hydrogel swelling is crucial in determining the success of the expansion procedure. Excessive expansion will result in a catastrophic device. The need for robust biocompatible hydrogel that is capable of creating super-slowing expansion might be of particular relevance in this application involving soft tissues. A ‘slow release’ coating such as cellulose acetate phthalate can be used to slow dissolution over a predetermined period. It can delay the expansion for a fortnight and might be possible to reduce the risk of wound complications.
3. It might be possible to replace non-degradable hydrogel with biodegradable hydrogels device such as 3.8% (w/w) PCL to minimize secondary surgery to reduce the pain of the patient. PCL is FDA approved polyester with nontoxic degradation products and high potential as a biomaterial for tissue regeneration.

4. Provide a better technique to implant hydrogel inside the intestine to reduce inflammation in the serosa wall. It might be possible to give an anti-inflammatory drug to reduce inflammation post-surgery.
5. The restoration of the lengthened intestinal segment back into the gastrointestinal tract to allow the intestine to relax after the mechanical force has been removed needs to be carried out.
6. With the larger surface area of intestinal tissue available, it can do sequential lengthening by applying multiple devices simultaneously within the same animal.
7. A more detailed study about signaling pathways (staining for mechanotransduction factors, proliferation, and apoptosis as well as protein immunoblotting) that are utilized during *mechanotransduction* are needed to conduct to potentially understand about the mechanism that led to optimize the potential approach to SBS.

References

[1] P. Munkholm, E. Langholz, M. Davidsen, and V. Binder, “Disease activity courses in a regional cohort of Crohn’s disease patients,” *Scandinavian journal of gastroenterology*, vol. 30, no. 7, pp. 699–706, 1995.

[2] P. Munkholm, E. Langholz, M. Davidsen, and V. Binder, “Intestinal cancer risk and mortality in patients with Crohn’s disease,” *Gastroenterology*, vol. 105, no. 6, pp. 1716–1723, Dec. 1993, doi: 10.1016/0016-5085(93)91068-s.

[3] B. N. Limketkai, A. M. Parian, N. D. Shah, and J.-F. Colombel, “Short Bowel Syndrome and Intestinal Failure in Crohn’s Disease,” *Inflammatory Bowel Diseases*, vol. 22, no. 5, pp. 1209–1218, Jan. 2016, doi: 10.1097/MIB.0000000000000698.

[4] J. S. Thompson, “Comparison of massive vs. repeated resection leading to short bowel syndrome,” *Journal of Gastrointestinal Surgery*, vol. 4, no. 1, pp. 101–104, Jan. 2000, doi: 10.1016/S1091-255X(00)80039-6.

[5] J. S. Thompson, K. R. Iyer, J. K. DiBaise, R. L. Young, C. R. Brown, and A. N. Langnas, “Short bowel syndrome and crohn’s disease,” *Journal of Gastrointestinal Surgery*, vol. 7, no. 8, pp. 1069–1072, Dec. 2003, doi: 10.1016/j.gassur.2003.08.007.

[6] S. J. O’Keefe, M. W. Haymond, W. M. Bennet, B. Oswald, D. K. Nelson, and R. G. Shorter, “Long-acting somatostatin analogue therapy and protein metabolism in patients with jejunostomies,” *Gastroenterology*, vol. 107, no. 2, pp. 379–388, 1994.

[7] E. Carlsson, I. Bosaeus, and S. Nordgren, “Quality of life and concerns in patients with short bowel syndrome,” *Clinical Nutrition*, vol. 22, no. 5, pp. 445–452, Oct. 2003, doi: 10.1016/S0261-5614(03)00042-6.

[8] R. Coletta, B. A. Khalil, and A. Morabito, “Short bowel syndrome in children: Surgical and medical perspectives,” *Seminars in Pediatric Surgery*, vol. 23, no. 5, pp. 291–297, Oct. 2014, doi: 10.1053/j.sempedsurg.2014.09.010.

[9] P. W. Wales, N. de Silva, J. Kim, L. Lecce, T. To, and A. Moore, “Neonatal short bowel syndrome: population-based estimates of incidence and mortality rates,” *Journal of Pediatric Surgery*, vol. 39, no. 5, pp. 690–695, May 2004, doi: 10.1016/j.jpedsurg.2004.01.036.

[10] S. S. Kaufman *et al.*, “Indications for pediatric intestinal transplantation: A position paper of the American Society of Transplantation,” *Pediatric Transplantation*, vol. 5, no. 2, pp. 80–87, Apr. 2001, doi: 10.1034/j.1399-3046.2001.005002080.x.

[11] J. Thulesen *et al.*, “Glucagon-like peptide 2 (GLP-2) accelerates the growth of colonic neoplasms in mice,” *Gut*, vol. 53, no. 8, p. 1145, Aug. 2004, doi: 10.1136/gut.2003.035212.

[12] S. Layec *et al.*, “Increased intestinal absorption by segmental reversal of the small bowel in adult patients with short-bowel syndrome: a case-control study,” *The American Journal of Clinical Nutrition*, vol. 97, no. 1, pp. 100–108, Jan. 2013, doi: 10.3945/ajcn.112.042606.

[13] T. R. Weber and M. A. Powell, “Early improvement in intestinal function after isoperistaltic bowel lengthening,” *Journal of Pediatric Surgery*, vol. 31, no. 1, pp. 61–64, Jan. 1996, doi: 10.1016/S0022-3468(96)90320-6.
[14] A. Rege and D. Sudan, “Intestinal transplantation,” *Best Practice & Research Clinical Gastroenterology*, vol. 30, no. 2, pp. 319–335, Apr. 2016, doi: 10.1016/j.bpg.2016.02.010.
[15] O. B. Lao, P. J. Healey, J. D. Perkins, S. Horslen, J. D. Reyes, and A. B. Goldin, “Outcomes in children after intestinal transplant,” *Pediatrics*, vol. 125, no. 3, pp. e550–e558, Mar. 2010, doi: 10.1542/peds.2009-1713.
[16] J. O. Al Madani, “Second Generation Self-Inflating Tissue Expanders: A Two-Year Experience,” *Plastic Surgery International*, vol. 2014, p. 457205, Jan. 2014, doi: 10.1155/2014/457205.
[17] F. Shanahan, “Crohn’s disease,” *The Lancet*, vol. 359, no. 9300, pp. 62–69, Jan. 2002, doi: 10.1016/S0140-6736(02)07284-7.
[18] D. King *et al.*, “Changing patterns in the epidemiology and outcomes of inflammatory bowel disease in the United Kingdom: 2000-2018,” *Alimentary Pharmacology & Therapeutics*, vol. 51, no. 10, pp. 922–934, May 2020, doi: 10.1111/apt.15701.
[19] T. J. Pasvol *et al.*, “Incidence and prevalence of inflammatory bowel disease in UK primary care: a population-based cohort study,” *BMJ Open*, vol. 10, no. 7, p. e036584, Jul. 2020, doi: 10.1136/bmjopen-2019-036584.
[20] W. Y. Mak, A. L. Hart, and S. C. Ng, “Crohn’s disease,” *Medicine*, vol. 47, no. 6, pp. 377–387, Jun. 2019, doi: 10.1016/j.mpmed.2019.03.007.
[21] F. Pallone and G. Monteleone, “Mechanisms of tissue damage in inflammatory bowel disease,” *Current Opinion in Gastroenterology*, vol. 17, no. 4, 2001, [Online]. Available: https://journals.lww.com/co-gastroenterology/Fulltext/2001/07000/Mechanisms_of_tissue_damage_in_inflammatory_bowel.2.aspx
[22] M. F. Graham, “Pathogenesis of Intestinal Strictures in Crohn’s Disease—An Update,” *Inflammatory Bowel Diseases*, vol. 1, no. 3, pp. 220–227, Aug. 1995, doi: 10.1097/00054725-199509000-00008.
[23] G. Van Assche, “Can we influence fibrosis in Crohn’s disease?,” *Acta gastro-enterologica Belgica*, vol. 64, no. 2, pp. 193–196, 2001.
[24] J. P. Burke, J. J. Mulsow, C. O’Keane, N. G. Docherty, R. W. G. Watson, and P. R. O’Connell, “Fibrogenesis in Crohn’s Disease,” *Official journal of the American College of Gastroenterology | ACG*, vol. 102, no. 2, 2007, [Online]. Available: https://journals.lww.com/ajg/Fulltext/2007/02000/Fibrogenesis_in_Crohn_s_Disease.29.aspx
[25] F. Rieder and C. Fiocchi, “Mechanisms of Tissue Remodeling in Inflammatory Bowel Disease,” *Digestive Diseases*, vol. 31, no. 2, pp. 186–193, 2013, doi: 10.1159/000353364.
[26] T. Hisamatsu, “Typical Endoscopic Findings and Diagnostic Criteria for Crohn’s Disease,” in *Advances in Endoscopy in Inflammatory Bowel Disease*, T. Hibi, T. Hisamatsu, and T. Kobayashi, Eds. Tokyo: Springer Japan, 2018, pp. 77–83. doi: 10.1007/978-4-431-56018-0_8.

[27] D. C. Stewart *et al.*, “Quantitative assessment of intestinal stiffness and associations with fibrosis in human inflammatory bowel disease,” *PLOS ONE*, vol. 13, no. 7, p. e0200377, Jul. 2018, doi: 10.1371/journal.pone.0200377.
[28] M. F. Graham *et al.*, “Collagen content and types in the intestinal strictures of Crohn’s disease,” *Gastroenterology*, vol. 94, no. 2, pp. 257–265, Feb. 1988, doi: 10.5555/uri:pii:0016508588904118.
[29] A. Stallmach, D. Schuppan, H. H. Riese, H. Matthes, and E. O. Riecken, “Increased collagen type III synthesis by fibroblasts isolated from strictures of patients with Crohn’s disease,” *Gastroenterology*, vol. 102, no. 6, pp. 1920–1929, Jun. 1992, doi: 10.1016/0016-5085(92)90314-O.
[30] H. P. Ehrlich, “The Role of the Connective Tissue Matrix in Wound Healing: Fibroblast and Collagen Interactions,” in *Wound Healing and Skin Physiology*, Berlin, Heidelberg, 1995, pp. 89–104.
[31] A. J. Bailey, S. Bazin, T. J. Sims, M. Le Lous, C. Nicoletis, and A. Delaunay, “Characterization of the collagen of human hypertrophic and normal scars,” *Biochimica et Biophysica Acta (BBA) - Protein Structure*, vol. 405, no. 2, pp. 412–421, Oct. 1975, doi: 10.1016/0005-2795(75)90106-3.
[32] H. Paul Ehrlich and B. S. White, “The identification of αA and αB collagen chains in hypertrophic scar,” *Experimental and Molecular Pathology*, vol. 34, no. 1, pp. 1–8, Feb. 1981, doi: 10.1016/0014-4800(81)90030-7.
[33] C. Gao, L. Arendt-Nielsen, W. Liu, P. Petersen, A. M. Drewes, and H. Gregersen, “Sensory and biomechanical responses to ramp-controlled distension of the human duodenum,” *American Journal of Physiology-Gastrointestinal and Liver Physiology*, vol. 284, no. 3, pp. G461–G471, Mar. 2003, doi: 10.1152/ajpgi.00456.2001.
[34] P. Petersen *et al.*, “Sensory and Biomechanical Responses to Distension of the Normal Human Rectum and Sigmoid Colon,” *Digestion*, vol. 64, no. 3, pp. 191–199, 2001, doi: 10.1159/000048861.
[35] M. Zhao, D. Liao, and J. Zhao, “Diabetes-induced mechanophysiological changes in the small intestine and colon,” *World J Diabetes*, vol. 8, no. 6, pp. 249–269, Jun. 2017, doi: 10.4239/wjd.v8.i6.249.
[36] J. B. Frokjaer, S.-D. Andersen, N. Ejskjaer, P. Funch-Jensen, A.-M. Drewes, and H. Gregersen, “Impaired contractility and remodeling of the upper gastrointestinal tract in diabetes mellitus type-1,” *World J Gastroenterol*, vol. 13, no. 36, pp. 4881–4890, Sep. 2007, doi: 10.3748/wjg.v13.i36.4881.
[37] M. J. Siegman, M. Eto, and T. M. Butler, “Remodeling of the rat distal colon in diabetes: function and ultrastructure,” *American Journal of Physiology-Cell Physiology*, vol. 310, no. 2, pp. C151–C160, Jan. 2016, doi: 10.1152/ajpcell.00253.2015.
[38] L. A. Johnson *et al.*, “Matrix stiffness corresponding to strictured bowel induces a fibrogenic response in human colonic fibroblasts,” *Inflamm Bowel Dis*, vol. 19, no. 5, pp. 891–903, Apr. 2013, doi: 10.1097/MIB.0b013e3182813297.
[39] R. W. Stidham *et al.*, “Ultrasound Elasticity Imaging for Detecting Intestinal Fibrosis and Inflammation in Rats and Humans With Crohn’s Disease,” *Gastroenterology*, vol. 141, no. 3, pp. 819-826.e1, Sep. 2011, doi: 10.1053/j.gastro.2011.07.027.

[40] A. Fichera and F. Michelassi, “Surgical Treatment of Crohn’s Disease,” *Journal of Gastrointestinal Surgery*, vol. 11, no. 6, pp. 791–803, Jun. 2007, doi: 10.1007/s11605-006-0068-9.
[41] O. Bernell, A. Lapidus, and G. Hellers, “Risk factors for surgery and postoperative recurrence in Crohn’s disease,” *Ann Surg*, vol. 231, no. 1, pp. 38–45, Jan. 2000, doi: 10.1097/00000658-200001000-00006.
[42] A. J. Greenstein, D. B. Sachar, B. S. Pasternack, and H. D. Janowitz, “Reoperation and Recurrence in Crohn’s Colitis and Ileocolitis,” *N Engl J Med*, vol. 293, no. 14, pp. 685–690, Oct. 1975, doi: 10.1056/NEJM197510022931403.
[43] D. W. Dietz *et al.*, “Strictureplasty in Diffuse Crohn’s Jejunoileitis,” *Diseases of the Colon & Rectum*, vol. 45, no. 6, pp. 764–770, Jun. 2002, doi: 10.1007/s10350-004-6294-x.
[44] J. Polito 2nd, B. Childs, E. Mellits, A. Tokayer, M. Harris, and T. Bayless, “Crohn’s disease: Influence of age at diagnosis on site and clinical type of disease,” *Gastroenterology*, vol. 111, no. 3, pp. 580–586, Sep. 1996, doi: 10.1053/gast.1996.v111.pm8780560.
[45] T. Yamamoto, R. N. Allan, and M. R. B. Keighley, “Long-term outcome of surgical management for diffuse jejunoileal Crohn’s disease,” *Surgery*, vol. 129, no. 1, pp. 96–102, Jan. 2001, doi: 10.1067/msy.2001.109497.
[46] C. Chardavoyne, G. W. Flint, S. Pollack, and L. Wise, “Factors affecting recurrence following resection for Crohn’s disease,” *Diseases of the Colon & Rectum*, vol. 29, no. 8, pp. 495–502, Aug. 1986, doi: 10.1007/BF02562601.
[47] A. O. Agwunobi, G. L. Carlson, I. D. Anderson, M. H. Irving, and N. A. Scott, “Mechanisms of intestinal failure in Crohn’s disease,” *Diseases of the Colon & Rectum*, vol. 44, no. 12, pp. 1834–1837, Dec. 2001, doi: 10.1007/BF02234463.
[48] M. Kristensen, K. Lenz, O. V. Nielsen, and S. Jarnum, “Short Bowel Syndrome Following Resection for Crohn’s Disease,” *null*, vol. 9, no. 6, pp. 559–565, Sep. 1974, doi: 10.1080/00365521.1974.12096875.
[49] J. Vanderhoof and A. Langnas, “Short-bowel syndrome in children and adults,” *Gastroenterology*, vol. 113, no. 5, pp. 1767–1778, Nov. 1997, doi: 10.1053/gast.1997.v113.pm9352883.
[50] M. E. Höllwarth, “Short bowel syndrome: pathophysiological and clinical aspects,” *Pathophysiology*, vol. 6, no. 1, pp. 1–19, 1999.
[51] Y. Wouters, B. Roosenboom, E. Causevic, W. Kievit, H. Groenewoud, and G. J. A. Wanten, “Clinical outcomes of home parenteral nutrition patients using taurolidine as catheter lock: A long-term cohort study,” *Clinical Nutrition*, vol. 38, no. 5, pp. 2210–2218, Oct. 2019, doi: 10.1016/j.clnu.2018.09.020.
[52] O. Pichitchaipitak, S. Ckumdee, S. Apivanich, D. Chotiprasitsakul, and P. C. Shantavasinkul, “Predictive factors of catheter-related bloodstream infection in patients receiving home parenteral nutrition,” *Nutrition*, vol. 46, pp. 1–6, Feb. 2018, doi: 10.1016/j.nut.2017.08.002.
[53] A. L. Buchman, K. Iyer, and J. Fryer, “Parenteral nutrition–associated liver disease and the role for isolated intestine and intestine/liver transplantation,” *Hepatology*, vol. 43, no. 1, pp. 9–19, Jan. 2006, doi: 10.1002/hep.20997.
[54] T. R. Weber, “Isoperistaltic bowel lengthening for short bowel syndrome in children,” *The American Journal of Surgery*, vol. 178, no. 6, pp. 600–603, Dec. 1999, doi: 10.1016/S0002-9610(99)00218-4.

[55] A. Bianchi, “From the Cradle to Enteral Autonomy: The Role of Autologous Gastrointestinal Reconstruction,” *Gastroenterology*, vol. 130, no. 2, Supplement, pp. S138–S146, Feb. 2006, doi: 10.1053/j.gastro.2005.09.070.
[56] B. P. Modi *et al.*, “First report of the international serial transverse enteroplasty data registry: indications, efficacy, and complications,” *J Am Coll Surg*, vol. 204, no. 3, pp. 365–371, Mar. 2007, doi: 10.1016/j.jamcollsurg.2006.12.033.
[57] A. Rege, “The Surgical Approach to Short Bowel Syndrome - Autologous Reconstruction versus Transplantation,” *Viszeralmedizin*, vol. 30, no. 3, pp. 179–189, Jun. 2014, doi: 10.1159/000363589.
[58] B. N. Limketkai, B. Orandi, X. Luo, J.-F. Colombel, and D. L. Segev, “Sa1151 intestinal transplantation for Crohn’s disease: a 5-year nationwide follow-up,” *Gastroenterology*, vol. 148, no. 4, p. S-241, 2015.
[59] J. Park, D. P. Puapong, B. M. Wu, J. B. Atkinson, and J. C. Y. Dunn, “Enterogenesis by mechanical lengthening: Morphology and function of the lengthened small intestine,” *Journal of Pediatric Surgery*, vol. 39, no. 12, pp. 1823–1827, Dec. 2004, doi: 10.1016/j.jpedsurg.2004.08.022.
[60] P. C. Y. Chang *et al.*, “Sustainability of mechanically lengthened bowel in rats,” *Journal of Pediatric Surgery*, vol. 41, no. 12, pp. 2019–2022, Dec. 2006, doi: 10.1016/j.jpedsurg.2006.08.014.
[61] S. Shekherdimian, A. Scott, A. Chan, and J. C. Y. Dunn, “Intestinal lengthening in rats after massive small intestinal resection,” *Surgery*, vol. 146, no. 2, pp. 291–295, Aug. 2009, doi: 10.1016/j.surg.2009.03.034.
[62] S. D. Safford, A. J. Freemerman, K. M. Safford, R. Bentley, and M. A. Skinner, “Longitudinal mechanical tension induces growth in the small bowel of juvenile rats,” *Gut*, vol. 54, no. 8, p. 1085, Aug. 2005, doi: 10.1136/gut.2004.061481.
[63] D. P. Puapong, B. M. Wu, M. M. Lam, J. B. Atkinson, and J. C. Y. Dunn, “Distension enterogenesis: increasing the size and function of small intestine,” *Journal of Pediatric Surgery*, vol. 41, no. 4, pp. 763–767, Apr. 2006, doi: 10.1016/j.jpedsurg.2006.02.017.
[64] A. U. Spencer *et al.*, “Enterogenesis in a clinically feasible model of mechanical small-bowel lengthening,” *Surgery*, vol. 140, no. 2, pp. 212–220, Aug. 2006, doi: 10.1016/j.surg.2006.03.005.
[65] J. Luntz, D. Brei, D. Teitelbaum, and A. Spencer, “Mechanical Extension Implants for Short-Bowel Syndrome,” *Proc SPIE Int Soc Opt Eng*, vol. 6173, pp. 617309–617309, 2006, doi: 10.1117/12.659112.
[66] S. Shekherdimian, M. K. Panduranga, G. P. Carman, and J. C. Y. Dunn, “The feasibility of using an endoluminal device for intestinal lengthening,” *Journal of Pediatric Surgery*, vol. 45, no. 8, pp. 1575–1580, Aug. 2010, doi: 10.1016/j.jpedsurg.2010.03.015.
[67] R. Stark, T. Zupekan, S. Bondada, and J. C. Y. Dunn, “Restoration of mechanically lengthened jejunum into intestinal continuity in rats,” *Journal of Pediatric Surgery*, vol. 46, no. 12, pp. 2321–2326, Dec. 2011, doi: 10.1016/j.jpedsurg.2011.09.019.
[68] N. Huynh *et al.*, “Feasibility and scalability of spring parameters in distraction enterogenesis in a murine model,” *Journal of Surgical Research*, vol. 215, pp. 219–224, Jul. 2017, doi: 10.1016/j.jss.2017.04.009.
[69] G. Dubrovsky, N. Huynh, A.-L. Thomas, S. Shekherdimian, and J. C. Dunn, “Double plication for spring-mediated in-continuity intestinal lengthening in a

porcine model," *Surgery*, vol. 165, no. 2, pp. 389–392, Feb. 2019, doi: 10.1016/j.surg.2018.07.028.
[70] G. Dubrovsky, N. Huynh, A.-L. Thomas, S. Shekherdimian, and J. C. Dunn, "Intestinal lengthening via multiple in-continuity springs," *Journal of Pediatric Surgery*, vol. 54, no. 1, pp. 39–43, Jan. 2019, doi: 10.1016/j.jpedsurg.2018.10.036.
[71] V. F. Sullins *et al.*, "Intestinal lengthening in an innovative rodent surgical model," *Journal of Pediatric Surgery*, vol. 49, no. 12, pp. 1791–1794, Dec. 2014, doi: 10.1016/j.jpedsurg.2014.09.022.
[72] V. F. Sullins, J. P. Wagner, A. T. Suwarnasarn, S. L. Lee, B. M. Wu, and J. C. Y. Dunn, "A novel biodegradable device for intestinal lengthening," *Journal of Pediatric Surgery*, vol. 49, no. 1, pp. 109–113, Jan. 2014, doi: 10.1016/j.jpedsurg.2013.09.040.
[73] A. Scott *et al.*, "Repeated Mechanical Lengthening of Intestinal Segments in a Novel Model," *Journal of Pediatric Surgery*, vol. 50, no. 6, pp. 954–957, Jun. 2015, doi: 10.1016/j.jpedsurg.2015.03.020.
[74] A. Scott *et al.*, "Mechanical lengthening in multiple intestinal segments in-series," *Journal of Pediatric Surgery*, vol. 51, no. 6, pp. 957–959, Jun. 2016, doi: 10.1016/j.jpedsurg.2016.02.058.
[75] M. Okawada, H. Mustafa Maria, and D. H. Teitelbaum, "Distraction Induced Enterogenesis: A Unique Mouse Model Using Polyethylene Glycol1," *Journal of Surgical Research*, vol. 170, no. 1, pp. 41–47, Sep. 2011, doi: 10.1016/j.jss.2011.03.041.
[76] R. Sueyoshi, K. M. Woods Ignatoski, M. Okawada, and D. H. Teitelbaum, "Distraction-induced intestinal growth: the role of mechanotransduction mechanisms in a mouse model of short bowel syndrome," *Tissue Eng Part A*, vol. 20, no. 3–4, pp. 830–841, Feb. 2014, doi: 10.1089/ten.TEA.2013.0383.
[77] E. D. Austad and G. L. Rose, "A self-inflating tissue expander.," *Plastic and reconstructive surgery*, vol. 70, no. 5, pp. 588–594, 1982.
[78] K. F. Kobus, "Cleft palate repair with the use of osmotic expanders: a preliminary report," *Journal of Plastic, Reconstructive & Aesthetic Surgery*, vol. 60, no. 4, pp. 414–421, Apr. 2007, doi: 10.1016/j.bjps.2006.01.053.
[79] K. Gu, "Tissue expander inflating due to osmotic driving forces of a shaped body of hydrogel and an aqueous solution," Mar. 1996.
[80] K. G. Wiese, "Osmotically induced tissue expansion with hydrogels: a new dimension in tissue expansion? A preliminary report," *Journal of Cranio-Maxillofacial Surgery*, vol. 21, no. 7, pp. 309–313, Oct. 1993, doi: 10.1016/S1010-5182(05)80353-1.
[81] M. C. Obdeijn, J.-P. A. Nicolai, and P. M. N. Werker, "The osmotic tissue expander: a three-year clinical experience," *Journal of Plastic, Reconstructive & Aesthetic Surgery*, vol. 62, no. 9, pp. 1219–1222, Sep. 2009, doi: 10.1016/j.bjps.2007.12.088.
[82] S. Chummun, P. Addison, and K. J. Stewart, "The osmotic tissue expander: A 5-year experience," *Journal of Plastic, Reconstructive & Aesthetic Surgery*, vol. 63, no. 12, pp. 2128–2132, Dec. 2010, doi: 10.1016/j.bjps.2010.02.002.
[83] O. WICHTERLE and D. LÍM, "Hydrophilic Gels for Biological Use," *Nature*, vol. 185, p. 117, Jan. 1960.

[84] J. Kopeček and J. Yang, "Hydrogels as smart biomaterials," *Polymer International*, vol. 56, no. 9, pp. 1078–1098, Sep. 2007, doi: 10.1002/pi.2253.
[85] A. S. Hoffman, "Hydrogels for biomedical applications," *Advanced Drug Delivery Reviews*, vol. 64, pp. 18–23, Dec. 2012, doi: 10.1016/j.addr.2012.09.010.
[86] Q. Chai, Y. Jiao, and X. Yu, "Hydrogels for Biomedical Applications: Their Characteristics and the Mechanisms behind Them," *Gels*, vol. 3, no. 1, p. 6, Jan. 2017, doi: 10.3390/gels3010006.
[87] B. D. RATNER and A. S. HOFFMAN, "Synthetic Hydrogels for Biomedical Applications," in *Hydrogels for Medical and Related Applications*, vol. 31, 0 vols., AMERICAN CHEMICAL SOCIETY, 1976, pp. 1–36. doi: 10.1021/bk-1976-0031.ch001.
[88] E. Vasheghani-Farahani, D. G. Cooper, J. H. Vera, and M. E. Weber, "Concentration of large biomolecules with hydrogels," *Chemical Engineering Science*, vol. 47, no. 1, pp. 31–40, Jan. 1992, doi: 10.1016/0009-2509(92)80197-K.
[89] D. Gao, H. Xu, M. A. Philbert, and R. Kopelman, "Ultrafine Hydrogel Nanoparticles: Synthetic Approach and Therapeutic Application in Living Cells," *Angewandte Chemie International Edition*, vol. 46, no. 13, pp. 2224–2227, Mar. 2007, doi: 10.1002/anie.200603927.
[90] M. Hamidi, A. Azadi, and P. Rafiei, "Hydrogel nanoparticles in drug delivery," *Advanced drug delivery reviews*, vol. 60, no. 15, pp. 1638–1649, 2008.
[91] U. S. K. Madduma-Bandarage and S. V. Madihally, "Synthetic hydrogels: Synthesis, novel trends, and applications," *Journal of Applied Polymer Science*, vol. 138, no. 19, p. 50376, May 2021, doi: 10.1002/app.50376.
[92] B. T. Raimi-Abraham, S. Mahalingam, M. Edirisinghe, and D. Q. M. Craig, "Generation of poly(N-vinylpyrrolidone) nanofibres using pressurised gyration," *Materials Science and Engineering: C*, vol. 39, pp. 168–176, Jun. 2014, doi: 10.1016/j.msec.2014.02.016.
[93] M. Teodorescu and M. Bercea, "Poly(vinylpyrrolidone) – A Versatile Polymer for Biomedical and Beyond Medical Applications," *Polymer-Plastics Technology and Engineering*, vol. 54, no. 9, pp. 923–943, Jun. 2015, doi: 10.1080/03602559.2014.979506.
[94] N. Sultana, S. Arayne, and Z. Saify, "Polyvinyl pyrrolidone as plasma expander," *J Pak Med Assoc*, vol. 28, no. 10, pp. 147–153, Oct. 1978.
[95] G. J. M. Fechine, J. A. G. Barros, and L. H. Catalani, "Poly(N-vinyl-2-pyrrolidone) hydrogel production by ultraviolet radiation: new methodologies to accelerate crosslinking," *Polymer*, vol. 45, no. 14, pp. 4705–4709, Jun. 2004, doi: 10.1016/j.polymer.2004.05.006.
[96] S. Kadłubowski, A. Henke, P. Ulański, J. M. Rosiak, L. Bromberg, and T. A. Hatton, "Hydrogels of polyvinylpyrrolidone (PVP) and poly(acrylic acid) (PAA) synthesized by photoinduced crosslinking of homopolymers," *Polymer*, vol. 48, no. 17, pp. 4974–4981, Aug. 2007, doi: 10.1016/j.polymer.2007.06.033.
[97] R. Ma, D. Xiong, F. Miao, J. Zhang, and Y. Peng, "Novel PVP/PVA hydrogels for articular cartilage replacement," *Materials Science and Engineering: C*, vol. 29, no. 6, pp. 1979–1983, Aug. 2009, doi: 10.1016/j.msec.2009.03.010.
[98] M. Yang *et al.*, "Effects of polyvinylpyrrolidone both as a binder and pore-former on the release of sparingly water-soluble topiramate from ethylcellulose coated

pellets," *International Journal of Pharmaceutics*, vol. 465, no. 1, pp. 187–196, Apr. 2014, doi: 10.1016/j.ijpharm.2014.02.021.
[99] F. Yañez, A. Concheiro, and C. Alvarez-Lorenzo, "Macromolecule release and smoothness of semi-interpenetrating PVP–pHEMA networks for comfortable soft contact lenses," *European Journal of Pharmaceutics and Biopharmaceutics*, vol. 69, no. 3, pp. 1094–1103, Aug. 2008, doi: 10.1016/j.ejpb.2008.01.023.
[100] K. Halake *et al.*, "Review Recent application developments of water-soluble synthetic polymers," *Journal of Industrial and Engineering Chemistry*, vol. 20, pp. 3913–3918, Jan. 2014, doi: 10.1016/j.jiec.2014.01.006.
[101] T. Jaeblon, "Polymethylmethacrylate: Properties and Contemporary Uses in Orthopaedics," *JAAOS - Journal of the American Academy of Orthopaedic Surgeons*, vol. 18, no. 5, 2010, [Online]. Available: https://journals.lww.com/jaaos/Fulltext/2010/05000/Polymethylmethacrylate__Properties_and.6.aspx
[102] P. Galibert, H. Deramond, P. Rosat, and D. Le Gars, "[Preliminary note on the treatment of vertebral angioma by percutaneous acrylic vertebroplasty]," *Neurochirurgie*, vol. 33, no. 2, pp. 166–168, 1987.
[103] R. Q. Frazer, R. T. Byron, P. B. Osborne, and K. P. West, "PMMA: an essential material in medicine and dentistry," *Journal of long-term effects of medical implants*, vol. 15, no. 6, 2005.
[104] A. W. Lloyd, R. G. A. Faragher, and S. P. Denyer, "Ocular biomaterials and implants," *Biomaterials*, vol. 22, no. 8, pp. 769–785, Apr. 2001, doi: 10.1016/S0142-9612(00)00237-4.
[105] K. K. H. Gundlach, R. F. Guthoff, V. H. M. Hingst, M. P. Schittkowski, and U. C. Bier, "Expansion of the socket and orbit for congenital clinical anophthalmia," *Plastic and reconstructive surgery*, vol. 116, no. 5, pp. 1214–1222, 2005.
[106] M. A. Ronert, H. Hofheinz, E. Manassa, H. Asgarouladi, and R. R. Olbrisch, "The beginning of a new era in tissue expansion: self-filling osmotic tissue expander—four-year clinical experience," *Plastic and Reconstructive Surgery*, vol. 114, no. 5, pp. 1025–1031, 2004.
[107] M. C. Swan, D. G. Bucknall, J. T. Czernuszka, D. W. Pigott, and T. E. Goodacre, "Development of a novel anisotropic self-inflating tissue expander: in vivo submucoperiosteal performance in the porcine hard palate," *Plastic and reconstructive surgery*, vol. 129, no. 1, pp. 79–88, 2012.
[108] Y. Zhu and J. T. Czernuszka, "Inter-penetrating Polymer Network Hydrogel Tissue Expanders with Controlled Expansion and Anisotropic Properties," *Journal of Medical and Bioengineering Vol*, vol. 4, no. 2, 2015.
[109] M. C. Swan, D. G. Bucknall, T. E. E. Goodacre, and J. T. Czernuszka, "Synthesis and properties of a novel anisotropic self-inflating hydrogel tissue expander," *Acta Biomaterialia*, vol. 7, no. 3, pp. 1126–1132, Mar. 2011, doi: 10.1016/j.actbio.2010.10.017.
[110] P. H. Corkhill, A. M. Jolly, C. O. Ng, and B. J. Tighe, "Synthetic hydrogels: 1. Hydroxyalkyl acrylate and methacrylate copolymers - water binding studies," *Polymer*, vol. 28, no. 10, pp. 1758–1766, 1987, doi: 10.1016/0032-3861(87)90021-8.
[111] T. P. Davis and M. B. Huglin, "Effect of composition on properties of copolymeric N-vinyl-2-pyrrolidonemethyl methacrylate hydrogels and

organogels," *Polymer*, vol. 31, no. 3, pp. 513–519, Mar. 1990, doi: 10.1016/0032-3861(90)90395-F.
[112] T. P. Davis and M. B. Huglin, "Studies on copolymeric hydrogels of N-vinyl-2-pyrrolidone with 2-hydroxyethyl methacrylate," *Macromolecules*, vol. 22, no. 6, pp. 2824–2829, 1989.
[113] N. A. Peppas, Y. Huang, M. Torres-Lugo, J. H. Ward, and J. Zhang, "Physicochemical Foundations and Structural Design of Hydrogels in Medicine and Biology," *Annu. Rev. Biomed. Eng.*, vol. 2, no. 1, pp. 9–29, Aug. 2000, doi: 10.1146/annurev.bioeng.2.1.9.
[114] C.-C. Lin and A. T. Metters, "Hydrogels in controlled release formulations: Network design and mathematical modeling," *Advanced Drug Delivery Reviews*, vol. 58, no. 12, pp. 1379–1408, Nov. 2006, doi: 10.1016/j.addr.2006.09.004.
[115] P. J. Flory and J. Rehner, "Statistical Mechanics of Cross-Linked Polymer Networks I. Rubberlike Elasticity," *J. Chem. Phys.*, vol. 11, no. 11, pp. 512–520, Nov. 1943, doi: 10.1063/1.1723791.
[116] J. Wang, W. Wu, and Z. Lin, "Kinetics and thermodynamics of the water sorption of 2-hydroxyethyl methacrylate/styrene copolymer hydrogels," *Journal of Applied Polymer Science*, vol. 109, no. 5, pp. 3018–3023, Sep. 2008, doi: 10.1002/app.28403.
[117] M. N. Mason, A. T. Metters, C. N. Bowman, and K. S. Anseth, "Predicting Controlled-Release Behavior of Degradable PLA-b-PEG-b-PLA Hydrogels," *Macromolecules*, vol. 34, no. 13, pp. 4630–4635, Jun. 2001, doi: 10.1021/ma010025y.
[118] G. M. Cruise, D. S. Scharp, and J. A. Hubbell, "Characterization of permeability and network structure of interfacially photopolymerized poly(ethylene glycol) diacrylate hydrogels," *Biomaterials*, vol. 19, no. 14, pp. 1287–1294, Jul. 1998, doi: 10.1016/S0142-9612(98)00025-8.
[119] T. Canal and N. A. Peppas, "Correlation between mesh size and equilibrium degree of swelling of polymeric networks," *Journal of Biomedical Materials Research Part A*, vol. 23, no. 10, pp. 1183–1193, 1989.
[120] M. L. Oyen, "Mechanical characterisation of hydrogel materials," *null*, vol. 59, no. 1, pp. 44–59, Jan. 2014, doi: 10.1179/1743280413Y.0000000022.
[121] T. P. Davis, M. B. Huglin, and D. C. Yip, "Properties of poly (N-vinyl-2-pyrrolidone) hydrogels crosslinked with ethyleneglycol dimethacrylate," *Polymer*, vol. 29, no. 4, pp. 701–706, 1988.
[122] T. P. Davis and M. B. Huglin, "Effect of crosslinker on properties of copolymeric N-vinyl-2-pyrrolidone/methyl methacrylate hydrogels and organogels," *Die Makromolekulare Chemie*, vol. 191, no. 2, pp. 331–343, 1990.
[123] E. Lee, S. Kim, S. Kim, J. Cardinal, and H. Jacobs, "Drug release from hydrogel devices with ratecontrolling barriers," *Journal of membrane science*, vol. 7, no. 3, pp. 293–303, 1980.
[124] A. M. Lowman, "Smart pharmaceuticals," 2008.
[125] H. Omidian, J. G. Rocca, and K. Park, "Advances in superporous hydrogels," *Journal of Controlled Release*, vol. 102, no. 1, pp. 3–12, Jan. 2005, doi: 10.1016/j.jconrel.2004.09.028.
[126] J. Chen, H. Park, and K. Park, "Synthesis of superporous hydrogels: hydrogels with fast swelling and superabsorbent properties," *Journal of Biomedical Materials Research: An Official Journal of The Society for Biomaterials, The*

Japanese Society for Biomaterials, and the Australian Society for Biomaterials, vol. 44, no. 1, pp. 53–62, 1999.
[127] F. A. Dorkoosh, J. C. Verhoef, G. Borchard, M. Rafiee-Tehrani, J. H. M. Verheijden, and H. E. Junginger, "Intestinal absorption of human insulin in pigs using delivery systems based on superporous hydrogel polymers," *International Journal of Pharmaceutics*, vol. 247, no. 1, pp. 47–55, Oct. 2002, doi: 10.1016/S0378-5173(02)00361-7.
[128] R. Gemeinhart and H. Park, "Pore structure of superporous hydrogels," *Polymers for Advanced Technologies - POLYM ADVAN TECHNOL*, vol. 11, pp. 617–625, Aug. 2000, doi: 10.1002/1099-1581(200008/12)11:8/12<617::AID-PAT12>3.0.CO;2-L.
[129] F. Ganji, F. S. Vasheghani, and F. E. VASHEGHANI, "Theoretical description of hydrogel swelling: a review," 2010.
[130] M. F. REFOJO, "Vapor Pressure and Swelling Pressure of Hydrogels," in *Hydrogels for Medical and Related Applications*, vol. 31, 0 vols., AMERICAN CHEMICAL SOCIETY, 1976, pp. 37–51. doi: 10.1021/bk-1976-0031.ch002.
[131] R. W. Korsmeyer, E. Von Meerwall, and N. A. Peppas, "Solute and penetrant diffusion in swellable polymers. II. Verification of theoretical models," *Journal of Polymer Science Part B: Polymer Physics*, vol. 24, no. 2, pp. 409–434, Feb. 1986, doi: 10.1002/polb.1986.090240215.
[132] C. L. Bell and N. A. Peppas, *Biomedical membranes from hydrogels and interpolymer complexes*, vol. 122. 2006. doi: 10.1007/3540587888_15.
[133] P. L. Ritger and N. A. Peppas, "A simple equation for description of solute release I. Fickian and non-fickian release from non-swellable devices in the form of slabs, spheres, cylinders or discs," *Journal of Controlled Release*, vol. 5, no. 1, pp. 23–36, Jun. 1987, doi: 10.1016/0168-3659(87)90034-4.
[134] P. L. Ritger and N. A. Peppas, "A simple equation for description of solute release II. Fickian and anomalous release from swellable devices," *Journal of Controlled Release*, vol. 5, no. 1, pp. 37–42, Jun. 1987, doi: 10.1016/0168-3659(87)90035-6.
[135] R. A. Grinsted, L. Clark, and J. L. Koenig, "Study of cyclic sorption-desorption into poly(methyl methacrylate) rods using NMR imaging," *Macromolecules*, vol. 25, no. 4, pp. 1235–1241, Feb. 1992, doi: 10.1021/ma00030a006.
[136] J. Singh, "Swelling of polymer gels," 1993.
[137] H. Li, T. Y. Ng, Y. K. Yew, and K. Y. Lam, "Modeling and Simulation of the Swelling Behavior of pH-Stimulus-Responsive Hydrogels," *Biomacromolecules*, vol. 6, no. 1, pp. 109–120, Jan. 2005, doi: 10.1021/bm0496458.
[138] A. El Afif and M. Grmela, "Non-Fickian mass transport in polymers," *Journal of Rheology*, vol. 46, no. 3, pp. 591–628, May 2002, doi: 10.1122/1.1470520.
[139] A. K. Bajpai and A. Giri, "Swelling dynamics of a macromolecular hydrophilic network and evaluation of its potential for controlled release of agrochemicals," *Reactive and Functional Polymers*, vol. 53, no. 2, pp. 125–141, Dec. 2002, doi: 10.1016/S1381-5148(02)00168-2.
[140] C. Rogers, "Solubility and diffusivity," *Physics and chemistry of the organic solid state*, vol. 2, pp. 509–635, 1965.
[141] H. Fujita, "Organic vapors above the glass transition temperature," *Diffusion in polymers*, pp. 75–105, 1968.
[142] J. Crank, *The mathematics of diffusion*. Oxford university press, 1979.

[143] T. Alfrey Jr., E. F. Gurnee, and W. G. Lloyd, "Diffusion in glassy polymers," *Journal of Polymer Science Part C: Polymer Symposia*, vol. 12, no. 1, pp. 249–261, Jan. 1966, doi: 10.1002/polc.5070120119.
[144] C. S. Brazel and N. A. Peppas, "Modeling of drug release from Swellable polymers," *European Journal of Pharmaceutics and Biopharmaceutics*, vol. 49, no. 1, pp. 47–58, Jan. 2000, doi: 10.1016/S0939-6411(99)00058-2.
[145] E. Karadağ, D. Saraydin, Y. Çaldiran, and O. Güven, "Swelling studies of copolymeric acrylamide/crotonic acid hydrogels as carriers for agricultural uses," *Polymers for Advanced Technologies*, vol. 11, no. 2, pp. 59–68, Feb. 2000, doi: 10.1002/(SICI)1099-1581(200002)11:2<59::AID-PAT937>3.0.CO;2-Z.
[146] K. S. Anseth, C. N. Bowman, and L. Brannon-Peppas, "Mechanical properties of hydrogels and their experimental determination," *Biomaterials*, vol. 17, no. 17, pp. 1647–1657, 1996.
[147] S. R. Lustig, J. M. Caruthers, and N. A. Peppas, "Dynamic mechanical properties of polymer-fluid systems: characterization of poly (2-hydroxyethyl methacrylate) and poly (2-hydroxyethyl methacrylate-co-methyl methacrylate) hydrogels," *Polymer*, vol. 32, no. 18, pp. 3340–3353, 1991.
[148] D. Katz, "The correlation between some mechanical properties of highly cross-linked polymers and the nature of their cross-linking site," presented at the Colloq. Int. CNRS, 1975, vol. 231, pp. 261–269.
[149] A. Greenberg and R. Kusy, "Viscoelastic behavior of highly crosslinked poly (acrylic acid)," *Journal of Applied Polymer Science*, vol. 25, no. 12, pp. 2795–2805, 1980.
[150] O. Ariga, M. Kato, T. Sano, Y. Nakazawa, and Y. Sano, "Mechanical and kinetic properties of PVA hydrogel immobilizing β-galactosidase," *Journal of fermentation and bioengineering*, vol. 76, no. 3, pp. 203–206, 1993.
[151] J. H. Lee and D. G. Bucknall, "Swelling behavior and network structure of hydrogels synthesized using controlled UV-initiated free radical polymerization," *Journal of Polymer Science Part B: Polymer Physics*, vol. 46, no. 14, pp. 1450–1462, 2008.
[152] N. J. Amoroso, A. D'Amore, Y. Hong, C. P. Rivera, M. S. Sacks, and W. R. Wagner, "Microstructural manipulation of electrospun scaffolds for specific bending stiffness for heart valve tissue engineering," *Acta Biomaterialia*, vol. 8, no. 12, pp. 4268–4277, Dec. 2012, doi: 10.1016/j.actbio.2012.08.002.
[153] M. Ahearne, Y. Yang, and K. Liu, "Mechanical characterisation of hydrogels for tissue engineering applications," *Topics in tissue Engineering*, vol. 4, no. 12, pp. 1–16, 2008.
[154] W. D. Callister and D. G. Rethwisch, *Materials science and engineering*, vol. 5. John wiley & sons New York, 2011.
[155] Q. Liu, G. Subhash, and D. F. Moore, "Loading velocity dependent permeability in agarose gel under compression," *Journal of the Mechanical Behavior of Biomedical Materials*, vol. 4, no. 7, pp. 974–982, Oct. 2011, doi: 10.1016/j.jmbbm.2011.02.009.
[156] T. P. Davis and M. B. Huglin, "Effect of composition on properties of copolymeric N-vinyl-2-pyrrolidonemethyl methacrylate hydrogels and organogels," *Polymer*, vol. 31, no. 3, pp. 513–519, Mar. 1990, doi: 10.1016/0032-3861(90)90395-F.

[157] K. K. Reed and R. Wickham, “Review of the Gastrointestinal Tract: From Macro to Micro,” *Seminars in Oncology Nursing*, vol. 25, no. 1, pp. 3–14, Feb. 2009, doi: 10.1016/j.soncn.2008.10.002.
[158] M. Mir, U. Ansari, M. N. Ali, and J. Sami, “Structure and Motility of the Esophagus from a Mechanical Perspective,” *Esophagus*, vol. 13, Apr. 2015, doi: 10.1007/s10388-015-0497-1.
[159] J. S. Lowe, P. G. Anderson, and S. Anderson, *Stevens & Lowe’s Human Histology-E-Book*. Elsevier Health Sciences, 2018.
[160] H. Gregersen, *Biomechanics of the gastrointestinal tract: new perspectives in motility research and diagnostics*. Springer Science & Business Media, 2003.
[161] E. H. Epstein and N. H. Munderloh, “Isolation and characterization of CNBr peptides of human (alpha 1 (III)) 3 collagen and tissue distribution of (alpha 1 (I)) 2 alpha 2 and (alpha 1 (III)) 3 collagens.,” *Journal of Biological Chemistry*, vol. 250, no. 24, pp. 9304–9312, 1975.
[162] J. Carneiro and L. C. Junqueira, *Basic histology: text & atlas*. McGraw-Hill, 2005.
[163] W. Yang, T. C. Fung, K. S. Chian, and C. K. Chong, “Directional, Regional, and Layer Variations of Mechanical Properties of Esophageal Tissue and its Interpretation Using a Structure-Based Constitutive Model,” *Journal of Biomechanical Engineering*, vol. 128, no. 3, pp. 409–418, Nov. 2005, doi: 10.1115/1.2187033.
[164] W. Yang, T. C. Fung, K. S. Chian, and C. K. Chong, “3D Mechanical Properties of the Layered Esophagus: Experiment and Constitutive Model,” *Journal of Biomechanical Engineering*, vol. 128, no. 6, pp. 899–908, May 2006, doi: 10.1115/1.2354206.
[165] K. Schulze, S. Ellerbroek, and J. Martin, “Matrix composition in opossum esophagus,” *Digestive diseases and sciences*, vol. 46, no. 5, pp. 968–975, 2001.
[166] H. Gregersen, I. M. Giversen, L. M. Rasmussen, and A. Tøttrup, “Biomechanical wall properties and collagen content in the partially obstructed opossum esophagus,” *Gastroenterology*, vol. 103, no. 5, pp. 1547–1551, Nov. 1992, doi: 10.5555/uri:pii:0016508592911765.
[167] L. Bonavina, M. Venturi, L. Colombo, A. Segalin, E. Mussini, and A. Peracchia, “Elastic Properties of the Normal Human Esophagus-A Biochemical Study,” presented at the Gastroenterology, 1995, vol. 108, pp. A573–A573.
[168] A. N. Natali, E. L. Carniel, and H. Gregersen, “Biomechanical behaviour of oesophageal tissues: Material and structural configuration, experimental data and constitutive analysis,” *Medical Engineering & Physics*, vol. 31, no. 9, pp. 1056–1062, Nov. 2009, doi: 10.1016/j.medengphy.2009.07.003.
[169] V. I. Egorov, I. V. Schastlivtsev, E. V. Prut, A. O. Baranov, and R. A. Turusov, “Mechanical properties of the human gastrointestinal tract,” *Journal of Biomechanics*, vol. 35, no. 10, pp. 1417–1425, Oct. 2002, doi: 10.1016/S0021-9290(02)00084-2.
[170] S. La Francesca *et al.*, “Long-term regeneration and remodeling of the pig esophagus after circumferential resection using a retrievable synthetic scaffold carrying autologous cells,” *Scientific reports*, vol. 8, no. 1, p. 4123, 2018.
[171] E. A. Stavropoulou, Y. F. Dafalias, and D. P. Sokolis, “Biomechanical behavior and histological organization of the three-layered passive esophagus as

a function of topography," *Proc Inst Mech Eng H*, vol. 226, no. 6, pp. 477–490, Apr. 2012, doi: 10.1177/0954411912444073.
[172] J. King, "Gastrointestinal Anatomy," *Critical Care Nursing: Synergy for Optimal Outcomes*, p. 413, 2007.
[173] A. Doig and S. Huether, "Structure and function of the digestive system," in *Pathophysiology*, Elsevier Mosby, St Louis (MO), 2006, pp. 1393–1422.
[174] I. Alcamo, *Anatomy and physiology*. Hauppauġe: NY: Barron's Educational Series, Inc, 1996.
[175] G. L. Rapaccini *et al.*, "Gastric wall thickness in normal and neoplastic subjects: A prospective study performed by abdominal ultrasound," *Gastrointestinal Radiology*, vol. 13, no. 1, pp. 197–199, Dec. 1988, doi: 10.1007/BF01889058.
[176] A. L. Kierszenbaum and L. Tres, *Histology and cell biology: an introduction to pathology E-book*. Elsevier Health Sciences, 2015.
[177] S. Brandstaeter, S. L. Fuchs, R. C. Aydin, and C. J. Cyron, "Mechanics of the stomach: A review of an emerging field of biomechanics," *GAMM-Mitteilungen*, vol. 42, no. 3, p. e201900001, Sep. 2019, doi: 10.1002/gamm.201900001.
[178] N. Mori *et al.*, "Helicobacter pylori induces matrix metalloproteinase-9 through activation of nuclear factor κB," *Gastroenterology*, vol. 124, no. 4, pp. 983–992, 2003.
[179] M. F. de Mello, A. Pissinatti, and A. M. Ferreira, "Distribution of collagen types I, III, and IV in gastric tissue of marmosets (Callithrix spp., Callitrichidae: Primates)," *Pesquisa Veterinária Brasileira*, vol. 30, no. 4, pp. 317–320, 2010.
[180] A. Gillessen, B. Voß, J. Rauterberg, and W. Domschke, "Distribution of Collagen Types I, III, and IV in Peptic Ulcer and Normal Gastric Mucosa in Man," *Scandinavian Journal of Gastroenterology*, vol. 28, no. 8, pp. 688–689, Jan. 1993, doi: 10.3109/00365529309098273.
[181] M. Shahin *et al.*, "Gastric ulcer healing in the rat: Kinetics and localisation of de novo procollagen synthesis," *Gut*, vol. 41, pp. 187–94, Sep. 1997, doi: 10.1136/gut.41.2.187.
[182] M. Aumailley and B. Gayraud, "Structure and biological activity of the extracellular matrix," *Journal of Molecular Medicine*, vol. 76, no. 3–4, pp. 253–265, 1998.
[183] T. Guszczyn and K. Sobolewski, "Deregulation of Collagen Metabolism in Human Stomach Cancer," *Pathobiology*, vol. 71, no. 6, pp. 308–313, 2004.
[184] F. Azpiroz and J. R. Malagelada, "Physiological variations in canine gastric tone measured by an electronic barostat," *American Journal of Physiology-Gastrointestinal and Liver Physiology*, vol. 248, no. 2, pp. G229–G237, Feb. 1985, doi: 10.1152/ajpgi.1985.248.2.G229.
[185] F. Azpiroz and J.-R. Malagelada, "Gastric Tone Measured by an Electronic Barostat in Health arid Postsurgical Gastroparesis," *Gastroenterology*, vol. 92, no. 4, pp. 934–943, Apr. 1987, doi: 10.1016/0016-5085(87)90967-X.
[186] W. E. Whitehead and M. Delvaux, "Standardization of Barostat Procedures for Testing Smooth Muscle Tone and Sensory Thresholds in the Gastrointestinal Tract," *Digestive Diseases and Sciences*, vol. 42, no. 2, pp. 223–241, Feb. 1997, doi: 10.1023/A:1018885028501.
[187] D. Liao, J. Zhao, and H. Gregersen, "Regional surface geometry of the rat stomach based on three-dimensional curvature analysis," *Physics in Medicine*

and Biology, vol. 50, no. 2, pp. 231–246, Dec. 2004, doi: 10.1088/0031-9155/50/2/004.
[188] J. Zhao, D. Liao, and H. Gregersen, "Tension and stress in the rat and rabbit stomach are location- and direction-dependent," *Neurogastroenterology & Motility*, vol. 17, no. 3, pp. 388–398, 2005, doi: 10.1111/j.1365-2982.2004.00635.x.
[189] J. Zhao, D. Liao, P. Chen, P. Kunwald, and H. Gregersen, "Stomach stress and strain depend on location, direction and the layered structure," *Journal of Biomechanics*, vol. 41, no. 16, pp. 3441–3447, Dec. 2008, doi: 10.1016/j.jbiomech.2008.09.008.
[190] Z. G. Jia, W. Li, and Z. R. Zhou, "Mechanical characterization of stomach tissue under uniaxial tensile action," *Journal of Biomechanics*, vol. 48, no. 4, pp. 651–658, Feb. 2015, doi: 10.1016/j.jbiomech.2014.12.048.
[191] J. T. Collins, A. Nguyen, and M. Badireddy, *Anatomy, Abdomen and Pelvis, Small Intestine*. StatPearls Publishing, Treasure Island (FL), 2021. [Online]. Available: http://europepmc.org/abstract/MED/29083773
[192] R. K. Clark, *Anatomy and physiology: understanding the human body*. Jones & Bartlett Learning, 2005.
[193] T. KOMURO and Y. HASHIMOTO, "Three-dimensional structure of the rat intestinal wall (mucosa and submucosa)," *Archives of histology and cytology*, vol. 53, no. 1, pp. 1–21, 1990.
[194] D. Rumsey, "SMALL INTESTINE | Structure and Function," in *Encyclopedia of Human Nutrition (Second Edition)*, B. Caballero, Ed. Oxford: Elsevier, 2005, pp. 126–133. doi: 10.1016/B0-12-226694-3/02255-9.
[195] G. Gabella, "The cross-ply arrangement of collagen fibres in the submucosa of the mammalian small intestine," *Cell and Tissue Research*, vol. 248, no. 3, pp. 491–497, Jun. 1987, doi: 10.1007/BF00216474.
[196] J. Orberg, L. Klein, and A. Hiltner, "Scanning electron microscopy of collagen fibers in intestine," *Connective tissue research*, vol. 9, no. 3, pp. 187–193, 1982.
[197] J. Orberg, E. Baer, and A. Hiltner, "Organization of Collagen Fibers in the Intestine," *Connective Tissue Research*, vol. 11, no. 4, pp. 285–297, Jan. 1983, doi: 10.3109/03008208309004861.
[198] T. Komuro, "The lattice arrangement of the collagen fibres in the submucosa of the rat small intestine: scanning electron microscopy," *Cell and Tissue Research*, vol. 251, no. 1, pp. 117–121, Jan. 1988, doi: 10.1007/BF00215455.
[199] S. F. Badylak *et al.*, "The use of xenogeneic small intestinal submucosa as a biomaterial for Achille's tendon repair in a dog model," *Journal of Biomedical Materials Research*, vol. 29, no. 8, pp. 977–985, Aug. 1995, doi: 10.1002/jbm.820290809.
[200] J. P. Hodde, S. F. Badylak, A. O. Brightman, and S. L. Voytik-Harbin, "Glycosaminoglycan Content of Small Intestinal Submucosa: A Bioscaffold for Tissue Replacement," *Tissue Engineering*, vol. 2, no. 3, pp. 209–217, Sep. 1996, doi: 10.1089/ten.1996.2.209.
[201] J. Hodde, R. Record, R. Tullius, and S. Badylak, "Fibronectin peptides mediate HMEC adhesion to porcine-derived extracellular matrix," *Biomaterials*, vol. 23, no. 8, pp. 1841–1848, Apr. 2002, doi: 10.1016/S0142-9612(01)00310-6.
[202] STORKHOLM J. H., VILLADSEN G. E., JENSEN S. L., and GREGERSEN H., "Mechanical properties and collagen content differ between isolated guinea

pig duodenum, jejunum, and distal ileum," *Digestive diseases and sciences*, vol. 43, no. 9, pp. 2034–2041, 1998.
[203] C. Alexakis *et al.*, "Reversal of abnormal collagen production in Crohn's disease intestinal biopsies treated with regenerating agents," *Gut*, vol. 53, no. 1, p. 85, Jan. 2004, doi: 10.1136/gut.53.1.85.
[204] L. L. Azzouz and S. Sharma, "Physiology, Large Intestine," in *StatPearls [Internet]*, StatPearls Publishing, 2019.
[205] E. L. Carniel, V. Gramigna, C. G. Fontanella, C. Stefanini, and A. N. Natali, "Constitutive formulations for the mechanical investigation of colonic tissues," *Journal of Biomedical Materials Research Part A*, vol. 102, no. 5, pp. 1243–1254, May 2014, doi: 10.1002/jbm.a.34787.
[206] A. Inan, Ö. SÜRGİT, M. Şen, A. Akpinar, and M. Bozer, "Etofenamate and anastomoses of the colon in rats," *Turkish Journal of Medical Sciences*, vol. 39, no. 5, pp. 713–718, 2009.
[207] L. Wess, M. A. Eastwood, T. J. Wess, A. Busuttil, and A. Miller, "Cross linking of collagen is increased in colonic diverticulosis.," *Gut*, vol. 37, no. 1, p. 91, Jul. 1995, doi: 10.1136/gut.37.1.91.
[208] C. Gao and H. Gregersen, "Biomechanical and morphological properties in rat large intestine," *Journal of Biomechanics*, vol. 33, no. 9, pp. 1089–1097, Sep. 2000, doi: 10.1016/S0021-9290(00)00067-1.
[209] Y. Qiao, E. Pan, S. S. Chakravarthula, F. Han, J. Liang, and S. Gudlavalleti, "Measurement of mechanical properties of rectal wall," *Journal of Materials Science: Materials in Medicine*, vol. 16, no. 2, pp. 183–188, Jan. 2005, doi: 10.1007/s10856-005-5988-5.
[210] Y. Fung, *Biomechanics. In: Mechanical Properties of Living Tissues*. New York: Springer Science & Business Media-Verlag, 1993.
[211] D. P. Sokolis, I. K. Orfanidis, and M. Peroulis, "Biomechanical testing and material characterization for the rat large intestine: regional dependence of material parameters," *Physiological Measurement*, vol. 32, no. 12, pp. 1969–1982, Nov. 2011, doi: 10.1088/0967-3334/32/12/007.
[212] A. Östman, "RAFT-Polymerization of N-Vinyl Pyrrolidone and MethylMethacrylate for Synthesis of Functional Co-BlockpolymerBinders for Solid Electrolyte Batteries.," 2015.
[213] F. Svec and J. M. J. Frechet, "Temperature, a Simple and Efficient Tool for the Control of Pore Size Distribution in Macroporous Polymers," *Macromolecules*, vol. 28, no. 22, pp. 7580–7582, Oct. 1995, doi: 10.1021/ma00126a044.
[214] O. Okay, "Macroporous copolymer networks," *Progress in Polymer Science*, vol. 25, no. 6, pp. 711–779, Aug. 2000, doi: 10.1016/S0079-6700(00)00015-0.
[215] J. R. Smith, "Developing P(MMA-co-NVP) Hydrogels for Use in Self-Inflating Anisotropic Tissue Expanders," DPhil Thesis, University of Oxford, 2015.
[216] M. C. Swan, "Development of Anisotropic Self-Inflating Tissue Expanders for Clinical Applications," DPhil Thesis, University of Oxford, 2007.
[217] Z. Lin, W. Wu, J. Wang, and X. Jin, "Studies on swelling behaviors, mechanical properties, network parameters and thermodynamic interaction of water sorption of 2-hydroxyethyl methacrylate/novolac epoxy vinyl ester resin copolymeric hydrogels," *Reactive and Functional Polymers*, vol. 67, no. 9, pp. 789–797, Sep. 2007, doi: 10.1016/j.reactfunctpolym.2006.12.010.

[218] N. Yacob and K. Hashim, “Morphological effect on swelling behaviour of hydrogel,” presented at the AIP Conference Proceedings, 2014, vol. 1584, pp. 153–159.
[219] K. Wiese, D. Heinemann, D. Ostermeier, and J. Peters, “Biomaterial properties and biocompatibility in cell culture of a novel self-inflating hydrogel tissue expander,” *Journal of Biomedical Materials Research Part A*, vol. 54, no. 2, pp. 179–188, 2001.
[220] B. Nair, “Final Report On the Safety Assessment of Polyvinylpyrrolidone (PVP),” *Int J Toxicol*, vol. 17, no. 4_suppl, pp. 95–130, Feb. 1998, doi: 10.1177/109158189801700408.
[221] Y. Sakai and K. Nakazawa, “Technique for the control of spheroid diameter using microfabricated chips,” *Acta Biomaterialia*, vol. 3, no. 6, pp. 1033–1040, Nov. 2007, doi: 10.1016/j.actbio.2007.06.004.
[222] V. Sankar, T. S. Kumar, and K. P. Rao, “Preparation, characterisation and fabrication of intraocular lens from photo initiated polymerised poly (methyl methacrylate),” *Trends in Biomaterials and Artificial Organs*, vol. 17, no. 2, p. 24+, Jan. 2004.
[223] DiMaio Frank R, “The Science of Bone Cement: A Historical Review,” *Orthopedics*, vol. 25, no. 12, pp. 1399–1407, Dec. 2002, doi: 10.3928/0147-7447-20021201-21.
[224] G. F. Pauli *et al.*, “Importance of Purity Evaluation and the Potential of Quantitative 1H NMR as a Purity Assay,” *J. Med. Chem.*, vol. 57, no. 22, pp. 9220–9231, Nov. 2014, doi: 10.1021/jm500734a.
[225] B. C. Smith, *Fundamentals of Fourier transform infrared spectroscopy*. CRC press, 2011.
[226] B. Smith, *Infrared spectral interpretation: a systematic approach*. CRC press, 2018.
[227] B. C. Smith, *Quantitative spectroscopy: theory and practice*. Elsevier, 2003.
[228] J. M. Hollas, *Modern spectroscopy*. John Wiley & Sons, 2004.
[229] Y. Borodko, S. E. Habas, M. Koebel, P. Yang, H. Frei, and G. A. Somorjai, “Probing the Interaction of Poly(vinylpyrrolidone) with Platinum Nanocrystals by UV−Raman and FTIR,” *J. Phys. Chem. B*, vol. 110, no. 46, pp. 23052–23059, Nov. 2006, doi: 10.1021/jp063338+.
[230] N. Vijaya *et al.*, “Structural, vibrational, thermal, and conductivity studies on proton-conducting polymer electrolyte based on poly (N-vinylpyrrolidone),” *Ionics*, vol. 18, no. 1, pp. 91–99, 2012.
[231] C. Ambika and G. Hirankumar, “Characterization of CH3SO3H-doped PMMA/PVP blend-based proton-conducting polymer electrolytes and its application in primary battery,” *Applied Physics A*, vol. 122, no. 2, p. 113, Feb. 2016, doi: 10.1007/s00339-016-9642-5.
[232] A. Saroj, R. Singh, and S. Chandra, “Studies on polymer electrolyte poly(vinyl) pyrrolidone (PVP) complexed with ionic liquid: Effect of complexation on thermal stability, conductivity and relaxation behaviour,” *Materials Science and Engineering: B*, vol. 178, pp. 231–238, Mar. 2013, doi: 10.1016/j.mseb.2012.11.007.
[233] A. Moshaverinia *et al.*, “Effects of N-vinylpyrrolidone (NVP) containing polyelectrolytes on surface properties of conventional glass-ionomer cements

(GIC)," *Dental Materials*, vol. 25, no. 10, pp. 1240–1247, Oct. 2009, doi: 10.1016/j.dental.2009.05.006.
[234] C. Menaka, K. S. Velu, P. Manisankar, and T. Stalin, "Conductivity, structural and electrochemical behavior of plasticized polymer electrolytes for dye-sensitised solar cell," 2013.
[235] S. Rajendran, M. Sivakumar, R. Subadevi, N.-L. Wu, and J.-Y. Lee, "Electrochemical investigations on the effect of dispersoid in PVA based solid polymer electrolytes," *Journal of Applied Polymer Science*, vol. 103, no. 6, pp. 3950–3956, Mar. 2007, doi: 10.1002/app.24863.
[236] S. Rajendran and V. S. Bama, "A study on the effect of various plasticizers in poly (vinyl acetate)-poly (methyl methacrylate) based gel electrolytes," *Journal of non-crystalline solids*, vol. 356, no. 50–51, pp. 2764–2768, 2010.
[237] W. A. Zisman, "INFLUENCE OF CONSTITUTION ON ADHESION," *Ind. Eng. Chem.*, vol. 55, no. 10, pp. 18–38, Oct. 1963, doi: 10.1021/ie50646a003.
[238] E. A. Vogler, "Structure and reactivity of water at biomaterial surfaces," *Advances in colloid and interface science*, vol. 74, no. 1–3, pp. 69–117, 1998.
[239] Z. Guo, X. Xu, S. Lu, Y. Xiang, and S. Jiang, "New anhydrous proton exchange membranes for high-temperature fuel cells based on PVDF-PVP blended polymers," *J. Mater. Chem. A*, vol. 3, Nov. 2014, doi: 10.1039/C4TA04952G.
[240] X. Liu *et al.*, "Hydrophilicity, morphology and excellent adsorption ability of poly(vinylidene fluoride) membranes induced by graphene oxide and polyvinylpyrrolidone," *Colloids and Surfaces A: Physicochemical and Engineering Aspects*, vol. 486, pp. 172–184, Sep. 2015, doi: 10.1016/j.colsurfa.2015.09.036.
[241] Q. Wei, Y. Zhang, Y. Wang, W. Chai, and M. Yang, "Measurement and modeling of the effect of composition ratios on the properties of poly(vinyl alcohol)/poly(vinyl pyrrolidone) membranes," *Materials & Design*, vol. 103, pp. 249–258, Aug. 2016, doi: 10.1016/j.matdes.2016.04.087.
[242] D.-G. Yu, X.-X. Shen, C. Branford-White, K. White, L.-M. Zhu, and S. W. Annie Bligh, "Oral fast-dissolving drug delivery membranes prepared from electrospun polyvinylpyrrolidone ultrafine fibers," *Nanotechnology*, vol. 20, no. 5, p. 055104, Jan. 2009, doi: 10.1088/0957-4484/20/5/055104.
[243] D. Rymuszka, K. Terpiłowski, D. Sternik, M. Tomczyńska-Mleko, and O. Goncharuk, "Wettability and thermal analysis of hydrophobic poly(methyl methacrylate)/silica nanocomposites," *Adsorption Science & Technology*, vol. 35, no. 5–6, pp. 560–571, Jun. 2017, doi: 10.1177/0263617417701922.
[244] Y. Ma, X. Cao, X. Feng, Y. Ma, and H. Zou, "Fabrication of super-hydrophobic film from PMMA with intrinsic water contact angle below 90°," *Polymer*, vol. 48, no. 26, pp. 7455–7460, Dec. 2007, doi: 10.1016/j.polymer.2007.10.038.
[245] J. Ko *et al.*, "Hydrophilic surface modification of poly(methyl methacrylate)-based ocular prostheses using poly(ethylene glycol) grafting," *Colloids and Surfaces B: Biointerfaces*, vol. 158, pp. 287–294, Oct. 2017, doi: 10.1016/j.colsurfb.2017.07.017.
[246] R. N. King, J. D. Andrade, S. M. Ma, D. E. Gregonis, and L. R. Brostrom, "Interfacial tensions at acrylic hydrogel-water interfaces," *Journal of Colloid and Interface Science*, vol. 103, no. 1, pp. 62–75, Jan. 1985, doi: 10.1016/0021-9797(85)90077-3.

[247] W. Wu and G. H. Nancollas, “Determination of interfacial tension from crystallization and dissolution data: a comparison with other methods,” *Advances in Colloid and Interface Science*, vol. 79, no. 2, pp. 229–279, Feb. 1999, doi: 10.1016/S0001-8686(98)00072-4.
[248] M. Palencia, “Surface free energy of solids by contact angle measurements,” *J Sci Technol Appl*, vol. 2, pp. 84–93, 2017.
[249] J. A. Clark, J. C. Y. Cheng, and K. S. Leung, “Mechanical properties of normal skin and hypertrophic scars,” *Burns*, vol. 22, no. 6, pp. 443–446, Sep. 1996, doi: 10.1016/0305-4179(96)00038-1.
[250] J. L. Leveque, P. Corcuff, J. de Rigal, and P. Agache, “In Vivo Studies of the Evolution of Physical Properties of the Human Skin with Age,” *International Journal of Dermatology*, vol. 23, no. 5, pp. 322–329, Jun. 1984, doi: 10.1111/j.1365-4362.1984.tb04061.x.
[251] W. Chen *et al.*, “Improved polyvinylpyrrolidone microneedle arrays with non-stoichiometric cyclodextrin,” *J. Mater. Chem. B*, vol. 2, no. 12, pp. 1699–1705, 2014, doi: 10.1039/C3TB21698E.
[252] A. Boger, A. Bisig, M. Bohner, P. Heini, and E. Schneider, “Variation of the mechanical properties of PMMA to suit osteoporotic cancellous bone,” *Journal of Biomaterials Science, Polymer Edition*, vol. 19, no. 9, pp. 1125–1142, Jan. 2008, doi: 10.1163/156856208785540154.
[253] J. Shen, C. C. Chen, and J. A. Sauer, “Effects of sorbed water on properties of low and high molecular weight PMMA: 1. Deformation and fracture behaviour,” *Polymer*, vol. 26, no. 4, pp. 511–518, Apr. 1985, doi: 10.1016/0032-3861(85)90150-8.
[254] O. Okay, “General Properties of Hydrogels,” in *Hydrogel Sensors and Actuators: Engineering and Technology*, G. Gerlach and K.-F. Arndt, Eds. Berlin, Heidelberg: Springer Berlin Heidelberg, 2010, pp. 1–14. doi: 10.1007/978-3-540-75645-3_1.
[255] J. Hao and R. A. Weiss, “Viscoelastic and Mechanical Behavior of Hydrophobically Modified Hydrogels,” *Macromolecules*, vol. 44, no. 23, pp. 9390–9398, Dec. 2011, doi: 10.1021/ma202130u.
[256] D. J. Arnold, *Synthesis and 1H-NMR Characterization of Amphiphilic Acrylate Block Copolymers to Investigate the Effect of Chain Rigidity on Micelle Formation in Solution*. Eastern Michigan University, 2012.
[257] K. Yokota, A. Abe, S. Hosaka, I. Sakai, and H. Saitô, “A 13C nuclear magnetic resonance study of covalently cross-linked gels. Effect of chemical composition, degree of cross-linking, and temperature to chain mobility,” *Macromolecules*, vol. 11, no. 1, pp. 95–100, 1978.
[258] J. E. Mark, “Polymer data handbook,” 2009.
[259] J. Winterflood, D. G. Blair, and B. Slagmolen, “High performance vibration isolation using springs in Euler column buckling mode,” *Physics Letters A*, vol. 300, no. 2, pp. 122–130, Jul. 2002, doi: 10.1016/S0375-9601(02)00258-X.
[260] K. Kiran Kumar, M. Ravi, Y. Pavani, S. Bhavani, A. K. Sharma, and V. V. R. Narasimha Rao, “Investigations on the effect of complexation of NaF salt with polymer blend (PEO/PVP) electrolytes on ionic conductivity and optical energy band gaps,” *Physica B: Condensed Matter*, vol. 406, no. 9, pp. 1706–1712, Apr. 2011, doi: 10.1016/j.physb.2011.02.010.

[261] M. Gordon and J. S. Taylor, "Ideal copolymers and the second-order transitions of synthetic rubbers. I. Non-crystalline copolymers," *Journal of Applied Chemistry*, vol. 2, no. 9, pp. 493–500, 1952.
[262] J. G. Huddleston, A. E. Visser, W. M. Reichert, H. D. Willauer, G. A. Broker, and R. D. Rogers, "Characterization and comparison of hydrophilic and hydrophobic room temperature ionic liquids incorporating the imidazolium cation," *Green chemistry*, vol. 3, no. 4, pp. 156–164, 2001.
[263] S. V. Kurmaz, N. V. Fadeeva, V. M. Ignat'ev, V. A. Kurmaz, S. A. Kurochkin, and N. S. Emel'yanova, "Structure and State of Water in Branched N-Vinylpyrrolidone Copolymers as Carriers of a Hydrophilic Biologically Active Compound," *Molecules*, vol. 25, no. 24, p. 6015, Dec. 2020, doi: 10.3390/molecules25246015.
[264] S. Shukla, A. K. Bajpai, and J. Bajpai, "Swelling controlled delivery of antibiotic from a hydrophilic macromolecular matrix with hydrophobic moieties," *Macromolecular Research*, vol. 11, no. 4, pp. 273–282, Aug. 2003, doi: 10.1007/BF03218364.
[265] H. Kaplan and A. Güner, "Characterization and determination of swelling and diffusion characteristics of poly(n-vinyl-2-pyrrolidone) hydrogels in water," *Journal of Applied Polymer Science*, vol. 78, no. 5, pp. 994–1000, Oct. 2000, doi: 10.1002/1097-4628(20001031)78:5<994::AID-APP80>3.0.CO;2-R.
[266] M. B. Ahmad and M. B. Huglin, "States of water in poly(methyl methacrylate-co-N-vinyl-2-pyrrolidone) hydrogels during swelling," *Polymer*, vol. 35, no. 9, pp. 1997–2000, Jan. 1994, doi: 10.1016/0032-3861(94)90995-4.
[267] L. M. Muratore, K. Steinhoff, and T. P. Davis, "Self-reinforcing hydrogels comprised of hydrophobic methyl methacrylate macromers copolymerised with either N-vinyl-2-pyrrolidone or 2-hydroxyethyl acrylate," *Journal of Materials Chemistry*, vol. 9, no. 8, pp. 1687–1691, 1999.
[268] A. R. Berens and H. B. Hopfenberg, "Diffusion and relaxation in glassy polymer powders: 2. Separation of diffusion and relaxation parameters," *Polymer*, vol. 19, no. 5, pp. 489–496, May 1978, doi: 10.1016/0032-3861(78)90269-0.
[269] D. Saraydin, E. Karadağ, and O. Güven, "The releases of agrochemicals from radiation induced acrylamide/crotonic acid hydrogels," *Polymer Bulletin*, vol. 41, no. 5, pp. 577–584, 1998.
[270] M. Malak, D. J. Hill, and A. K. Whittaker, "Water sorption into poly[(2-hydroxyethyl methacrylate)-co-(1-vinyl-2-pyrrolidone)]at 310 K," *Polymer International*, vol. 52, no. 11, pp. 1740–1748, Nov. 2003, doi: 10.1002/pi.1284.
[271] C. L. Bell and N. A. Peppas, "Water, solute and protein diffusion in physiologically responsive hydrogels of poly(methacrylic acid-g-ethylene glycol)," *Biomaterials*, vol. 17, no. 12, pp. 1203–1218, Jun. 1996, doi: 10.1016/0142-9612(96)84941-6.
[272] Y. Marcus, "Effect of Ions on the Structure of Water: Structure Making and Breaking," *Chem. Rev.*, vol. 109, no. 3, pp. 1346–1370, Mar. 2009, doi: 10.1021/cr8003828.
[273] K. L. Spiller, S. J. Laurencin, and A. M. Lowman, "Characterization of the behavior of porous hydrogels in model osmotically-conditioned articular cartilage systems," *Journal of Biomedical Materials Research Part B: Applied*

Biomaterials, vol. 90B, no. 2, pp. 752–759, Aug. 2009, doi: 10.1002/jbm.b.31344.
[274] G. Evmenenko and T. Budtova, "Structural changes in hydrogels immersed in a linear polymer solution, studied by SANS," *Polymer*, vol. 41, no. 13, pp. 4943–4947, Jun. 2000, doi: 10.1016/S0032-3861(99)00759-4.
[275] K. Janáček and K. Sigler, "Osmotic pressure: Thermodynamic basis and units of measurement," *Folia Microbiologica*, vol. 41, no. 1, pp. 2–9, Feb. 1996, doi: 10.1007/BF02816331.
[276] Y. Zhao, H. Su, L. Fang, and T. Tan, "Superabsorbent hydrogels from poly(aspartic acid) with salt-, temperature- and pH-responsiveness properties," *Polymer*, vol. 46, no. 14, pp. 5368–5376, Jun. 2005, doi: 10.1016/j.polymer.2005.04.015.
[277] W. Illeperuma, J.-Y. Sun, Z. Suo, and J. Vlassak, "Force and stroke of a hydrogel actuator," *Soft Matter*, vol. 9, p. 8504, Sep. 2013, doi: 10.1039/c3sm51617b.
[278] A. R. Khare, N. A. Peppas, G. Massimo, and P. Colombo, "Measurement of the swelling force in ionic polymeric networks I. Effect of pH and ionic content," *Journal of controlled release*, vol. 22, no. 3, pp. 239–244, 1992.
[279] S. Zhao, "Osmotic Pressure versus Swelling Pressure: Comment on 'Bifunctional Polymer Hydrogel Layers As Forward Osmosis Draw Agents for Continuous Production of Fresh Water Using Solar Energy,'" *Environ. Sci. Technol.*, vol. 48, no. 7, pp. 4212–4213, Apr. 2014, doi: 10.1021/es5006994.
[280] Y. Li and T. Tanaka, "Kinetics of swelling and shrinking of gels," *J. Chem. Phys.*, vol. 92, no. 2, pp. 1365–1371, Jan. 1990, doi: 10.1063/1.458148.
[281] R. Garg, E. Heinzle, and F. Noor, "Hepatocytes of Wistar and Sprague Dawley rats differ significantly in their central metabolism," *Journal of Cellular Biochemistry*, vol. 119, no. 1, pp. 909–917, Jan. 2018, doi: 10.1002/jcb.26255.
[282] C. Marques *et al.*, "High-fat diet-induced obesity Rat model: a comparison between Wistar and Sprague-Dawley Rat," *null*, vol. 5, no. 1, pp. 11–21, Feb. 2016, doi: 10.1080/21623945.2015.1061723.
[283] A. C. Guyton and J. E. Hall, *Textbook of medical physiology*, vol. 548. Saunders Philadelphia, 1986.
[284] S.-I. Murtada, M. Kroon, and G. A. Holzapfel, "Modeling the dispersion effects of contractile fibers in smooth muscles," *Journal of the Mechanics and Physics of Solids*, vol. 58, no. 12, pp. 2065–2082, Dec. 2010, doi: 10.1016/j.jmps.2010.09.003.
[285] Y. Dou, J. Zhao, and H. Gregersen, "Morphology and Stress-Strain Properties Along the Small Intestine in the Rat," *Journal of Biomechanical Engineering*, vol. 125, no. 2, pp. 266–273, Apr. 2003, doi: 10.1115/1.1560140.
[286] J. Whiteway and B. Morson, "Elastosis in diverticular disease of the sigmoid colon.," *Gut*, vol. 26, no. 3, pp. 258–266, 1985.
[287] S. Gay and E. J. Miller, *Collagen in the physiology and pathology of connective tissue*. Fischer, 1978.
[288] G. M. Hass, "Elastic tissue," *Arch. Path.*, vol. 27, p. 334, 1939.
[289] R. E. Neuman and M. A. Logan, "The determination of collagen and elastin in tissues," *Journal of Biological Chemistry*, vol. 186, no. 2, pp. 549–556, 1950.

[290] L. Klein, H. Eichelberger, M. Mirian, and A. Hiltner, “Ultrastructural Properties of Collagen Fibrils in Rat Intestine,” *Connective Tissue Research*, vol. 12, no. 1, pp. 71–78, Jan. 1983, doi: 10.3109/03008208309005613.

[291] J. Diamant, A. Keller, E. Baer, M. Litt, R. G. C. Arridge, and F. C. Frank, “Collagen; ultrastructure and its relation to mechanical properties as a function of ageing,” *Proceedings of the Royal Society of London. Series B. Biological Sciences*, vol. 180, no. 1060, pp. 293–315, Mar. 1972, doi: 10.1098/rspb.1972.0019.

[292] C. S. Chen, M. Mrksich, S. Huang, G. M. Whitesides, and D. E. Ingber, “Geometric control of cell life and death,” *Science*, vol. 276, no. 5317, pp. 1425–1428, 1997.

[293] S. Huang and D. E. Ingber, “The structural and mechanical complexity of cell-growth control,” *Nature Cell Biology*, vol. 1, no. 5, pp. E131–E138, Sep. 1999, doi: 10.1038/13043.

[294] F. Wernig, M. Mayr, and Q. Xu, “Mechanical Stretch-Induced Apoptosis in Smooth Muscle Cells Is Mediated by β1-Integrin Signaling Pathways,” *Hypertension*, vol. 41, no. 4, pp. 903–911, Apr. 2003, doi: 10.1161/01.HYP.0000062882.42265.88.

[295] Y. Knies, A. Bernd, R. Kaufmann, J. Bereiter-Hahn, and S. Kippenberger, “Mechanical stretch induces clustering of β1-integrins and facilitates adhesion,” *Experimental Dermatology*, vol. 15, no. 5, pp. 347–355, May 2006, doi: 10.1111/j.0906-6705.2006.00422.x.

[296] F. Robicsek, J. P. Rielly, and M.-C. Marroum, “The Use of Cyanoacrylate Adhesive (Krazy Glue) in Cardiac Surgery,” *Journal of Cardiac Surgery*, vol. 9, no. 3, pp. 353–356, Apr. 1994, doi: 10.1111/j.1540-8191.1994.tb00855.x.

[297] E. D. Austad, K. A. Pasyk, K. D. McClatchey, and G. W. Cherry, “Histomorphologic Evaluation of Guinea Pig Skin and Soft Tissue after Controlled Tissue Expansion,” *Plastic and Reconstructive Surgery*, vol. 70, no. 6, 1982, [Online]. Available: https://journals.lww.com/plasreconsurg/Fulltext/1982/12000/Histomorphologic_Evaluation_of_Guinea_Pig_Skin_and.8.aspx

[298] S. Yano, M. Komine, M. Fujimoto, H. Okochi, and K. Tamaki, “Mechanical Stretching In Vitro Regulates Signal Transduction Pathways and Cellular Proliferation in Human Epidermal Keratinocytes,” *Journal of Investigative Dermatology*, vol. 122, no. 3, pp. 783–790, Mar. 2004, doi: 10.1111/j.0022-202X.2004.22328.x.

[299] C. C. DuFort, M. J. Paszek, and V. M. Weaver, “Balancing forces: architectural control of mechanotransduction,” *Nature Reviews Molecular Cell Biology*, vol. 12, no. 5, pp. 308–319, May 2011, doi: 10.1038/nrm3112.

[300] Swartz M. A., Tschumperlin D. J., Kamm R. D., and Drazen J. M., “Mechanical stress is communicated between different cell types to elicit matrix remodeling,” *Proceedings of the National Academy of Sciences*, vol. 98, no. 11, pp. 6180–6185, May 2001, doi: 10.1073/pnas.111133298.

[301] F. H. Silver, L. M. Siperko, and G. P. Seehra, “Mechanobiology of force transduction in dermal tissue,” *Skin Research and Technology*, vol. 9, no. 1, pp. 3–23, Feb. 2003, doi: 10.1034/j.1600-0846.2003.00358.x.

[302] R. O. Hynes, “Integrins: Bidirectional, Allosteric Signaling Machines,” *Cell*, vol. 110, no. 6, pp. 673–687, Sep. 2002, doi: 10.1016/S0092-8674(02)00971-6.

[303] S. Chien, “Mechanotransduction and endothelial cell homeostasis: the wisdom of the cell,” *American Journal of Physiology-Heart and Circulatory Physiology*, vol. 292, no. 3, pp. H1209–H1224, Mar. 2007, doi: 10.1152/ajpheart.01047.2006.
[304] Tadokoro Seiji *et al.*, “Talin Binding to Integrin ß Tails: A Final Common Step in Integrin Activation,” *Science*, vol. 302, no. 5642, pp. 103–106, Oct. 2003, doi: 10.1126/science.1086652.
[305] N. O. Carragher and M. C. Frame, “Focal adhesion and actin dynamics: a place where kinases and proteases meet to promote invasion,” *Trends in Cell Biology*, vol. 14, no. 5, pp. 241–249, May 2004, doi: 10.1016/j.tcb.2004.03.011.
[306] M. A. Wozniak, K. Modzelewska, L. Kwong, and P. J. Keely, “Focal adhesion regulation of cell behavior,” *Biochimica et Biophysica Acta (BBA) - Molecular Cell Research*, vol. 1692, no. 2, pp. 103–119, Jul. 2004, doi: 10.1016/j.bbamcr.2004.04.007.
[307] S. K. Mitra, D. A. Hanson, and D. D. Schlaepfer, “Focal adhesion kinase: in command and control of cell motility,” *Nature Reviews Molecular Cell Biology*, vol. 6, no. 1, pp. 56–68, Jan. 2005, doi: 10.1038/nrm1549.
[308] R. M. Ray, S. A. McCormack, C. Covington, M. J. Viar, Y. Zheng, and L. R. Johnson, “The Requirement for Polyamines for Intestinal Epithelial Cell Migration Is Mediated through Rac1 *,” *Journal of Biological Chemistry*, vol. 278, no. 15, pp. 13039–13046, Apr. 2003, doi: 10.1074/jbc.M208741200.
[309] S. Zhang *et al.*, “Rho Family GTPases Regulate p38 Mitogen-activated Protein Kinase through the Downstream Mediator Pak1 (∗),” *Journal of Biological Chemistry*, vol. 270, no. 41, pp. 23934–23936, Oct. 1995, doi: 10.1074/jbc.270.41.23934.
[310] K. M. Diehl, N. Grewal, S. P. Ethier, and K. M. Woods-Ignatoski, “p38MAPK-Activated AKT in HER-2 Overexpressing Human Breast Cancer Cells Acts as an EGF-Independent Survival Signal,” *Journal of Surgical Research*, vol. 142, no. 1, pp. 162–169, Sep. 2007, doi: 10.1016/j.jss.2007.01.025.
[311] V. Bouchard *et al.*, “Fak/Src signaling in human intestinal epithelial cell survival and anoikis: Differentiation state-specific uncoupling with the PI3-K/Akt-1 and MEK/Erk pathways,” *Journal of Cellular Physiology*, vol. 212, no. 3, pp. 717–728, Sep. 2007, doi: 10.1002/jcp.21096.
[312] X. Zhong and F. J. Rescorla, “Cell surface adhesion molecules and adhesion-initiated signaling: Understanding of anoikis resistance mechanisms and therapeutic opportunities,” *Cellular Signalling*, vol. 24, no. 2, pp. 393–401, Feb. 2012, doi: 10.1016/j.cellsig.2011.10.005.
[313] P. J. Newman *et al.*, “Activation-dependent changes in human platelet PECAM-1: phosphorylation, cytoskeletal association, and surface membrane redistribution.,” *Journal of Cell Biology*, vol. 119, no. 1, pp. 239–246, Oct. 1992, doi: 10.1083/jcb.119.1.239.
[314] E. Rijcken *et al.*, “PECAM-1 (CD 31) mediates transendothelial leukocyte migration in experimental colitis,” *American Journal of Physiology-Gastrointestinal and Liver Physiology*, vol. 293, no. 2, pp. G446–G452, Aug. 2007, doi: 10.1152/ajpgi.00097.2007.
[315] G. M. SCHUERMANN *et al.*, “Altered expression of cell adhesion molecules in uninvolved gut in inflammatory bowel disease,” *Clinical and Experimental Immunology*, vol. 94, no. 2, pp. 341–347, Nov. 1993, doi: 10.1111/j.1365-2249.1993.tb03455.x.